THE PURSUIT OF MECHANISTIC INSIGHTS UNDERPINNING CALCIUM-DEPENDENT INACTIVATION OF L-TYPE CALCIUM CHANNELS: ALL ROADS LEAD TO CALMODULIN

by

Worawan (Boombim) Limpitikul

A dissertation submitted to Johns Hopkins University in conformity with
the requirements for the degree o f Doctor of Philosophy

Baltimore, MD

March, 2018

ABSTRACT

L-type calcium channels (LTCCs) are critical conduits for Ca^{2+} entry into many excitable cells. In ventricular myocytes, they are responsible for shaping the action potential and triggering Ca^{2+} release from the sarcoplasmic reticulum leading to myocyte contraction. In the brain, these channels are vital for excitation-transcription coupling, synaptic plasticity, and neuronal firing. To perform their functions properly LTCCs employed two principal forms of feedback regulation which include voltage-dependent inactivation (VDI) and Ca^{2+}-dependent inactivation (CDI). Disruptions in either of these two processes were linked to multiple disorders. For example, mutations in a Ca^{2+} sensor calmodulin (CaM), a known mediator of CDI, have been associated with long-QT syndrome (LQTS). Patients afflicted with these mutations (calmodulinopathies) suffer from life-threatening arrhythmias, refractory to conventional treatments. First, we dissected the mechanistic underpinnings of the LQTS form of calmodulinopathies. We found that disruption of CDI of $Ca_V1.2$ was a major culprit behind this disease. Leveraging off this knowledge, we created a customizable therapy for patients suffering from this group of diseases. Moreover, we investigated mechanisms underlying an autism-associated mutation A760G in $Ca_V1.3$ channels. Interestingly, this mutation disrupts both VDI and CDI of $Ca_V1.3$ which enables us to explore the intimate interplay between VDI and CDI. The knowledge gained from studying these two diseases extend beyond facilitation of therapy development and prove to be valuable in further our understanding in LTCC regulation under a physiologic state.

Next, we utilized an *in silico* approach to complement our *in vitro* disease-based models of LTCC regulations. Although it is well known that each lobe of CaM is capable of responding spatially distinct Ca^{2+} sources, most CDI models fail to capture this unique property of CaM.

Therefore, we developed the first kinetic model of CDI which truly captured the bi-lobal nature of CaM. From this model, we were able to gain deeper insight into the extent of interaction between the two lobes of CaM and explained the pathophysiology behind the LTQS form of calmodulinopathies. Once incorporated into a whole-cell or tissue level model, this novel CDI model could be an invaluable asset in understanding of both physiological and pathological states of the overall cardiac and neuronal electrical activities.

Lastly, we developed an animal model as a new tool to investigate regulations of cardiac LTCCs *in situ*. Understanding of these channels' modulation with high fidelity relies on examining LTCCs in their native environment with intact interacting proteins. Thus, such studies would benefit from genetic manipulation of endogenous LTCCs and their binding partners which often proves cumbersome in mammalian models. We have identified *Drosophila* as an alternative model to study LTCC regulation. Not only is *Drosophila* genetically pliable, but it also possesses conserved Ca^{2+} channels in its cardiomyocytes. Thus, this model may serve as a robust and effective platform for studying *in situ* LTCC regulation.

In all, we utilized multiple approaches to dissect the mechanistic underpinnings of VDI and CDI modulation of LTCCs. We wish that this knowledge could help propel further scientific understanding of these channels' regulations and brought hope to those suffering from dysregulations of these processes.

Thesis Committee: Gordon F. Tomaselli, MD (primary advisor and reader); Ivy E. Dick, PhD (reader); Leslie Tung, PhD; Raimond L. Winslow, PhD; and Anthony Cammarato, PhD.

ACKNOWLEDGEMENTS

No one can say that my nine years of MD-PhD journey was conventional. A lot of the unexpected had happened but with help, support, and love from those around me, I was able to power through. And for this, I am forever grateful.

First, I would like to extend my unreserved appreciation to Dr. Gordon Tomaselli. In the time of need, he stepped up and lent a warm support to all the lost souls of our laboratory. There is no doubt that without his heroic measure, our laboratory would not have been able to carry on for the next few years. On a personal note, he took me under his wing and showed me the fascinating world of clinical electrophysiology. I still remember our first clinic session together. He quizzed me about a wide split S2 heart sound on the patient we examined. Yes, I know now that it is a right bundle branch block but at that time, it was purely magical to me.

Next, I would like to give my biggest thank to Dr. Ivy Dick. She has always been my friend, my moral support, and a magnificent role model. I always believe that how people act during the dire time reflects who they truly are as a person. Through her selfless act and nurturing personality, she managed to keep our laboratory together after David was gone. I am still mesmerized by how she handled herself and us during this hard time. Ivy, there is one thing I want to promise you. One day, I will push myself as hard as I can to become a great and nurturing mentor like you were to me.

I would like to also extent my great appreciation to Dr. Leslie Tung. He has known me since I was a teeny-weeny undergraduate in BME. Despite knowing very little about me, he gave me my first biggest shot at science when I was only in my freshman year. He accepted me into his laboratory and started me along the greatest scientific path of my life. Despite his stoic

exterior, he cares deeply about all of his students. I distinctly and fondly recall how he lovingly fuzzed over the tie and jacket his students, me included, wore to an award ceremony. Moreover, his support extended far beyond my years as an undergraduate student. Right after David was gone, he selflessly stepped in and helped me find funding to continue my research. I superbly worship his generosity and caring nature.

Moreover, I would like to thank my thesis committee. You all have lent a helping hand when I had nowhere else to go. Drs. Winslow and Greenstein, thank you so much for introducing me to the wonder of computational modeling. I had so much fun working with the two of you. Dr. Cammarato, your good humor and optimism towards science have never ceased to amaze me. I cannot say how lucky I am to have crossed path and worked with all of you.

I would like to also thank my family and friends for supporting me throughout this long journey. Thank you so much, mom, for believing in me even when I did not myself. You were the reason I kept doing what I did. Thank you, Pae Sriswasdi, for always being my rock and keeping me grounded. Thank you, Pat Limphong, for taking me under your wing and teaching me everything I needed to know about stem cells. Thank you Hogan and Holly Tang for helping me with fruit fly work at the very beginning when I knew absolutely nothing about the itsy-bitsy fruit flies. Thank you my best of friends, Nui Phimphilai, Tom Yimsiriwattana, Nanoy and Wallace Roberts for being there when I was at my most vulnerable state and nurturing me back to my functional self. Without your help, I would have never been able to pursue my passion in science.

Lastly and most importantly, I want to give my greatest and everlasting appreciation to David Yue, the greatest teacher and most loving mentor I have ever had. David has taught me

how to think critically and nurtured me to become a scientist I am today. He created a sense of family in his laboratory by loving and treating all his students like they were his own children. His everlasting passion for science was undeniably infectious and his love for his students was pure. David, wherever you are, please know this, I would not have been who I am today without you. And for that, I am forever grateful and proud to be trained by you.

TABLE OF CONTENTS

LIST OF TABLES

LIST OF FIGURES

CHAPTER 2

CHAPTER 1

Introduction and background

L-type voltage-gated Ca^{2+} channels (LTCCs) are critical conduits for Ca^{2+} entry into many excitable cells, including skeletal muscle, cardiomyocytes, neurons, and endocrine cells. There are four major types of LTCCs which include $Ca_V1.1$ (skeletal muscle), $Ca_V1.2$ (ventricular cardiomyocytes, neurons, pancreatic β-cells, and adrenal chromaffin cells), $Ca_V1.3$ (atrial cardiomyocytes, neurons, auditory and vestibular hair Cells, and adrenal chromaffin cells), and $Ca_V1.4$ (retinal cells) (Zamponi et al., 2015), each with unique biophysical properties precisely tuned to their functions. Here, we focus on detailed mechanisms underlying regulations of $Ca_V1.2$ and $Ca_V1.3$, the major types of LTCCs in cardiomyocytes and neurons, in both physiologic and pathologic states.

$Ca_V1.2$ and $Ca_v1.3$ channels employ two major forms of feedback regulation, voltage-dependent inactivation (VDI) and Ca^{2+}-dependent inactivation (CDI). The mediator of CDI in these channels is the ubiquitously expressed Ca^{2+} sensor calmodulin (CaM), a 17 kDa protein comprised of N- and C-terminal lobes linked by a flexible helix. Each lobe of CaM contains two EF hands, canonical Ca^{2+} binding motifs, with the N-lobe having slightly lower Ca^{2+} binding affinity. Ca^{2+} binding to these EF hands induces a conformational change that alters function of target molecules to which CaM is bound, thus transducing changes of intracellular Ca^{2+} concentration (Mori et al., 2004) into modulation of molecular function. At a resting level of Ca^{2+}, Ca^{2+}-free CaM (apoCaM) preassociates with the carboxy-tail of the channel (Erickson et al., 2001; Pitt et al., 2001; Mori et al., 2004). This apoCaM bound channel possesses a high open-probability (P_O), known as mode 1 gating (Imredy and Yue, 1994). Upon Ca^{2+} binding,

Ca^{2+}/CaM departs from its preassociation site, resulting in a reduction of the channel P_O (mode Ca gating). Ca^{2+}/CaM then tether to the channel via the Ca^{2+}/CaM effector sites within the amino and carboxy termini of the channel (Ben Johny et al., 2013). Moreover, CaM has the remarkable ability to respond differentially to Ca^{2+} originating from distinct spatial sources. This feature is enabled by the bi-lobal design of CaM, where each lobe is capable of binding Ca^{2+} with different affinities (Dick et al., 2008; Tadross et al., 2008). Specifically, the C-lobe of CaM senses the fluctuation of local Ca^{2+} concentration at the mouth of the channel, while the N-lobe detects the global cytosolic Ca^{2+} level, arising from the cumulative effect of multiple Ca^{2+} sources (Dick et al., 2008; Tadross et al., 2008).

Besides orchestrating CDI, CaM also controls signaling cascades via Ca^{2+}-dependent adjustment of numerous proteins. So important are the functions of CaM that it has long been thought that naturally occurring mutations within this molecule would prove lethal, and that such mutations would thereby play little role in disease processes afflicting living individuals. Yet, a role for CaM in a number of diseases has begun to emerge. Alterations in the overall level of CaM have been implicated in heart failure (Ikeda et al., 2009), schizophrenia (Chambers et al., 2005), and Parkinson disease (Lee et al., 2002; Chan et al., 2007; Bazzazi et al., 2013). Very recently, human genetic studies uncovered *de novo* and heritable CaM mutations (calmoduilnopathies) that are associated with life-threatening cardiac arrhythmias. This new group of diseases includes catecholaminergic polymorphic ventricular tachycardia (CPVT) (Nyegaard et al., 2012; Makita et al., 2014), severe long-QT syndrome (LQTS) (Crotti et al., 2013; Makita et al., 2014; Reed et al., 2014; Boczek et al., 2016), and idiopathic ventricular fibrillation (IVF) (Marsman et al., 2013). The symptoms of these patients are often resistant to conventional therapy, suggesting alternate underlying disease mechanisms which require novel therapeutic

strategies. In Chapter 2, we dissected the mechanistic underpinnings of the LQTS form of calmodulinopathies. We found that a major underlying mechanism concerned the attenuation of $Ca_V1.2$ CDI and that apoCaM preassociation with the channel amplifies the phenotypes of a limited fraction of CaM mutants in the cells. Equipped with this knowledge, we devised customizable therapies for this group of patients (Chapter 3).

In Chapter 4, we utilized an *in silico* approach to gain further understanding of $Ca_V1.2$ CDI. To date, several methods have been deployed to model the CDI of cardiac $Ca_V1.2$ channels. However, they do not take into account the true allosteric and bi-lobal nature of CaM, thus limiting their utility in describing $Ca_V1.2$ gating in response to variable spatial Ca^{2+} signals. One critical barrier to achieving a detailed kinetic model of CDI has been the difficulty in uncoupling channel gating from the Ca^{2+} initiating CDI. To overcome this obstacle, we use Ca^{2+}-photouncaging to deliver a measurable Ca^{2+} input to CaM/$Ca_V1.2$. These high-resolution measurements enable us to build the first full-scale bi-lobal kinetic model of CDI which can accurately recapitulate the kinetics and steady-state properties of CDI in both physiologic and pathologic states. Thus, this model offers powerful new insight into the mechanistic alterations underlying system-level (patho)physiology.

We also examined dysregulation of $Ca_V1.3$, another major type of LTCCs, in Chapter 5. Although $Ca_V1.2$ and $Ca_V1.3$ possess unique biophysical properties finely tuned to each of their biological functions, they shared multiple mechanisms of channel regulation, including VDI and CDI. Here, we focus on the *de novo* missense mutation A760G which has been linked to autism spectrum disorder (ASD) (O'Roak et al., 2012). To explore the role of this mutation in ASD pathogenesis, we examined the effects of A760G on $Ca_V1.3$ channel gating and regulation. Using an allosteric model of channel gating, we found that the underlying mechanism of CDI reduction

is likely due to enhanced channel opening within the Ca^{2+}-inactivated mode. Remarkably, the A760G mutation also caused an opposite increase in VDI, resulting in a multifaceted mechanism underlying ASD. When combined, these regulatory deficits appear to increase the intracellular Ca^{2+} concentration, thus potentially disrupting neuronal development and synapse formation, ultimately leading to ASD.

Besides investigating LTCC regulation in mammalian systems, we also developed an animal model that allows investigating LTCCs in their native environment with intact interacting proteins (Chapter 6). *Drosophila* offers a potentially efficient alternative to mammalian models as it possesses a relatively simple heart, is genetically pliable, and expresses well-conserved genes. Through genetic and functional characterizations, we found that *Drosophila* heart possessed a conserved compendium of Ca^{2+} channels (LTCCs and T-type Ca^{2+} channels). Moreover *Drosophila* LTCCs maintained major regulations observed in mammalian cardiac LTCCs, such as VDI, CDI, and current augmentation via adrenergic stimulation. Thus, the *Drosophila* heart may serve as a robust and effective platform for studying LTCC modulations *in situ.*

In all, this work utilized multiple approaches to dissect the mechanistic underpinnings of LTCC regulation, including *in vitro* investigation of LTCC current in both physiologic and pathologic states, construction of an *in silico* model of $Ca_V1.2$ CDI, and development of a genetically pliable animal model to study modulation of $Ca_V1.2$ *in situ*. The knowledge gained from this study could offer invaluable insight into mechanisms underlying LTCC regulation in both human's physiologic and diseased states.

CHAPTER 2

Mechanistic dissection of calmodolinopathies

2.1 Introduction

CaM is a ubiquitous Ca^{2+}-sensor molecule that modulates a vast array of proteins, thereby controlling signaling cascades via Ca^{2+}-dependent adjustment of relevant proteins. As such, CaM critically orchestrates numerous functions, including cellular excitability, muscle contraction, memory, and immunological responses (Hoeflich and Ikura, 2002; Pitt, 2007). So important are the functions of CaM that it has long been thought that naturally occurring mutations within this molecule would prove lethal, and that such mutations would thereby play little role in disease processes afflicting living individuals. Yet, a role for CaM in numerous diseases has begun to emerge. Perturbations in the overall level of CaM have been implicated in heart failure (Ikeda et al., 2009), schizophrenia (Chambers et al., 2005), and Parkinson's disease (Lee et al., 2002; Chan et al., 2007; Bazzazi et al., 2013). Outright CaM mutations in *Drosophila* have been associated with muscle malfunction (Wang et al., 2003). Very recently, human genetic studies uncovered *de novo* and heritable CaM mutations associated with CPVT (N54I and N98S) (Nyegaard et al., 2012) and LQTS (D96V, D130G, and F142L) (Crotti et al., 2013). Each of the LQTS mutations resides at or near Ca^{2+} coordinating residues within the EF hands of the C-lobe of CaM, and have been shown to decrease affinity for Ca^{2+} binding (Crotti et al., 2013). By contrast, the reported CPVT mutations in CaM imparted little-to-mild reduction of Ca^{2+} binding affinity (Nyegaard et al., 2012). It is perhaps interesting to speculate that the contrasting effects on Ca^{2+} binding may underlie the elaboration of distinguishable LQTS and CPVT phenotypes by these two classes of

mutations. At present, however, the mechanisms linking these mutations in CaM to their corresponding disease phenotypes are essentially unknown.

That being said, progress towards elucidating these mechanisms will ultimately prove invaluable in devising personalized therapeutics for afflicted individuals and in gleaning general lessons about LQTS pathogenesis from these single-point-mutation case examples. Among the most prominent mechanistic unknowns are the following. First, do the LQTS CaM mutations actually cause the emergence of LQTS substrates in heart? Currently, no experimental evidence directly establishes such causality. Second, what are the predominant molecular targets through which CaM mutations exert their actions in heart? Likely cardiomyocyte targets abound, including ryanodine receptors (RyR2), voltage-gated Na channels ($Na_V1.5$), slowly activating delayed-rectifier K channels (I_{Ks}), and LTCCs (Mori et al., 2004; Saucerman and Bers, 2012; Crotti et al., 2013) ($Ca_V1.2$). All of these contribute to shaping action-potential morphology and thereby represent plausible candidates. Third, the severity of the LQTS fits in a seemingly incongruous fashion with the redundancy of human CaM genes (*CALM1*, *CALM2*, and *CALM3*), each of which encodes for an identical CaM molecule at the protein level. Given the heterozygosity of these LQTS patients (Crotti et al., 2013), this redundancy implies that only one of six alleles of CaM would possess a mutation, yielding only a portion of mutant versus wild-type CaM.

Here, therefore, we acutely introduce LQTS CaM mutants into adult guinea-pig ventricular myocytes (aGPVMs) and demonstrate marked prolongation of action potentials, along with intense disturbance of Ca^{2+} cycling. As these effects are reminiscent of those we observed previously by man-made CaM mutants acting strongly through diminished CaM-mediated regulation of LTCCs (Alseikhan et al., 2002), we tested directly for the effects of

naturally occurring LQTS CaM mutants on these very channels. Indeed, we establish that Ca^{2+} regulation of LTCCs can be strongly suppressed by overexpression of LQTS CaM mutants, posturing altered regulation of these channels as an important contributor to the LQTS phenotype. By contrast, overexpressing CPVT CaM mutants caused weaker or undetectable perturbation of LTCC function and action potentials. Finally, we note the requirement that a single Ca^{2+}-free CaM (apoCaM) must first preassociate with LTCCs for subsequent Ca^{2+} regulation to occur (Erickson et al., 2001; Pitt et al., 2001; Mori et al., 2004; Liu et al., 2010; Bazzazi et al., 2013; Ben Johny et al., 2013), and substantiate how this feature rationalizes how a limited fraction of LQTS CaM mutants can nonetheless elaborate significant perturbation of channel regulation, sufficient to appreciably prolong action potentials.

2.2 Materials and methods

2.2.1 Adult guinea-pig ventricular myocyte isolation and adenoviral transduction

Adult guinea-pig ventricular myocytes (aGPVMs) were isolated from whole hearts of adult guinea pigs (Hartley strain, 3–4 wk old, weight 250–350 g). Hearts were excised after guinea pigs were anesthetized with pentobarbital (35 mg/ kg, intraperitoneal injection). Single ventricular myocytes were isolated from both ventricles according to a published protocol (Joshi-Mukherjee et al., 2013) and plated on glass coverslips coated with laminin (20 μg/ml overnight at 4 °C). Cells were transduced with adenovirus carrying wild-type or mutant CaM upon plating in the presence of M199 medium supplemented with 20% fetal bovine serum. Expression of wild-type CaM had little effect on action-potential morphology or duration, as compared to uninfected myocytes (Supplementary Figure 2.1). After 4 hours, the medium was replaced by M199

medium with 0% fetal bovine serum to maintain the phenotype of acutely dissociated myocytes. Cells were maintained at 37 ºC and recording was done at room temperature 20-36 hours later.

2.2.2 Molecular biology

LQTS CaM mutations were generated using QuikChange™ site-directed mutagenesis (Agilent) on rat brain CaM (M17069) in the pcDNA3 vector (Alseikhan et al., 2002) (Invitrogen). CPVT CaM mutations were generated on human *CALM1* gene in the pcDNA3 vector (a kind gift from Michael T. Overgaard (Nyegaard et al., 2012)). For electrophysiological recordings in HEK293 cells, both wild-type and LQTS mutant CaMs were cloned into the pIRES2-EGFP vector (Clontech Laboratories, Inc.) using *NheI* and *BglII*. For adenoviral expression in aGPVMs, wild-type and mutant CaMs were cloned into the pAdCiG viral shuttle vector using *XhoI* and *SpeI*. Adenovirus was amplified via a standard cre-recombinase method as previously described (Alseikhan et al., 2002).

The human cardiac α_{1C} cDNA was constructed by cloning in an ~1.6 kb upstream fragment of the cardiac (containing exon 8a) channel variant (kind gift from Tuck Wah Soong (Tang et al., 2004)) into a human $\alpha_{1C\text{-}1}$ backbone (NM_000719 kindly gifted from Charlie Cohen of Merck Pharmaceuticals) contained within pcDNA3.1, via *HindIII* and *ClaI* sites.

For FRET two-hybrid constructs, CaM and CI region of $Ca_V1.2$ channels (as defined in Figure 5A and described previously (Ben Johny et al., 2013)) were tagged on their amino termini with fluorophores (cerulean and venus, respectively) with a linker of 3 alanines, and cloned into the pcDNA3.0 (Invitrogen) using *KpnI* and *XbaI*.

2.2.3 Transfection of HEK293 cells

For whole-cell patch clamp experiments, HEK293 cells were cultured on glass coverslips in 10-cm dishes and Ca^{2+} channels were transiently transfected using a standard calcium phosphate method (Peterson et al., 1999). 8 μg of human cardiac α_{1C} cDNA (as described above) was co-expressed heterologously with 8 μg of rat brain β_{2a} (M80545), 8 μg of rat brain $\alpha_2\delta$ (NM012919.2) subunits, and 8 μg of wild-type or mutant CaMs, except for mixing experiments (Figure 2.6) where various molar ratios of wild-type to mutant CaM were transfected. The auxiliary β_{2a} subunit was chosen so as to minimize the confounding effects of voltage-dependent inactivation on CDI (Dafi et al., 2004). To increase expression levels, 2 μg of simian virus 40 T antigen cDNA was co-transfected. Expression of all constructs was driven by a cytomegalovirus promoter.

For FRET two-hybrid experiments, HEK293 cells were cultured on glass-bottom dishes and transfected with polyethylenimine (Lambert et al., 1996) (PEI) before epifluorescence imaging. Whole-cell patch clamp and FRET two-hybrid experiments were performed 1-2 days after transfection.

2.2.4 Electrophysiology

Whole-cell voltage-clamp recordings of HEK293 cells were done 1-2 days after transfection at room temperature. Recordings were obtained using an Axopatch 200B amplifier (Axon Instruments). Whole-cell voltage-clamp records were lowpass filtered at 2 kHz, and then digitally sampled at 10 kHz. P/8 leak subtraction was used, with series resistances of 1-2 MΩ. For voltage-clamp experiments, internal solutions contained (in mM): $CsMeSO_3$, 114; CsCl, 5; $MgCl_2$, 1; MgATP, 4; HEPES (pH 7.3), 10; and either BAPTA, 10 or EGTA, 1; at 295 mOsm

adjusted with $CsMeSO_3$. The free Ca^{2+} concentrations in these BAPTA- and EGTA-containing solutions were respectively estimated to be ~2.4 and 0.45 pM (Moretti et al., 2010), assuming a contaminant Ca^{2+} concentration of 25 μM (standard conversion at http://maxchelator.stanford.edu/). External solutions contained (in mM): TEA-$MeSO_3$, 140; HEPES (pH 7.4), 10; and $CaCl_2$ or $BaCl_2$, 40; at 300 mOsm, adjusted with TEA-$MeSO_3$. These solutions produced the following uncorrected junction potentials: 10 BAPTA/40 Ca^{2+}: 10.5 mV; 10 BAPTA/40 Ba^{2+}: 10.2 mV; 1 EGTA/40 Ca^{2+}: 11.4 mV; 1 EGTA/40 Ba^{2+}: 11.1 mV (Barry, 1994). Fraction of peak current remaining after 300-ms depolarization (r_{300}) at various voltages were measured. The extent of Ca^{2+}/CaM-dependent inactivation (CDI) was calculated as $f_{300} = (r_{300/\mathrm{Ba}} - r_{300/\mathrm{Ca}}) / r_{300/\mathrm{Ba}}$.

Whole-cell recordings of aGPVMs were performed 20-36 hours post isolation on the same recording setup. Internal solutions for voltage clamp experiments contained, (in mM): $CsMeSO_3$, 114; CsCl, 5; $MgCl_2$, 1; MgATP, 4; HEPES (pH 7.3), 10; BAPTA, 10; and ryanodine, 0.005; at 295 mOsm adjusted with $CsMeSO_3$. External solutions contained (in mM): TEA-$MeSO_3$, 140; HEPES (pH 7.4), 10; and $CaCl_2$ or $BaCl_2$, 5; at 300 mOsm, adjusted with TEA-$MeSO_3$. These solutions produced an 8.4 mV uncorrected junction potential (Barry, 1994). For current clamp, experiments, internal solutions contained (in mM): K glutamate, 130; KCI, 9; NaCl,10; $MgCl_2$, 0.5; EGTA, 0.5; MgATP, 4; HEPES, 10 (pH 7.3 with KOH). External solution (Tyrode's solution) contained (in mM): NaCl, 135; KCl, 5.4; $CaCl_2$, 1.8; $MgCl_2$, 0.33; NaH_2PO_4, 0.33; HEPES, 5; glucose, 5 (pH 7.4). Junction potentials for current-clamp solutions were calculated to be only 0.5 mV (Barry, 1994). The time from upstroke to 80% repolarization (APD_{80}) was used as the metric for action potential duration throughout. SD_{cell}, the mean standard deviation of APD_{80} within individual cells, was used to assess the dispersion of APD_{80}

at the same expression level of CaM. Throughout, whole-cell voltage-clamp records were lowpass filtered at 2 kHz, and then digitally sampled at 10 kHz. Current-clamp recordings were filtered at 5 kHz, and sampled at 25 kHz.

2.2.5 Ratiometric Ca^{2+} imaging

Single aGPVMs were plated on glass-bottom dishes coated with laminin. Cells were loaded with Indo-1 AM (1 μM) at room temperature for 5 minutes, rinsed, and further incubated for 10 minutes in Tyrode's solution at room temperature to allow for de-esterification of Indo-1 AM. Cells were stimulated by application of an electric field across individual cells using a Grass stimulator (SDD9) and bipolar point platinum electrodes. Recordings were made at room temperature in Tyrode's solution supplemented with 10 μM ascorbic acid (Sathaye et al., 2006) to buffer free radicals generated from electrical pacing and exposure to UV light. Fluorescence was measured using 340-nm excitation and 405- to 485-nm emission wavelengths. The intracellular Ca^{2+} concentration ($[Ca^{2+}]$) was calculated as $[Ca^{2+}] = K_{d/Indo} \cdot \beta \cdot (R - R_{\min})/(R_{\max} - R)$. R is the ratio of fluorescence signal at 405 and 485 nm. $K_{d/Indo}$ was determined as 800 nM (Bassani et al., 1995). $R_{\min}$ was determined to be 0.53 in a 0 mM Ca^{2+} Tyrode's with 5 mM EGTA and 1 μM ionomycin. $R_{\max}$ was determined to be 2.60 in a Na^+-free Tyrode's (Na^+ was replaced with choline ion to minimize the action of Na-Ca exchanger) with 10 mM Ca^{2+}, 1 μM ionomycin and 10 mM 2,3-butanedione monoxime. β, as defined by the ratio of fluorescence signal at 485 nM under Ca^{2+}-free and Ca^{2+}-bound conditions, was determined to be 2.33. Cells were stimulated with a single electrical pulse after steady-state pacing at 0.1 Hz. The total amount of Ca^{2+} entry was determined by integration of the area under Ca^{2+}-versus-time waveforms. Sarcoplasmic reticulum Ca^{2+} content (SR content) was determined

by application of 5 mM caffeine to aGPVMs superfused with a Na^+-free Tyrode's (Na^+ was replaced with choline), containing 1.8 mM Ca^{2+} and 10 mM 2,3-butanedione monoxime. The concentration of caffeine was chosen to minimize Indo-1 quenching (McKemy et al., 2000) but was still sufficient to empty the sarcoplasmic reticulum.

2.2.6 FRET two-hybrid measurement

Three-cube FRET measurements were performed on HEK293 cells cultured on glass-bottom dishes using an inverted fluorescence microscope in modified Tyrode's solution (in mM, NaCl, 138; KCl, 4; $CaCl_2$, 2; $MgCl_2$, 1; HEPES, 10; glucose, 10). FRET efficiency (E_A) of individual cells was computed based on a published protocol (Erickson et al., 2001). Differential expression of test constructs across individual cells allowed decoration of a binding curve. Effective dissociation constants ($K_{d,EFF}$) were calculated by fitting the binding curve with the equation $E_A = [D]_{free} / (K_{d,EFF} + [D]_{free}) \cdot E_{A,max}$, where $[D]_{free}$ is the free concentration of donor molecules.

2.2.7 Data analysis and statistics

All data were analyzed in MATLAB (The MathWorks) using custom-written scripts. For APD_{80} and Ca^{2+} transient measurements the Wilcox rank sum test was used to assess statistical significance of differences between cells expressing wild-type and mutant CaMs. In addition, variability not due to expression differences was assessed by calculating the standard deviation within each cell (SD_{cell}) for both APD_{80} and Ca^{2+} transient measurements. Statistical significance for variability was determined by a student's t-test with the Bonferroni correction for multiple samples as appropriate. Average Ca^{2+} transients are displayed ± SD. Statistical significance for SR content was assessed using a Student's t-test with a Bonferroni correction for multiple

samples. The values are displayed as mean ± SEM. For electrophysiology and FRET two-hybrid measurements, f_{300} and E_A values were expressed as mean ± SEM, and a student's t-test was used to assess statistical significance.

2.3 Results

2.3.1 CaM mutants promote proarrhythmic electrical and Ca^{2+} activity in ventricular myocytes

CaM mutations have been associated with severe LQTS and recurrent cardiac arrest (Crotti et al., 2013), but to date, no direct evidence exists that these mutations can actually promote proarrhythmic properties in an experimental cardiac model. Accordingly, before investigating specific Ca^{2+} regulatory disturbances relating to the interaction of LQTS CaM mutants and individual molecular targets, we tested whether the expression of these mutants at all perturbed the overall electrical and Ca^{2+} cycling properties of aGPVMs. This particular model was chosen because it features action potentials with a prominent plateau phase reminiscent of that in humans, making this system particularly suitable for understanding long-QT phenomena.

Figure 2.1A displays the prototypic action potentials of a single such myocyte expressing only wild-type CaM (CaM_{WT}), obtained at 0.5-Hz stimulation under whole-cell current clamp. The timing of current injection stimuli is shown underneath for orientation. The waveforms are nearly identical from one stimulus to the next, with a mean action potential duration (APD_{80}) of ~300 ms (Alseikhan et al., 2002). Population behavior for APD_{80} is summarized in Figure 2.1B, which plots the cumulative distribution of durations drawn from 285 responses in 10 cells, where P_{APD} is the probability that APD_{80} is less than the value on the abscissa. The sharp rise of the distribution confirms a mean duration of 349.6 ms, with a modest standard deviation of 79.6 ms. Additionally, the mean standard deviation of APDs within individual myocytes (SD_{cell}, intra-cell

standard deviation) was only 21 ms, further indicating relatively homogeneous behavior. By contrast, adenoviral-mediated expression of CaM_{D96V} induced a strikingly different profile (Figure 2.1C). Here, action potentials could be enormously elongated (red), exceeding even the inter-stimulus interval of 2 seconds. For reference, the control waveform with only CaM_{WT} present is reproduced in gray. Population data, displayed in cumulative histogram format (Figure 2.1D), reveal marked lengthening and dispersion of APD_{80} values (red), with mean and standard-deviation values of 897.3 and 222.9 ms ($p < 0.001$). Here, SD_{cell} increased to 156.3 ms, indicating significant variability within each cell as compared to CaM_{WT} ($p < 0.01$). Both of these features furnish the cellular substrates for electrically driven arrhythmias at the tissue and organ level (Arevalo et al., 2007). Similar results were obtained for expression of CaM_{D130G} (Figures 2.1E-F, APD_{80} = 915.3 ± 231.7 ms, $p < 0.001$; SD_{cell} = 78.5 ms, $p \leq 0.01$) and CaM_{F142L} (Figures 2.1G-H, APD_{80} = 864.9 ± 320.1 ms, $p < 0.001$; SD_{cell} = 179.1 ms, $p < 0.01$). The exemplar for CaM_{D130G} illustrates the occurrence of alternans (Figure 2.1E), and that for CaM_{F142L} exemplifies simple APD prolongation. All these behaviors (Figures 2.1C, E, and G) could be observed in the presence of any of the CaM mutants and persist at faster pacing rates (Supplementary Figure 2.2). Detailed parameters for action potential recordings are in Table 2.1 and Supplementary Table 2.1.

Beyond electrical disturbances, Ca^{2+} cycling dysfunction may also drive arrhythmogenesis (Xie and Weiss, 2009). Accordingly, we examined the effect of LQTS CaM mutant expression on intracellular Ca^{2+} transients. Figure 2.1I displays the typical Ca^{2+} waveform in a myocyte expressing only CaM_{WT}. Ratiometric Indo-1 imaging was used to gauge Ca^{2+} activity, and data are shown as the mean ± SD drawn from multiple cells. The black trace plots the mean, and standard deviation bounds are shown by gray shadows. Upon expression of

CaM_{D96V}, Ca^{2+} transients are markedly amplified and prolonged (Figure 2.1J, red). Reproduction of the control CaM_{WT} waveform (gray) serves to emphasize the strong changes in Ca^{2+} activity. Likewise, expression of CaM_{D130G} and CaM_{F142L} produced similarly striking increases of Ca^{2+} transients (Figures 2.1K-L). Representing these data in cumulative histogram format serves to emphasize the increased dispersion of peak Ca^{2+} transient amplitude produced by CaM mutants (Figures 2.1M-N). Shown here are the cumulative probabilities of the area under Ca^{2+} transients (P_Q) for CaM_{WT} and CaM mutants as labeled. The precipitous rise of the wild-type distribution confirms the similarity of Ca^{2+} amplitudes among cells (Figure 2.1M, black relation). By contrast, the sluggish rise of distributions for CaM mutants (Figures 2.1M and N, red relations) reveals marked heterogeneity of Ca^{2+} transients among cells, as confirmed by significantly larger intra-cell standard deviations (gray bars, $p < 0.05$). Additionally, both diastolic Ca^{2+} concentrations and SR Ca^{2+} content were significantly elevated by overexpressing LQTS CaM mutants (Supplementary Figure 2.3). In all, CaM mutants furnish the cellular substrates for Ca^{2+}-driven arrhythmias (Xie and Weiss, 2009), by increasing amplitude and dispersion of Ca^{2+} transients, heightening diastolic Ca^{2+} concentration, and augmenting SR Ca^{2+} content.

2.3.2 LQTS calmodulin mutants suppress CDI of $Ca_V1.2$ Ca^{2+} channels

The ability of naturally occurring LQTS CaM mutants to prolong and disperse action potentials was reminiscent of effects we and others observed previously under expression of man-made CaM mutants in the same and similar model systems (Alseikhan et al., 2002; Mahajan et al., 2008a). There, many of the action potential effects could be attributed to the suppression of CDI of $Ca_V1.2$ Ca^{2+} channels. We therefore tested for the effects of the naturally occurring LQTS-related CaM mutants on $Ca_V1.2$ CDI, heterologously expressed in HEK293 cells for maximal biophysical resolution. In this regard, $Ca_V1.2$ expression here included the use of an

auxiliary β_{2a} subunit to better visualize CDI effects by minimizing voltage-dependent inactivation (Dafi et al., 2004).

Figure 2.2A displays exemplar currents of $Ca_V1.2$ channels coexpressed with CaM_{WT}. The sharp decay of Ca^{2+} current (red) evoked by a 30- mV depolarizing step is the well-known result of the CDI process. As confirmation, Ba^{2+} current (black) evoked in the same cell hardly decays, as Ba^{2+} binds poorly to CaM. Population data shown below (Figures 2.2B-C) rounds out characterization of the baseline behavior of channels in the presence of CaM_{WT}. Figure 2.2B displays the average of the peak normalized Ba^{2+} current as a function of step potentials, and Figure 2.2C plots the fraction of peak current remaining after 300-ms depolarization to various voltages (r_{300}). The U-shaped Ca^{2+} r_{300} relation (red) recapitulates the classic hallmark of CDI (Brehm and Eckert, 1978; Brehm et al., 1980), while the flat $Ba^{2+}r_{300}$ relation (black) confirms the lack of appreciable inactivation without activation of CaM. Hence, the difference between Ba^{2+} and Ca^{2+} r_{300} relations at 30 mV, as normalized by the corresponding Ba^{2+} r_{300} value, formally gauges the extent of CDI ($f_{300} = 0.690 \pm 0.028$).

Upon coexpressing $Ca_V1.2$ channels with mutant CaM_{D96V}, a starkly different functional profile is observed (Figures 2.2D-F). Here, CDI is strongly suppressed ($f_{300} = -0.009 \pm 0.008$, $p < 0.001$), without shift in the voltage activation profile (Figure 2.2E). Similarly, coexpression of channels with CaM_{D130G} or CaM_{F142L} also sharply diminished CDI (Figures 2.2G-I and Figures 2.2J-L, $f_{300} = -0.002 \pm 0.011$, $p < 0.001$ and 0.065 ± 0.005, $p < 0.001$, respectively). The above results were obtained with strong intracellular Ca^{2+} buffering by 10 mM BAPTA, to restrict Ca^{2+} elevations to those in the nanodomains of individual channels, and thereby minimize cell-to-cell variations owing to differences in current amplitudes. Importantly, however, under more physiological Ca^{2+} buffering (1 mM EGTA) that allows global elevation of Ca^{2+}, strong but

incomplete blunting of CDI was produced by the CaM mutants (Supplementary Figure 2.4). This residual CDI can be attributed to signaling through the N-terminal lobe of CaM (largely unaffected in LQTS CaM mutants), which is sensitive to sustained global elevation of calcium (Dick et al., 2008; Tadross et al., 2008). Overall, the naturally occurring CaM mutants suppressed $Ca_V1.2$ channel CDI, in a manner indistinguishable from that of a man-made mutant CaM_{34} molecules that selectively eliminate Ca^{2+} binding to the C- but not N-terminal lobe of this molecule (Peterson et al., 1999; Dick et al., 2008; Tadross et al., 2008).

By contrast, overexpressing CPVT CaM mutants had weaker effects on $Ca_V1.2$ channel CDI. CaM_{N54I} yielded no appreciable change in CDI compared to CaM_{WT} (Figures 2.3A-C, f_{300} = 0.583 ± 0.043, $p > 0.01$). On the other hand, CaM_{N98S} managed only to partially diminish CDI (Figures 2.3F-H, f_{300} = 0.367 ± 0.023, $p < 0.001$). Both results in Figure 2.3 were obtained under high Ca^{2+} buffering conditions (10 mM BAPTA). Under more physiological Ca^{2+} buffering (1 mM EGTA), we observed a similar trend wherein CaM_{N54I} and CaM_{N98S} exerted at most modest diminution of CDI (Supplementary Figure 2.5). To assess further the more integrative consequences of these CDI profiles (Figures 2.3A-C, F-H), we investigated the effects of these CPVT CaM mutants within aGPVMs. As might be expected, action potentials in the presence of CaM_{N54I} were nearly identical to those with CaM_{WT} (Figures 2.3D-E). On the other hand, CaM_{N98S} significantly prolonged action potentials (Figures 2.3I-J, red $p < 0.01$) as compared to CaM_{WT} (gray). Additionally, intra-cell standard deviation (Figure 2.3J, gray bar) was also larger than CaM_{WT} ($p < 0.05$), positioning CaM_{N98S} for moderate LQTS and affiliated arrhythmias. For CaM_{N54I}, the nearly complete lack of effect on CDI helps explain why this mutation was not associated with LQTS. Interestingly, the intermediate effects of CaM_{N98S} on CDI and action potentials match well with reports of LQTS in an unrelated patient (Makita et al., 2013).

Thus far, we have demonstrated the ability of the naturally occurring LQTS CaM mutants to markedly attenuate CDI of $Ca_V1.2$ channels heterologously expressed in HEK293 cells, to facilitate biophysical resolution. Nonetheless, we next wondered whether similar effects would be observed in native L-type Ca^{2+} currents, as present in the same aGPVMs as used in Figure 2.1. Figure 2.4A displays exemplar L-type currents evoked under whole-cell voltage clamp, using 10 mM BAPTA as the intracellular Ca^{2+} buffer, so as to mimic the condition of Figure 2.2. Ryanodine (5 μM) was included in the intracellular dialyzate to eliminate phasic Ca^{2+} release from the sarcoplasmic reticulum, and limit CDI to that driven by Ca^{2+} entry through individual L-type Ca^{2+} channels (Grandi et al., 2010). We again observed strong CDI when Ca^{2+} was used as the charge carrier (red) as compared to a limited amount of voltage-dependent inactivation (VDI) seen in the Ba^{2+} current (black). This additional VDI component is expected in this native setting due to a mix of endogenous beta subunits (Hullin et al., 1992; Olcese et al., 1994), compared to the pure population of β_{2a} subunits utilized in HEK293 cell experiments. That said, the baseline f_{300} value estimating isolated CDI in control myocytes (Figures 2.4A-C) was nonetheless 0.67 ± 0.04 (obtained at 20-mV step), which is quite similar to that obtained in recombinant channel expression experiments (Figure 2.2C). Likewise, population data shows a similar current-voltage relationship and U-shaped Ca^{2+} r_{300} curve (Figures 2.4B-C). Importantly, expression of mutant CaM_{D96V} essentially abolished CDI in this native setting (f_{300}= -0.18 ± 0.03, $p < 0.001$, Figures 2.4D-F) and so did CaM_{D130G} and CaM_{F142L} (f_{300}= 0.02 ± 0.09, $p < 0.001$, Figures 2.4G-I and -0.09 ± 0.03 , $P < 0.001$, Figures 2.4J-L , respectively), supporting a strong mechanistic link between $Ca_V1.2$ channel deficits and the LQTS effects seen in patients carrying the CaM mutations.

2.3.3 Limited expression of LQTS CaM molecules still affects $Ca_V1.2$ channel CDI

We have so far demonstrated that strong overexpression of LQTS-associated CaM molecules in myocytes can produce both strongly dysfunctional electrical and Ca^{2+} cycling, and potently diminished CDI. However, in the actual related patient population, only one of six alleles encodes a mutant CaM, while the other alleles would elaborate wild-type CaM. Accordingly, we would anticipate that only a limited fraction of CaM molecules would bear the pathogenic mutation (Crotti et al., 2013). How then could the significant cardiac deficits encountered by patients be rationalized? Previous mechanistic studies of L-type channel CDI offer a potential explanation. In particular, it has been shown that for CDI to occur, channels must initially preassociate with a Ca^{2+}-free CaM (apoCaM), to which subsequent Ca^{2+} binding triggers CDI (Zuhlke et al., 1999; Erickson et al., 2001). That is, bulk CaM in the cytoplasm does not appreciably trigger CDI. Thus, if LQTS-associated mutant CaM molecules can still preassociate on par with wild-type CaM, then a sizeable fraction of channels would be bound to mutant CaM, and thus unable to undergo strong CDI (Figures 2.2 and 2.3). Thus, the overall decrease in CDI should be appreciable, reflecting the aggregate fractional presence of mutant CaM in cells.

Accordingly, we utilized a well-established live-cell FRET two-hybrid binding assay to determine whether mutant CaMs can still interact with $Ca_V1.2$, in a manner similar to wild-type CaM. Figure 2.5A (top) cartoons the relevant sites of apoCaM interaction with $Ca_V1.2$ channels, in particular the CI region of the channel carboxy tail. Our FRET assay therefore paired the $Ca_V1.2$ CI region with CaM (Figure 2.5A, bottom). As baseline reference, Figure 2.5B shows the canonical binding curve between the CI region and CaM_{WT}, where this plot displays the acceptor-centric FRET efficiency of interaction (E_A) as a function of the relative free

concentration of donor-tagged molecules D_{free} (cerulean-CaM_{WT}). The curve resembles a typical binding reaction, and the D_{free} that produces half-maximal E_A yields an effective dissociation constant ($K_{d,EFF}$) of 12,000 D_{free} units (Bazzazi et al., 2013). Reassuringly all three mutant CaM molecules bind at least as well as wild-type CaM (Figures 2.5B-5E), demonstrating that mixed expression of mutant and wild-type CaM will result in some fraction of channels bound to mutant CaM.

To test this notion quantitatively, we first devised simple means to control the expression ratio of wild-type to mutant CaM molecules ($\hat{\gamma}$) (Supplementary Note 2.6.6). Then, we performed whole-cell electrophysiology experiments to test explicitly whether the strength of CDI in $Ca_V1.2$ channels would be graded by different $\hat{\gamma}$ values, just as anticipated by the relative binding affinities of channels for mutant versus wild-type apoCaM (Figures 2.5B-E). Here, our approach was to strongly overexpress variable ratios of such molecules so that the contribution of endogenous CaM would be negligible. If such a scenario were to hold true, we could quantitatively predict that the aggregate CDI strength (*CDI*) as a function of the protein expression ratio of wild-type to mutant CaM, as the Langmuir equation in Figure 2.6A (Supplementary Note 2.6.7). CDI_{WT} is the full-strength CDI measured with only wild-type CaM strongly overexpressed, and $K_{d/WT}$ and $K_{d/MUT}$ are the dissociation constants for channel preassociation with wild-type and mutant apoCaM, as specified in Figures 2.5B-E. Figure 2.6B plots this relation explicitly as the smooth black curve. Colored data symbols, with corresponding exemplar traces in Figure 2.6C, nicely decorate this Langmuir function, as do data from numerous other cells (open symbols in Figure 2.6B). Similar results were obtained for the other two LQTS-associated CaM mutants (Supplementary Figure 2.9). Thus, mixtures of wild-type and mutant CaM would weaken L-type channel CDI as predicted by the relative channel

affinities for these two molecules in their Ca^{2+}-free form. Based on the relative expression profile of each *CALM* during infancy (Crotti et al., 2013), heterozygous D96V mutation on *CALM2* gene yields $\hat{\gamma}$ ~7, predicting the substantial decrement of CDI indicated by the light rose shading in Figure 2.6B, likely sufficient to appreciably prolong APDs (Mahajan et al., 2008a; Morotti et al., 2012). Interestingly, the corresponding prediction for a hypothetical homozygous scenario ($\hat{\gamma}$ ~3, dark rose shading) suggests a severe reduction in CDI, potentially incompatible with life. This would perhaps predict the absence of living homozygous individuals.

In all, we would argue that the electrical and calcium dysfunction affiliated with LQTS-associated CaM mutations arises as summarized in Figure 2.7. Mutant CaM elaborated by a single allele among three *CALM* genes would yield a mixture of wild-type and mutant CaM molecules, as specified by the expression ratio $\hat{\gamma}$. Because channels must first preassociate with apoCaM to undergo subsequent CDI, this fractional expression of mutant CaM would produce graded reduction of overall CDI in myocytes, as demonstrated in Figure 2.6. This decrement of Ca^{2+} feedback inhibition would elaborate abnormally long action potentials and QT intervals (Alseikhan et al., 2002), likely in a cell-specific manner dependent on both the precise value of $\hat{\gamma}$, and complex interactions with the configuration of other ion-channel and Ca^{2+}-cycling molecules present. The latter interaction factors likely contribute to the impressive dispersion of properties documented in Figure 2.1. Given the variable propensity for action potential prolongation and calcium augmentation within different cells, arrhythmogenic behavior at the tissue and organ level could thus result. Although other effects of mutant CaM molecules are likely to contribute to overall pathogenesis (Figure 2.7, gray pathway with arrow), this study furnishes strong evidence that a major underlying mechanism concerns the attenuation of L-type

calcium channel CDI by the presence of LQTS-associated mutant CaM molecules. This outcome furnishes at least one major molecular target that merits scrutiny for potential therapeutics.

2.4 Discussion

Our experiments demonstrate that CaM bearing LQTS mutations induce the cellular substrates that would favor a LQTS phenotype. Acute introduction of LQTS mutant CaMs into aGPVMs lead to: (1) electrical disturbances including prolonged APD and electrical alternans, as well as (2) Ca^{2+} cycling disturbances, such as increased Ca^{2+} transients and SR Ca^{2+} load. Importantly, such alterations manifested in a highly dispersed fashion across and within cells, thus furnishing a critical ingredient for arrhythmogenesis at the tissue and organ levels (Arevalo et al., 2007). The present study also clearly indicates that a key contributor to these effects involves the disruption of L-type channel CDI by LQTS CaM mutants. Such CDI attenuation would elaborate increased Ca^{2+} current during phases 2 and 3 of the action potentials, thus prolonging APD and increasing SR Ca^{2+} load. Finally, we have established one scenario by which a small fraction of CaM mutants would suffice to create an appreciable prolongation of action potentials. Preassociation of apoCaM to the $Ca_V1.2$ channels plays a critical role, enabling a fraction of channels to be occupied by the CaM mutants with resulting failure to undergo CDI.

Interestingly, CaM mutants commonly affiliated with CPVT exhibited negligible or weaker effects on action potential duration and L-type channel CDI. The complete lack of effect of CaM_{N54I} on CDI and action potential duration is well explained by its near wild-type Ca^{2+} binding affinity (Hwang et al., 2014), and these molecular and cellular outcomes fit nicely with the lack of appreciable QT prolongation in corresponding probands (Nyegaard et al., 2012). This CPVT-associated mutant could nonetheless interact with other targets like RyR2 calcium release

channels to potentially contribute to pathogenesis (Hwang et al., 2014). On the other hand, the CPVT CaM mutant N98S is capable of producing either CPVT (Nyegaard et al., 2012; Hwang et al., 2014) or LQTS in patients (Makita et al., 2013). This dual effect may well arise from the overlapping effects of these mutations on multiple CaM targets in the heart. Indeed, CaM_{N98S} turned out to both reduce L-type channel CDI and moderately prolong cardiac action potentials (Figure 2.3). The intermediate effects of this CaM mutant thus rationalize how LQTS or CPVT may become the more prominent clinical phenotype, perhaps as a function of differing expression levels among patients.

In addition to L-type ($Ca_V1.2$) channels, other molecular targets of CaM remain as potential contributors to LQTS pathogenesis. Focusing in particular on targets that preassociate with Ca^{2+}-free CaM, voltage-gated Na channels (Van Petegem et al., 2012) ($Na_V1.5$) and slow delayed rectifier K channels (Shamgar et al., 2006) (I_{Ks}) loom among likely targets. In $Na_V1.5$ channels, Ca^{2+}/CaM is proposed to both facilitate initial opening and stabilize the inactivated state (Van Petegem et al., 2012). However, a recent study reports that LQTS CaM mutants lacked significant effects on most splice variants of $Na_V1.5$ channels, though the CaM_{D130G} mutant appeared to moderately enhance persistent current in one fetal splice variant (Murphy et al., 2013). For I_{Ks}, Ca^{2+}-free CaM may help traffic channels to plasmalemma (Roden, 2006), and Ca^{2+}/CaM is believed to facilitate opening. In fact, mutations in I_{Ks} that disrupt CaM binding result in decreased K current, thus causing LQTS (Ghosh et al., 2006; Shamgar et al., 2006). More broadly, because CaM regulates many other Ca^{2+} channel subtypes, including those predominate in neurons and immune cells, disruption of CDI could lead to a multi-system disorder similar to Timothy syndrome (Splawski et al., 2004; Splawski et al., 2005; Raybaud et al., 2006). It may well be that extra-cardiac effects are also present in patients possessing LQTS

CaM mutants, but that these effects were not recognized in the face of immediately life-threatening cardiac-related sequelae. For other CaM-modulated signaling molecules that do not preassociate with Ca^{2+}-free CaM, the present study would suggest that a limited fraction of LQTS CaM mutants would matter little. Only when the fraction of CaM mutants approaches unity would this class of targets be predicted to exhibit altered function. Key members of this class of CaM targets in cardiac myocytes would include Ca^{2+}/CaM-dependent kinase II (CaMKII) and calcineurin (CN). CaMKII has been argued to influence the electrical properties of cardiomyocytes by phosphorylation of ryanodine receptors, phospholamban, SERCA, and L-type Ca^{2+} channels, all of which could alter electrical and Ca^{2+} function (Rokita and Anderson, 2012). By contrast, the Ca^{2+}/CaM-activated phosphatase CN dephosphorylates numerous targets including the transcription factor NFAT, implicated in regulating expression levels of numerous ion channels in heart (Eder and Molkentin, 2011). Nonetheless, if our insights are correct regarding the necessary role of target preassociation with apoCaM to amplify the effects of a limited fraction of CaM mutants, molecules like CaMKII and CN may play little role in the LQTS phenotype at hand.

Even before testing for a role of the additional target molecules alluded to above, potential targeted therapeutic strategies in patients expressing LQTS CaM mutants are suggested by our finding that LTCC dysfunction likely contributes in this particular setting. In addition to beta-adrenergic blockade, as per the general standard of care for LQTS patients, immediate benefits may arise by seeking appropriate modulators of LTCCs such as roscovitine, which has demonstrated beneficial effects within certain *in vitro* models of LTCC-related LQTS (Yazawa et al., 2011). Additionally, a recent study implicates a non-linear threshold effect between the extent of CDI diminution in LTCCs and onset of outright arrhythmias (Dick et al., 2012), rather

than a continuously graded interrelation. Accordingly, only a few-fold decrease in the fraction of CaM mutants ($\hat{\gamma}$) may yield marked improvement of electrical stability and decrease in the incidence of cardiac arrest. The limited alteration of $\hat{\gamma}$ potentially required to bring about these benefits may considerably improve the feasibility of devising novel therapies towards this end.

Although the prevalence of diseases caused by *de novo* CaM mutations is limited, investigating their pathogenesis may offer revealing opportunities to expand our basic knowledge of LQTS-related arrhythmogenesis. Moreover, additional discoveries of CaM mutations will help expand our database of related genotype-phenotype correlations, lending further resources for understanding. Indeed, following the first discoveries of CaM mutations, three more recent preliminary studies (Boczek et al., 2013; Makita et al., 2013; Marsman et al., 2013) have uncovered further CaM-affiliated arrhythmias. These include the following, listed according to gene and syndrome: D134H (*CALM2*; LQTS), N98S (*CALM2*; LQTS), D132F (*CALM2*; LQTS and CPVT), N54I (*CALM1*; LQTS and/or sudden unexplained death in the young (SUDY)), A103V (*CALM3*; CPVT and/or SUDY), F90L (*CALM1*; ventricular fibrillation). These exciting discoveries suggest that a small yet substantial population of patients with CaM mutations is emerging, thus necessitating the inclusion of *CALM* genes in genetic test panels for LQTS and CPVT, and providing added motivation for the discovery of new therapies. In this light, it may be warranted to dub this expanding group of CaM-related disorders as calmodulinopathies.

2.5 Tables and figures

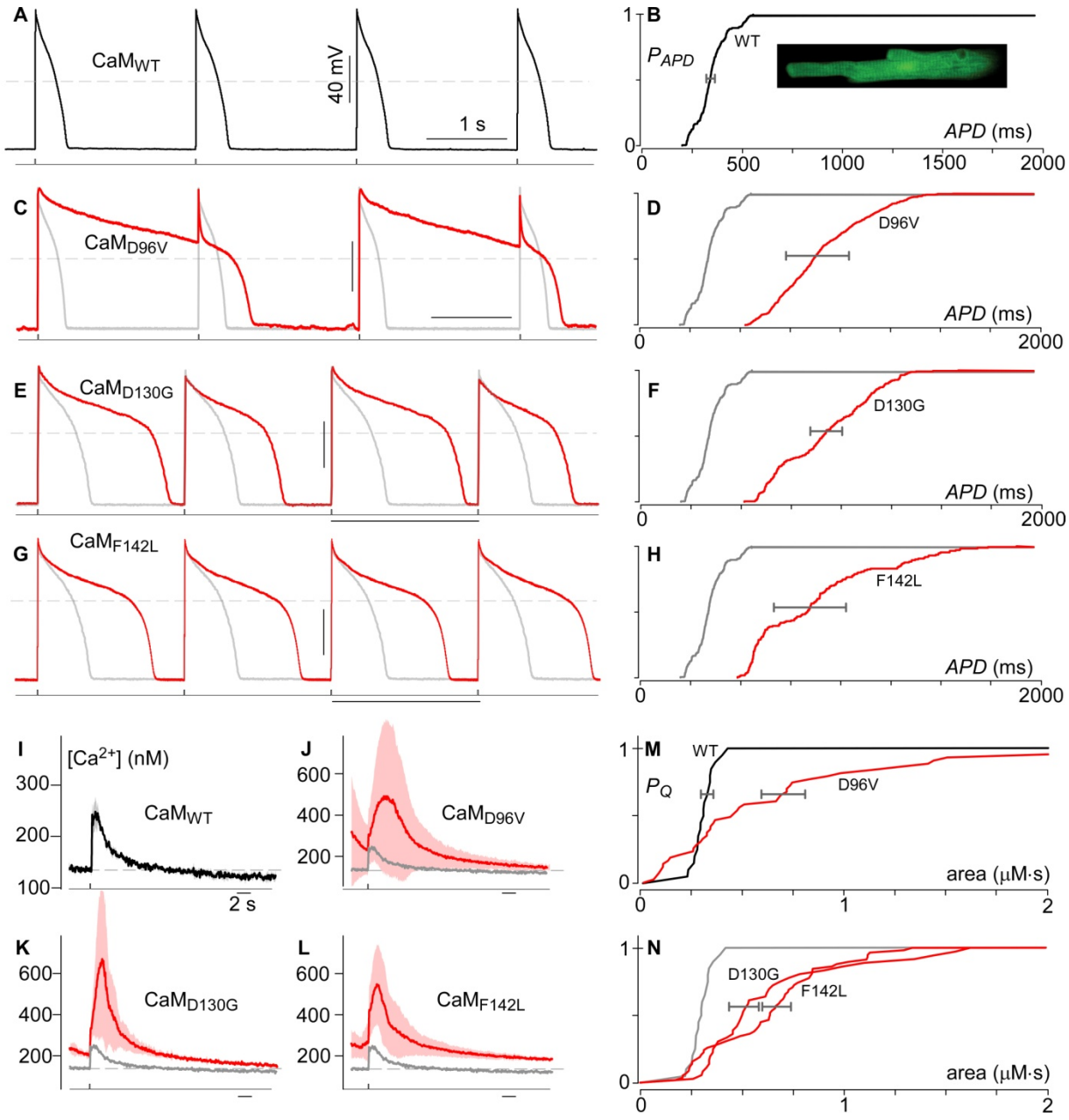

Figure 2.1 CaM mutants induce arrhythmia. (**A**) Exemplar action potentials recorded via current clamp from one-day-old aGPVMs transduced with CaM_{WT}. The stimulus waveform is depicted below. The dashed horizontal gray line indicates 0 mV, here and throughout. (**B**) Population data corresponding to **A** plotted as the cumulative distribution of APD_{80} (285 responses from 10 cells). All APD_{80} population data in panels **B**, **D**, **F**, and **H** from myocytes stimulated at 0.5 Hz. Gray bar in **B** displays SD_{cell}. Inset shows confocal image of typical myocyte expressing GFP as a marker of transduction by adenoviral CaM_{WT}. (**C**) Transduction of

the mutant CaM_{D96V} induced marked prolongation of action potentials in this exemplar recording (red) as compared to CaM_{WT} transduction (gray, reproduced from **A**). (**D**) The cumulative distribution for APD_{80} from CaM_{D96V} transduced aGPVMs (red) demonstrates a dramatic increase in APD_{80} and much greater APD_{80} variability (gray bar, $p < 0.01$), both as compared to myocytes transduced with CaM_{WT}. (**E-H)** Similar AP disturbances were induced via transduction of CaM_{D130G} (**E, F**) and CaM_{F142L} (**G, H**). Example of electrical alternans in aGPVM expressing CaM_{D130G} (**E**). Data displayed in **E** and **G** were obtained during pacing at 1 Hz. (**I**) Average Ca^{2+} transient (black) recorded from aGPVMs transduced with CaM_{WT} after steady-state pacing at 0.1 Hz, n =5 cells. Standard deviation range shown as gray shading. Indo-1 AM was used as the inorganic Ca^{2+}-sensitive fluorescent dye. (**J-L**) Transduction of mutant CaMs resulted in dramatic increases in the amplitude and variability of the Ca^{2+} transients. Solid gray trace reproduces the CaM_{WT} data for reference, while red and rose depict average and standard deviation of Ca^{2+} transients from aGPVMs expressing the three mutants as labeled. Data averaged from n = 11, 9, and 15 myocytes for respective panels **J**-**L**. (**M**) Population data for CaM_{WT} (black) and CaM_{D96V} (red), plotted as cumulative histograms for the area integrated under the Ca^{2+} transient waveform recorded from each myocyte. Horizontal error bars depict average standard deviation of Ca^{2+} entry for transients within the same cells, and is significantly larger for each LQTS CaM mutant ($p < 0.05$). The significant right shift due to transduction of CaM_{D96V} demonstrates a remarkable increase in Ca^{2+} entry during single APs, while the slower rise indicates greater heterogeneity across myocytes transduced with CaM mutants. (**N**) Cumulative histograms of Ca^{2+} entry for CaM_{D130G} (red, left) and CaM_{F142L} (red, right), with the fit for CaM_{WT} reproduced in gray.

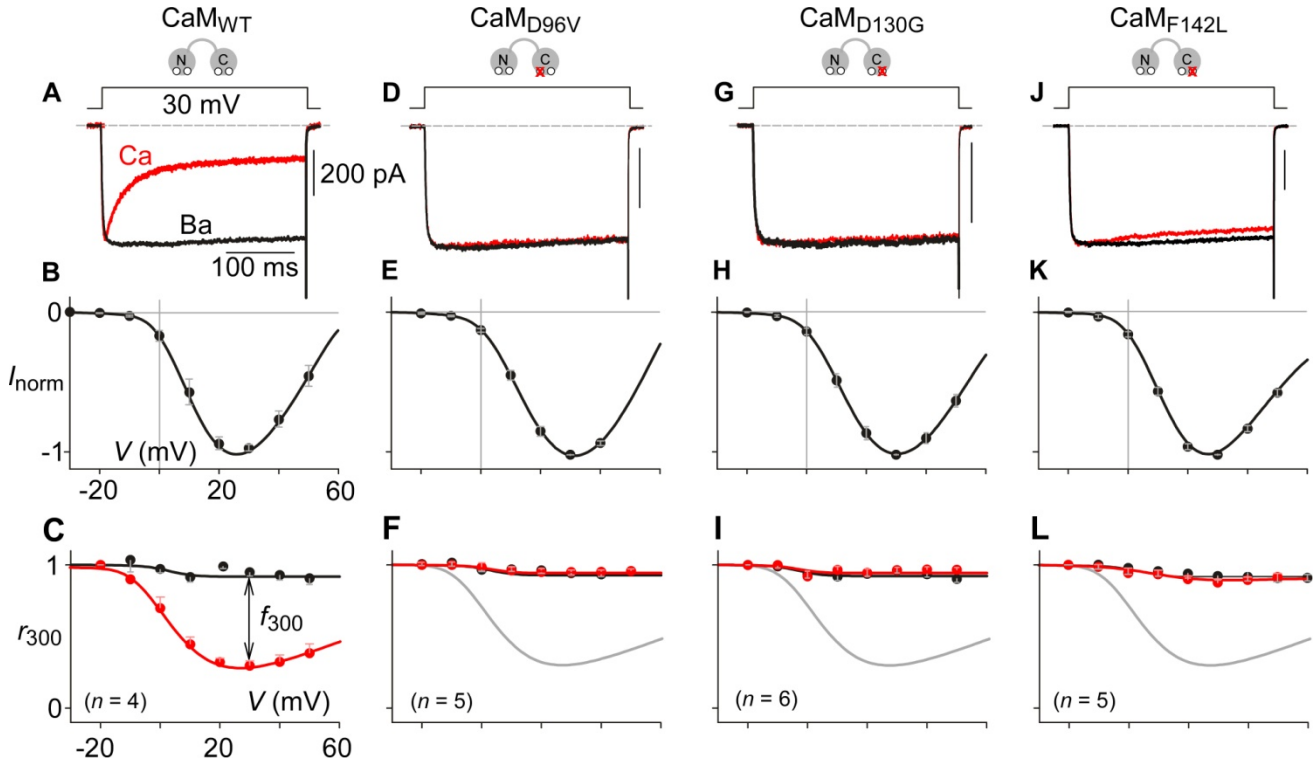

Figure 2.2 LQTS CaM mutants diminish CDI in HEK293 cells. (**A**) Exemplar currents evoked by 30-mV voltage step (top) in cells co-transfected with $Ca_V1.2$ and CaM_{WT}. CDI manifests as the stronger decay in Ca^{2+} (red) current as compared to Ba^{2+} (black). Ba^{2+} trace is scaled downward to match the peak of the Ca^{2+} trace, thus facilitating comparison of decay kinetics, and the scale bar for current references the Ca^{2+} trace, here and throughout. (**B**) Average normalized peak current versus voltage relation obtained with Ba^{2+} for the same cells as in **A**. Data are plotted as mean ± SEM here and throughout. (**C**) Population data for CDI across voltages. r_{300} measures the current remaining after 300 ms, after normalization to peak current. f_{300} is the difference between Ca^{2+} and Ba^{2+} at 30 mV, after normalization by the Ba^{2+} r_{300} value. (**D**) Expression of CaM_{D96V} severely blunts CDI of $Ca_V1.2$. (**E**) The current-voltage relation for the CaM_{D96V} scenario remains unaltered. (**F**) Population data bears out the CaM_{D96V} reduction of CDI across voltages. For reference, the Ca^{2+} r_{300} curve for CaM_{WT} is reproduced in gray. (**G-L**) CaM_{D130G} and CaM_{F142L} also induce dramatic CDI deficits. Format as in **D-F**.

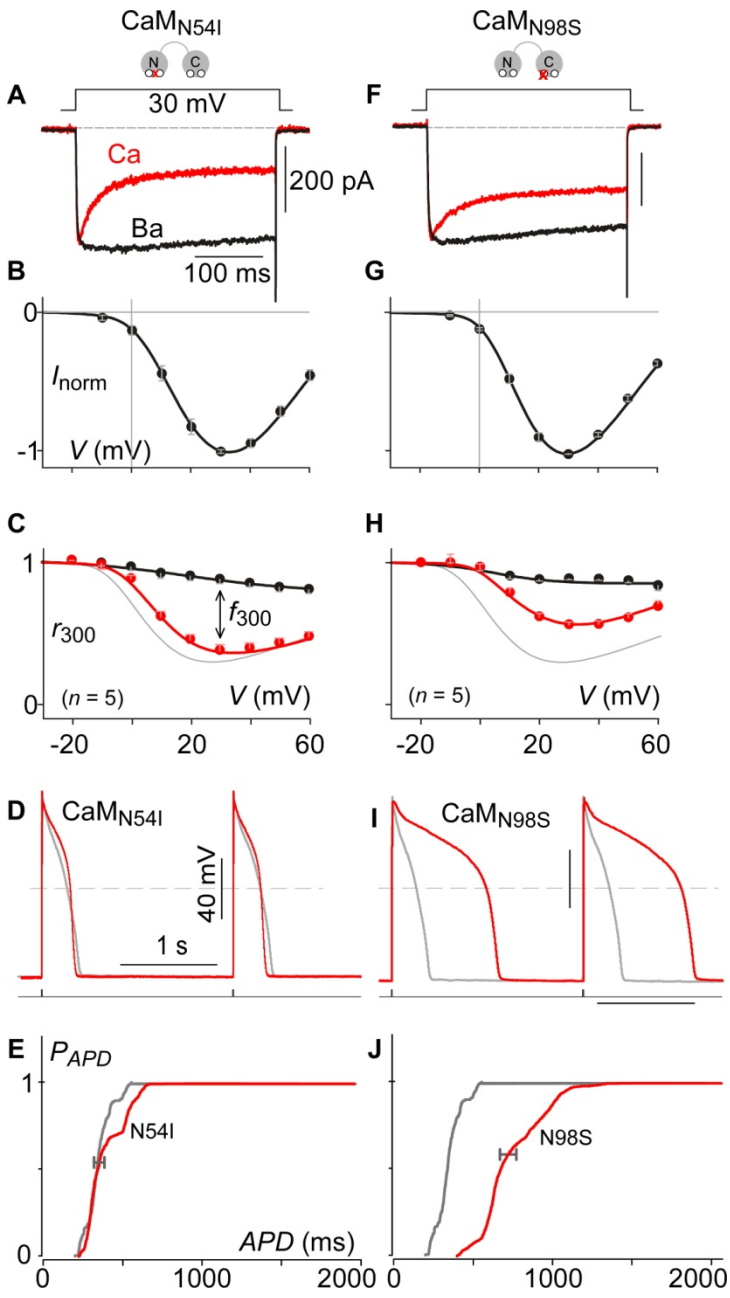

Figure 2.3 CPVT CaM mutants exert weaker effects on CDI. (**A**) Exemplar currents evoked by 30-mV voltage step (top) in HEK293 cells co-transfected with $Ca_V1.2$ and CaM_{N54I}. Here, coexpression of CaM_{N54I} did not disrupt CDI compared to CaM_{WT} (Figure 2.2A). (**B**) Average normalized peak current-voltage relationship for same cells as in **A**. Compared to CaM_{WT} (Figure 2B), there is no shift in voltage activation. (**C**) Voltage dependence of r_{300} values for Ca^{2+} (red) and Ba^{2+} (black). Ca^{2+} relation for CaM_{WT} configuration reproduced in gray for reference. No significant alteration of CDI across all test voltages. (**D-E**) Coexpression of

CaM_{N54I} does not appreciably affect action potentials (red) as compared to co-expression of CaM_{WT} (gray). Format as in Figure 2.1. Data for panel **E** from 679 action potentials drawn from 6 myocytes. (**F**) Expression of CaM_{N98S}, however, modestly diminishes CDI, without affecting voltage activation (**G**). (**H**) Population data of r_{300} values confirm a small, but significant reduction of CDI across voltages. (**I-J**) Overexpression of CaM_{N98S} has the ability to lengthen and increase heterogeneity of action potentials ($p < 0.01$). Format as in Figure 2.1B. Horizontal error bars in panels **E** and **J** display standard deviation of APD_{80} within cells. Data for panel **J** from 1100 action potentials drawn from 6 myocytes.

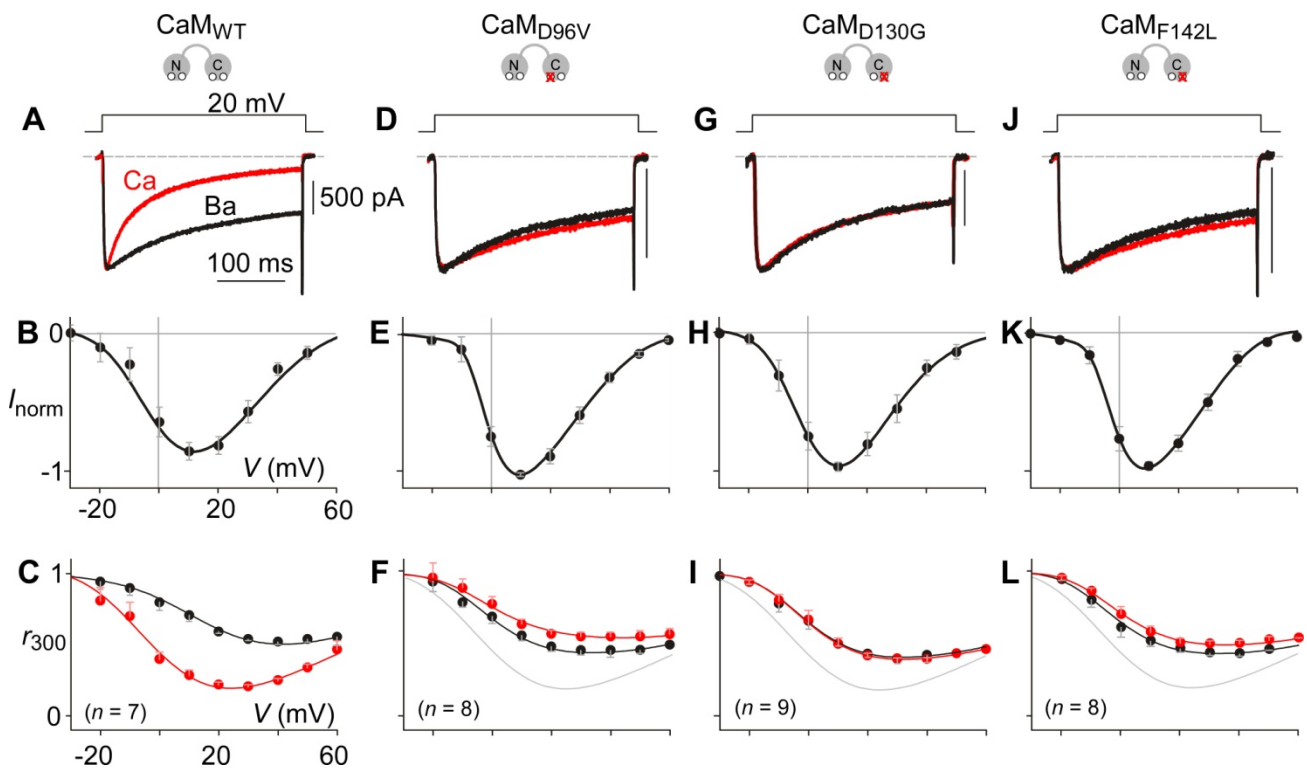

Figure 2.4 CaM mutants diminish CDI in aGPVMs. (**A**) CDI in native LTCCs recorded from one-day-old aGPVMs transduced with CaM_{WT}. Exemplar current traces elicited by a 20-mV voltage step (top) display strong CDI with Ca^{2+} (red), and a small amount VDI with Ba^{2+} (black). (**B**) Average normalized peak current-voltage relation obtained in Ba^{2+} for the same cells as in **A**. (**C**) Population data for CDI across voltages. f_{300} is measured at 20 mV. (**D**) Expression of CaM_{D96V} severely blunts CDI in the native setting. (**E**) Current-voltage relation in the presence of CaM_{D96V} remains unaltered. (**F**) Population data confirms the CaM_{D96V} reduction of CDI across voltages. For reference, the Ca^{2+} r_{300} curve for CaM_{WT} is reproduced in gray. (**G-L**) CaM_{D130G} and CaM_{F142L} also induce dramatic CDI deficits. Format as in **D-F**.

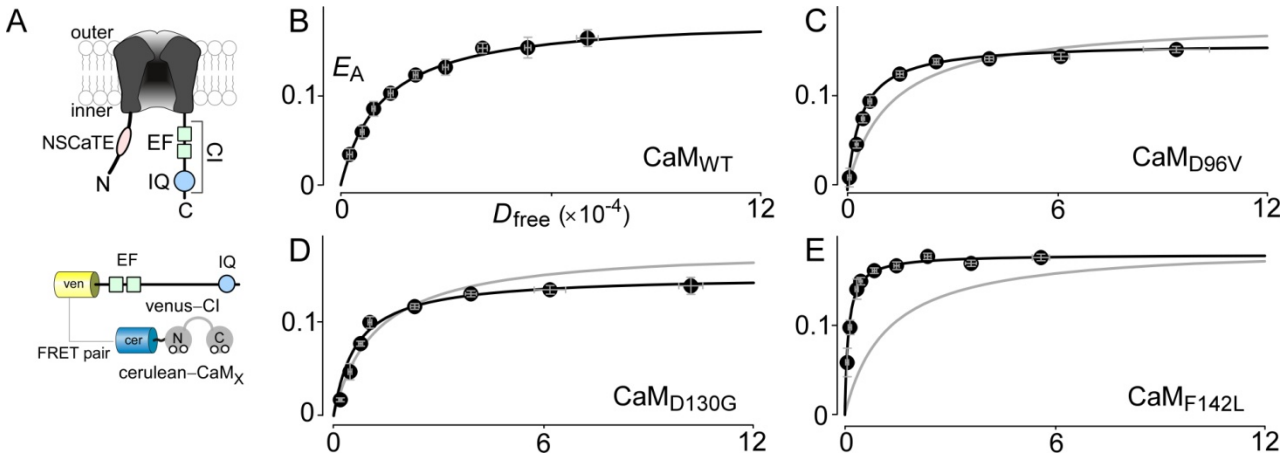

Figure 2.5 Mutant CaMs bind to $Ca_V1.2$ channels at least as well as wild-type CaM. (**A**) Cartoon depicting CaM interaction domains on the $Ca_V1.2$ calcium channel (CI segment). Below, construct schematics depicting FRET interaction pairs used for binding assessment. (**B**) The canonical FRET binding curve between the CI region and CaM_{WT}. In particular, an acceptor-centric FRET efficiency (E_A) is plotted as a function of the relative free concentration of donor-tagged molecules D_{free} (cerulean-CaM_{WT}). $K_{d/EFF}$ for CaM_{WT} binding to CI region is 12000 D_{free} units (Bazzazi et al., 2013). (**C-E**) FRET binding curves between the CI region and CaM_{D96V} (**C**), CaM_{D130G} (**D**) and CaM_{F142L} (**E**). $K_{d/EFF}$ are 4000, 6500, and 1000 D_{free} units, respectively. The binding curve for CaM_{WT} is reproduced in gray for reference.

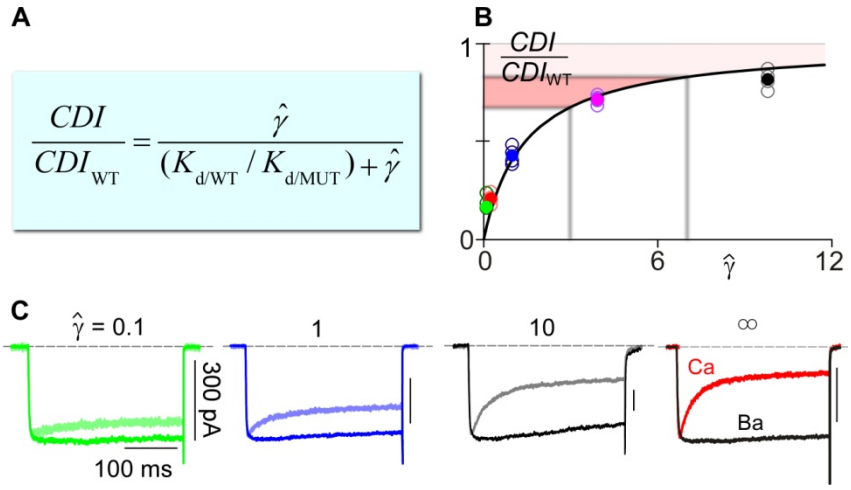

Figure 2.6 Dose-dependent effect of mutant CaMs. (**A**) Langmuir equation relating the extent of CDI and wild-type versus mutant CaM expression ratio $\hat{\gamma}$. (**B**) Predicted CDI as a function of $\hat{\gamma}$ (black). Solid circles indicate average data for each ratio $\hat{\gamma}$; open circles pertain to data for individual cells. Light rose shaded region indicates the deficit in CDI expected for a expression ratio corresponding to heterozygous mutation in *CALM2* gene, while dark rose shaded region indicates predicted extent of CDI reduction for homozygous mutation. (**C**) Exemplar current traces with the colors corresponding to the Langmuir plot in **B**. For each set of records, the Ca^{2+} trace is the lighter color waveform, and the corresponding Ba^{2+} trace is normalized to the peak of the Ca^{2+} trace for comparison of decay kinetics. Scale bar corresponds to Ca^{2+}. Exemplar traces on far right are from a cell expressing CaM_{WT} only $(\hat{\gamma} = \infty)$, as reproduced from Figure 2.2A for reference.

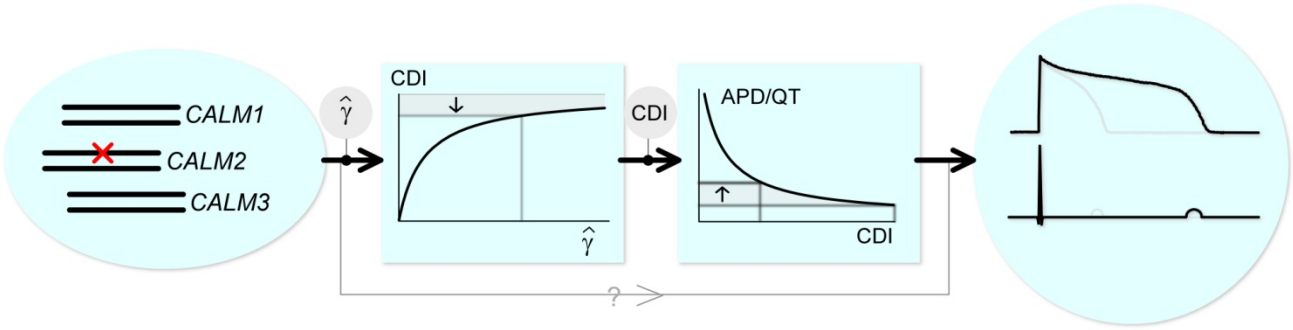

Figure 2.7 Proposed mechanism of electrical and calcium dysfunction for LQTS CaM mutants. Flow diagram schematizing how heterozygous *CALM2* mutation might lead to fractional decrease in CDI, yielding action potential prolongation and ultimately long QT phenomena.

CaM	APD_{80} (ms)	$(dV/dt)_{max}$ (mV/ms)	V_{rest} (mV)**	V_{max} (mV)
WT	417.0 ± 6	119.9 ± 3.2	-62.0 ± 0.2	55.7 ± 0.4
D130G	824.2 ± 16*	112.5 ± 2.1	-61.3 ± 0.2	48.4 ± 0.6
D96V	973.6 ± 12*	139.5 ± 1.7	-62.6 ± 0.1	56.3 ± 0.3
F142L	874.8 ± 22*	131.7 ± 3.8	-61.8 ± 0.2	51.8 ± 0.5
N54I	391 ± 4.5	128.7 ± 1.4	-64.9 ± 0.3	53.6 ± 0.3
N98S	751.8 ± 5.8*	160.6 ± 1.0	-62.4 ± 0.1	58.1 ± 0.1

Table 2.1. **Average values for APs recorded at 0.5 Hz pacing**

* $p < 0.01$; **Values consistent with those expected for aGPVMs after one day in culture (Busch et al., 1996; Mitcheson et al., 1996).

2.6 Supplementary materials

2.6.1 WT CaM overexpression has minimal effects on action potential morphology or duration.

To ensure that transduction of heterologous CaM via adenovirus does not alter the baseline action potential, we compared the action potentials of non-transduced aGPVMs with those of aGPVMs transduced with CaM_{WT}. Supplementary Figures 2.1A-B compare action potential waveforms from uninfected one-day-old aGPVMs (endogenous CaM) and with one-day old aGPVMs overexpressing CaM_{WT}. There was no observable change in the action potential shape or duration at either 0.5 or 1 Hz pacing. Population data shown in panel C not only demonstrate negligible change in action potential duration due to expression of CaM_{WT}, but document just how stable and reproducible the action potential durations of these cells are. These data thus confirm one-day old aGPVMs as a robust model for the study of action potential perturbations. In all, transduction of CaM via adenovirus is well tolerated by aGPVMs, producing no appreciable perturbations across multiple pacing frequencies.

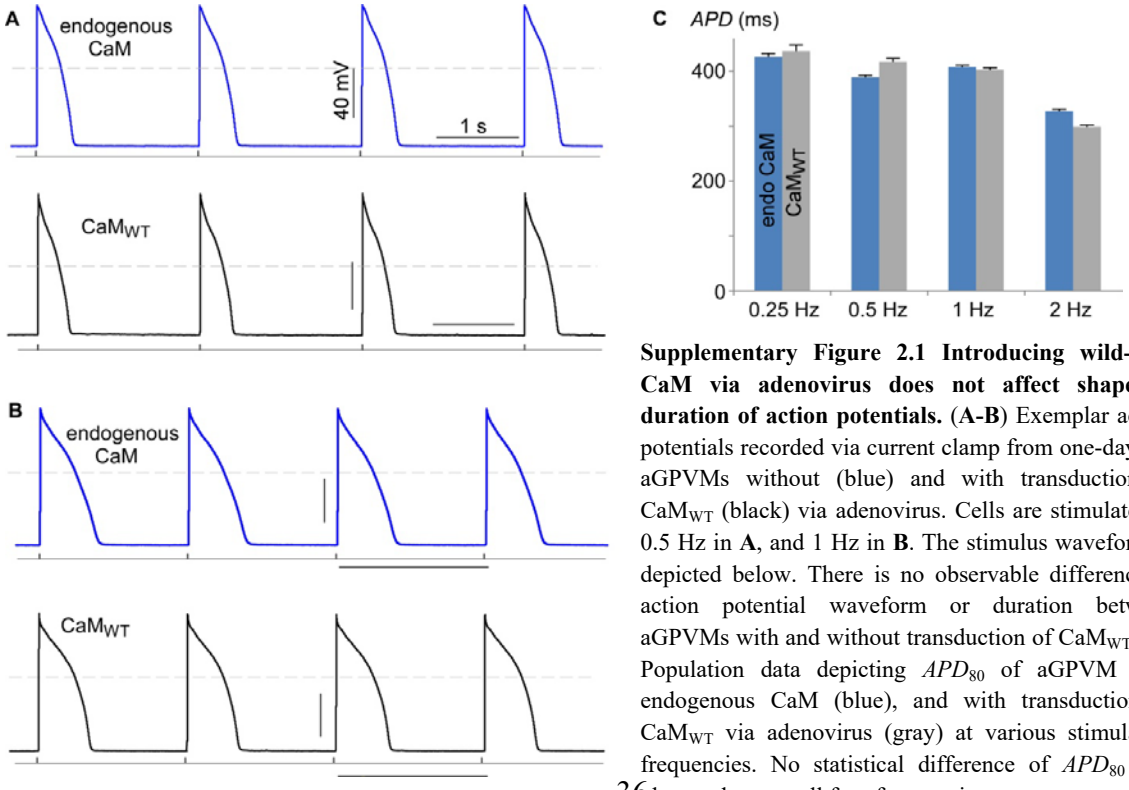

Supplementary Figure 2.1 Introducing wild-type CaM via adenovirus does not affect shape or duration of action potentials. (**A-B**) Exemplar action potentials recorded via current clamp from one-day-old aGPVMs without (blue) and with transduction of CaM_{WT} (black) via adenovirus. Cells are stimulated at 0.5 Hz in **A**, and 1 Hz in **B**. The stimulus waveform is depicted below. There is no observable difference in action potential waveform or duration between aGPVMs with and without transduction of CaM_{WT}. (C) Population data depicting APD_{80} of aGPVM with endogenous CaM (blue), and with transduction of CaM_{WT} via adenovirus (gray) at various stimulation frequencies. No statistical difference of APD_{80} was observed across all four frequencies.

2.6.2 CaM mutants produce similar effects at an alternate pacing rate.

To confirm our findings that LQTS CaM mutants can recapitulate the long-QT phenotypes at more than a single pacing rate, we also recorded action potential waveforms at faster pacing frequencies. Supplementary Figure 2.2 shows the cumulative histograms of APD_{80} for aGVPMs transduced with wild-type and mutant CaMs (as labeled) and paced at 1 Hz. Here, we observe a similar trend as compared to the 0.5 Hz pacing rate from the main text (Figures 2.1 and 2.3). Both action potential prolongation and increased APD dispersion are evident at the faster pacing rate.

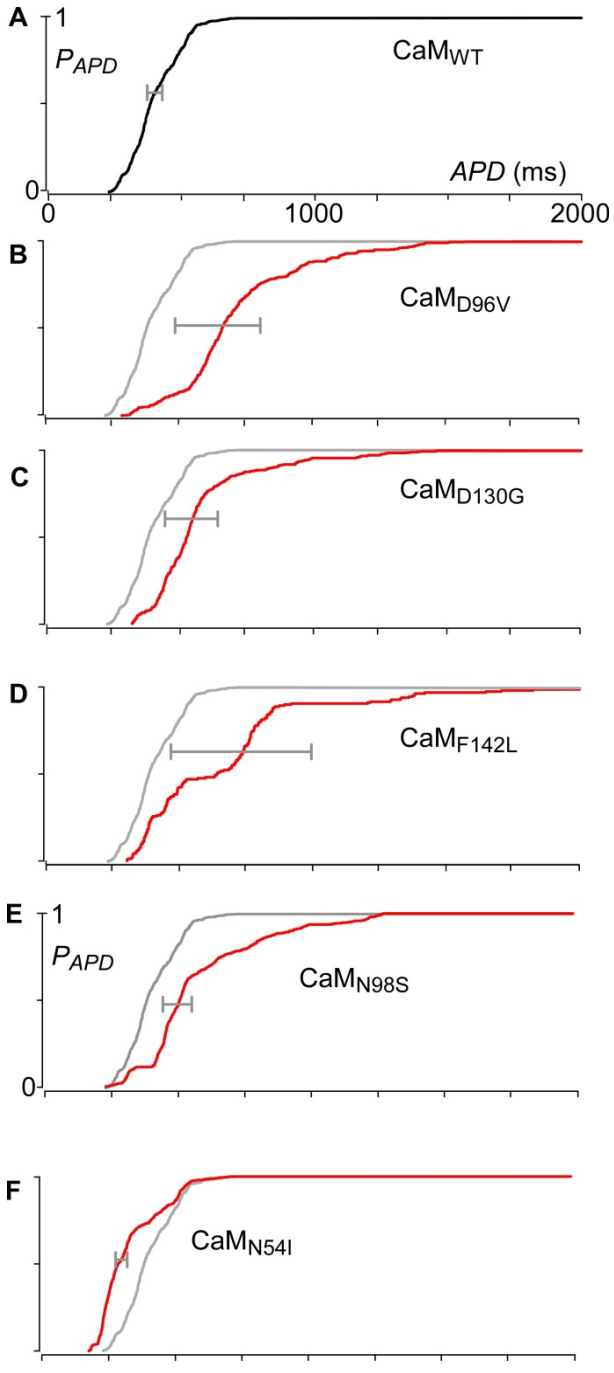

Supplementary Figure 2.2 LQTS CaM mutants consistently prolong APD and increase heterogeneity during pacing at 1 Hz. (**A**) Population data of APD_{80} from one-day-old aGPVMs expressing CaM_{WT} stimulated at 1 Hz, shown as a cumulative histogram (black). Horizontal gray bars depict averaged standard deviation of APD_{80} within the same cells (SD_{cell}), here and throughout. 547 APs from n = 12 cells. (**B**) Cumulative histogram of APD_{80} from aGPVMs expressing CaM_{D96V} stimulated at 1 Hz (red) demonstrates a dramatic increase in APD_{80} ($P < 0.01$), consistent with data from aGPVMs stimulated at 0.5 Hz (Figure 1D). Cumulative histogram from aGPVMs expressing CaM_{WT} is shown here in gray for reference. Moreover, the CaM_{D96V} also significantly increases the heterogeneity of APD, shown here as a longer gray horizontal bar (SD_{cell}), compared to panel **A**. 526 APs from n = 9 cells. (**C-D**) CaM_{D130G} and CaM_{F142L} remarkably prolong APD and increase APD heterogeneity in aGPVMs stimulated at 1 Hz, consistent with data observed in aGPVMs stimulated at 0.5 Hz (Figures 1F and 1H). For D130G, 415 APs from n = 8 cells. For F142L, 172 APs from n = 4 cells. (**E**) The CPVT CaM mutant CaM_{N98S} also maintains its ability to increase APD at 1 Hz pacing. 724 APs from n = 7 cells. (**F**) CPVT CaM mutant N54I, on the other hand, has no effect on APD. 785 APs from n = 5 cells.

2.6.3 SR content and diastolic Ca^{2+}.

The increased Ca^{2+} load in the presence of LQTS CaM mutants is likely to affect the Ca^{2+} content of myocytes in several ways. Importantly, the sarcoplasmic reticulum (SR) is likely to take up some of the excess Ca^{2+} entry from slowly inactivating LTCCs, yielding a higher SR Ca^{2+} content. We tested this hypothesis by transducing aGPVMs with each LQTS CaM mutant and evaluating the SR Ca^{2+} content, gauged by undertaking Indo-1 imaging during emptying of SR Ca^{2+} by caffeine application (Supplementary Figure 2.3A). The result was a significantly larger SR Ca^{2+} content in the presence of LQTS CaM mutants, in agreement with the increase in Ca^{2+} transient amplitude seen in main text Figure 2.1. Moreover, expression of LQTS CaM mutants also significantly increased the diastolic Ca^{2+} level (Supplementary Figure 2.3B), measured after steady state pacing. Thus it appears that the marked increase in Ca^{2+} influx via LTCCs (due to diminished CDI), conspires with the resulting increased SR Ca^{2+} load, to produce large phasic Ca^{2+} transients during repetitive pacing.

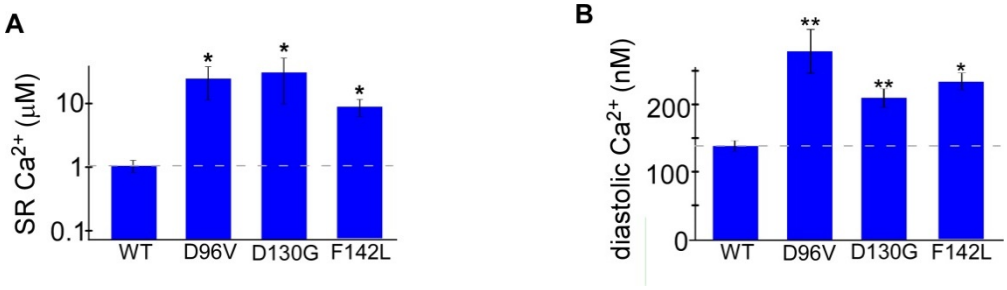

Supplementary Figure 2.3 SR Ca^{2+} load and diastolic Ca^{2+} concentrations. (**A**) SR Ca^{2+} content of aGPVMs transduced with LQTS CaM mutants is significantly higher than that of CaM_{WT} (*, $p < 0.01$, $n = 9$, 3, 4 and 4 cells, respectively). Load obtained after steady-state pacing. (**B**) Transduction of LQTS CaM mutants significantly increases the diastolic Ca^{2+} level of aGPVMs. Data obtained after steady-state pacing. (*, $p < 0.01$; ** $p < 0.05$, $n = 6$, 15, 12, 18 cells, respectively).

2.6.4 Summary of AP parameters for 1 Hz pacing.

To confirm phenotypes observed at 0.5 Hz pacing rate upon expression of LQTS and CPVT CaM mutants (Table 2.1 in the main text), we also recorded action potentials at other pacing rates. Supplementary Table 2.1 summarizes parameters from action potential recordings from 1 Hz pacing rate.

CaM	APD_{80} (ms)	$(dV/dt)_{max}$ (mV/ms)	V_{rest} (mV)	V_{max} (mV)
WT	402.5 ± 4	104.5 ± 2	-63.7± 0.2	54.0 ± 0.3
D130G	567.5 ± 10*	112.2 ± 2	-63.7 ± 0.2	50.8 ± 0.7
D96V	720.2 ± 11*	100.3 ± 2	-63.7 ± 0.2	57.6 ± 0.6
F142L	685.7 ± 31*	129.7 ± 6	-63.7 ± 0.3	50.6 ± 0.9
N54I	326.9 ± 4	119.4 ± 1	-65.27 ± 0.3	50.7 ± 0.2
N98S	580.2 ± 8.6*	170.2 ± 2	-63.2 ± 0.2	53.7 ± 0.2

Supplementary Table 2.1 Detailed parameters from action potential recordings.
Besides large increase in APD_{80} upon expression of LQTS and CPVT CaM mutants, there was no statistically significant change in $(dV/dt)_{max}$ (maximum upstroke velocity), V_{rest} (resting membrane potential), or V_{max} (maximum membrane potential), as measured in aGPVMs expressing CaM mutants. (*, $p < 0.01$ versus WT).

2.6.5 Reduction of CDI due to LQTS CaM mutants under more physiological buffering conditions.

The data displayed in Figures 2.2-2.3 of the main text was obtained under high Ca^{2+} buffering conditions (10 mM BAPA). This high buffering condition limits Ca^{2+} elevations to within the local domain of Ca^{2+} channels, resulting in a component of Ca^{2+} regulation triggered predominantly by the C-lobe of CaM (Dick et al., 2008; Tadross et al., 2008). This configuration was advantageous because CDI measures became independent of the level of channel expression, and the main effect of C-lobe CaM mutations was nicely observed in this arrangement. However, under more native Ca^{2+} buffering, a sustained global elevation of Ca^{2+} is present, which permits additional induction of a CDI component contributed by the N-lobe of CaM (Dick et al., 2008).

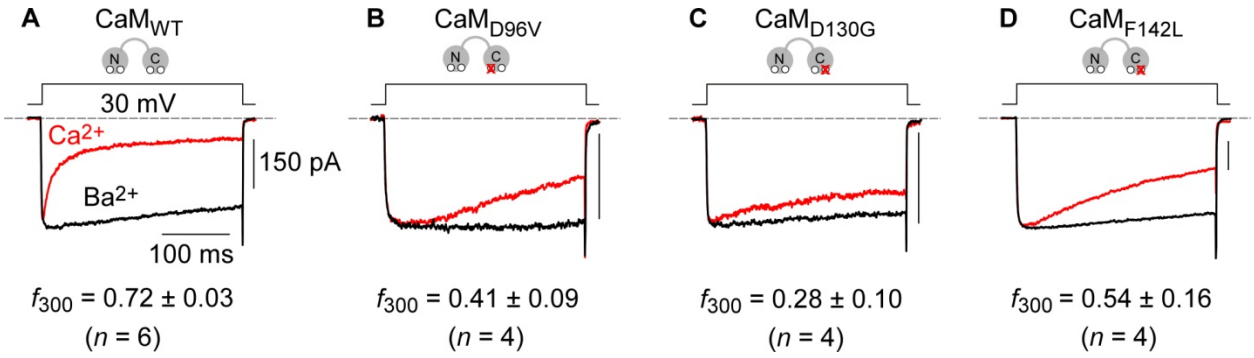

Supplementary Figure 2.4 LQTS CaM mutants diminish CDI under modest Ca^{2+}-buffering. (**A**) Exemplar current traces recorded using 1 mM EGTA as intracellular Ca^{2+} buffer in HEK293 cells co-transfected with $Ca_V1.2$ and CaM_{WT}. Currents were evoked by a voltage step to 30 mV (top). Stronger decay in Ca^{2+} (red) current as compared to Ba^{2+} (black) represents CDI. Ba^{2+} current was scaled to the same magnitude as Ca^{2+} to facilitate comparison of decay kinetics, and the current scale bar pertains to Ca^{2+} here and throughout. f_{300}, representing the extent of CDI, is expressed as mean ± SEM here and throughout. (**B**) Expression of CaM_{D96V} strongly blunts CDI, although to a smaller extent than in high Ca^{2+} buffering (10 mM BAPTA). (**C-D**) Strong but incomplete blunting of CDI is also observed upon expression of CaM_{D130G} and CaM_{F142L}, respectively.

To assess the effects of CaM mutations under this more physiological buffering, we therefore obtained the equivalent whole-cell patch-clamp data (Supplementary Figures 2.4-2.5) under modest Ca^{2+} buffering (1 mM EGTA). Such conditions now allow for both local (C-lobe) and global (N-lobe) Ca^{2+}/CaM signaling. As the N-lobe remains unperturbed in the LQTS mutant CaMs, a small residual CDI due to N-lobe CaM regulation now emerges (Supplementary Figures 2.4B-D). Importantly, compared to CaM_{WT}, each of the LQTS CaM mutants demonstrate a dramatic reduction in CDI, validating the overall results under high buffering condition. Conversely, neither of the CPVT CaM mutants have a large enough effect on CDI for any deficit to be observed under the modest Ca^{2+} buffering condition (Supplementary Figure 2.5).

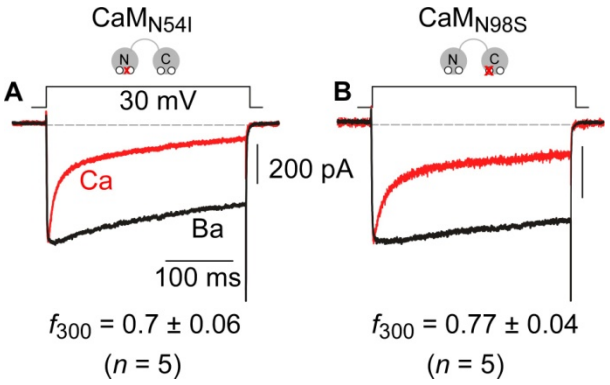

Supplementary Figure 2.5 CPVT mutants minimally affect CDI under modest Ca^{2+} buffering. (**A**) Full CDI is seen in the presence of CaM_{N54I}. (**B**) The small CDI deficit seen under high buffering conditions due to CaM_{N98S} is masked under modest internal Ca^{2+} buffering. Format is as in Supplementary Figure 2.4.

2.6.6 Calibrating the expression ratio of wild-type to mutant CaM

Before being able to accurately test the graded response of CDI at different expression ratios of wild-type to mutant CaM, we first needed to devise a method to control and validate the protein expression ratio relative to a transfected cDNA ratio. Through a simplistic yet powerful imaging method, we were able to determine a scaling factor *m* that relates the protein expression ratio ($\hat{\gamma}$) to cDNA transfection ratio (γ) as

$$\hat{\gamma} = m \cdot \gamma \tag{2.1}$$

First, we assessed the relative brightness of venus- and cerulean-tagged CaM_{WT} (V-CaM_{WT} and C-CaM_{WT}, in Supplementary Figure 2.6A). An equimolar ratio of cDNAs encoding these moities was transfected into HEK293 cells, and cell-by-cell epifluorescence imaging undertaken 1-2 days thereafter. Under these conditions, cells should on average express equal amounts of V-CaM_{WT} and C-CaM_{WT}. Indeed, this outcome is experimentally verified by: (a) the close adherence of cell-by-cell fluorescence measurements to a straight line, and (b) a slope (1/β) indistinguishable from the relative brightness of venus compared to cerulean (gauged from venus-cerulean dimer analysis, not shown). Indeed, if f_V is the venus fluorescence per molar concentration of venus in a HEK293 cells, and f_C the corresponding cerulean metric, then

$$1/\beta = f_V / f_C \tag{2.2}$$

Second, we accounted for potential differences in the expression of wild-type versus mutant CaM molecules, as elaborated from equimolar transfected cDNA. The approach is illustrated for the CaM_{D96V} mutant. Mixtures of V-CaM_{WT} and C-CaM_{D96V} were expressed, using different molar ratios of transfected DNA (γ). Supplementary Figure 6B displays cell-by-cell plots of whole-cell venus fluorescence ($F_{V\text{-}CaM/WT}$) versus corresponding cerulean fluorescence ($F_{C\text{-}CaM/D96V}$), where different-colored relations correspond to different cDNA transfection ratios γ, as labeled. The tight adherence of data points to corresponding linear relations confirms that each transfection ratio γ largely specifies a specific protein expression ratio ($\hat{\gamma}$), irrespective of total protein expression levels. Accordingly, the slope of each relation yields a value α, which relates to $\hat{\gamma}$ as

$$\alpha = \frac{F_{\text{V-CaM/WT}}}{F_{\text{C-CaM/D96V}}} = \frac{f_{\text{V}}[V - CaM_{\text{WT}}]}{f_{\text{C}}[C - CaM_{\text{D96V}}]} = \frac{f_{\text{V}}}{f_{\text{C}}} \cdot \frac{[V - CaM_{\text{WT}}]}{[C - CaM_{\text{D96V}}]} = \frac{1}{\beta} \cdot \hat{\gamma} \tag{2.3}$$

where [V–CaM_{WT}] and [C–CaM_{D96V}] are the molar concentrations of the corresponding species in HEK293 cells. Thus, the protein expression ratio of CaM_{WT} to CaM_{96V} can be calculated as

$$\hat{\gamma} = \alpha \cdot \beta \tag{2.4}$$

for each cDNA transfection ratio γ. Supplementary Figure 2.6C plots these entities ($\hat{\gamma} = \alpha \cdot \beta$ versus γ) against each other, furnishing a linear relationship whose slope yields the desired conversion factor m (= 0.98) for Equation 1. Thus, we could now specify the protein expression ratio of wild-type to mutant CaM ($\hat{\gamma}$) from cDNA ratios (γ) used for transfection.

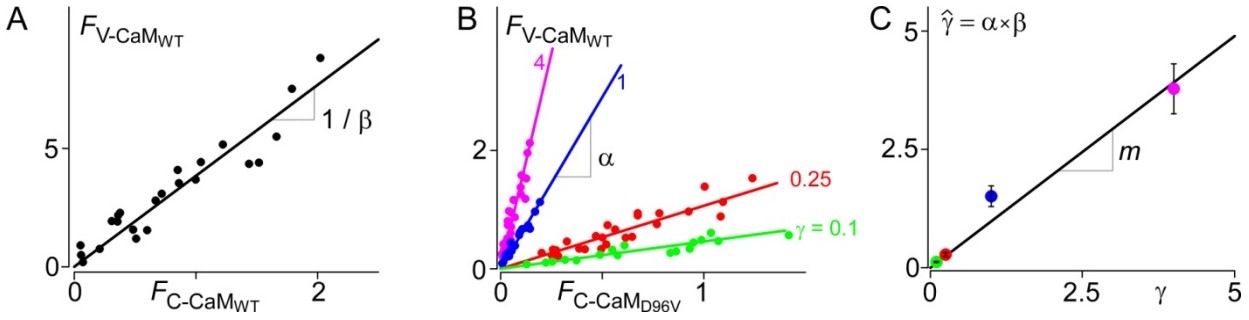

Supplementary Figure 2.6 Calibration of protein expression ratio between CaM_{WT} and CaM_{D96V}. (**A**) Cell-by-cell plot of venus versus cerulean fluorescence intensity, derived from venus- and cerulean-tagged CaM_{WT} (V-CaM_{WT} and C-CaM_{WT}), demonstrating a linear correlation with a slope of $1/\beta$. (**B**) Cell-by-cell plots of whole-cell venus fluorescence ($F_{\text{V-CaM/WT}}$) versus corresponding cerulean fluorescence ($F_{\text{C-CaM/D96V}}$) for various cDNA transfection ratios γ. Slopes of each relation specify α for each γ. (**C**) Plotting $\hat{\gamma}$ as a function of γ yields a linear relation with a slope equal to the final conversion factor *m*.

For the remaining two LQTS mutants, we confirmed that these mutations exhibit a similar *m* value, as follows. Holding γ = 1 (equimolar cDNA ratio of wild-type to mutant CaM) fixed for CaM_{D130G} and CaM_{F142L}, the resulting $\hat{\gamma}$ data points (colored symbols, Supplementary

Figure 2.7) nicely superimpose on the $\hat{\gamma}$ versus γ relation for CaM_{D96V} (reproduced as black symbols and fit, from Supplementary Figure 2.6). Thus, we could use the same value of *m* throughout (~1).

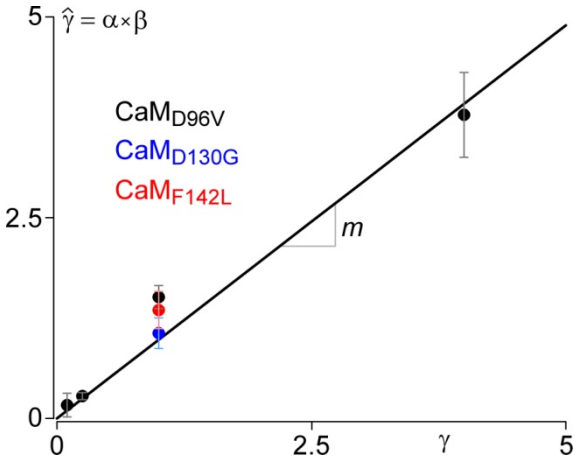

Supplementary Figure 2.7 Validation of conversion factor (*m*) for all CaM mutants. The linear relationship between $\hat{\gamma}$ and γ of CaM_{D96V} (Supplementary Figure 6C) is reproduced here in black. The slope of this line is the conversion factor (*m*). The relationship between $\hat{\gamma}$ and γ for CaM_{D130G} (blue) and CaM_{F142L} (red) fall nicely along this same line, obtained from CaM_{D96V} (black). Thus, a similar conversion factor *m* ~1 may be utilized for all three CaM mutants.

2.6.7 Derivation of Langmuir CaM Ratio Equation

With careful calibrations of CaM protein expression in hand, we could quantify the graded CDI effects of the mutant CaMs. Since all three LQTS mutations are in the C-lobe of CaM, we continued to utilize high intracellular buffering (10 mM BAPTA) such that we need only consider C-lobe CaM regulation (Dick et al., 2008; Tadross et al., 2008) in our derivations. In addition, we have shown that the mutant apoCaMs can bind to the channels at least as well as the wild-type counterpart (Figures 2.5B-E). Therefore, at baseline, each channel will be in one of the first three configurations depicted in Supplementary Figure 2.8: empty (state 1); occupied by a wild-type apoCaM (state 2), or occupied by a mutant apoCaM (state 3). Furthermore, to minimize the effect of endogenous CaM, we strongly expressed a mixture of wild-type and mutant CaM molecules. Under this condition, essentially all channels will be occupied by

apoCaM at rest, restricting occupancy to either state 2 or 3 at baseline. Upon a rise in intracellular Ca^{2+}, CaM_{WT} will bind Ca^{2+} and induce conformational changes which result in CDI (state 4). All LQTS CaM mutants, on the other hand, feature disrupted Ca^{2+} binding sites in the C-terminal lobe, yielding a complete absence of CDI (Supplementary Figure 2.8, bottom, grayed out state 5).

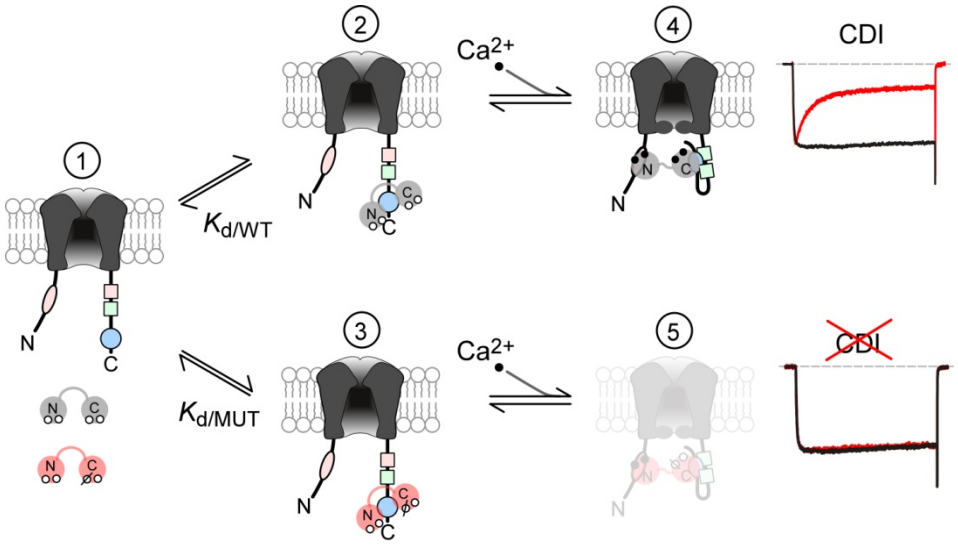

Supplementary Figure 2.8 Model of CaM/channel interactions. Model depicting the configurations of CaM interacting with $Ca_V1.2$ channels. CaM_{WT} is depicted as the gray dumbbell-shaped molecule, and mutant CaM as the red dumbbell-shaped molecule. At low, resting Ca^{2+} levels, channels are either empty (state 1) or preassociated with either a wild-type apoCaM (state 2) or a mutant apoCaM (state 3). Upon a rise in intracellular, Ca^{2+} channels bound to a wild type CaM will transition from state 2 to state 4 upon Ca^{2+} binding to CaM, yielding CDI. Channels in state 3, however, are pre-bound to a mutant CaM which is unable to bind Ca^{2+} effectively. These channels are therefore unable to transition to state 5 and will thus lack CDI.

Since overexpression of LQTS CaM mutants produces *CDI* ~0 (in 10 mM BAPTA), the aggregate amount of CDI directly reflects fraction of channels in state 2 (f_2):

$$CDI = CDI_{WT} \cdot f_2 \tag{2.5}$$

At equilibrium, f_2 can be calculated as

$$\frac{f_2}{f_1} = \frac{C_{\mathrm{WT}}}{K_{\mathrm{d/WT}}} \text{ which gives } f_2 = f_1 \cdot \frac{C_{\mathrm{WT}}}{K_{\mathrm{d/WT}}} \tag{2.6}$$

$$\frac{f_3}{f_1} = \frac{C_{\mathrm{MUT}}}{K_{\mathrm{d/MUT}}} \text{which gives } f_3 = f_1 \cdot \frac{C_{\mathrm{MUT}}}{K_{\mathrm{d/MUT}}} \tag{2.7}$$

where f_1 and f_3 represent fractions of channels in state 1 and 3, respectively; C_{WT} and C_{MUT} represent the concentration of wild-type and mutant CaM, respectively; and $K_{\mathrm{d/WT}}$ and $K_{\mathrm{d/MUT}}$ represent dissociation constants for wild-type or mutant CaM interaction with channels.

At baseline (before elevation of Ca^{2+}), we have that

$$f_1 + f_2 + f_3 = 1 \tag{2.8}$$

such that, we can combine Equations 6, 7 and 8 to obtain

$$f_1 \cdot (1 + \frac{C_{\mathrm{WT}}}{K_{\mathrm{d/WT}}} + \frac{C_{\mathrm{MUT}}}{K_{\mathrm{d/MUT}}}) = f_1 \cdot D = 1 \tag{2.9}$$

Since we strongly overexpressed wild-type and mutant CaM, C_{WT} and C_{MUT}, which yields

$$\lim_{C_{\mathrm{WT}},\, C_{\mathrm{MUT}} \to \infty} D = \frac{C_{\mathrm{WT}}}{K_{\mathrm{d/WT}}} + \frac{C_{\mathrm{MUT}}}{K_{\mathrm{d/MUT}}} \tag{2.10}$$

Hence,

$$f_2 = f_1 \cdot \frac{C_{\mathrm{WT}}}{K_{\mathrm{d/WT}}} = \frac{1}{D} \cdot \frac{C_{\mathrm{WT}}}{K_{\mathrm{d/WT}}} = \frac{C_{\mathrm{WT}} / C_{\mathrm{MUT}}}{K_{\mathrm{d/WT}} / K_{\mathrm{d/MUT}} + C_{\mathrm{WT}} / C_{\mathrm{MUT}}} = \frac{\hat{\gamma}}{K_{\mathrm{d/WT}} / K_{\mathrm{d/MUT}} + \hat{\gamma}} \tag{2.11}$$

finally, yielding aggregate CDI as

$$CDI = CDI_{WT} \cdot \frac{\hat{\gamma}}{K_{d/WT} / K_{d/MUT} + \hat{\gamma}} \text{ or } \frac{CDI}{CDI_{WT}} = \frac{\hat{\gamma}}{\Lambda + \hat{\gamma}} \quad (2.12)$$

where $\Lambda = K_{d/WT} / K_{d/MUT}$.

2.6.8 Dose-Dependent Effect of CaM_{D130G} and CaM_{F142L}

In Figure 2.6 of the main text, we focused on the graded effects of variable expression ratios of CaM_{WT} to CaM_{D96V}. Here, we show that the mutants CaM_{D130G} and CaM_{F142L} also result in similar graded reductions of CDI (Supplementary Figure 2.9). Because of the preassociation of apoCaM and Ca^{2+} channels (Zuhlke et al., 1999; Erickson et al., 2001), and the fact that mutant apoCaM can bind to the channels at least as well as the wild-type apoCaM (Figures 2.5D-E), the CDI dose response to the relative protein expression ratio of wild-type and mutant CaMs ($\hat{\gamma}$) follows the Langmuir predictioin (Equation 2.12) precisely for all three LQTS mutant CaMs.

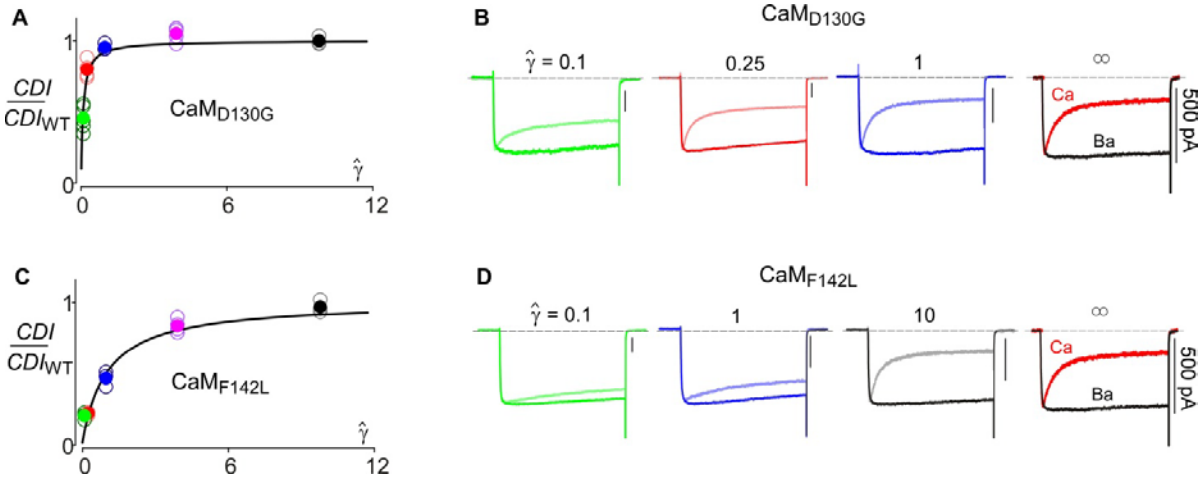

Supplementary Figure 2.9 Dose-dependent effect of CaM_{D130G} and CaM_{F142L}. (**A**) Langmuir plot of normalized *CDI* as a function of $\hat{\gamma}$, ratio of protein expression levels of CaM_{WT} and CaM_{D130G}. Solid circles indicate average data for each ratio $\hat{\gamma}$; open circles are data from individual cells. Black curve drawn with $\Lambda \sim 0.1$. (**B**) Exemplar current traces corresponding to the data in panel **A** with the similar color code for each value of $\hat{\gamma}$. For each, the Ca^{2+} trace is the lighter color, with the corresponding Ba^{2+} trace normalized to the peak of the Ca^{2+} trace for comparison. Scale bar corresponds to Ca^{2+}. Exemplar current traces from cells expressing CaM_{WT} only $(\hat{\gamma} = \infty)$ is reproduced from Figure 2.2A for reference. (**C**) Langmuir plot of normalized *CDI* as a function of $\hat{\gamma}$, ratio of protein expression levels of CaM_{WT} and CaM_{F142L} in a similar format as **A**. Black curve drawn with $\Lambda \sim 1$. (**D**) Exemplar current traces corresponding to the data in **C**. Same format as **B**.

CHAPTER 3

A precision medicine approach to the rescue of function in malignant calmodulinopathic long QT syndrome

3.1 Introduction

In the previous chapter, we have shown that LQTS-associated calmodulinopathy mutations (D96V, D130G, and F142L) mediate a decrease in CDI of $Ca_V1.2$. This would result in the failure of calmodulinopathy-affected $Ca_V1.2$ channels to inactivate during the plateau of the cardiac action potential (AP), and is predicted to prolong the AP duration (APD), a cellular correlate of prolonged QT intervals identified on the electrocardiogram (Limpitikul et al., 2014; Yin et al., 2014). In human, there are three distinct CaM genes, *CALM1* (chr14q31), *CALM2* (chr2p21), and *CALM3* (chr19q13), with 85% nucleotide sequence homology that encode for completely identical 149 amino-acid CaM proteins. In all reported cases of LQTS-associated calmodulinopathies, the mutation occurs heterozygously in one of these three redundant *CALM* genes, i.e. with only one out of six alleles harboring the mutation. Thus, only a small fraction of mutant CaM protein causes the severe phenotype. This large dominant negative effect may be rationalized by the known pre-association of Ca^{2+}-free CaM to the LTCCs (Erickson et al., 2001; Limpitikul et al., 2014). In fact, the reduction of CDI due to mutant CaM expression corresponds to a highly non-linear effect such that a relatively small amount of mutant CaM can significantly decrease CDI in HEK293 cells (Limpitikul et al., 2014). However, this phenomenon remains to be substantiated in a cardiac system under conditions mimicking that of a calmodulinopathy patient. To this end, we generated induced pluripotent stem cells (iPSCs) from a patient harboring a heterozygous p.D130G-CaM mutation (Boczek et al., 2016) resulting from a single

nucleotide substitution (c.389 A>G) within the *CALM2* gene. Cardiomyocytes (CMs) differentiated from these cells (iPSC-CMs) offer an ideal platform for exploring the dominant negative effect of mutant CaM within a patient-specific genetic background and provide a model system with which to understand the pathogenesis and treatment options of CaM-mediated LQTS.

The non-linear CDI effect in calmodulinopathies may also provide an opportunity for novel therapeutic interventions. Impaired repolarization resulting from a deficit of LTCC CDI exhibits a non-linear threshold such that the fraction of channels harboring a CDI deficit can increase without overt electrical dysfunction up to a critical threshold. At this point, addition of even a minute fraction of affected channels generates the substrate for flagrant arrhythmogenesis (Dick et al., 2016). Should this threshold behavior hold true, a relatively small decrease in mutant CaM could result in a significant increase in electrical stability and thus lead to substantial clinical improvement. To this end, we exploit the precise genetic control of a variant of CRISPR/Cas9 technology, CRISPR interference (CRISPRi) (Gilbert et al., 2013; Qi et al., 2013; Mandegar et al., 2016), to selectively down-regulate mutant CaM expression without permanently altering the genome. Taking advantage of the fact that patients with calmodulinopathies harbor mutations in only one of three *CALM* genes, mutant CaM could be attenuated while largely sparing wild-type CaM. As a test bed for therapeutic development, we utilize our D130G-CaM containing iPSC-CMs ($iPSC_{D130G\text{-}CaM}$-CMs), as these cells are able to form a functional syncytium with the genetic background of the patient. Such a disease model readily permits application of CRISPRi to down-regulate mutant *CALM* genes and enables analysis of the functional effects of such a manipulation.

In this chapter, we demonstrate that iPSC-CMs derived from a patient harboring the p.D130G-CaM missense mutation within *CALM2* accurately recapitulates the cellular LQTS phenotype. Specifically, the $iPSC_{D130G\text{-}CaM}$-CMs demonstrate prolonged APs, disrupted Ca^{2+} cycling, and diminished LTCC CDI, consistently across extended culture time. Having established a viable model system, we next use CRISPRi to selectively silence the expression of the *CALM2* gene (both mutant and wild-type *CALM2* alleles) and correlate this reduction with a functional rescue of the $iPSC_{D130G\text{-}CaM}$-CMs. In particular, we have corrected fully the magnitude of CDI in these cells, resulting in normalization of the AP profile and therapeutic attenuation of the APD.

3.2 Materials and methods

3.2.1 Study participant

A p.D130G-CaM missense mutation secondary to c.389 A>G-CALM2 was identified previously in a young female patient with severe LQTS that was referred to the Windland Smith Rice Sudden Death Genomics Laboratory (Michael J. Ackerman, MD, PhD) at Mayo Clinic, Rochester, MN for research-based genetic testing (Boczek et al., 2016). This study was approved by the Mayo Foundation Institutional Review Board and informed consent was obtained.

3.2.2 Generation of iPSCs

Dermal fibroblasts were isolated from a punch skin biopsy obtained from the p.D130G-CaM positive patient and expanded in DMEM containing 10% FBS. These fibroblasts were reprogrammed using the CytoTune-iPS 2.0 Sendai Reprogramming Kit (Invitrogen) according to manufacturer's recommendations. Colonies were isolated as separate clones and characterized for pluripotency based on immunofluorescent staining (Supplementary Figures 3.1 and 3.2).

Sanger sequencing of genomic DNA of each clone confirmed a heterozygous mutation c.389 A>G-CALM2. Wild-type iPSCs used for control experiments were a generous gift from Dr. Bruce Conklin (Spencer et al., 2014). All cell lines were tested negative for mycoplasma.

3.2.3 Cell culture

IPSCs were cultured and differentiated in a feeder-free and xeno-free system using a modified protocol described previously (Nakahama and Di Pasquale, 2016). Briefly, iPSCs were cultured on Geltrex matrix (Gibco)-coated tissue culture plates and fed daily with Essential 8 medium (Gibco). When cells were ~30% confluent, they were mechanically dissociated using 0.5 mM EDTA in Dulbecco`s Phosphate Buffered Saline (DPBS). For differentiation into cardiomyocytes, cells were dissociated and plated on fresh Geltrex matrix-coated plates. When confluent (day 0), media was exchanged with RPMI-1640 (Sigma-Aldrich) supplemented with B-27(-insulin) (Gibco) and 6 μmol/L CHIR99021. Cells were maintained in this media for the first 7 days, with medium exchange every 2 days. On day 3, 5 μM IWR-1 was added. On day 7, media was changed to RPMI-1640 with B-27 supplement (Gibco) and was exchanged every 2 days. Spontaneous contraction of iPSC-CMs was observed by day 12.

12-14 days post-differentiation, sheets of contracting iPSC-CMs were dissociated using 0.05% trypsin-EDTA (Gibco). The isolated cells were pre-plated for 4-8 min on Geltrex-coated tissue culture plates in order to decrease the number of non-cardiac cells, and the non-adherent cells were then plated on Geltrex matrix-coated glass coverslips at ~$2.5x10^4$ cells/cm^2 for electrophysiological studies and ~$3x10^5$ cells/cm^2 on plastic coverslips to create monolayers for imaging.

3.2.4 CRISPRi construction, transfection, and transduction

The lentiviral transfer vectors containing cDNA for enzymatically dead Cas9 fused with suppressor Krüppel-associated box (KRAB) and blue florescence protein (BFP) (pHR-SFFV-dCas9-BFP-KRAB) was purchased from Addgene (Plasmid #46911). BFP was replaced with monomeric ruby red fluorescence protein (mRuby). The entire construct (dCas9-mRuby-KRAB) was then cloned via Gibson assembly (New England Biolabs) into the lentiviral vector pRRLsin18.cPPT.CMV.eGFP.Wpre54 (Kapoor et al., 2014). The lentiviral vector (pKLV-U6gRNA(BbsI)-PGKpuro2ABFP) containing cDNA for the gRNA backbone (driven by the human U6 promoter) and a BFP marker (driven by PGK promoter) was purchased from Addgene (Plasmid #50946) and BFP was replaced with cyan fluorescence protein (CFP). E-CRISPR gRNA sequence prediction program (Heigwer et al., 2014) was used to generate candidate gRNA sequences that selectively complement to the human *CALM2* gene (Supplementary Table 3.1). The candidate gRNA sequences were then cloned into the aforementioned lentiviral transfer vector using Golden Gate assembly.

For gRNA screening, both dCas9-mRuby-KRAB and candidate gRNA were expressed in HEK293 cells by transfection with polyethylenimine (Limpitikul et al., 2014). For iPSC-CM transduction, lentivirus was generated using Lenti-X-Concentrator (Clontech) according to the manufacturer's recommendations and added to monolayers on day 21 post-differentiation. Expression was confirmed by mRuby and CFP visualization.

3.2.5 Quantification of mRNA level

Total RNA was extracted 4 days post-transfection in HEK293 cells and 8-9 days post-transduction in iPSC-CMs using an RNeasy kit (Qiagen). Complementary DNA was made using

the high-capacity cDNA reverse transcription kit (Applied Biosystems). Quantification of *CALM* mRNA levels was performed using real time PCR (qPCR) with TaqMan gene expression assay (Applied Biosystems). *CALM* expression level was normalized to the expression level of a house-keeping gene glyceraldehyde 3-phosphate dehydrogenase (*GAPDH*). Probe numbers: *CALM1*; Hs00300085_s1, *CALM2*; Hs00830212_s1, *CALM3*; Hs00968732_g1, and *GAPDH*; Hs02758991_g1.

3.2.6 Electrophysiology

Whole-cell recordings of iPSC-CMs were performed 28-30 days post-differentiation at room temperature using an Axopatch 200B amplifier (Axon Instruments). Traces were lowpass filtered at 2 kHz, and digitally sampled at 10 kHz. P/8 leak subtraction was used, with series resistances of 1-2 MΩ. Internal solutions contained, (in mM): $CsMeSO_3$, 114; CsCl, 5; $MgCl_2$, 1; MgATP, 4; HEPES (pH 7.3), 10; BAPTA, 10; and ryanodine, 0.005; at 295 mOsm adjusted with $CsMeSO_3$. Seals were formed in Tyrode's solution containing (in mmol/L): NaCl, 135; KCl, 5.4; $CaCl_2$, 1.8; $MgCl_2$, 0.33; NaH_2PO_4, 0.33; HEPES, 5; glucose, 5 (pH 7.4). Following patch rupture, bath solution was switched to Ca^{2+}- or Ba^{2+}- external solution containing (in mM): TEA-$MeSO_3$, 140; HEPES (pH 7.4), 10; and $CaCl_2$ or $BaCl_2$, 5 (for 30-day-old iPSC-CMs) or 40 (for 60-day-old iPSC-CMs); at 300 mOsm, adjusted with TEA-$MeSO_3$. The extent of CDI after a 50-ms depolarization (f_{50}) was calculated as:

$$f_{50} = (r_{50/Ba} - r_{50/Ca})/r_{50/Ba}$$

where $r_{50/Ba}$ and $r_{50/Ca}$ are currents remaining after 50-ms with Ba^{2+}- and Ca^{2+}-containing external solution.

3.2.7 Imaging

Monolayers of iPSC-CMs expressing either a genetically encoded voltage or Ca^{2+} sensor (ASAP1 (St-Pierre et al., 2014) or GCaMP6f (Chen et al., 2013) respectively via lentiviral transduction) were paced using a custom field stimulation apparatus in RPMI-1640 medium with B-27 supplement. Expression efficiency of the genetically encoded sensors was assessed via flow cytometry (Supplementary Figure 3.3). At 30, 45, and 60 days post-differentiation, green fluorescence was imaged with an Evolve 512delta camera at ≥ 190 frames per second and the relative change in fluorescence signal was measured. The time from upstroke to 80% repolarization (APD_{80}) was used to index the APD while the magnitude of peak transient, time to peak, and decay time constant were used as metrics for CaTs. All metrics were quantified using custom Matlab (Mathworks) scripts. For all experiments involving treatment with CRISPRi, control cells were recorded on the same day and were from the same culture, minimizing any culture dependent variability of the cells.

3.2.8 Statistical analysis

All parameters are shown as mean ± SEM. Technical and biological replicates are indicated in the figure legend. The D'Agostino & Pearson omnibus normality test was used to confirm a normal distribution prior to application of the statistical test for comparison of means. Data which did not initially correspond to a normal distribution were logarithmically transformed. The F-test was used to compare variances and a two-sided Student's t-test (adjusted for unequal variance where applicable) was used to compare the difference in means across sample groups. Reported p values are from the two-sided Student's t-test. Minimal sample size to ensure adequate power was determined as previously described (Parker and Berman, 2003).

3.3 Results

3.3.1 Proband identification and generation of mutation-harboring iPSCs

An increasing number of patients are being diagnosed with calmodulinopathies resulting from single heterozygous missense mutations within their *CALM1*, *CALM2*, or *CALM3* genes. Here, we focus on a p.D130G-CaM mutation identified within *CALM2* of a female infant with severe LQTS (Boczek et al., 2016). The proband was born at term, and noted to have bradycardia (Figure 3.1). An ECG, recorded 12 hours after birth, revealed a QTc of 740 ms and 2:1 atrioventricular block (Figure 3.1A). She was treated with beta-blockers, phenytoin, spironolactone, potassium, and placement of a single-chamber pacemaker within the first week of life. At 6-years-old, a single-chamber implantable cardioverter-defibrillator was implanted and beta-blocker therapy was continued. At 11 and 14 years old, she experienced appropriate defibrillator discharges for ventricular fibrillation.

Next-generation whole exome sequencing followed by *CALM1*, *CALM2*, and *CALM3* gene-specific analysis identified a p.D130G-CaM mutation (c.389 A>G, *CALM2*) within the patient (Figure 3.1B). The mutation maps to an EF-hand within CaM (Figure 3.1C) and, similar to other calmodulinopathic mutations, causes a reduction in the Ca^{2+} binding affinity (Crotti et al., 2013). In order to create a model system with which to understand the pathogenesis and treatment options for this type of CaM-mediated LQTS, multiple clones of iPSCs were generated from the patient's skin biopsy. Two clones with normal karyotypes at passage 25 and expressing the pluripotency markers (Nanog, Oct4, and SSEA4) were selected (Supplementary Figure 3.1). In addition, the ability to generate each of the three germ layers was confirmed by staining differentiated embryoid bodies for α-fetoprotein (endoderm), smooth muscle actin (mesoderm),

and glial fibrillary acidic protein (ectoderm) and by analysis of teratoma formation (Supplementary Figure 3.2). Monolayers of iPSC-CMs ($iPSC_{D130G\text{-}CaM}$-CMs) were then generated from these two clones of iPSCs.

To confirm that the background of these $iPSC_{D130G\text{-}CaM}$-CMs was not significantly different than iPSCs derived from healthy individuals, we quantified the mRNA levels for multiple proteins that could potentially alter cardiac action potential morphology and/or EC coupling. Compared to wild-type iPSC-CMs ($iPSC_{WT}$-CMs), we found no difference in the mRNA levels of *CALM1, CALM2, CALM3, CACNA1C, KCNH2, NCX1, SCN5A, PLN* or *SERCA2* (Supplementary Figure 3.4). Only KCNQ1 and RYR2 appeared somewhat elevated in the $iPSC_{D130G\text{-}CaM}$-CMs; however, this variation would not be expected to contribute to a LQT phenotype. Importantly, this validates our $iPSC_{WT}$-CMs as a relevant control, despite the potential variability which can occur due to differing genetic backgrounds (Sharma et al., 2013).

3.3.2 Altered APs and calcium transients (CaTs) in $iPSC_{D130G\text{-}CaM}$-CMs

Previous work has linked mutations in CaM with LQTS; however, direct evidence demonstrating AP prolongation due to the D130G-CaM mutation has yet to be shown in human cardiomyocytes. We therefore characterized the $iPSC_{D130G\text{-}CaM}$-CMs in order to confirm that these cells exhibit prolonged APDs that typically underlie LQTS. To measure APDs, the monolayers were transduced with the genetically encoded voltage sensor ASAP1, which features rapid kinetics and stable long-term expression, allowing accurate APD measurements over multiple time points (St-Pierre et al., 2014). The resultant APDs (Figures 3.1D, E) measured from wild-type iPSC-CMs ($iPSC_{WT}$-CMs) were comparable to those previously reported (Supplementary Table 3.1) (Ma et al., 2011; Spencer et al., 2014). Under these same conditions,

$iPSC_{D130G\text{-}CaM}$-CMs exhibited dramatically longer APs and APDs (Figures 3.1G, J; red) as compared to their WT counterparts (gray). This result could be observed at multiple pacing frequencies (Figures 3.1H, K), a feature associated with increased arrhythmogenic risk (Marban, 2002). Moreover, the phenotype was stable over long periods of time in culture, such that APDs measured at 30 days in culture were not significantly different than those measured after 45 days or 60 days (Figures 3.1F, I, L; Supplementary Figure 3.6).

In addition to the electrical disturbance, dysfunctions in Ca^{2+} cycling are often associated with arrhythmogenesis in LQTS (Xie and Weiss, 2009). As such, we examined the intracellular Ca^{2+} transients (CaTs) of iPSC-CMs using GCaMP6f, a genetically encoded Ca^{2+} sensor with a high signal-to-noise ratio and fast kinetics (Chen et al., 2013). Figure 3.2A shows the CaTs from a monolayer of $iPSC_{WT}$-CMs paced at 0.25 Hz with the rise and decay kinetics comparable to those previously reported (Hwang et al., 2015). However, monolayers of $iPSC_{D130G\text{-}CaM}$-CMs exhibit CaT amplitudes over three times larger than WT with slower rise and decay kinetics (Figures 3.2B-F), akin to the phenotype observed in CaM_{D130G}-overexpressing rodent myocytes (Limpitikul et al., 2014; Yin et al., 2014). Likewise, these CaT effects were stable over time (Supplementary Figure 3.7). While SR content of the $iPSC_{D130G\text{-}CaM}$-CMs was not significantly different from the WT myocytes (Supplementary Figure 3.8), the trend was in the direction of increased SR Ca^{2+}. Thus, the patient-derived $iPSC_{D130G\text{-}CaM}$-CMs recapitulate the LQTS phenotype, demonstrating significant proarrhythmic potential despite limited, native expression levels of CaM_{D130G}.

3.3.3 IPSC$_{D130G\text{-}CaM}$-CMs exhibit diminished CDI

Previous studies have implicated the cardiac LTCC as a major contributor to the LQT phenotype in patients with CaM-mediated LQTS (Limpitikul et al., 2014; Yin et al., 2014). In particular, the D130G mutation weakens the affinity of Ca^{2+} binding to CaM (Crotti et al., 2013), resulting in a significant decrease in CDI when CaM_{D130G} is overexpressed in rodent myocytes (Limpitikul et al., 2014; Yin et al., 2014). However, the relevance of these results remains to be established in human CMs with physiological levels of mutant CaM expression. We therefore examined the effect of the D130G mutation on LTCC CDI in patient-derived iPSC-CMs. To this end, we performed whole-cell patch clamp recordings of individual CMs. IPSC$_{WT}$-CMs exhibited a rapid decay in their Ca^{2+} current in response to a 10-mV depolarizing step (Figure 3.3A, red). To isolate the extent of pure CDI, Ba^{2+}, which binds poorly to CaM, was used as the charge carrier to gauge the extent of voltage-dependent inactivation (VDI) within the same cell (Limpitikul et al., 2014). CDI can be seen as the excess inactivation of the Ca^{2+} trace (Figure 3.3A, red), as compared to the Ba^{2+} trace (black). Population data showing the average normalized peak Ba^{2+} currents as a function of voltage is shown in Figure 3.3B. For CDI quantification, we first measure the fraction of current remaining after 50 ms (r_{50}) for both the Ca^{2+} and Ba^{2+} currents. By plotting the r_{50} values as a function of voltage, a hallmark U-shaped relationship is observed with Ca^{2+} as the charge carrier (Figure 3.3C, red). The difference between the Ba^{2+} and Ca^{2+} r_{50} values at 10 mV, normalized by the Ba^{2+} r_{50} value, quantifies the extent of pure CDI (Figure 3.3C). Applying this same protocol to the iPSC$_{D130G\text{-}CaM}$-CMs reveals a profound attenuation in the kinetics and extent of CDI (Figures 3.3D, G) without altering the voltage activation profile (Figures 3.3E, H). Quantifying this result across voltages (Figures 3.3F, I) confirms a significant decrease in CDI (red, $p < 0.01$), an effect which is maintained over

time in culture (Supplementary Figure 3.9). Importantly, this reduction of CDI is significant even in the $iPSC_{D130G\text{-}CaM}$-CM background, where the patient's other five *CALM* alleles are WT. Thus, these $iPSC_{D130G\text{-}CaM}$-CMs not only provide a viable model system for this LQTS-associated calmodulinopathy, but also suggest that the loss of LTCC CDI is a significant underlying mechanism leading to arrhythmogenesis in these patients.

To further bolster this LTCC centric hypothesis, we examined the effects of other potential CaM targets which might contribute to the LQT phenotype of calmodulinopathy patients. To date, only three genetic forms of LQTS result from mutations within a channel known to be modulated by CaM. LQTS type 1 results from loss of function mutations in *KCNQ1,* LQT3 results from gain-of-function mutations in *SCN5A*, and LQT8 is caused by inactivation altering mutations within *CACNA1C*, somewhat mirroring the LTCC effects described in this study. Of these forms of LQT, only LQT8 approaches the extreme APD prolongation seen in calmodulinopathy patients (Splawski et al., 2004; Splawski et al., 2005). To corroborate this in our model system, we mimicked the effect of each LQT mechanism pharmacologically. Consistent with clinical findings, enhancement of the current through the LTCC had a profound effect on APD, while blocking I_{KS} or enhancing $Na_V1.5$ produced more modest APD prolongation (Supplementary Figure 3.10). We next utilized a validated model of an adult mammalian cardiomyocyte (Luo and Rudy, 1994a, b; Livshitz and Rudy, 2007; Dick et al., 2016) to investigate the fraction of channels harboring a CaM_{D130G} required to produce electrical instability via and LTCC CDI specific mechanism *in silico* (Supplementary Figure 3.11). Indeed, only a small fraction of channels harboring CaM_{D130G} was necessary to achieve significant arrhythmogenesis in the model cells. Importantly, the simulation predicted a threshold for the induction of electrical instability precisely matching the expected levels of mutant CaM

expression in calmodulinopathy patients based on reported *CALM* gene expression (Petryszak et al., 2014). Such a threshold highlights an important therapeutic principle; namely, only a small reduction in the expression levels of the mutant CaM may be needed to provide significant clinical benefit to patients.

3.3.4 Toward a new therapeutic strategy

Having confirmed a major role for LTCC CDI deficits in generating the LQT phenotype in this calmodulinopathy patient, we next considered the implications of this mechanism on a novel therapeutic intervention. As our results predict a significant functional benefit conferred by even a small shift in the expression of mutant versus WT CaM (Supplementary Figure 3.11), we sought to reduce the fraction of mutant CaM expressed in patients with CaM-mediated LQTS. As all three *CALM* genes encode for identical CaM proteins, we reasoned that we might be able to take advantage of the sequence variation at the nucleotide level. We thus utilized CRISPRi (Gilbert et al., 2013; Qi et al., 2013; Mandegar et al., 2016) to decrease the transcription of the *CALM2* alleles, both the WT and the D130G-containing *CALM2* alleles.

The CRISPRi technology uses a short guide RNA (gRNA) which binds specifically to a target nucleotide sequence. By pairing this gRNA with a nuclease-dead Cas9 (dCas9) fused to suppressor Krüppel-associated box (KRAB), selective suppression of the target gene could be achieved. Our first step was therefore to optimize gRNA sequences capable of selectively targeting *CALM2*. Sequence optimization was first done *in silico* (Heigwer et al., 2014), followed by evaluation of the efficiency and specificity of each candidate gRNA in HEK293 cells via qPCR (Supplementary Figure 3.12, Supplementary Table 3.2). We choose design 21

(Figure 3.4A) as this gRNA specifically reduced the expression of *CALM2*, without appreciable alteration of either *CALM1* or *CALM3*.

Having identified a potential treatment strategy, we next sought to test this approach within our iPSC$_{D130G\text{-}CaM}$-CMs. Monolayers were lentivirally transduced with genes encoding dCas9-mRuby-KRAB and gRNA-CFP, and expression of both constructs was confirmed by visualization of red and blue fluorescence, respectively. Compared to untreated iPSC$_{D130G\text{-}CaM}$-CMs, the CRISPRi-treated iPSC$_{D130G\text{-}CaM}$-CMs exhibited significantly lower levels of *CALM2* mRNA with unaltered levels of *CALM1* and *CALM3* (Figure 3.4B) mRNA level with the overall reduction of total amount of CaM protein (Supplementary Figure 3.5). In addition, we probed the effect of treatment on multiple cardiac genes and found no significant change in the mRNA levels of *CACNA1C, KCNQ1, KCNH2, SCN5A, RYR2, SERCA2, NCX1* or *PLN* (Supplementary Figure 3.4). Having achieved a selective decrease in *CALM2* transcription, we next tested if this reduction correlated with a functional effect within the iPSC$_{D130G\text{-}CaM}$-CMs. Indeed, treatment of the monolayers resulted in a substantial shortening of the APDs in response to 0.5-Hz stimulation (Figure 3.4C, blue) as compared to untreated monolayers (gray). This effect was consistent across multiple trials, resulting in a significant decrease in APD as compared to untreated iPSC$_{D130G\text{-}CaM}$-CMs (Figure 3.4C, right), establishing CRISPRi as a robust and promising strategy for the treatment of CaM-mediated LQTS.

Having established functional rescue of the iPSC$_{D130G\text{-}CaM}$-CM monolayers, we next considered the underlying mechanism. Our previous results suggest that APD prolongation of these cells stems from a CDI deficit of the LTCC (Figure 3.3). We therefore predicted that successful treatment of these cells should correspond to a correction (increase) in the CDI of the LTCCs. Indeed, treated iPSC$_{D130G\text{-}CaM}$-CMs displayed significantly faster CDI (Figure 3.4D) as

compared to untreated cells. In fact, CDI in the treated cells was nearly identical to that of $iPSC_{WT}$-CMs (Figure 3.3). Thus, CRISPRi effectively reduced the expression of the mutant and WT *CALM2* alleles, resulting in normalization of the APD, and restoration of LTCC's CDI mechanism.

3.3.5 Generalization of the CRISPRi strategy across calmodulinopathy subtypes

Beyond the proband described in this study, the CRISPRi treatment strategy is readily generalizable to any calmodulinopathy. In contrast to the classic CRISPR/Cas9 genome editing technique where the gRNA sequence is tailored to an exact locus within the affected gene, CRISPRi targets the entire gene of interest itself, resulting in repression regardless of the specific base-pair alteration. This technique can therefore be adjusted to target *CALM1* or *CALM3* genes, providing efficacy across calmodulinopathy patient populations agnostic to the phenotype. We thus created gRNA sequences targeting each of the *CALM* genes (Figure 3.5A, Supplementary Figure 3.12, and Supplementary Table 3.2) and tested their efficacy in iPSC-CMs. Utilizing $iPSC_{WT}$-CMs, we are indeed able to specifically decrease the expression of either *CALM1* (Figure 3.5B) or *CALM3* (Figure 3.5C), thus providing a modular toolkit for the treatment of calmodulinopathies resulting from a mutation within any of the three *CALM* genes.

3.4 Discussion

$IPSC_{D130G\text{-}CaM}$-CMs provide a good model system for investigating the underlying pathology of LQTS-associated calmodulinopathies. Two distinct $iPSC_{D130G\text{-}CaM}$-CM clones each formed a stable contracting syncytium and exhibited prolonged APs, Ca^{2+} cycling disturbances, and diminished LTCC CDI across extended culture. Creation of this model system enabled the generation and testing of a new therapeutic strategy. Taking advantage of the genome targeting

precision of CRISPRi, we were able to selectively and efficiently silence both the WT and the D130G-containing *CALM2* alleles, resulting in functional rescue of both LTCC CDI and cardiac AP morphology. This proof-of-principle therapy thus represents a first step towards a novel, targeted therapeutic design for calmodulinopathies.

Previous studies on the underlying mechanism of LQTS-associated calmodulinopathies have involved the overexpression of mutant CaM in rodent myocytes (Limpitikul et al., 2014; Yin et al., 2014). While such studies have implicated the LTCC (Limpitikul et al., 2014) and ruled out the $Na_V1.5$ channel (Yin et al., 2014) as major contributors to the LQT phenotype of calmodulinopathy patients, they do not represent the native expression levels of mutant CaM. In particular, calmodulinopathy patients harbor a single heterozygous mutation in only one of three redundant *CALM* genes. The ability of the resultant small fraction of mutant CaM protein to produce the severe phenotype seen in patients has been attributed to CaM's pre-association to the LTCC (Limpitikul et al., 2014). In this context, a fraction of LTCCs pre-bound to mutant CaM will display diminished CDI, disrupting the precise tuning of the AP by Ca^{2+} influx. The profound prolongation of the APs and decreased CDI observed in the $iPSC_{D130G\text{-}CaM}$-CMs corroborate just such a dominant negative effect. Moreover, the amelioration of the LQTS phenotype of the $iPSC_{D130G\text{-}CaM}$-CMs via suppression of *CALM2* transcription firmly establishes this mutation as the causative genetic mechanism. However, this new mechanistic insight also presents a significant challenge to the treatment of these calmodulinopathy patients. The pre-association of LTCCs with both mutant and WT CaM makes selective targeting of the disrupted LTCCs nearly impossible. Thus, any treatment option for these patients must selectively target the mutant CaM, prior to cytosolic expression and binding to the LTCC.

Fortunately, CRISPRi provides just such a therapeutic option. In fact, recent work demonstrates that CRISPRi is capable of robust gene knock down within both iPSCs as well as iPSC-derived cardiomyocytes, making this a highly attractive method which has already been validated for our model system. Moreover, this technique offers the advantages of selectivity, reversibility, and generalizability (Gilbert et al., 2013; Qi et al., 2013; Mandegar et al., 2016). That is, RNA transcription of specific mutation-containing *CALM* genes can be repressed, without modifying the patient genome and risking permanent alteration of off-target or downstream elements (Gilbert et al., 2013; Qi et al., 2013). Further, this technique is generalizable to any calmodulinopathy. Here, we present a simple therapeutic toolbox in which three gRNAs targeting either *CALM1*, *CALM2*, or *CALM3* can be chosen to match any calmodulinopathy patient. Importantly, this means that while this study focused on the LQTS-associated calmodulinopathies, the therapy developed here should also be effective for the CPVT- and IVF-associated calmodulinopathies. Moreover, as expected due to the widespread distribution of CaM, calmodulinopathy patients also exhibit extra-cardiac phenotypes including seizures and developmental delays (Crotti et al., 2013). Importantly, the CRISPRi toolkit should be effective on these non-cardiac symptoms, as targeting of the CRISPRi can be adjusted to include any affected organ systems.

More broadly, this therapeutic principle could be applied to the treatment of any disease in which there is a redundancy of the affected gene. Thus, the CRISPRi strategy described here not only represents a promising new treatment option for calmodulinopathy patients, but could provide a generalizable strategy in the treatment of a variety of diseases. Fortuitously, development of CRISPR/Cas9 delivery into patients is already well underway (Ran et al., 2015), propelling the translation of these findings towards improving patients' health and quality of life

and in the case of patients with a LQTS/CPVT/IVF-associated calmodulinopathy, preventing sudden death in the young.

3.5 Tables and figures

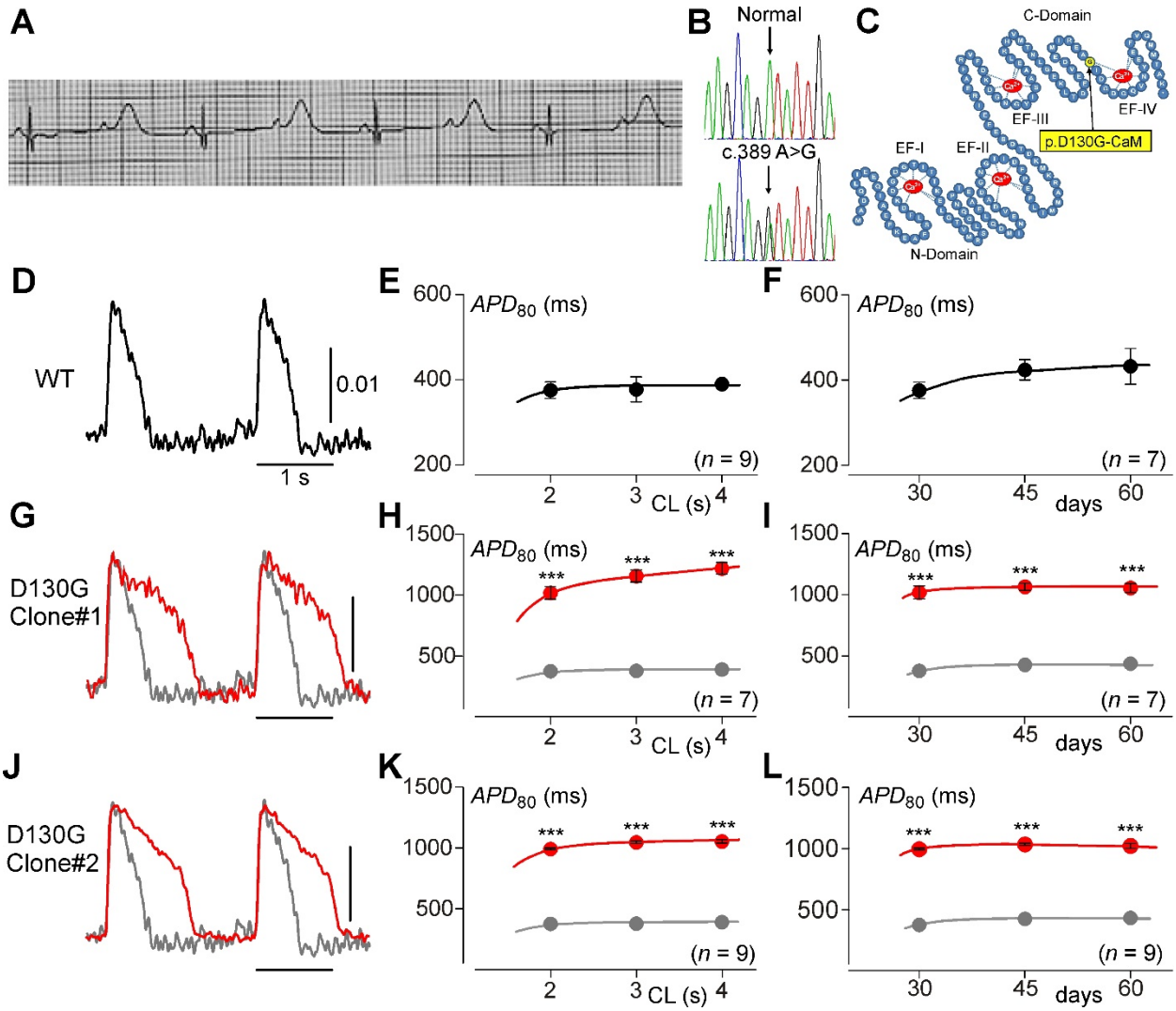

Figure 3.1 IPSCs recapitulate the calmodulinopathy phenotype. (**A**) The proband's electrocardiogram taken at 12 hours after birth, illustrating a QTc>700 ms. (**B**) DNA Sanger sequencing chromatograms for both a normal control (top) and the patient (bottom) revealing a heterozygous c.389 A>G single nucleotide substitution in *CALM2* resulting in the p.D130G-CaM amino acid substitution. (**C**) Schematic rendering of the CaM protein (blue) highlighting the N-domain and C-domain, each containing two EF hands (labeled EF-I through EF-IV) with Ca^{2+} (red) bound. Yellow circle indicates the D130G mutation identified in the LQTS patient. (**D**) Exemplar APs from $iPSC_{WT}$-CMs (WT) paced at 0.5 Hz, recorded via fluorescence imaging using ASAP1. Scale bar indicates change in fluorescence as measured by $\Delta F/F_0$. (**E**) Population data for mean APDs at various pacing cycle lengths (CL) for $iPSC_{WT}$-CMs (n=9). Error bars indicate ±SEM throughout. Each biological replicate (n) is an average value of 2 technical replicates, here and throughout this figure. (**F**) Population data for $iPSC_{WT}$-CM APDs at a 2-

second cycle length across multiple time points (n=9, 9, and 7 on day 30, 45, and 60, respectively). **G**, Exemplar APs from $iPSC_{D130G\text{-}CaM}$-CMs (red). WT reproduced in gray. (**H**) Average APD data for $iPSC_{D130G\text{-}CaM}$-CMs (red) (n=7). WT reproduced in gray (*** $p < 0.001$ compared to WT; corrected for unequal variance of normal distributions). (**I**) Average APDs at a 2-second cycle length from D130G iPSCs are stable across time (n=7, 7, and 7 on day 30, 45, and 60, respectively). (**J-L**) Alternate D130G clone demonstrating the same result as (**G-I)** (n=9, *** $p < 0.001$ compared to WT and corrected for unequal variance of normal distributions).

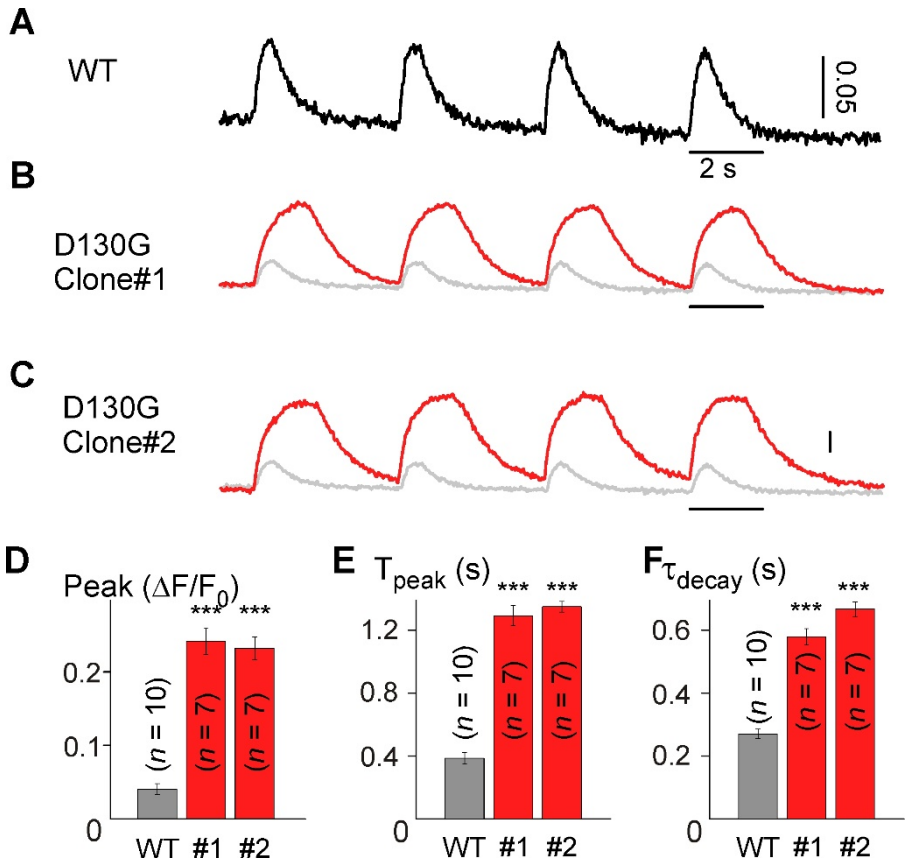

Figure 3.2 Disruption of calcium handling in calmodulinopathy iPSCs. **A**, Exemplar CaTs recorded from $iPSC_{WT}$-CMs (WT) using GCaMP6f. Scale bar indicates change in fluorescence as measured by $\Delta F/F_0$. **B**, Exemplar CaTs recorded from $iPSC_{D130G\text{-}CaM}$-CMs (red) as compared to WT (gray). **C**, Exemplar CaTs from an alternate D130G clone. **D-F**, Population data demonstrating larger amplitude and slower kinetics for both $iPSC_{D130G\text{-}CaM}$-CMs clones (red) (Peak, mean peak fluorescence change; T_{peak}, mean time to peak; τ_{decay}, mean decay time constant; *** $p < 0.001$ compared to WT and corrected for unequal variance, all populations were normally distributed). Error bars indicate ± SEM throughout. Biological replicates (n) are 10, 7, and 7 for WT, D130G clone #1, D130G clone#2, respectively. Each biological replicate (n) is an average value of 2 technical replicates.

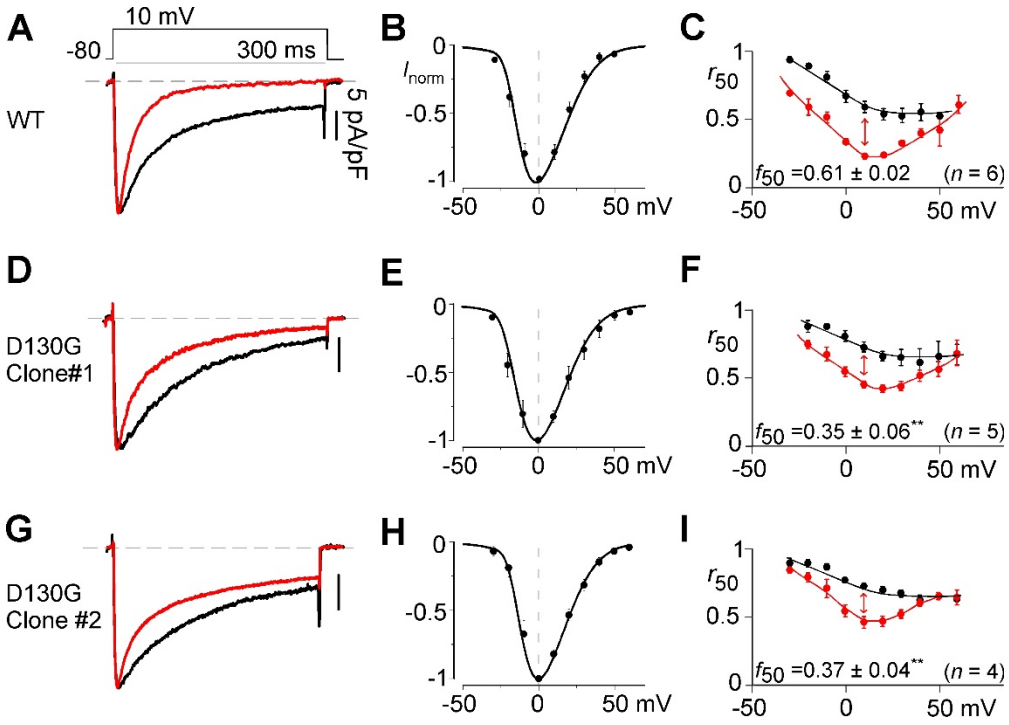

Figure 3.3 CDI deficits in calmodulinopathy iPSCs. A, Exemplar whole-cell current recordings in Ca^{2+} (red) and Ba^{2+} (black) for $iPSC_{WT}$-CMs. Ba^{2+} current is normalized to Ca^{2+} peak, scale bar corresponds to Ca^{2+} here and throughout. **B**, Mean normalized current and voltage relationship obtained in Ba^{2+} for $iPSC_{WT}$-CMs. Error bars indicate ± SEM throughout. **C**, Population data for Ca^{2+} (red) and Ba^{2+} (black) for $iPSC_{WT}$-CMs, where r_{50} quantifies the extent of current inactivation across voltages. Red arrow depicts extent of CDI (f_{50}) at 10-mV test potential here and throughout (n=6 separate cells for **B-C**). **D**, Exemplar whole-cell current recordings in Ca^{2+} (red) and Ba^{2+} (black) for $iPSC_{D130G\text{-}CaM}$-CMs (n=5). **E**, There is no significant shift ($p > 0.05$ compared to WT) in the current voltage relationship for $iPSC_{D130G\text{-}CaM}$-CMs as compared to WT **B**. **F**, Population data demonstrates a significant decrease in CDI for the $iPSC_{D130G\text{-}CaM}$-CMs (**$p < 0.01$ compared to WT, corrected for unequal variance). **G-I**, Alternate D130G clone (n=4) demonstrating the same result as **D-F**.

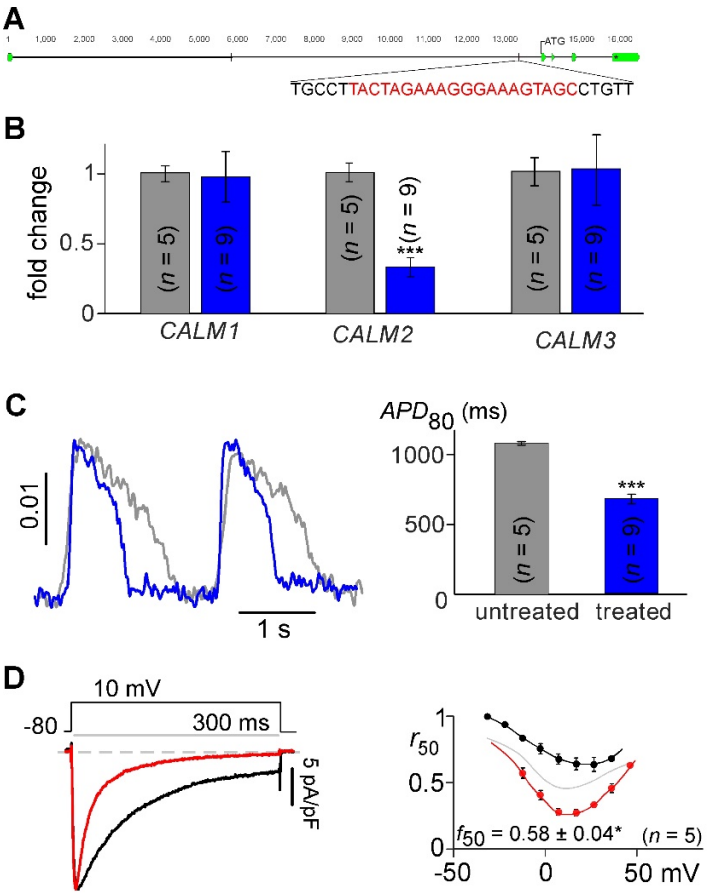

Figure 3.4 Functional rescue of calmodulinopathy via CRISPRi treatment. A, The genomic *CALM2* gene showing the location of each exon (green). The gRNA sequence (red) is located in an intron prior to the start codon. **B**, QPCR results indicating mean relative mRNA levels of *CALM1-3* in iPSC$_{D130G\text{-}CaM}$-CMs at baseline (gray, n=5) and after CRISPRi treatment (blue, n=9). *CALM2* level is significantly reduced (*** $p < 0.001$ compared to untreated and corrected for unequal variance) with relatively unchanged levels of *CALM1* and *CALM3* expression ($p > 0.05$) following the treatment. Error bars indicate ±SEM throughout. **C**, iPSC$_{D130G\text{-}CaM}$-CM APs recorded at 0.5-Hz stimulation using ASAP1 at baseline (gray) and after CRISPRi treatment (blue). Cells correspond to the same monolayers utilized in **B**. APD significantly shortens following CRISPRi treatment (*** $p < 0.001$ compared to untreated, corrected for unequal variance). Scale bar indicates change in fluorescence as measured by $\Delta F/F_0$. **D**, Exemplar whole cell current recordings in Ca^{2+} (red) and Ba^{2+} (black) for iPSC$_{D130G\text{-}CaM}$-CMs treated with CRISPRi (left panel). Population data demonstrates a return of CDI following treatment for the Ca^{2+} r_{50} values (red) as compared to untreated cells (gray, reproduced from **Figure 3I**). Black shows the r_{50} values for treated cells in Ba^{2+}. (n=5, * $p < 0.05$, compared to untreated, no significant difference in variance between populations). Each biological replicate (n) is an average value of 3 technical replicates/measurements for **B** and **C**. There are no technical replicates in **D**.

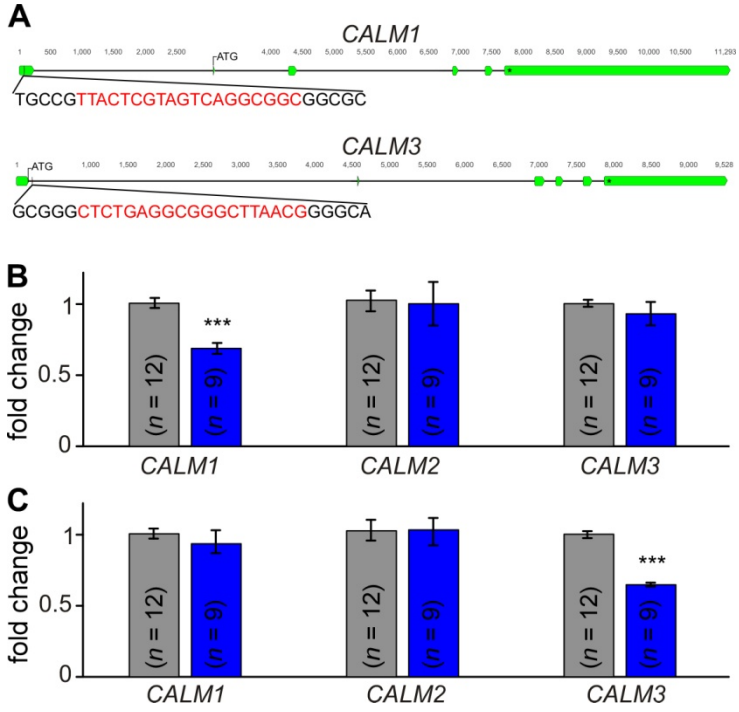

Figure 3.5 CRISPRi can also be used to target either *CALM1* or *CALM3*. **A**, The genomic *CALM1* and *CALM3* genes showing location of each exon (green). The gRNA sequence (red) is located in an untranslated exon prior to the start codon of *CALM1*, and in an intron just past the start codon of *CALM3*. **B**, QPCR results indicating mean relative mRNA levels of *CALM1-3* in $iPSC_{WT}$-CMs at baseline (gray, n=12) and after treatment by CRISPRi targeting *CALM1* (blue, n=9). *CALM1* expression is significantly reduced (*** $p < 0.001$ compared to untreated, no significant difference in variance between populations) with unaltered levels of *CALM2* and *CALM3* ($p > 0.05$). Error bars indicate ±SEM throughout. **C**, QPCR results indicating mean relative mRNA levels of *CALM1-3* in $iPSC_{WT}$-CMs at baseline (gray) and after treatment by CRISPRi targeting *CALM3* (blue, n=9). *CALM3* expression level is significantly reduced (*** $p < 0.001$ compared to untreated, no significant difference in variance between populations) with unaltered levels of *CALM1* and *CALM2* ($p > 0.05$). Each biological replicate (n) is an average value of 3 technical replicates/measurements.

3.6 Supplementary materials

3.6.1 Characterization of the iPSC clones

The iPSC clones generated in this study were derived from a skin biopsy from a patient harboring a p.D130G-CaM mutation residing in the *CALM2* gene[1]. In order to ensure the quality of the generated iPSCs, the karyotype and pluripotency of the cells were fully characterized and validated (Supplementary Figure 3.1).

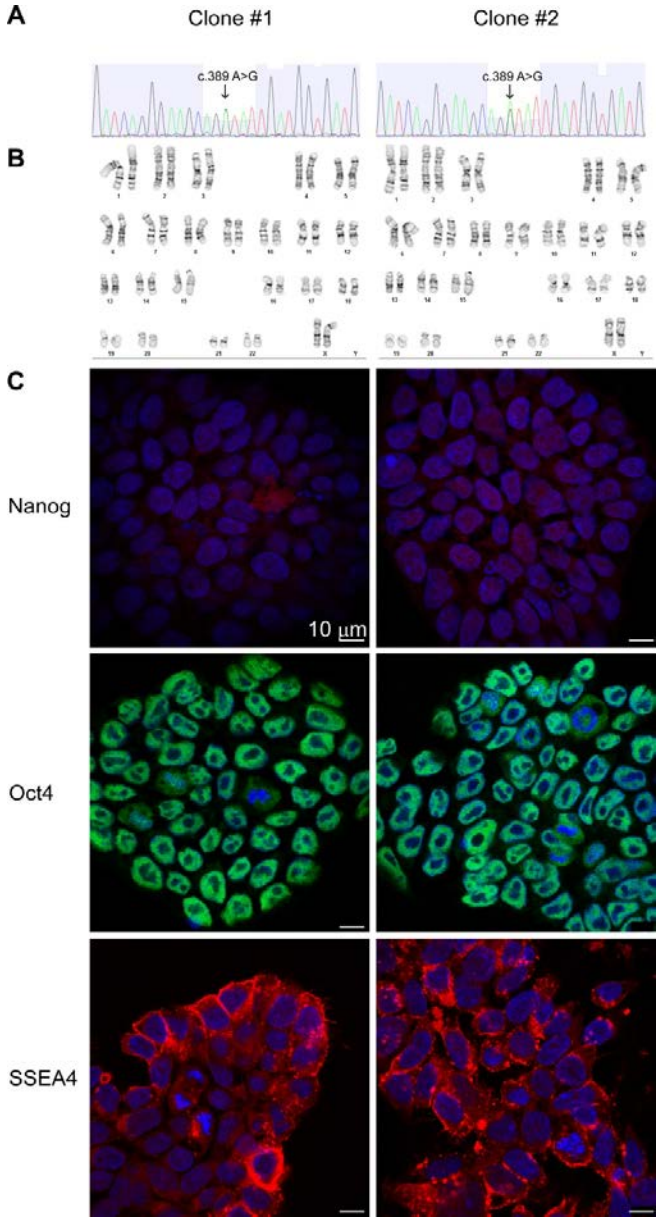

Supplementary Figure 3.1 Assessment of karyotype and pluripotency markers for the iPSC clones. (**A**) Sanger sequencing of *CALM2* genomic DNA confirms c.389 A>G. (**B**) Karyotyping results of both iPSC clones revealed normal size, shape, and number of chromosomes. Karyotyping was commercially performed by WiCell Cytogenetics. (**C**) Immunohistochemistry demonstrated the presence of pluripotency markers: Nanog (red), Oct4 (green), and SSEA4 (red). Nuclei are counter-stained with DAPI (blue).

3.6.2 iPSC$_{D130G\text{-}CaM}$ clones are capable of differentiating into three germ layers

An important feature of iPSC lines is pluripotency; that is, the ability to differentiate into all three germ layers, endoderm, mesoderm, and ectoderm. We have confirmed the pluripotency of iPSC$_{D130G\text{-}CaM}$ clones both *in vitro* and *in vivo*. First, embryoid bodies were generated *in vitro* and markers of three germ layers were labeled by immunohistochemistry (Supplementary Figure 3.2A). Next, the ability of iPSC clones to form teratomas *in vivo* was assessed by injection of iPSCs into immunodeficient mice (Supplementary Figure 3.2B). The hematoxyline and eosin staining of the harvested teratomas revealed tissues from endodermal, mesodermal and ectodermal origins.

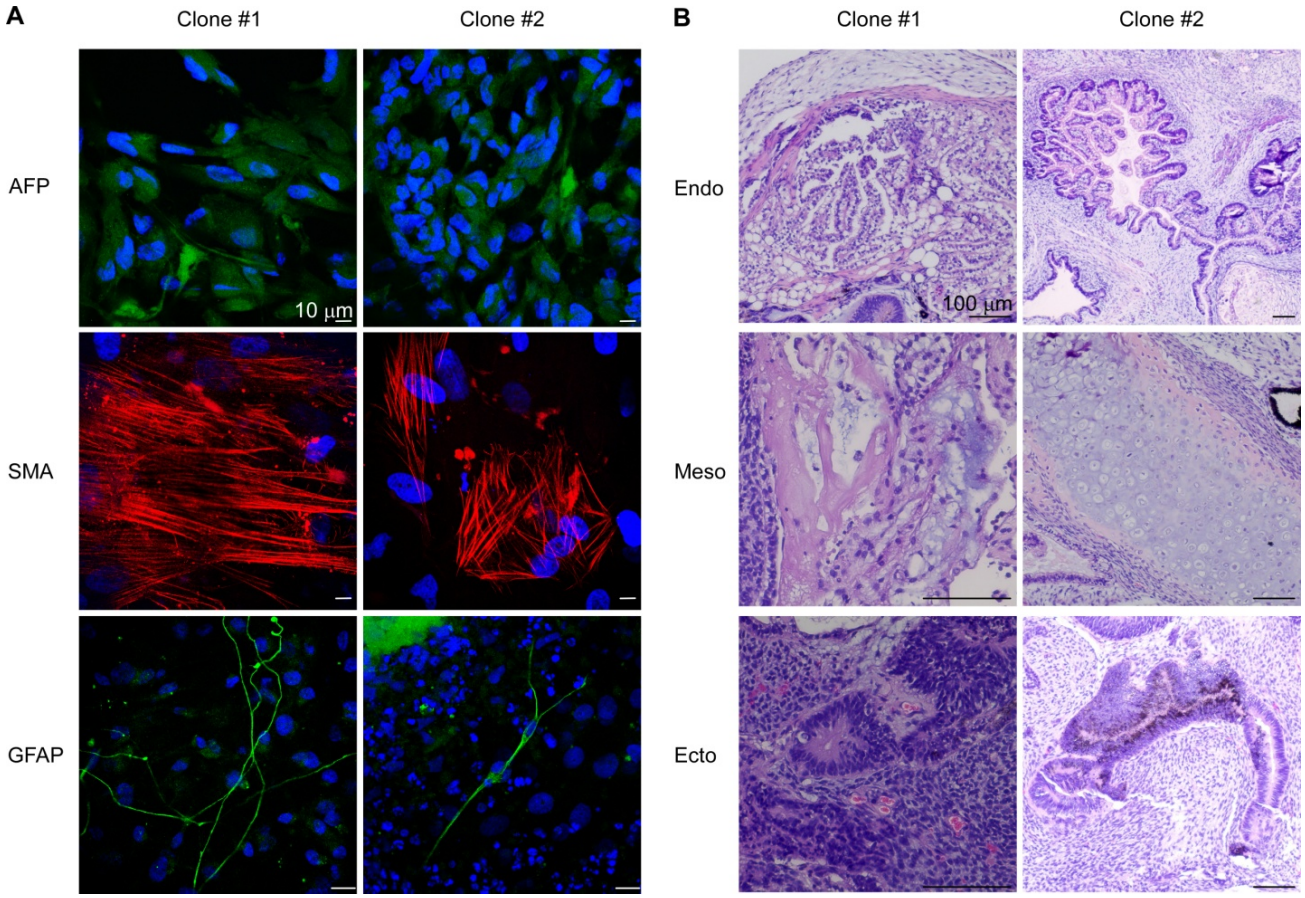

Supplementary Figure 3.2 Ability of iPSCs$_{D130G\text{-}CaM}$ to differentiate into all germ layers. (**A**) Immunostaining of differentiated embryoid bodies for the endoderm-specific α-fetoprotein (AFP, green), the mesoderm-specific smooth muscle actin (SMA, red), and the ectoderm-specific glial fibrillary acid protein (GFAP, green). Cells are counter-stained with DAPI for visualization of the nuclei (blue). (**B**) Five-to-eight-week-old teratomas harvested from mice injected with undifferentiated iPSCs$_{D130G\text{-}CaM}$. Tissue sections were stained with hematoxyline and eosin. All three germ layers, including gut-like structures (Endo: endoderm), immature bone and cartilage (Meso: mesoderm), and immature neural tube and neuroectoderm (Ecto: ectoderm), are identifiable in teratomas generated from both iPSCs$_{D130G\text{-}CaM}$ clones.

3.6.3 Expression of genetically encoded sensors

Expression of the voltage sensor ASAP1 and the calcium sensor GCaMP6f was assesed by flow cytometry 7-10 days aftter transduction (Supplementary Figure 3.3). A large fraction of cells expressed the ASAP sensor, while a smaller fraction expressed the GCaMP6f sensor. The expression of GCaMP6f was kept low so as to reduce the potential effect of the sensor on resting Ca^{2+} concentration.

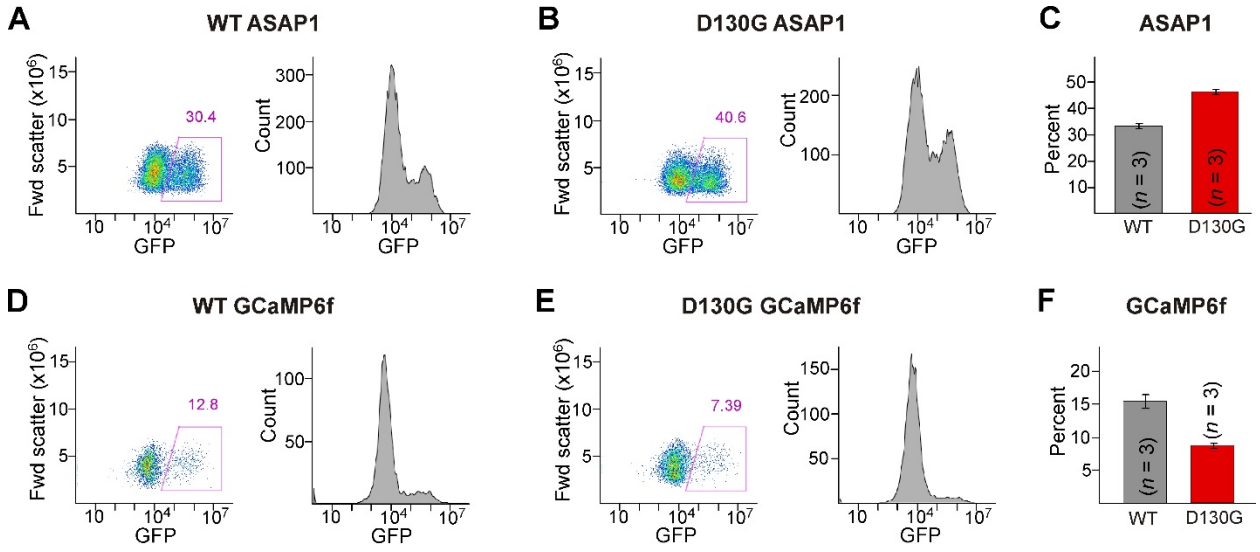

Supplementary Figure 3.3 Quantification of sensor expression. (**A-B**) Exemplar scatter and histogram plots of $iPSC_{WT}$-CMs and $iPSC_{D130G\text{-}CaM}$-CMs expressing ASAP1. (**C**) Population data of ASAP1 expression level gauged by percentage of fluorescent cells in both iPSC-CM clones. (**D-E**) Exemplar scatter and histogram plots of $iPSC_{WT}$-CMs and $iPSC_{D130G\text{-}CaM}$-CMs expressing GCaMP6f. (**F**) Population data of GCaMP6f expression level gauged by % of fluorescent cells in both iPSC-CM clones data indicating the percentage of $IPSC_{WT}$-CMs which express GCaMP6f.

3.6.4 qPCR analysis of iPSC-CM mRNA levels

In this study, we utilized iPSC-CMs with different individual genetic backgrounds for control (WT) and calmodulinopathy cells. In order to ensure that these cells are an appropriate control, we examined the RNA profile of the $iPSC_{WT}$-CMs as compared to the $iPSC_{D130G\text{-}CaM}$-CMs, focusing on those proteins which might contribute to alterations in QT interval or calcium handling (Supplementary Figure 3.4). Very little difference was found between the two iPSC-CM lines, with only a small elevation in KCNQ1 (Supplementary Figure 3.4E) and RYR2 (Supplementary Figure 3.4H) detected. Importantly, this difference cannot account for the LQT phenotype of these cells. In fact, increased levels of KCNQ1 would tend to decrease the QT interval. Moreover, treatment of the $iPSC_{D130G\text{-}CaM}$-CMs did not alter the mRNA level for any protein tested, with the exception of the targeted *CALM2* gene, indicating specificity of the treatment.

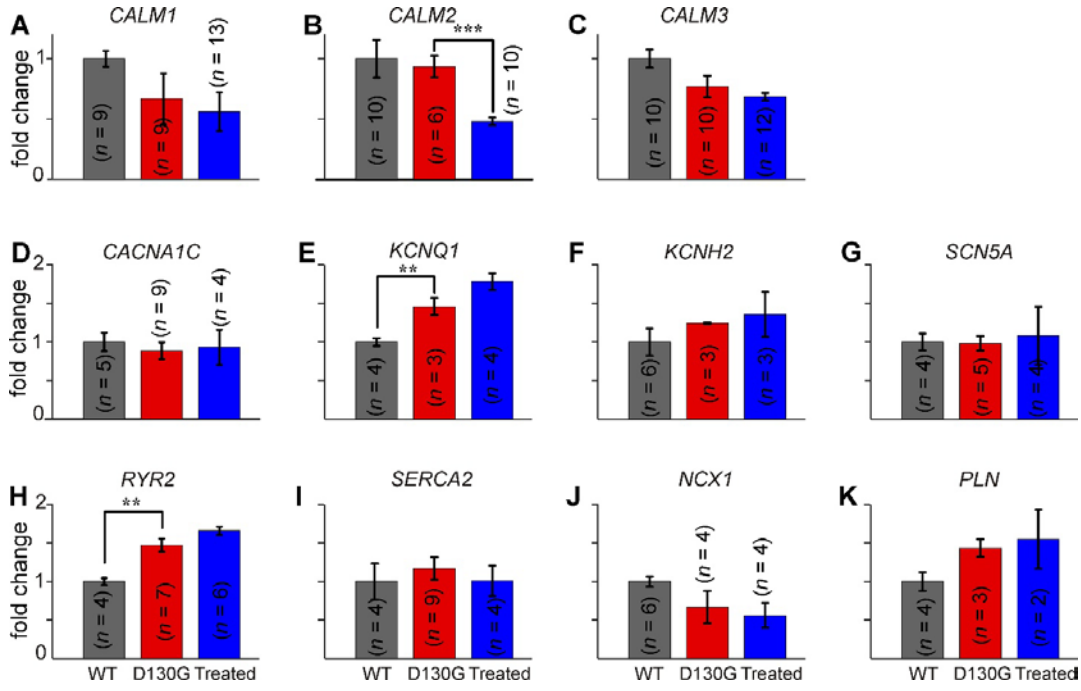

Supplementary Figure 3.4 Analysis of the genetic background of WT, D130G and D130G treated cells. QPCR results indicating mRNA levels of multiple relevant proteins from $IPSC_{WT}$-CMs (gray), $IPSC_{D130G\text{-}CaM}$-CMs (red) and treated $IPSC_{WT}$-CMs (Blue) (** $p < 0.01$, *** $p < 0.001$). Error bars indicate ± SEM. n indicates biological replicates.

3.6.5 Total calmodulin protein levels in iPSC-CMs

The total calmodulin protein levels in $iPSC_{WT}$-CMs and $IPSC_{D130G\text{-}CaM}$-CMs was assessed using western blot analysis (Supplementary Figure 3.5). No difference was seen between these two cell lines; however a small but statistically significant decrease in calmodulin protein was seen following treatment with CRISPRi, consistent with a decrease in *CALM2* expression.

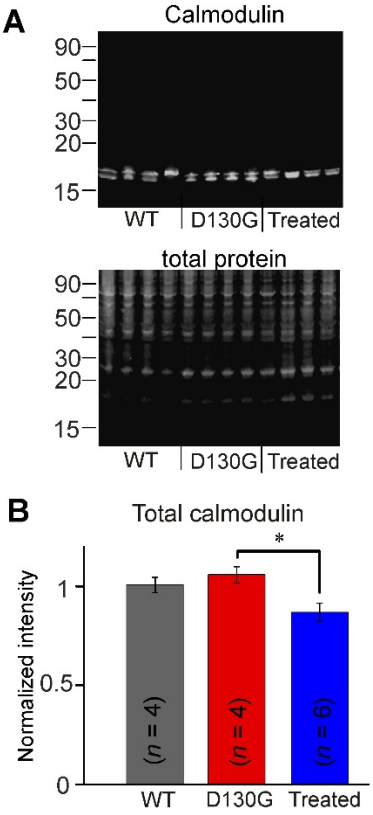

Supplementary Figure 3.5 Assessment of calmodulin protein expression. (**A**) Western blot of $iPSC_{WT}$-CMs, $iPSC_{D130G\text{-}CaM}$-CMs and treated $iPSC_{D130G\text{-}CaM}$-CMs probed with anit-calmodulin. Samples were normalized to total protein as determined with a Coomassie stain (inverted intensity image shown at the bottom). (**B**) Normalized intensity of the calmodulin protein bands. No difference in calmodulin levels were detected between $iPSC_{WT}$-CMs (gray) and $iPSC_{D130G\text{-}CaM}$-CMs (red), however treatment produced a small decrease in calmodulin protein (blue). * $p < 0.05$. Error bars indicate ± SEM.

3.6.6 The AP phenotype is stable at multiple time points

In the main text we demonstrated APD prolongation at multiple cycle lengths in iPSC$_{D130G\text{-}CaM}$-CMs 30 days post-differentiation (Figures 3.1D-L). The equivalent data was obtained 45 and 60 days post-differentiation (Supplementary Figure 3.6) on the same population of monolayers in Figure 3.1**,** demonstrating that the phenotype of the iPSC$_{D130G\text{-}CaM}$-CMs is stable over time. Summary data for a cycle length of 2 seconds is displayed in main text Figures 3.1F, I, L.

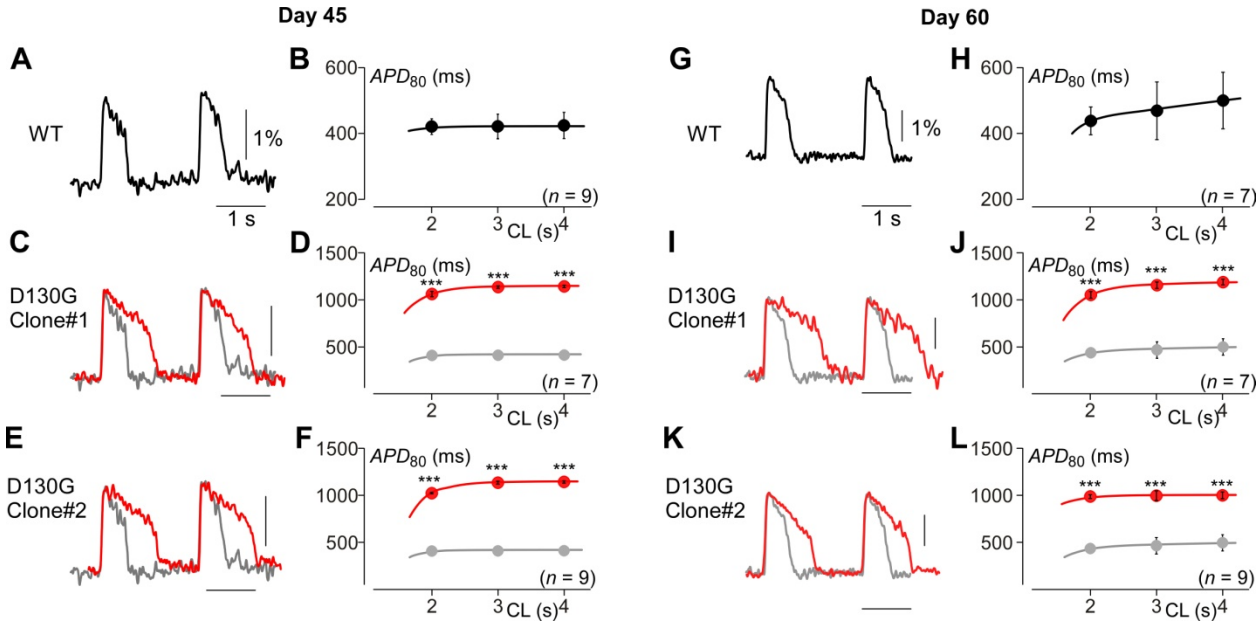

Supplementary Figure 3.6. Stability of iPSC-CM APs across multiple time points. (**A**) Exemplar APs from iPSC$_{WT}$-CMs paced at 0.5 Hz, recorded via fluorescence imaging using ASAP1 45 days post-differentiation. Scale bar indicates percent change in fluorescence. (**B**) Population data for average APDs at various cycle lengths (CL) for 45-day-old iPSC$_{WT}$-CMs (n=9). Each biological replicate (n) is an average value of 2 technical replicates/measurements for all data in this figure. Error bars indicate ± SEM throughout. (**C**) Exemplar APs from 45-day-old iPSC$_{D130G\text{-}CaM}$-CMs (red). WT reproduced in gray. (**D**) Average APD data for iPSC$_{D130G\text{-}CaM}$-CMs (red, n=7) across multiple pacing frequencies. WT reproduced in gray (*** $p < 0.001$ compared to WT and corrected for unequal variance, both populations normally distributed). (**E-F**) Alternate D130G clone demonstrating the same result as **C, D** (n=9, *** $p < 0.001$ compared to WT and corrected for unequal variance, both populations normally distributed). (**G-L**) Equivalent results were observed for iPSC$_{D130G\text{-}CaM}$-CMs 60 days post-differentiation. Format as in **A-F**. (n=7, 7, and 7 for WT, D130G clone#1, and D130G clone#2, respectively; (*** $p < 0.001$ compared to WT and corrected for unequal variance, both populations normally distributed)

3.6.7 Disruption of Ca^{2+} cycling across multiple time points

In the main text we demonstrated significant disruption of Ca^{2+} cycling, with CaT amplitudes several fold larger in $iPSC_{D130G\text{-}CaM}$-CMs as compared to their WT counterparts (Figures 3.2A-F). The data was collected 30 days post-differentiation, however comparable results could also be obtained 45 and 60 days post-differentiation from the same population of monolayers in Figure 3.2 (Supplementary Figure 3.7), indicating a stable phenotype of the D130G harboring monolayers.

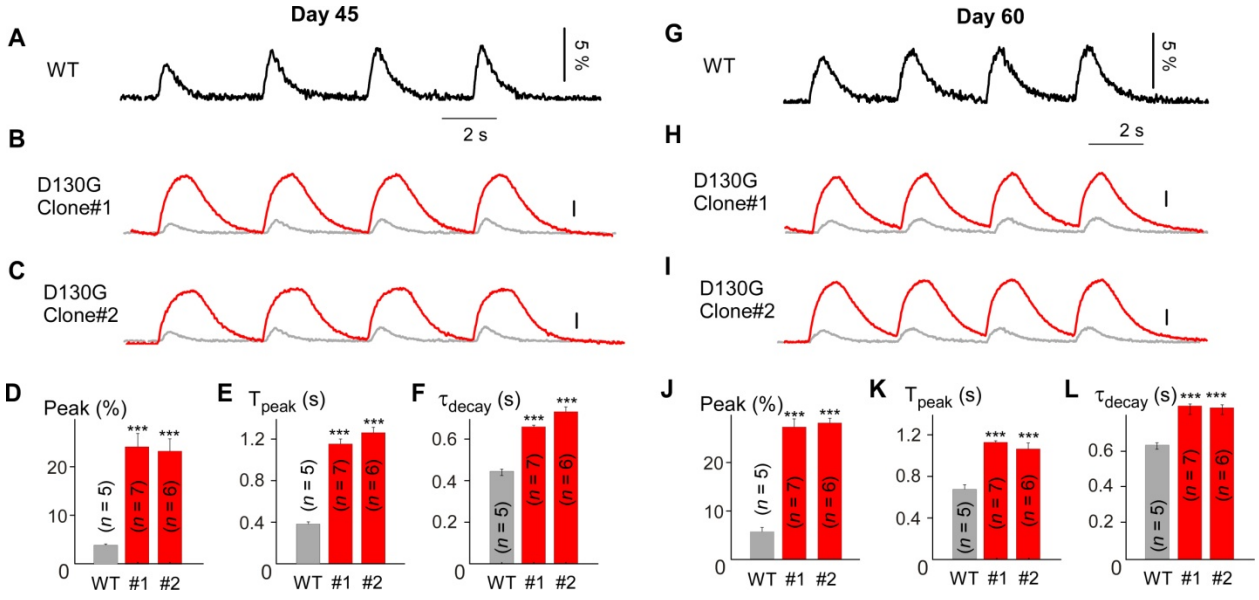

Supplementary Figure 3.7 Stability of iPSC-CM CaTs across multiple time points. (**A**) Exemplar CaTs recorded from 45-day-old $iPSC_{WT}$-CMs (WT) using GCaMP6f. Scale bar indicates percent change in fluorescence. (**B**) Exemplar CaTs recorded from $iPSC_{D130G\text{-}CaM}$-CMs (red) 45 days post-differentiation, as compared to WT (gray). (**C**) Exemplar CaTs from an alternate D130G clone 45 days post-differentiation. (**D-F**) Population data demonstrating larger amplitude and slower kinetics for both $iPSC_{D130G\text{-}CaM}$-CMs clones compared to WT after 45 days in culture (red) (Peak, average peak fluorescence change; Tpeak, average time to peak; τ_{decay}, average decay time constant; n=5, 7, and 6 for WT, D130G clone#1, and D130G clone#2, respectively; *** $p <$ 0.001 compared to WT and corrected for unequal variance, both populations normally distributed). Each biological replicate (n) is an average value of 2 technical replicates/measurements for all data in this figure. (**G-L**) Equivalent results were seen for $iPSC_{D130G\text{-}CaM}$-CMs 60 days post-differentiation. Format as in **A-F**. (n=5, 7, and 6 for WT, D130G clone#1, and D130G clone#2, respectively; *** $p <$ 0.001 compared to WT and corrected for unequal variance, both populations normally distributed)

3.6.8 SR content effects in iPSC$_{D130G\text{-}CaM}$-CMs

Given the large effects of the calmodulinopathy mutation on CaTs, we examined the SR content of these cells via application of 5 mM caffeine. While the SR content did appear somewhat enhanced in the iPSC$_{D130G\text{-}CaM}$-CMs as compared to their WT counterparts (Supplementary Figure 3.8), this increase did not reach a level of statistical significance. This lack of a significant effect may be representative of the relatively immature nature of the iPSC-CMs (Rocchetti et al.; Kane et al., 2015).

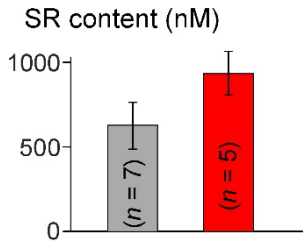

Supplementary Figure 3.8 SR content of iPSC$_{D130G\text{-}CaM}$-CMs. No statistical difference was seen in the SR content of iPSC$_{D130G\text{-}CaM}$-CMs (red) as compared to iPSC$_{WT}$-CMs (gray). SR content was assessed by application of caffeine while imaging the Ca^{2+} sensitive dye indo-1. Error bars indicate SEM across coverslips (biological replicates).

3.6.9 Disruption of Ca^{2+}/CaM-dependent inactivation (CDI) of LTCCs at the older differentiation age

In the main text we demonstrated significant disruption of CDI of LTCCs in $iPSC_{D130G\text{-}CaM}$-CMs as compared to their WT counterparts (Figure 3.3). The data was collected 30 days post-differentiation, however comparable results could also be obtained 60 days post-differentiation (Supplementary Figure 3.9), indicating a stable phenotype of the D130G harboring monolayers.

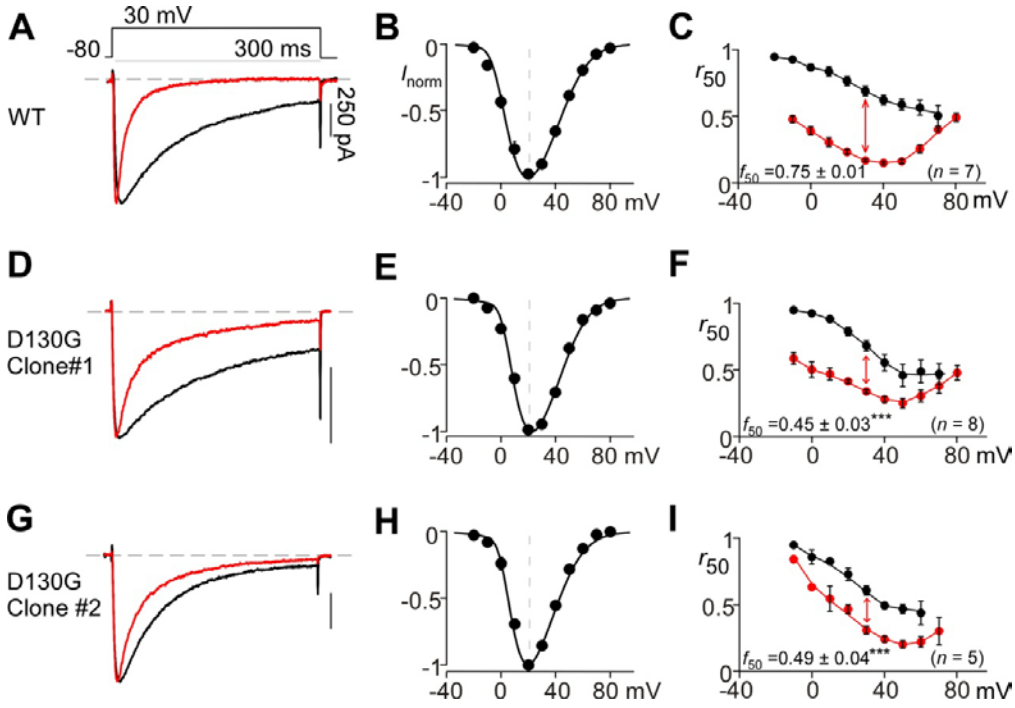

Supplementary Figure 3.9 Stability of iPSC-CM LTCC CDI at later time point in culture (**A**) Exemplar whole-cell current recordings in Ca^{2+} (red) and Ba^{2+} (black) for $iPSC_{WT}$-CMs 60 days post-differentiation. Ba^{2+} current is normalized to Ca^{2+} peak, scale bar corresponds to Ca^{2+}. (**B**) Average normalized current and voltage relationship for $iPSC_{WT}$-CMs (n=7, no technical replicate). Error bars indicate ± SEM throughout. (**C**) Population data for Ca^{2+} (red) and Ba^{2+} (black) for $iPSC_{WT}$-CMs (n=7, no technical replicate), where r_{50} quantifies the extent of current inactivation across voltages. Red arrow depicts extent of CDI (f_{50}) at 30-mV test potential here and throughout. (**D**) Exemplar whole-cell current recordings in Ca^{2+} (red) and Ba^{2+} (black) for $iPSC_{D130G\text{-}CaM}$-CMs 60 days post-differentiation. Ba^{2+} current is normalized to Ca^{2+} peak, scale bar corresponds to Ca^{2+}. (**E**) There is no significant shift in the current voltage relationship for $iPSC_{D130G\text{-}CaM}$-CMs ($p>0.05$) as compared to WT (**B**). (**F**) Population data demonstrates a significant decrease in CDI for the $iPSC_{D130G\text{-}CaM}$-CMs (n=8, *** $p < 0.001$ compared to WT, corrected for unequal variance). (**G-I**) Alternate D130G clone at 60 days post-differentiation demonstrating the same result as **D-F** (n=5, *** $p < 0.001$ compared to WT, corrected for unequal variance).

3.6.10 A pharmacological study of LQT effects in iPSC-CMs

Of the various forms of LQT, only three correspond to disruptions in membrane channels known to associate with calmodulin: LQT1 (loss of function mutations in KCNQ1), LQT3 (gain-of-function mutations in SCN5A), and LQT8 (gain-of-function mutations in CACNA1C). We therefore utilized a pharmacological approach to demonstrate that each of these LQT phenotypes could be recapitulated within our $iPSC_{WT}$-CMs. Application of the LTCC antagonist BayK 8644 more than doubled the APD_{80} of $iPSC_{WT}$-CMs (Supplementary Figure 3.10A). Such a profound effect on APD is matched in the clinical setting only by LQT8 (Timothy Syndrome) and LQT15 (calmodulinopathies) (Supplementary Figure 3.10C), supporting the supposition that the LQT seen in calmodulinopathy patients is due, in large part, to disruption of LTCC channels. Application of maximal doses of the I_{KS} blocker, chromanol 293B, or the $Na_V1.5$ channel agonist, ATX II, produced moderate APD prolongation (Supplementary Figures 3.10A,B), corresponding to the clinical phenotype of LQT1 and 3 patients (Supplementary Figures 3.10C).

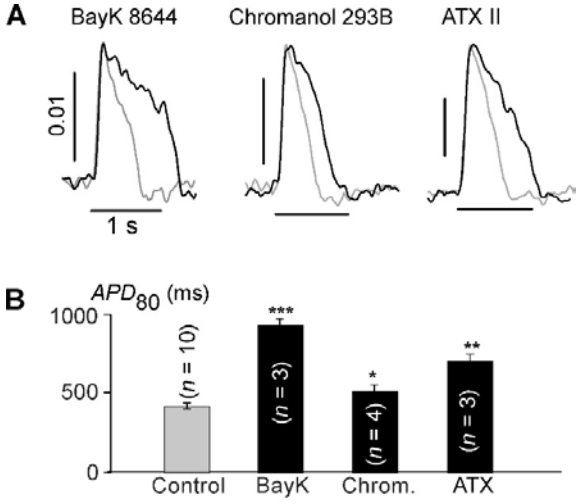

C

Type	Gene	QTc
LQT1	KCNQ1	400-600
LQT3	SCN5A	400-600
LQT8	CACNA1C	480-730
LQT15	CALM2	550-740

Supplementary Figure 3.10 Pharmacological study of APD prolongation in $iPSC_{WT}$-CMs. (**A**) Exemplar AP recordings of $iPSC_{WT}$-CMs (gray) in the presence of 10 µmol/L BayK 8644 (left, black), 10µmol/L chromanol 293B (middle, black) or 0.5 µmol/L ATX II (right, black). (**B**) Average APD_{80} values measured for each drug. Error bars indicate ± SEM throughout. (**C**) Comparison of reported QT intervals corresponding to LQT syndromes associated with channels known to interact with CaM.

3.6.11 A modeling study of calmodulinopathy CDI deficits

We have demonstrated a reduction in LTCC CDI underlying the LQTS phenotype of $iPSC_{D130G\text{-}CaM}$-CMs (Figure 3.3). However, it is not possible to rule out the contribution of other CaM targets to the overall phenotype. We therefore considered whether a CDI specific effect of CaM_{D130G} on the LTCC would be sufficient to produce a calmodulinopathy phenotype. To this end, we utilized a validated and publically available model of an adult mammalian ventricular myocyte (the Luo-Rudy model: LRd) (Luo and Rudy, 1994a, b; Livshitz and Rudy, 2007; Dick et al., 2016). With this *in silico* method, we were able to selectively adjust the CDI of the LTCC channel to match the CDI data obtained for this mutation (Figure 3.3) (Limpitikul et al., 2014). In addition, this model provides insight into calmodulinopathy associated arrhythmias in an adult myocyte featuring intact EC coupling (Livshitz and Rudy, 2007; Kane et al., 2015). In consideration of the variable expression of mutant CaM expected among calmodulinopathy patients, the model was run with variable fractions of LTCC channels harboring CaM_{D130G}. The result was APD prolongation which was dependent on expression levels of CaM_{D130G} in a non-linear manner (Supplementary Figure 3.11). At low levels of CaM_{D130G} expression, the APD increased monotonically, however a threshold for severe electrical instability was reached near a ratio of one in six LTCCs harboring a CaM_{D130G} versus CaM_{WT}. Importantly, this corresponds to the expected expression levels of mutant CaM among calmodulinopathy patients, where the cardiac expression of a single *CALM* allele was determined to be 0.17 ± 0.02 (*CALM1*), 0.12 ± 0.01 (*CALM2*), and 0.21 ± 0.03 (*CALM3*) based on the average expression levels from five different RNAseq databases (Petryszak et al., 2014). Thus calmodulinopathy patients appear to lie directly in the vicinity of the threshold for APD instability, making them highly susceptible to cardiac arrhythmia.

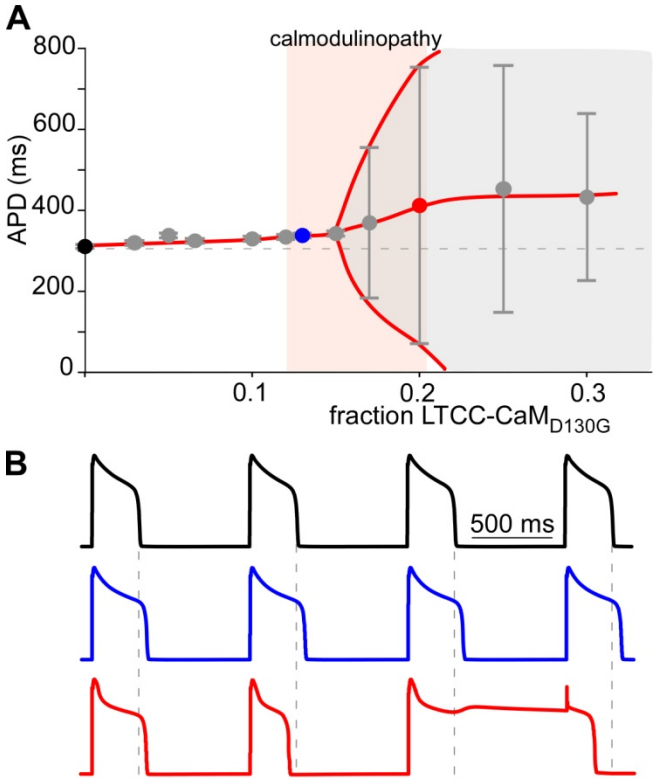

Supplementary Figure 3.11 Modeling of a non-linear dose dependence of APDs on mutant CaM expression. (**A**) Average APDs determined from an adult mammalian ventricular myocyte model (Luo and Rudy, 1994a, b; Livshitz and Rudy, 2007; Dick et al., 2016), plotted as a function of the fraction of LTCCs harboring CaM_{D130G} (relative to the total number of LTCCs). Data is plotted ±SEM. The gray area indicates electrical instability in the modeled action potentials. The rose shading depicts the range of physiologically relevant expression levels for mutant CaM based on RNAseq databases for normal human gene expression levels (Petryszak et al., 2014). (**B**) Exemplar action potentials simulated at 1-Hz pacing corresponding to the colored points in **A**. Black: no CaM_{D130G}; Blue: 0.12 CaM_{D130G}; Red: 0.2 CaM_{D130G}.

3.6.12 GRNA screening

Over twenty different gRNAs targeted to *CALM1*, *CALM2* and *CALM3* were screened (Supplementary Figure 3.12). Design 21 (Kg116) was chosen for treatment of the *CALM2* iPSC$_{D130G-CaM}$-CMs (Figure 3.4) as this design demonstrated significant efficacy against *CALM2*, and no appreciable effect against *CALM1* or *CALM3*. Similarly, design 2 was used for selective efficacy against *CALM1* (Figure 5B), and design 8 was utilized for *CALM3* (Figure 3.5C).

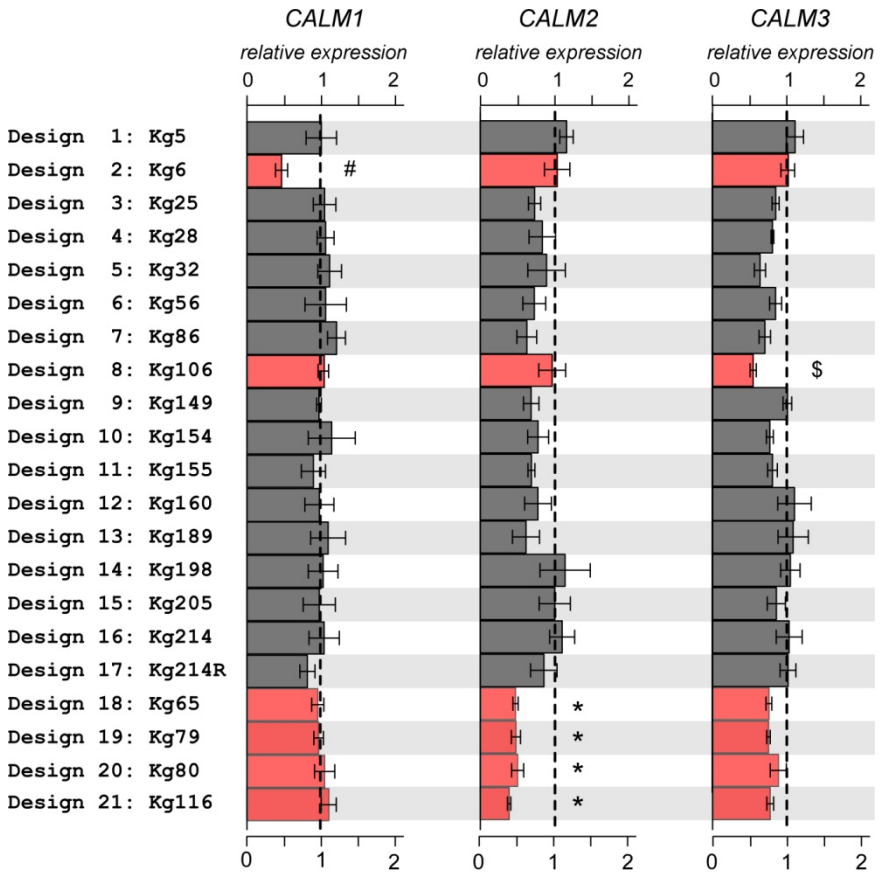

Supplementary Figure 3.12 GRNA screening. QPCR results indicating mRNA levels of *CALM1-3* in HEK293 cells after CRISPRi treatment using various candidate gRNA sequences. The dashed line at 1 indicates control cells treated with scrambled gRNA. Designs 18-21 (rose) caused a significant decrease in *CALM2* mRNA (n=3, * $p <$ 0.05 compared to control) without altering *CALM1* or *CALM3*, while design 2 selectively decreased *CALM1* (n=4, # $p < 0.05$ compared to control) and design 8 selectively decreased *CALM3* (n=6, $ $p < 0.05$ compared to control). Each biological replicate (n) is an average value of 3 technical replicates/measurements for all data in this figure.

Supplementary Table 3.1 Reported action potential duration in other control iPSC-CM lines.

APD_{90} (ms)	Reference
477	Du *et al*., 2015(Du et al., 2015)
548	Spencer *et al*., 2014(Spencer et al., 2014)
425	Scheel *et al*., 2014(Scheel et al., 2014)
340	Sinnecker *et al*., 2013(Sinnecker et al., 2013)
340	Lee *et al*., 2012(Lee et al., 2012)
286	Lopez-Izquierdo *et al*., 2014(Lopez-Izquierdo et al., 2014)
414	Ma *et al*., 2011(Ma et al., 2011)
392	This study

Supplementary Table 3.2 Sequence of candidate gRNAs.

gRNA design	Sequence
Target *CALM1*:	
Kg5	GGCCGTTACTCGTAGTCAGG
Kg6	GGCCGCCTGACTACGAGTAA
Kg160	GCTACCATGGTGCGAGCGAA
Target *CALM2*:	
Kg25	GACGTACCTTATCAAACACA
Kg28	GCCATCATTGTCAGAAATTC
Kg56	GGAGCTTCACTCTCTTGCCC
Kg65	GGACAATGACAGTAAGATAA
Kg79	GATCGCTGAGCTGCCGGCGC
Kg80	GTCGCTGAGCTGCCGGCGCT
Kg86	GTTGGAGTTTATCTAGTGAA
Kg116	GCTACTTTCCCTTTCTAGTA
Kg149	GCGCCTCCCTTACACCTTCA
Kg154	GCCCTTACACCTTCAAGGAG
Kg155	GACCACTCCTTGAAGGTGTA
Kg189	GGATGGCGCGAAAGAGGCCA
Kg198	GTTTCTACCCGCGTTGTCGG
Kg205	GCAACCGTCGCCGGCATCCC
Kg214	GCCGGCGACGGTTGTGTCGC
Kg214R	GCCTGCGACACAACCGTCGC
Target *CALM3*:	
Kg32	GGTCCGGAGCACGGGGATCA
Kg106	GCTCTGAGGCGGGCTTAACG
Kg198	GTTTCTACCCGCGTTGTCGG

3.6.13 Supplementary Methods

Flow cytometry

100 uL of 10^{11} PFU/ml of lentivirus containing either ASAP1 or GCaMP6f gene was added to a single well of a 24 well plate, with iPSC-CMs seeded at a density of 2.5 $x10^5$ cells/well. Flow cytometery was done 7-10 days after the addition of virus using an Accuri C6 flow cytometer (BD Biosciences).

Sequencing of CALM2 genomic DNA

Genomic DNA was isolated from iPSCs using DNeasy Blood & Tissue Kit (Qiagen) following manufacturer's protocol. A portion of CALM2 200 base pairs up and downstream from c.389 A>G mutation was cloned using standard PCR (forward primer: 5'-AGGTGTCACTTGACTTTGGGA-3'; reverse primer: 5'-ATTTCAGGGGAAGGGTCACT-3') Standard Sanger sequencing was performed on the PCR product using the aforementioned forward primer.

Immunohistochemistry

Standard fluorescent immunohistochemistry was performed on non-differentiated iPSCs and embryoid bodies. Briefly, cells were fixed with 4% paraformaldehyde, permeabilized with 0.1% Triton X, and stained with primary, secondary antibodies, and finally counter-stained with DAPI for nuclear visualization. Primary antibodies included (manufacturer, catalog number): polyclonal rabbit anti-Oct4 IgG (AbCaM, ab19857), polyclonal rabbit anti-nanog IgG (AbCaM, ab80892), monoclonal mouse anti-SSEA4 IgG (AbCaM, ab16287), polyclonal rabbit anti-glial fibrillary acidic protein Ig (Dako, Z0334), rabbit polyclonal anti-smooth muscle action IgG

(AbCaM, ab5694), and mouse monoclonal anti-α-fetoprotein IgG1 (R&D Systems, MAB1368). Secondary antibodies (all purchased from Invitrogen) include (catalog number): 594 goat anti-mouse IgG (A-11020), 594 donkey anti-rabbit IgG (A-21207), 488 goat anti-mouse IgG (A-31620), and 488 donkey anti-rabbit IgG (A-21206).

Embryoid body formation analysis

Embryoid bodies (EBs) were formed using a previously described method (Limphong et al., 2013). Briefly, iPSCs were enzymatically dissociated using Accutase (Sigma Aldrich) and transferred into low-attachment tissue culture plates filled with EB medium to allow clusters of cells grown in suspension. After 8 days, EBs were transferred into gelatin-coated treated tissue culture plates. EBs were then collected for analysis after 25 days in culture. EB medium included 20% FBS in knockout DMEM (ThermoFisher Scientific, 10829018) supplemented with 1% L-glutamine, 1% non-essential amino acids, 1% penicillin-streptomycin, and 0.1 mmol/L β-mercapto ethanol.

Teratoma formation

Teratoma formation analysis was performed as previously described (Ye et al., 2014). Briefly, $5x10^6$ of undifferentiated iPSCs were mixed with Matrigel (BD Biosicences) at a 1:1 ratio and injected intramuscularly into NOD/SCID IL2 receptor gamma chain knockout (NSG) mice. Teratomas were harvested 5-8 weeks post injection, paraffin-embedded, sectioned, and stained with hematoxylin and eosin.

Western blot for CaM protein quantification

IPSC-CMs were collected 8-9 post transduction. Cells were lyzed in a Tris-HCl based buffer and a western blot of the collected protein was as previously described (O'Rourke et al., 1999). All samples were run in duplicate on 12.5% Tris-HCl precast gels (Bio-Rad) in 25 mmol/L Tris, 192 mmol/L glycine, and 0.1% (wt/vol) SDS running buffer. Primary antibody incubations were performed overnight at 4°C using rabbit monoclonal anti-calmodulin antibody (Abcam, Cat. No. ab45689). Relative band densities were quantified using ImageJ software. The intensity of the bands is normalized by total amount of protein obtained from a Coomassie stain.

SR content measurement

SR content was measured using the ratiometric calcium dye Indo-1 AM. Cells were loaded with 1μmol/L dye for 30 minutes at 37 °C, and rinsed 3 times, followed by additional 10 minutes incubation in Tyrodes at 37 °C to allow for de-esterification of Indo-1 AM. Cells were stimulated for several minutes by application of an electric field across the coverslip using a C-Pace electrical stimulator (Ion Optix). The bath solution was then exchanged for a Na^+-free Tyrode's solution (Na^+ was replaced with choline ion to minimize the action of Na-Ca exchanger) with 1.8 mmol/L Ca^{2+}, and 10 mmol/L 2,3-butanedione monoxime. After baseline imaging, SR content was determined by the addition of 5 mmol/L caffeine. Fluorescence was measured using 340-nm excitation and 405- to 485-nm emission wavelengths. The intracellular Ca^{2+} concentration ($[Ca^{2+}]$) was calculated as $[Ca^{2+}] = K_{d/Indo} \cdot \beta \cdot (R - R_{\min})/(R_{\max} - R)$, where R is the ratio of fluorescence signal at 405 and 485 nm. $K_{d/Indo}$ was 800 nmol/L (Limpitikul et al., 2014). $R_{\min}$ was determined to be 0.33 in a ~ 0 mmol/L Ca^{2+} Tyrode's after 30 min incubation with BAPTA-AM. $R_{\max}$ was determined to be 20.85 in a Na^+-free Tyrode's (Na^+ was replaced

with choline ion to minimize the action of Na-Ca exchanger) with 10 mmol/L Ca^{2+}, 25 μmol/L digitonin and 10 mmol/L 2,3-butanedione monoxime. β, as defined by the ratio of fluorescence signal at 485 nM under Ca^{2+}-free and Ca^{2+}-bound conditions, was determined to be 0.85.

Ventricular myocyte model (LRd model)

The original LRd model(Livshitz and Rudy, 2007) was adjusted as previously described such that the duration and shape of the action potential was more similar to human(Dick et al., 2016). Additional adjustments were made to the LTCC module, primarily substituting a CDI specific deficit expected for calmodulinopathy into a variable fraction of LTCC channels. Equations governing the final LTCC channel pools are as follows:

For the CDI gate (f_{CDI}):

$$k_{on} = 4 \cdot 10^3 \quad \text{mM}^{-2}\text{ms}^{-1} \tag{3.1}$$

$$k_{off} = 1 \cdot (K_{CDI})^2 \cdot k_{on} \quad \text{ms}^{-1} \tag{3.2}$$

$$df_{CDI} = k_{on} \cdot [Ca]^2 \cdot f_{CDI} + k_{off} \cdot (1 - f_{CDI}) \tag{3.3}$$

$$K_{CDI} = 6.325\text{e}^{-4} \quad \text{mM} \tag{3.4}$$

The activation gate (d), followed standard Hodgkin and Huxley equations (Hodgkin and Huxley, 1952):

$$dd = \frac{d_{steadystate} - d}{\tau_d} \tag{3.5}$$

$$d^1_{steadystate} = \frac{1}{1 + e^{-(V+14)/(25/2)}} \tag{3.6}$$

$$d^2_{steadystate} = \frac{1}{1 + e^{-(V+14-15)/(25/1.5)}} \tag{3.7}$$

$$d_{steadystate} = d^{1}_{steadystate} \cdot d^{2}_{steadystate} \tag{3.8}$$

$$\tau_{d} = 0.59 + \frac{5}{1+e^{-3\cdot 0.052(V+20)+15}} \cdot \frac{1}{1+e^{2\cdot 0.052(V+20)-75}} \tag{3.9}$$

The voltage dependent inactivation gate (*f*):

$$df = \frac{f_{steadystate} - f}{\tau_{f}} \tag{3.10}$$

$$f_{steadystate} = 1 - 0.4 \cdot (1 - \frac{1}{1+e^{(V+32)/8}} \cdot \frac{0.8}{1+e^{(50-V)/20}}) \tag{3.11}$$

$$\tau_{f} = \frac{30}{0.0197 \cdot e^{-0.0337(V+10)^{2}+.02}} \tag{3.12}$$

With the gates set, the total current through the L-type channel, as well as the Na^{+}/Ca^{2+} exchange current and Ca^{2+} activated potassium channel was defined as:

$$i_{Ca,Ltype} = d \cdot f \cdot (f_{CDI} + P_{O}^{modeCa}(1 - f_{CDI})) \cdot i_{Ca} \tag{3.13}$$

$$i_{Na/Ca} = d \cdot f \cdot (f_{CDI} + P_{O}^{modeCa}(1 - f_{CDI})) \cdot i_{Na} \tag{3.14}$$

$$i_{K_{Ca}} = d \cdot f \cdot (f_{CDI} + P_{O}^{modeCa}(1 - f_{CDI})) \cdot i_{K} \tag{3.15}$$

$$P_{O}^{modeCa} = 0.1 \tag{3.16}$$

Where P_{O}^{modeCa} represents the relative open probability of the L-type channel in mode Ca^{2+} as compared to mode 1. i_{Ca}, i_{Na} and i_{K} represent the single channel open level as set by the GHK equation.

With the wild type channel in place, a second pool of LTCC channels was added to simulate the effect of CaM_{D130G} on the channel. Properties of this pool of channels were made based on this study and on the previous biophysical characterization of these channels

(Limpitikul et al., 2014). This pool of channels was modeled as above, except for the following alterations:

$$k_{on} = 1000 * 4 \cdot 10^3 \ \ \mathrm{mM^{-2}ms^{-1}} \tag{3.17}$$

$$k_{off} = 10^{-3} \cdot (K_{CDI})^2 \cdot k_{on} \quad \mathrm{ms^{-1}} \tag{3.18}$$

$$df_{CDI} = k_{on} \cdot [Ca]^2 \cdot f_{CDI} + k_{off} \cdot (1 - f_{CDI}) \tag{3.19}$$

$$P_O^{D130G,modeCa} = 0.95 \tag{3.20}$$

All other equations in the model not mentioned here were identical to those described(Dick et al., 2016) and are entirely based on the original 2007 LRd model (Livshitz and Rudy, 2007).

CHAPTER 4

Bi-lobal kinetic model of $Ca_V1.2$ calcium-dependent inactivation

4.1 Introduction

As described in previous chapters, $Ca_V1.2$ channel plays a major role in both shaping the action potential and triggering myocyte contraction (Bodi et al., 2005). Disruption of the normal function of this channel has been linked to multiple disorders, including severe forms of LQTS (Crotti et al., 2013; Limpitikul et al., 2014; Yin et al., 2014; Dick et al., 2016; Limpitikul et al., 2017). To properly perform these critical roles, $Ca_V1.2$ channels employ CDI as a major form of feedback regulation (Sun et al., 1997; Morotti et al., 2012). Thus accurate knowledge of the quantitative details of CDI progression is of critical importance to understanding normal cardiac physiology.

Thus far, we have discussed that the mediator of CDI in $Ca_V1.2$ is CaM which is known to preassociate with the carboxy-tail of the channel in its Ca^{2+}-free form (apoCaM) (Erickson et al., 2001; Pitt et al., 2001; Mori et al., 2004) and has an ability to module the open probability of the channel (Adams et al., 2014). This resident CaM also has the remarkable ability to respond differentially to Ca^{2+} originating from distinct spatial sources. Specifically, the C-lobe of CaM senses the fluctuation of local Ca^{2+} concentration at the mouth of the channel, while the N-lobe detects the global cytosolic Ca^{2+} level (Dick et al., 2008; Tadross et al., 2008). However, the extent of cooperativity between the two lobes in this bi-lobal scheme remains to be determined. This bi-lobal scheme plays an important role in human (patho)physiology, allowing channels to respond appropriately to both local and distant signals. In particular, mutations disrupting Ca^{2+} binding within the C-lobe of CaM were shown to cause a malignant form of LQTS via disruption

of $Ca_V1.2$ CDI (Crotti et al., 2013; Limpitikul et al., 2014; Yin et al., 2014; Limpitikul et al., 2017). Thus full understanding of both normal and pathologic states requires consideration of the bi-lobal regulation of CaM on $Ca_V1.2$.

Given the importance of CDI to physiological function, numerous *in-silico* models have been utilized to gain a more in-depth understanding of how CDI plays a role in the context of the cardiac action potential. To date, several methods have been deployed to model the CDI of cardiac $Ca_V1.2$ channels. One method involves treating both VDI and CDI like canonical Hodgkin and Huxley gates, dependent on voltage or Ca^{2+} concentration, respectively. That is, total Ca^{2+} current is a product of conductance, VDI 'gate,' CDI 'gate,' and a driving force based on Goldmann-Hodgkin-Katz equation (Hund and Rudy, 2004; ten Tusscher et al., 2004; ten Tusscher and Panfilov, 2006). Building on this, a second method includes Markovian models containing closed, open, and inactivated states of $Ca_V1.2$. Here, rate constants for the transition into a fraction of the inactivated states depend on voltage (representing VDI) while transitions into remaining inactivated states depend on Ca^{2+} concentration (representing CDI). However, these aforementioned models fail to consider the true allosteric mechanism of CDI, where Ca^{2+}-inactivated channels maintain the ability to open, but with a reduced (yet non-zero) P_o (Faber et al., 2007; Mahajan et al., 2008b). A few models have partially addressed this issue. However, in these models, the majority of inactivation is carried out by VDI (Jafri et al., 1998; Greenstein and Winslow, 2002; Decker et al., 2009), in contrast to the known dominance of CDI over VDI in $Ca_V1.2$ channels in a physiological setting (Sun et al., 1997; Morotti et al., 2012). Although these approximations of $Ca_V1.2$ inactivation can indeed produce Ca^{2+} current ($I_{Ca(L)}$) with kinetics that grossly resembles experimental $I_{Ca(L)}$ recorded during action potentials *in vitro*, they do not take into account the true allosteric and bi-lobal nature of CaM regulation of $Ca_V1.2$, thus limiting

their utility in describing $Ca_V1.2$ gating in response to variable spatial Ca^{2+} signals (Sun et al., 1997; Dick et al., 2008; Tadross et al., 2008). Attempting to capture this distinct CDI kinetics, some have included the addition of two time constants for CDI (Hund and Rudy, 2004; O'Hara et al., 2011). Yet the true bi-lobal response of $Ca_V1.2$ remains unexplored.

One obstacle to development of accurate CDI models is the quality of experimental data. As the $Ca_V1.2$ channel fluxes the very Ca^{2+} ions that modulate its own opening, it is challenging to accurately control and measure the amount of Ca^{2+} that the preassociated CaM actually senses. Moreover, during the action potential, there is at least ~ 10 fold difference in Ca^{2+} concentration in the dyadic space facing the mouth of the channel and the rest of the cytoplasm (Neher, 1998). Most experimental values of Ca^{2+} used to drive and/or validate the CDI models are measured by cytosolic Ca^{2+}-sensitive fluorescence dyes, of which the readout represents average of bulk/global and subspace/local Ca^{2+} concentrations. This readout thus does not accurately represent the concentration resident CaM actually sees. Here, we take advantage of a method called photo-uncaging (Lipp et al., 1996) to deliver a controlled amount of Ca^{2+} to the channels while simultaneously monitor the cytosolic concentration of Ca^{2+}.

Using this technique, we measured CDI for each lobe of CaM individually and resolved the kinetic response to known levels of Ca^{2+}. This new, high resolution data enabled the creation of a four state model for independent N- or C-lobe mediated CDI. Our models successfully recapitulate both the kinetic and steady-state properties of CDI for each lobe. Next, we considered the integrated effect of bi-lobal CaM on $Ca_V1.2$ CDI. Using experimental CDI measurements for wild-type CaM (CaM_{WT}), we constructed a sixteen-state model of bi-lobal CaM regulation. Not only can this full model effectively capture both the kinetics and steady-state behavior of CDI under physiological conditions, but it

also recapitulates the behavior of calmodulinopathic CaM. Thus, this novel CDI model could prove to be an invaluable asset in understanding of both physiological and pathological states of $Ca_V1.2$ regulation.

4.2 Materials and methods

4.2.1 Molecular Biology

The $Ca_V1.2$ channel used in this study was comprised of the human α_{1C} cardiac isoform corresponding to Acc# Z34810 within the pcDNA3 vector. The original channel backbone was a kind gift from Tuck Wah Soong (Tang et al., 2004) and was modified as previously described (Dick et al., 2016) to conform to the desired cardiac isoform. The point mutation E736A (in the S6 helix of domain II) (Ellinor et al., 1995) was introduced using standard overlap extension PCR, resulting in a Ca channel with increased selectivity for Li^+ ($Ca_V1.2^{E2A}$).

Engineered rat brain CaM_{12}, CaM_{34}, and CaM_{1234}, in which the aspartate-to-alanine mutations were introduced in the EF hands of N-lobe, C-lobe, and both lobes respectively, were kind gifts from John P. Adelman (Vollum Institute, Portland, OR). The LQTS CaM_{D130G} mutation was generated using QuikChange™ site-directed mutagenesis (Agilent) on rat brain CaM (M17069) in the pcDNA3 vector (Invitrogen). Both wild-type and engineered CaMs were cloned into the pIRES2-ECFP vector, modified from pIRES2-EGFP (Clontech Laboratories, Inc.), using *NheI* and *BglII*, thus allowing visualization of positively transfected cells.

4.2.2 Transfection of HEK293 cells

HEK293 cells were cultured on glass coverslips in 10-cm dishes. α_{1C} along with its auxiliary subunits β_{2a} (M80545) and $\alpha_2\delta$ (NM012919.2) were transiently transfected along with

either WT or mutant CaM using a standard calcium phosphate method (Peterson et al., 1999). 8 μg of each plasmid was used, along with 2 μg of simian virus 40 T antigen cDNA in order to ensure robust expression.

4.2.3 Whole Cell Electrophysiology

Whole-cell voltage-clamp recordings of HEK293 cells were performed at room temperature 1-2 days after transfection. Recordings were obtained using an Axopatch 200B amplifier (Axon Instruments). Whole-cell voltage-clamp records were digitally sampled at 10 kHz and low pass filtered at 5 kHz. P/8 leak subtraction was used, with series resistances of 1-2 MΩ. For Ca^{2+}-uncaging experiments, internal solutions contained (in mM): 135 CsCl, 40 HEPES (pH 7.4), 1-2 Citrate, either 5 μM Fluo-2 (TefLabs) + 5 μM Fluo-2 Low Affinity (TefLabs) or 10 μM Fluo-4FF (Invitrogen), 2.5 μM Alexa568 (Invitrogen), 2 DMNP-EDTA (Invitrogen) and 0.25-1 $CaCl_2$. In order to ensure proper quantification of Ca^{2+} at various levels, we selected ca dyes with variable Ca^{2+} affinities as required for the range of Ca^{2+} measured. For all Ca^{2+} steps below 10 μM, we utilized an internal solution containing the mixture (see above) of Fluo-2 Low Affinity (K_d = 6.7 μM) and Fluo-2 high Affinity (K_d = 230 nM). This allowed clear resolution of low basal Ca^{2+} (pre-flash) as well as the ability to distinguish even small or moderate Ca^{2+} steps (post-flash) (Lee et al., 2015). This enhanced range of Ca^{2+} measurements permitted precise measurement of the time varying Ca^{2+} concentration following the flash, allowing our model to account for the kinetic changes in both Ca^{2+} and CDI. In order to obtain accurate measurements of Ca^{2+} steps in the range above10 uM, Fluo-4FF (K_d = 9.7 μM) was used (Dick et al., 2016). To decrease the variability across experiments, each dye mixture was pre-mixed in a large stock and used throughout the study. Calibration of premixed stocks of Fluo-2/Alexa was performed by Lee *et al* (Lee et al., 2015) and Fluo-4FF/Alexa by Dick *et al*

(Dick et al., 2016). Experiments were performed in external solutions containing (in mM): 80 TEA-MeSO3, 10 HEPES (pH 7.4), 80 LiCl, and 2 EGTA at 300 mOsm adjusted with glucose.

During current recordings, Ca^{2+} concentration was measured by exciting the dyes with a 514-nm Argon laser, via a 545DCLP dichroic mirror and either a 545/40BP (Fluo) or 580LP (Alexa568) filter. Fluorescence intensity was measured via photomultiplier tubes. Brief UV pulses used to produce Ca^{2+} steps were generated by a Cairn UV flash photolysis system. The amount of Ca^{2+} delivered to channel was controlled by adding different ratios of $CaCl_2$ to DMN in the pipette solution and varying the UV intensities achieved by adjusting the voltage (50-200V) and total capacitance (500-4000 μF) of the flash photolysis system.

4.2.4 Computational Simulations

For all models of CDI, a set of ODEs was used to represent probability of being in each state (Figures 4.3A, 4.4A, and 4.5A) with the sum of all probabilities equal to 1. All simulations were performed using Matlab (MathWorks). ODEs were solved using `ode23t`. Ca^{2+} input, $[Ca^{2+}](t)$, was idealized from experimental data before feeding into the model. Model optimization was performed by using `patternsearch` to minimize the error between experimental and simulated current.

4.3 Results

4.3.1 Experimental quantification of CDI as a function of Ca^{2+}

In order to create a detailed kinetic model of CDI, we first need to address the paucity of high resolution experimental data at known Ca^{2+} concentrations. To do this, we must overcome the experimental challenge of coupled $Ca_V1.2$ gating and Ca^{2+} entry. We thus utilize Li^+ as the

charge carrier across the channel (Figure 4. 1A) (Ellinor et al., 1995), while controlling intracellular Ca^{2+} via the Ca^{2+} cage DM-nitrophen (DMN). We are thus able to deliver a spatially uniform concentration of intracellular Ca^{2+} such that measured bulk cytosolic Ca^{2+} is identical to that surrounding the CaM residing on the channel (Tadross et al., 2013; Lee et al., 2015). Specifically, during patch clamp recording, we dialyzed DMN into HEK293 cells co-transfected with CaM and human cardiac $Ca_V1.2$ channels. Then, upon delivery of a UV pulse, the ester bonds of DMN are cleaved and Ca^{2+} is released into the cytosol. In this setting, the magnitude of the Ca^{2+} step delivered can be controlled by adjusting the intensity of the UV light and the varying the ratio between Ca^{2+} and DMN in the dialysate (Figures 4.1B, C). To measure the real-time concentration of Ca^{2+}, we added Ca^{2+} sensitive dyes into the dialysate and simultaneously recorded the fluorescence intensity and Li current (Figure 4.1A). As the physiologically relevant range of Ca^{2+} is larger than the dynamic range of a single Ca^{2+} dye, we combined known ratios of low- and high-affinity Ca^{2+} dyes (Fluo-2 HighAff and Fluo-2 LowAff) to accurately measure [Ca^{2+}] across the entire range (Lee et al., 2015).

We next considered the effect of intracellular Ca^{2+} on Li^+ entry (Ellinor et al., 1995)through the channel. Due to the high affinity of Ca^{2+} for the channel pore, intracellular Ca^{2+} has been shown to block the entry of monovalent ions in a process known as pore block (Ellinor et al., 1995). In order to mitigate this artifact, we introduced a mutation (E736A) into the selectivity filter of domain II in the α_1 subunit of the $Ca_V1.2$ channel ($Ca_V1.2^{E2A}$) which is known to shift the selectivity of the channel in favor of Li^+ (Ellinor et al., 1995). In order to characterize the extent of residual Ca^{2+} pore block in $Ca_V1.2^{E2A}$, we co-expressed the channel with CaM_{1234}, an engineered CaM in which the Ca^{2+} binding of all four EF hands has been disrupted. Under these conditions, Li^+ current displays a slow decay in current amplitude, indicative of VDI

(Figure 4.1A). Upon Ca^{2+} photouncaging, a small instantaneous drop in current demonstrates the remaining pore block of the $Ca_V1.2^{E2A}$ channel (Figures 4.1B, C). This residual pore block can be quantified as:

$$f_{block} = 1 - \frac{\frac{I_{end,f}}{I_{preUV,f}}}{\frac{I_{end,nf}}{I_{preUV,nf}}} \quad (4.1)$$

where I_{preUV} is current measured 20 ms before the UV pluses, I_{end} is current remaining at the end of the voltage step, and '*nf*' and *'f'* represent current without and with UV flash delivered at 150 ms after channel activation, respectively. For $Ca_V1.2^{E2A}$, f_{block} increases monotonically as a function of Ca^{2+} (Figure 4.1D) and can be fitted with the Hill equation,

$$f_{\text{block}} = \text{amp}_{\text{block}} * \frac{[\text{Ca}]^{\text{nHill}}}{[\text{Ca}]^{\text{nHill}} + \text{K}_{\text{d/block}}^{\text{nHill}}} \quad (4.2)$$

with amplitude (amp_{block}) = 1, Hill coefficient ($nHill$) = 1, and $K_{d/block}$ = 33 μM for Fluo-2/Alexa or 55 μM for Fluo-4FF/Alexa, which are comparable to what was previously described (Ellinor et al., 1995; Dick et al., 2016).

This setup can now be used to probe the extent of CDI of $Ca_V1.2$ at various cytosolic level of Ca^{2+}. When $Ca_V1.2^{E2A}$ is now co-expressed with wild-type CaM (CaM_{WT}), step release of Ca^{2+} (Figure 4.1F, red) results in robust inactivation of the Li^+ current (Figure 4.1F, black) indicating CDI. Importantly, the confounding effects of VDI can be eliminated in two ways. First, we co-expressed our channels with the beta2A isoform, which is known to minimize the extent of VDI in the channel complex (Dafi et al., 2004). Second, we can eliminate any residual VDI by utilizing the pre-flash current as our baseline for CDI measurements (Eqn. 3). Further, by varying the amplitude of the Ca^{2+} step, we can quantify the extent of steady-state CDI as a

function of Ca^{2+} (Figure 4.1G). Here, the normalized ratio of current reduction after Ca^{2+} delivery ($f_{CDI,app}$, Figure 4.1G) represents the combination of true CDI ($f_{CDI,true}$, Figure 4.1H) and residual pore block (f_{block}, Figure 4.1D):

$$f_{CDI,app} = 1 - \frac{\frac{I_{end,f}}{I_{preUV,f}}}{\frac{I_{end,nf}}{I_{preUV,nf}}} = 1 - (1 - f_{block}) * \left(1 - f_{CDI,true}\right) \quad (4.3)$$

(see APPENDIX [1] for derivation). Thus, the true CDI can be calculated (Figure 4.1H) and fit with a Hill equation of the form

$$f_{CDI} = CDI_{max} * \frac{[\mathrm{Ca}]^{\mathrm{nHill}}}{[\mathrm{Ca}]^{\mathrm{nHill}} + \mathrm{K_d^{nHill}}} \quad (4.4)$$

where $CDI_{max,WT}$ = 0.88, $nHill_{WT}$ = 2.5, and $K_{d,WT}$ = 0.52 μM, comparable to previously described values (Dick et al., 2016). Thus, we have a robust method for quantifying the extent of CDI in response to controlled concentrations of intracellular Ca^{2+}, providing parameters which will serve as a foundation for *in silico* models.

4.3.2 Measurement of N- and C-lobe mediated CDI

Prior studies have demonstrated separate forms of CDI mediated independently by the N- or C-lobe of CaM. Importantly, these two forms of CDI respond to spatially distinct Ca sources, each utilizing different mechanistic schemes (Dick et al., 2008; Tadross et al., 2008). However, this unique feature of CaM is not represented in published *in silico* models of CDI. This lack of lobe-specific detail is, in large part, the result of limited data pertaining to each lobe of CaM. We therefore undertook detailed characterization of the N- and C-lobe mediated CDI.

To begin, we utilize an engineered CaM (Keen et al., 1999), in which Ca^{2+} binding of the C-lobe is abolished (CaM_{34}), allowing the resolution of N-lobe mediated CDI alone (Peterson et al., 1999). $Ca_V1.2^{E2A}$ co-expressed with CaM_{34} displays robust Li^+ current at baseline (Figure 4.2A). However, upon photouncaging of Ca2+, the current decays exponentially (Figure 4.2B, black) with notably different kinetics as compared to CaM_{WT} (Figure 4.1F). By varying the amount of Ca^{2+} delivered, we can describe the extent of steady-state N-lobe-mediated CDI as a function of intracellular Ca^{2+} (Figure 4.2C). This relationship can be fitted with a Hill equation (Eqn. 4) with $CDI_{max,N} = 0.62$, Hill coefficient $nHill_N = 1.8$, and $K_{d,N} = 0.9$ μM.

Similarly, CDI mediated by the C-lobe CaM can be probed by measuring Li^+ current through $Ca_V1.2^{E2A}$ co-expressed with an engineered CaM with restricted C-lobe only Ca^{2+} binding (CaM_{12}) (Keen et al., 1999). Here, photouncaging Ca^{2+} results in a rapid inactivation of the Li^+ current (Figure 4.2E, black) at a faster rate than in the presence of CaM_{34} (Figure 4.2B). Notably, this increased kinetic response of C-lobe CaM occurs at each level of Ca^{2+} measured. Moreover, steady-state CDI mediated by the C-lobe of CaM can also be fit by a Hill equation (Eqn. 4), with $CDI_{max,C} = 0.66$, Hill coefficient $nHill_C = 1.4$, and $K_{d,C} = 1.15$ μM. Importantly, the K_d values obtained for N- and C-lobe CaM are each greater than that obtained for CaM_{WT} (0.9, 1.15 and .5 μM respectively), indicating that the two lobes are not functioning entirely independently, and cooperativity between the two lobes must be considered in determining the behavior of CaM_{WT}.

4.3.3 CaM lobe specific models of CDI

Having achieved robust experimental measurements of CDI mediated by each lobe of CaM, we now have the necessary components to build a kinetic model of CDI *in silico*. We

begin by first considering each lobe of CaM independently, utilizing the experimental results obtained for CaM_{34} and CaM_{12}. As current models sufficiently address the voltage dependent component of inactivation (VDI), we restrict our model to the context of CDI. Importantly, this focus does not ignore the importance of VDI, as this component can be added into any model due to the independence of these two processes (Luo and Rudy, 1994a; Jafri et al., 1998; Hirano and Hiraoka, 2003; Findlay et al., 2008) as such:

$$I(t) = I_{max}(t) * VDI(t) * CDI(t) \quad (4.5)$$

where *I(t)* is the total current remaining after CDI and VDI are considered, $I_{max}(t)$ is the maximum current amplitude based solely on channel activation.

To create our CDI models, we first considered the allosteric nature of CDI, in which channels bound to apoCaM open with a relatively high P_o (mode 1 gating), while channels harboring a Ca^{2+}-bound CaM transition into a low P_o mode of gating 'mode Ca'(Imredy and Yue, 1994; Adams et al., 2014). Once in mode Ca, channels maintain the ability to open, but with a reduced open probability, resulting in CDI. Importantly, recent work indicates that this mode transition occurs upon the departure of apoCaM, such that channels devoid of apoCaM may be indistinguishable from channels bound to Ca^{2+}/CaM. We first applied these principles to create a model of N-lobe mediated CDI. Here, we assume that the C-lobe will remain in the apo-state and thus will not contribute to CDI, while the N-lobe will independently orchestrate its own form of CDI (Figure 4.2C). We therefore created a 4-state model of N-lobe CDI, such that each individual state represents a channel in either the mode 1 (apoCaM bound, high P_o) or mode Ca (empty channel or Ca-CaM bound; low P_o) (Figure 4.3A). Specifically, state 1 represents $apoCaM_{34}$ bound to the carboxy-terminus of the channel, while state 2 depicts a departure of the

N-lobe from the channel, allowing Ca^{2+} to bind (state 3) and the calcified N-lobe to subsequently bind to its effector site on the amino-terminus of the channel (state 4) (Dick et al., 2008; Tadross et al., 2010). For the binding of Ca to CaM, we employed simultaneous Ca^{2+} (un)binding, as has been demonstrated for the two EF hands within each lobe of CaM (Martin et al., 1985; Linse et al., 1991). Moreover, we define the open probability of state 1 (apoCaM_{34} bound) to be $P_{O,max}$ while assuming the open probability of states 2, 3 and 4 is reduced by a factor f_N (fractional open probability in mode Ca) (Tadross et al., 2008; Tadross et al., 2010) such that

$$f_N = 1 - CDI_{max,N} \tag{4.6}$$

And the open probability of these mode Ca states is f_N*$P_{O,max}$. From our experimental measurements (Figure 4.2C) we obtain f_N = 0.38. We can then express the time-varying extent of CDI as

$$CDI(t) = \frac{I_f(t)}{I_{nf}(t)} = M_1(t) + f_N * (M_2(t) + M_3(t) + M_4(t)) \tag{4.7}$$

where $M_x(t)$ is the probability of channels being in state x at time t (see APPENDIX [2] for detailed differential equations).

We next optimized our model parameters (Table 4.1) to create the best fit to our kinetic (Figure 4.2B) and steady state (Figure 4.2C) experimental data for CaM_{34}. To begin, we idealized our experimental Ca^{2+} measurements, to be used as a model input (Figure 4.3B, bottom). Accordingly, we simulated currents in response to three different Ca^{2+} step inputs, yielding optimized rate constants as described in Table 4.1. Notably, our model accurately recapitulates the kinetic and steady state aspects of our experimental data (Figures 4.3B, C red = simulation, black = experiment), with $k_{on,N}$ and $k_{off,N}$, comparable to values previously reported

(Bayley et al., 1984; Martin et al., 1985; Stemmer and Klee, 1994; Black et al., 2005; Saucerman and Bers, 2008).

We next considered whether the parameters of this N-lobe model preserve the spatial Ca^{2+} selectivity of N-lobe CaM. In particular, the N-lobe of CaM is known to respond preferentially to local vs. global Ca^{2+}, dependent on the channel context (Dick et al., 2008; Tadross et al., 2008). This ability to switch between spatial Ca^{2+} selectivity is an important feature of N-lobe CaM regulation, allowing some channels to tune their response to different Ca^{2+}sources (Tadross et al., 2008). It is therefore necessary to ensure that our model remains consistent with this feature. To address this, we consider the closed form solution of steady-state CDI described by Tadross *et al* which defines the spatial selectivity of N-lobe CaM:

$$CDI(\infty) = CDI_{max} * \frac{P_O * r}{P_O * (r-1) + 1/\varepsilon + 1} \tag{4.8}$$

where $CDI(\infty)$ is steady-state CDI; CDI_{max} is the extent of CDI when all channels are in mode Ca; P_o is the open probability; $\varepsilon = b_N/a_N$; and $r = e_N/(d_N * \varepsilon)$ (Tadross et al., 2008). Here, $r > 1$ and $r < 1$ represents local and global Ca^{2+} selectivity, respectively. Based on our N-lobe model parameters (Table 4.1), r = 1.1, which confirms a local Ca^{2+} selectivity with a relatively intermediate profile (r close to 1), as expected for this channel (Dick et al., 2008; Tadross et al., 2008). Thus, while the model was optimized using a spatially uniform release of Ca^{2+}, the local selectivity of N-lobe CaM remains intact.

Having established a functional model of N-lobe CaM signaling, we next sought to create a similar model for C-lobe mediated CDI. Using the same approach as with the N-lobe model, we created a 4-state model of C-lobe mediated CDI (Figure 4.4A, see APPENDIX [2] for detailed differential equations for each mode). We again defined the open probability of state 1

(apoCaM12 bound) to be $P_{O,max}$ while assuming the open probability of states 2, 3 and 4 to be f_C*$P_{O,max}$ with f_C defined as:

$$f_C = 1 - CDI_{max,C}=0.34 \tag{4.9}$$

We then express the time-varying extent of CDI as

$$CDI(t) = \frac{I_f(t)}{I_{nf}(t)} = M_1(t) + f_C * (M_2(t) + M_3(t) + M_4(t)) \tag{4.10}$$

where $M_x(t)$ is the probability of channels being in state x at time t (see APPENDIX [2] for detailed differential equations). We then optimized the parameters (Table 4.1) by matching the kinetic (Figure 4.2E) and steady state (Figure 4.2F) experimental data for CaM_{12}. The simulated currents (Figure 4.4B) align well with the experimental data, capturing both the initial rapidly inactivating and the following slowly inactivating phases, as well as the steady-state response to Ca^{2+} (Figure 4.4C). Again, the kinetics of Ca^{2+} binding and unbinding to C-lobe of CaM, $k_{on,C}$ and $k_{off,C}$, are comparable to those previously described for this lobe (Bayley et al., 1984; Martin et al., 1985; Stemmer and Klee, 1994; Black et al., 2005; Saucerman and Bers, 2008).

Next, we confirmed that the invariably local Ca^{2+} selectivity of C-lobe CaM (Dick et al., 2008; Tadross et al., 2008) is preserved in our model. Previous reports have demonstrated that the C-lobe of CaM consistently responds to local Ca^{2+} signals due to the relatively slow kinetics of Ca^{2+} release from the C-lobe as compared to channel closings ('slow CaM' mechanism) (Tadross et al., 2008). Quantitatively this can be expressed as a constraint of the parameter K_{eff}, which represents the balance between Ca^{2+} entry through the channel and the affinity of C-lobe CaM for Ca^{2+} (Tadross et al., 2008) such that:

$$K_{eff} = \frac{1+b/a}{1+e/d} * \frac{k_{off,C}}{k_{on,C} * Ca_{local}{}^2} \quad (4.11)$$

where Ca_{local} is the Ca^{2+} concentration at mouth of the channel (Tadross et al., 2008). When K_{eff} <<1, CaM will invariably produce a local Ca selectivity. For our model, is we approximate the local Ca^{2+} concentration to be that expected for Ca^{2+} entry during a single channel opening (Ca_{local} ~ 100 μM) we obtain a value of K_{eff} = 3.3e-3, thus validating that the C-lobe of CaM will function as a local Ca^{2+} sensor.

4.3.4 Integrated model of CaM regulated CDI

Having established independent models of lobe-specific CaM mediated CDI, we next sought to integrate these models into a full model representing the kinetic response of both lobes of CaM simultaneously (CaM_{WT}). Cognizant of the potential interdependence of the two lobes of CaM, we created a 16-state bi-lobal model of CDI (Figure 4.5A). Our model incorporates the rate constants from both the N- and C-lobe models (Figures 4.3A, 4A, and Table 4.1), as well as multiple cooperativity factors (*g*, *h*, *k*, *l*, *m*, *n*, *p*, and *q*) representing potential communication between the lobes (Figure 4.5A). In addition, we assumed that a transiently dissociated CaM (states 6, 7, 10, 11) is unlikely to diffuse away from the channel alcove due to the limiting rate of exchange between cytosolic and channel-associated CaMs (Chaudhuri et al., 2005). As in the reduced models, the open probability in state 1 (both lobes of apoCaM bound) is defined to be $P_{0,max}$, while the open probability in states 2, 3 and 4 is defined as $f_N * P_{0,max}$, the open probability in states 5, 9 and 13 is $f_C * P_{0,max}$, and the open probability in states 6, 7, 8, 10, 11, 12, 14, 15, 16 is $f_{WT} * P_{0,max}$, where f_{WT} = 1-CDI_{max}=0.12 and CDI is defined as

$$CDI(t) = \frac{I_f(t)}{I_{nf}(t)} = M_1(t) + f_N * \big(M_2(t) + M_3(t) + M_4(t)\big) + f_C * (M_5(t) + M_9(t) + M_{13}(t)) + f_{WT} * (M_6(t) + M_7(t) + M_8(t) + M_{10}(t) + M_{11}(t) + M_{12}(t) + M_{14}(t) + M_{15}(t) + M_{16}(t)) \quad (4.12)$$

where $M_x(t)$ is the probability of channels being in state x at time *t* (see detailed equations in APPENDIX [3]).

Fitting our experimental data for $Ca_V1.2^{E2A}$ co-expressed with CaM_{WT} with our model enabled us to optimize the parameters (Table 4.1), resulting in a bi-lobal model which accurately recapitulates both the kinetic (Figure 4.5B) and steady state (Figure 4.5C) behavior of CaM mediated CDI. In addition, our model predicts cooperativity factors with both positive (>1, increased likelihood of the transition) and negative (<1, decreased likelihood of the transition) cooperativity. Scrutinizing these cooperativity factors, we see that the unbinding of a single apoCaM lobe from the channel appears to result in a less favorable conformation, promoting transitions out of these states (*g, m* >1). Moreover, states in which CaM has fully dissociated from the channel (states 6, 7, 10, 11) reveal decreased transitions to CaM bound states (*n*, *h* <1), fitting with an effectively decreased local CaM concentration (Mori et al., 2004). Finally, transitions to full CDI (state 16) proceed more rapidly following single lobe CDI (states 12, 15, *q* and *l* >> 1). Thus our model successfully captures the interplay between the two lobes of CaM, commenting on an important feature of CDI.

4.3.5 Modeling calmodulinopathy

To gauge the utility of our bi-lobal CDI model, we applied it in the context of a known calmodulinopathic mutation D130G. This missense mutation occurs within the fourth EF hand of CaM, resulting a ~ 50 fold decrease in the Ca binding affinity of the C-lobe (Crotti et al., 2013;

Hwang et al., 2014) and results in a significantly increased QT interval, rendering patients susceptible to arrhythmogenic activities (Arevalo et al., 2007). At the cellular level, this is demonstrated by a prolongation of the action potential (Figure 4.6A), which is largely due to disruption of $Ca_V1.2$ CDI. We thus applied our 16-state model to CaM_{D130G} mediated CDI. To begin, we probed CDI from $Ca_V1.2$ channels co-expressed CaM_{D130G} using our photouncaging technique (Figure 4.6B, C black). Here, the CDI is significantly reduced even at very high concentrations of calcium (Figure 4.6C). Moreover, the steady-state CDI mediated by CaM_{D130G} (Figure 4.6C) can be fit with a Hill equation (Eqn. 4) with $CDI_{max,D130G}$ = 0.62, $nHill_{D130G}$ = 1.8, and $K_{d,D130G}$ = 0.9 μM. Notably, this represents the identical parameters used to describe the steady-state behavior of the N-lobe-mediated CDI. Thus, this mutation in a single EF hand appears to disrupt CDI to the same extent as CaM_{34}, in which both C-lobe EF hands are ablated.

In order to incorporate this mutation within our 16-state CDI model, we decreased $k_{on,C}$ by 50 fold in accordance with the loss of Ca binding affinity for this lobe, and dramatically reduced the cooperativity factors g and m, preventing CDI from proceeding via C-lobe CaM (Table 4.2). The resultant model was able to accurately predict the kinetic (Figure 4.6B) and steady-state (Figure 4.6C) properties of CaM_{D130G} mediated CDI, thus demonstrating the utility of this bi-lobal CDI model in both physiologic and pathologic conditions.

4.4 Discussion

CDI is a critical regulatory feature of $Ca_V1.2$ channels, playing a critical role in setting the action potential duration in the heart. Disruption of the normal CDI of these channels has been linked to severe LQTS and life-threatening arrhythmias (Limpitikul et al., 2014; Yin et al., 2014; Dick

et al., 2016; Limpitikul et al., 2017), demonstrating the importance of improving our mechanistic understanding of CDI. While multiple cardiac and neuronal models employ CDI components (Hund and Rudy, 2004; ten Tusscher et al., 2004; Faber et al., 2007; Mahajan et al., 2008b), few take into account the detailed kinetics or bi-lobal nature of CaM binding to the channel. This is due, in part, to a paucity of quantitative experimental data determining the Ca^{2+} dependence of CDI. Here, we address this by obtaining rigorous experimental data, and using it to create a detailed kinetic model of $Ca_V1.2$ CDI featuring full bi-lobal CaM regulation. Specifically, we measured the kinetic response of channel inactivation due to measurable changes in intracellular Ca^{2+} by pairing photouncaging with simultaneous patch clamp recording (Tadross et al., 2013; Lee et al., 2015; Dick et al., 2016). This method allowed us to uncouple channel gating from intracellular Ca^{2+} dynamics, allowing precise control of bulk cytosolic Ca^{2+} and overcoming the ambiguity caused by diffusion limited Ca^{2+} dispersion in traditional patch clamp experiments. Moreover, by using single and combinations of Ca^{2+}-sensitive dyes with different affinities, we were able to accurately measure Ca^{2+} at both resting (~ 0.01 μM) and elevated Ca^{2+}(as high as 100 μM right at the mouth of the channel (Neher, 1998)). As such, we concurrently measured CDI in response to known concentrations of Ca^{2+} on a sub-millisecond timescale. This use of high-resolution data enabled the development of two independent single-lobe models of $Ca_V1.2$ CDI, which were then used as building blocks to create a 16 state bi-lobal model of CDI. Overall, this full-scale model recapitulates the kinetics of CDI in both physiological and pathologic conditions, and provides significant insights into the cooperativity of the N and C lobe of CaM in the context of $Ca_V1.2$ binding.

To build this bi-lobal model of CDI, we utilized a reductionist approach, first examining the CDI elicited by each lobe of CaM independently. To do this, we isolated N- or C-lobe mediated CDI

by utilizing engineered CaM with only one lobe capable of Ca^{2+} binding (CaM_{34} and CaM_{12}, respectively (Peterson et al., 1999). Our experimental data showed that despite minimal difference in steady-state CDI profiles, N-lobe mediated CDI exhibits much slower kinetics as compared to C-lobe mediated CDI. Using this data, we created a 4-state single-lobe model for each lobe of CaM, which accurately captured both the steady-state and dynamic properties of CDI. In addition, these models preserve the spatial Ca^{2+} selectivity of N- and C-lobe mediated CDI (Dick et al., 2008; Tadross et al., 2008), an important feature allowing $Ca_V1.2$ to respond differentially to Ca^{2+} elicited by various Ca^{2+} sources. Next, we incorporated these two models into a 16-state bi-lobal model of CDI, enabling us to describe the integrated kinetic behavior of the two lobes of CaM. Importantly, this allowed us to gauge the extent of cooperativity between the two lobes in the context of $Ca_V1.2$ binding. While cooperativity between the N- and C-lobe of CaM is well known in response to Ca^{2+} binding (Teleman et al., 1986; Yazawa et al., 1987; Jaren et al., 2002), the extent of cooperativity in the initiation of $Ca_V1.2$ CDI remains undetermined. Given the importance of this feature, we can corroborate the positive cooperativity factor determined by our model by scrutinizing our experimental data. Specifically, we express the closed-form solution of steady-state bi-lobal mediated CDI as:

$$CDI(\infty) = \frac{K_C * Ca^{nHill,C} * (1-P_C) + K_N * Ca^{nHill,N} * (1-P_N) + K_C * K_N * \lambda * Ca^{nHill,WT} * (1-P_{WT})}{1 + K_C * Ca^{nHill,C} + K_N * Ca^{nHill,N} + K_C * K_N * \lambda * Ca^{nHill,WT}} \quad (4.12)$$

where K_N and K_C are the K_d of N- and C-lobe CaM respectively. P_N, P_C, and P_{WT} are the relative open probabilities of mode Ca compared to mode 1 for N-, C- and both lobes of CaM respectively, and λ is the cooperativity factor (see SOM [4] for derivation). Here, $\lambda > 1$ and < 1 represent positive and negative cooperativity between CaM lobes. Applying this equation to our steady-state CaM_{WT} CDI data (Figure 4.1H) reveals $\lambda \sim 5$, demonstrating that both lobes of CaM

modulate $Ca_V1.2$ in an inter-dependent manner with positive cooperativity. Thus, this finding substantiates the necessity for a 16-state model for bi-lobal CaM mediated CDI, as opposed to two independent 4-state models. Moreover, this cooperativity implies that perturbation in one lobe of CaM can affect the overall CDI to a larger extent than what would be predicted based on an alteration within a single lobe, and may be an important feature in understanding the pathogenesis of diseases such as calmodulinopathies.

Calmodulinopathies are caused by genetic mutations within the calmodulin gene, and result in a severe, multisystem phenotype associated with significant cardiac deficits. We therefore applied our bi-lobal CDI model to simulate the effect of the LQTS-associated calmodulinopathy mutation, D130G (Crotti et al., 2013; Limpitikul et al., 2014; Yin et al., 2014; Limpitikul et al., 2017). Residing in the fourth EF hand of CaM, this mutation minimally increases the apoCaM binding affinity to $Ca_V1.2$ (~ 2 fold) (Limpitikul et al., 2014) while dramatically diminishing the Ca^{2+} binding affinity of C-lobe CaM (~ 50 fold) (Crotti et al., 2013; Hwang et al., 2014), with no discernable effect on the Ca^{2+} binding affinity of N-lobe CaM (Hwang et al., 2014). Interestingly, although the C-lobe of CaM_{D130G} maintains some Ca^{2+}-binding capacity, our experimental data shows that overall, CaM_{D130G} behaves nearly identically to CaM_{34} (Figs 2C and 6C). Moreover, prediction from our bi-lobal CDI model corroborates this finding. Decreasing decreasing $k_{on,C}$ by 50 fold and dramatically reducing the cooperativity factors *g* and *m*, preventing CDI from proceeding via C-lobe CaM, the model can accurately recapitulate both the kinetic and steady-state behavior of CaM_{D130G}. Such strong inter-lobal cooperativity implies that when the Ca^{2+}-binding affinity of one lobe of CaM falls under a certain threshold, CDI from that lobe may become physiologically irrelevant. In fact, it appears that even a 5 fold reduction in the C-lobe Ca^{2+} binding affinity (F142L mutation (Crotti et al., 2013; Hwang et al., 2014)) can

alter the overall behavior of CaM to resemble that of CaM_{34} (Limpitikul and Yue, 2014). Thus, our bi-lobal CDI model predicts that any mutation causing at least a 5-fold reduction in C-lobe CaM Ca^{2+} binding affinity will manifest a nearly identical effect on $Ca_V1.2$ as CaM_{D130G}, furthering our understanding of the pathogenesis of calmodulinopathies.

Beyond predicting the CDI profile of a LQTS-associated calmodulinopathies, our model could be applied in a broader context to gain insights into (patho)physiology of cardiac electrical activity. Previous studies have implicated that CDI, as compared to VDI, may be the dominant form of feedback regulation of $Ca_V1.2$ in the context of the cardiac action potential (Sun et al., 1997; Morotti et al., 2012), and the development of arrhythmia (Tanskanen et al., 2005; Morotti et al., 2012). Therefore, it is critical to employ a realistic mathematical representation of CDI that can capture the distinct kinetics, spatial Ca^{2+} selectivity, and cooperativity of the two lobes of CaM. Our bi-lobal kinetic model of CDI not only serves this purpose but also serves as a self-contained and versatile module. That is, this model does not explicitly include specific parameters for channel gating, and thus, can be readily utilized in a variety of settings with known channel gating paradigms. Specifically, this CDI model utilizes an input Ca(t), and generates CDI(t) as output while using minimal computational power. Moreover, as VDI and CDI are generally treated as independent processes (Luo and Rudy, 1994a; Jafri et al., 1998; Hirano and Hiraoka, 2003; Findlay et al., 2008), the final current magnitude is simply a product of maximal current, VDI(t), and CDI(t), allowing our model to be modularly incorporated into existing cellular and tissue-level cardiac action potential models (Luo and Rudy, 1994a; Jafri et al., 1998; Findlay et al., 2008). Finally, the model can be utilized within other cellular contexts, including neurons, vascular and gastrointestinal smooth muscles, and chromaffin cells (Zamponi

et al., 2015). Therefore, this ‘plug-and-play’ model could be an invaluable asset to the field of computational electrophysiology.

4.5 Tables and figures

Table 4.1Parameters used in CDI simulation.

Parameters	Values (units)
N-lobe-mediated CDI (CaM_{34})	
a_N	1.07e-1
b_N	2.46
d_N	2.15e-4
e_N	5.44e-3
$k_{on,N}$	1.236e5 ($mM^{-2} * ms^{-1}$)
$k_{off,N}$	5.273e-2 (ms^{-1})
$n_{Hill,N}$	1.8
f_N	0.38
C-lobe-mediated CDI (CaM_{12})	
a_C	14
b_C	2.7e3
d_C	1.5e-3
e_C	3.5e-3
$k_{on,C}$	2.15e4 ($mM^{-2} * ms^{-1}$)
$k_{off,C}$	1.2e-2 (ms^{-1})
$n_{Hill,C}$	1.4
f_C	0.34
Bi-lobal CDI (CaM_{WT})	
g	7.5
h	7.51e-1
n	2.656e-2
q	1.93e6
$m = g$	7.5
$p = g*h$	5.63
$k = g*n$	1.99e-1
$l = q*h/n$	5.46e7
f_{WT}	0.12

Table 4.2 Parameters used in long-QT CaM (CaM_{D130G}) simulation.

Parameters	Values (units)
a_N'	unchanged
b_N'	unchanged
d_N'	unchanged
e_N'	unchanged
$k_{on,N}$'	unchanged
$k_{off,N}$'	unchanged
$n_{Hill,N}$'	unchanged
f_N'	unchanged
a_C'	unchanged
b_C'	unchanged
d_C'	unchanged
e_C'	unchanged
$k_{on,C}$'	4.3e2 ($mM^{-2} * ms^{-1}$)
$k_{off,C}$'	unchanged
$n_{Hill,C}$'	unchanged
f_C'	unchanged
g'	7.5e-4
h'	unchanged
n'	unchanged
q'	unchanged
f_{WT}'	unchanged

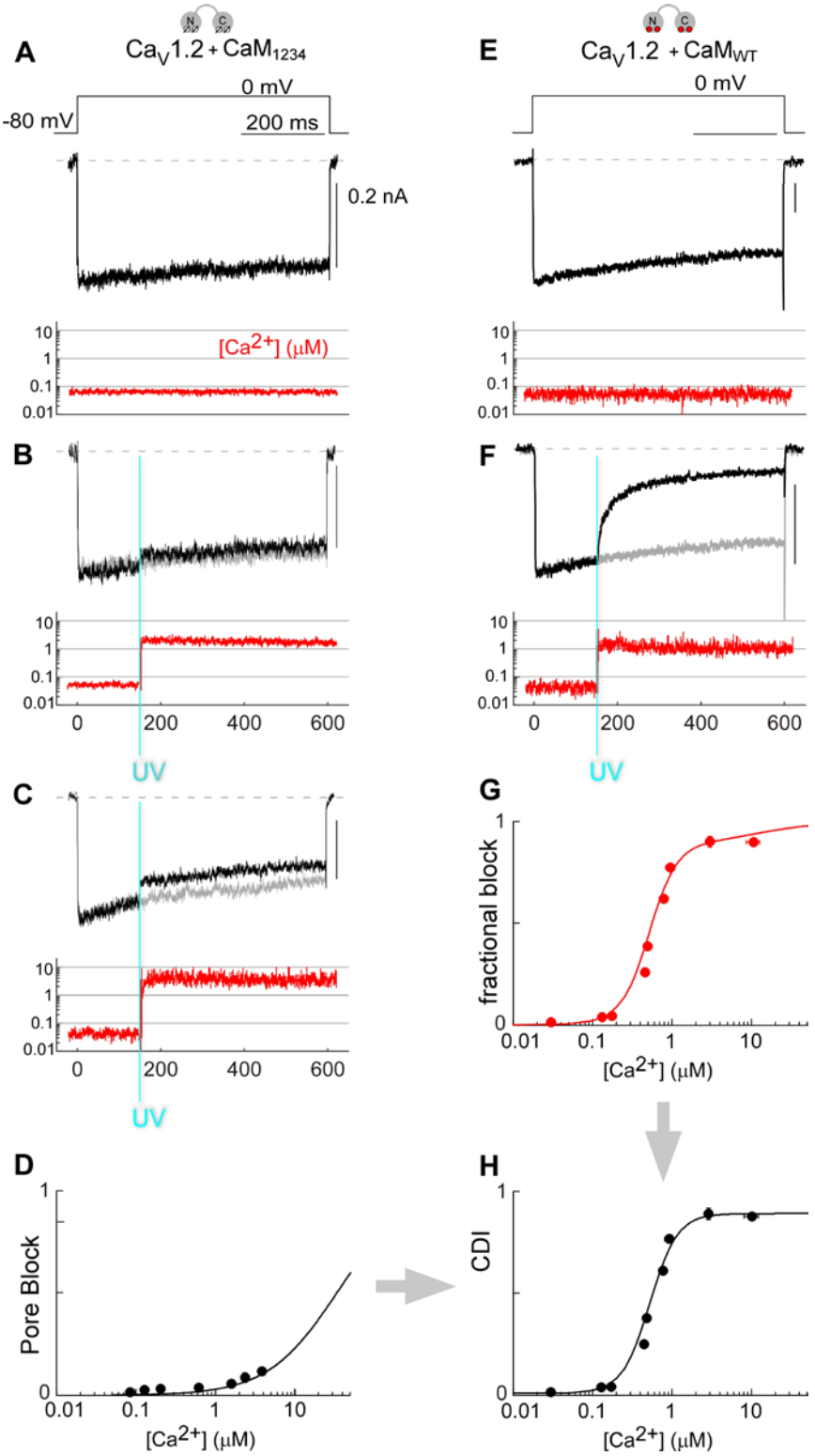

Figure 4.1 Steady-state behavior of bi-lobal CDI. (**A-D**) Behavior of $Ca_V1.2^{E2A}$ channels coexpressed with mutant CaM_{1234} in HEK293 cells, so as to characterize residual pore block. (**A**) Li^+ currents prior to Ca^{2+} uncaging with simultaneously measured resting $[Ca^{2+}]$ deduced from mixture of two Fluo-2 and red Alexa568 dyes (bottom panel). (**B**) Same cell during UV Ca^{2+}

uncaging during steady activation of current (black trace). Gray trace, taken from panel **A** as reference. (**C**) Li^+ current from another cell before (gray trace) and after (black trace) delivery of with higher Ca^{2+} step. (**D**) Steady-state pore block as a function of [Ca^{2+}] measured by Fluo-2/Alexa dye mixture, fitting with binding isotherm with Hill coefficient of 1 and large K_d of 33 μM (black curve). Similarly, pore block characterization experiment using Fluo-4FF/Alexa dye mixture was performed, resulting in Hill coefficient of 1 and large K_d of 55 μM. (**E**-**H**) Bi-lobal CDI from $Ca_V1.2^{E2A}$ channel co-expressed with CaM_{WT}. Li^+ current at resting [Ca^{2+}] (**E**) and after Ca^{2+} step (**F**). (**G**) Fraction of current diminution in panel **I** reflects both CDI and pore block. Using Eq 4.3, these data can be corrected (with fit in panel **D**) for pore block to isolate CDI alone as a function of [Ca^{2+}] (shown in **H**).

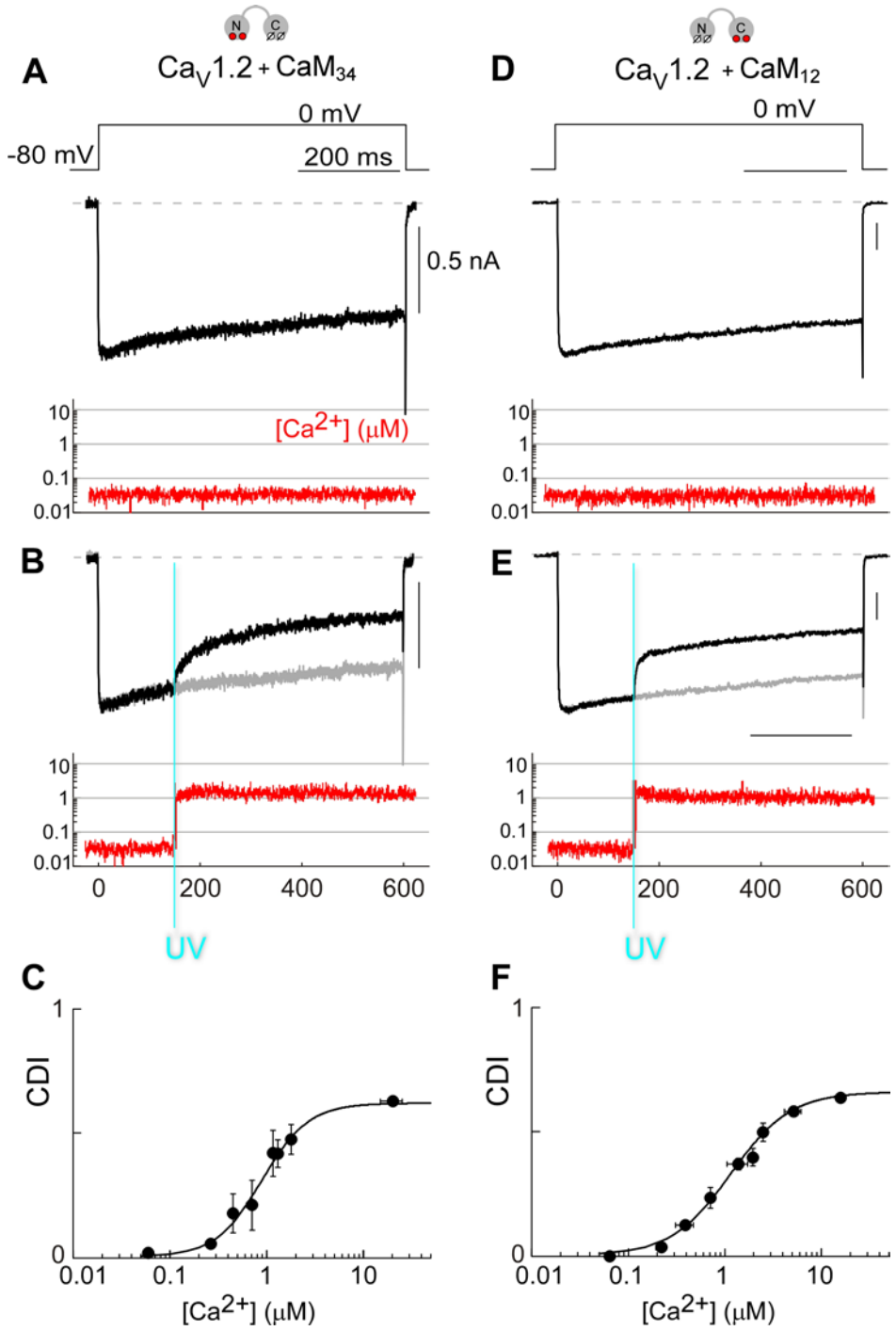

Figure 4.2 Steady-state CDI mediated by N- and C-lobes of CaM. (**A-C**) Behavior of $Ca_V1.2^{E2A}$ channels coexpressed with enigneered CaM_{34} to isolate N-lobe component of CDI. (**A**) Li^+ current in the absence of Ca^{2+} uncaging. (**B**) N-lobe-mediated CDI triggered upon Ca^{2+} uncaging. (**C**) Steady-state N-lobe-mediated CDI as function of [Ca^{2+}] defining relation with Hill coefficient of 1.8 and K_d of 0.9 μM. (**D-F**) $Ca_V1.2^{E2A}$ channels coexpressed with mutant CaM_{12} to isolate C-lobe component of CDI. (**F**) Steady-state C-lobe-mediated CDI as function of [Ca^{2+}] defining relation with Hill coefficient of 1.4, and K_d of 1.15 μM.

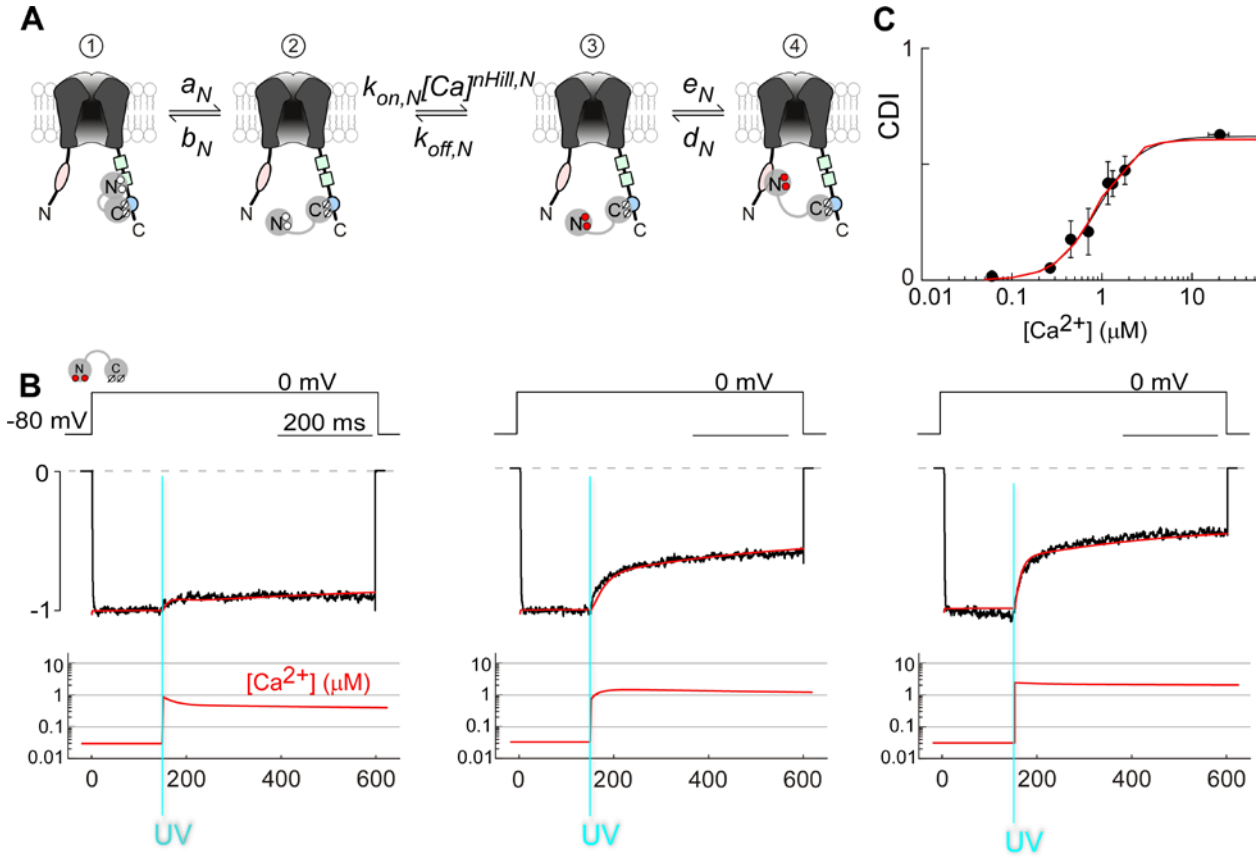

Figure 4.3 Kinetic model of CDI mediated by N-lobe of CaM. (**A**) Schematic representation of N-lobe-mediated CDI of $Ca_V1.2$ channels. This minimal model contains four states where each state contains five closed and one open channel configurations. Rate constants were written above and below the arrows depicting the direction of state transition (see Table 4.1 for values). (**B**) Simulated $I_{Ca(L)}$ (red) in response to three different level of $[Ca^{2+}](t)$ can recapitulate the N-lobe CDI kinetics of current recorded from $Ca_V1.2^{E2A}$ coexpressed with CaM_{34} (black) at various levels of Ca^{2+} step. Idealized $[Ca^{2+}](t)$ bottom row. (**C**) Steady-state N-lobe-mediated CDI predicted by this simple 4-state N-lobe model (red) matches almost precisely to the experimental data (black, taken from Figure 4.2C as reference).

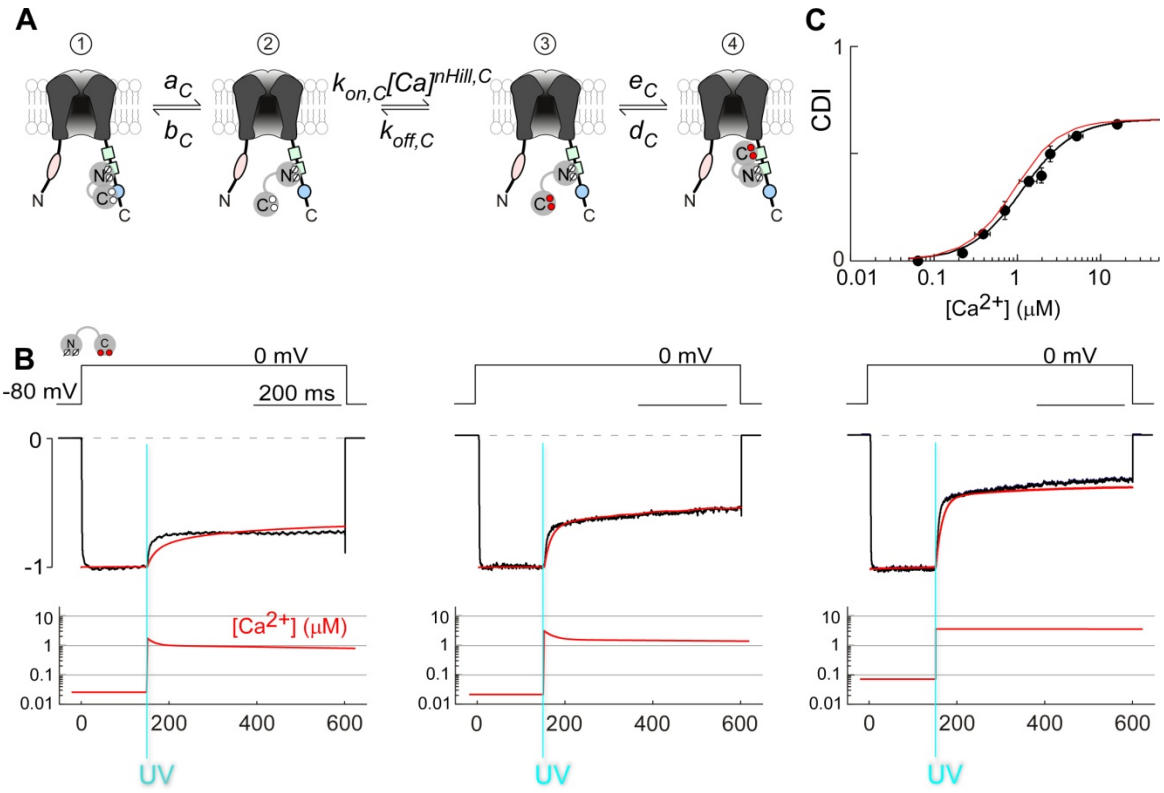

Figure 4.4 Kinetic model of CDI mediated by C-lobe of CaM. (**A**) Schematic representation of C-lobe-mediated CDI of $Ca_V1.2$ channels with similar assumption as Figure 4.3A. (**B**) When compared to experimental data from $Ca_V1.2^{E2A}$ coexpressed with CaM_{12}, this kinetic model (red) can recapitulate the kinetics of C-lobe-mediated CDI obtained experimentally (black) relatively well. Idealized $[Ca^{2+}](t)$ bottom row. (**C**) Steady-state C-lobe-mediated CDI predicted by this simple 4-state C-lobe model (red) matches almost precisely to the experimental data (black, taken from Figure 4.2F as reference).

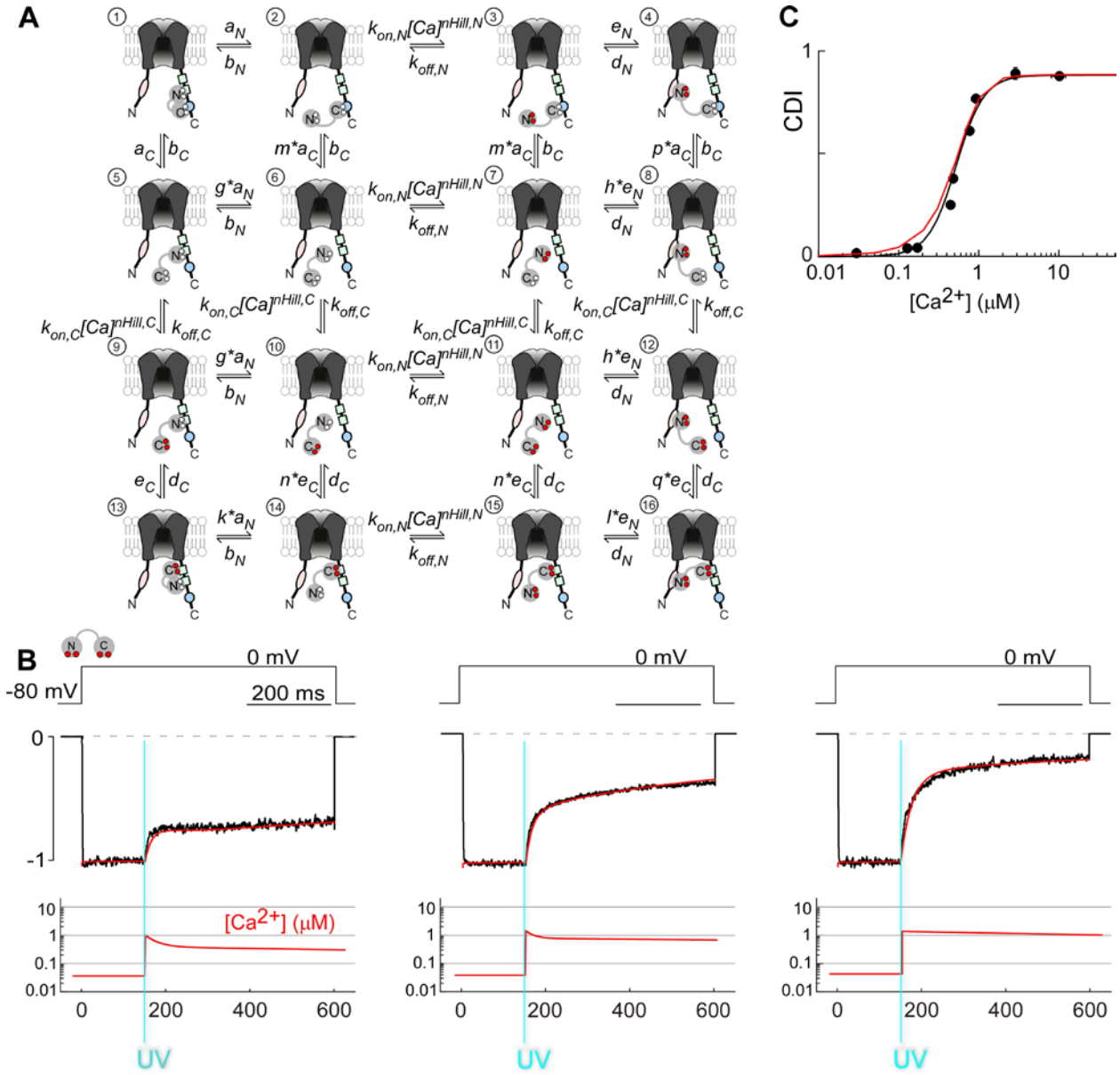

Figure 4.5 Kinetic model of bi-lobal CDI. (**A**) Schematic representation of CDI generated from both lobes of CaM ($Ca_V1.2^{E2A}$ + CaM_{WT}). (**B**) Bi-lobal model of CDI can precisely recapitulate the kinetic behavior of both lobes of CaM at various Ca^{2+} levels. Idealized $[Ca^{2+}](t)$ bottom row. (**C**) Steady-state CDI predicted by 16-state bi-local CDI model (red) matches almost precisely to the experimental data at physiologically relevant level of Ca^{2+} (black, taken from Figure 4.1H as reference).

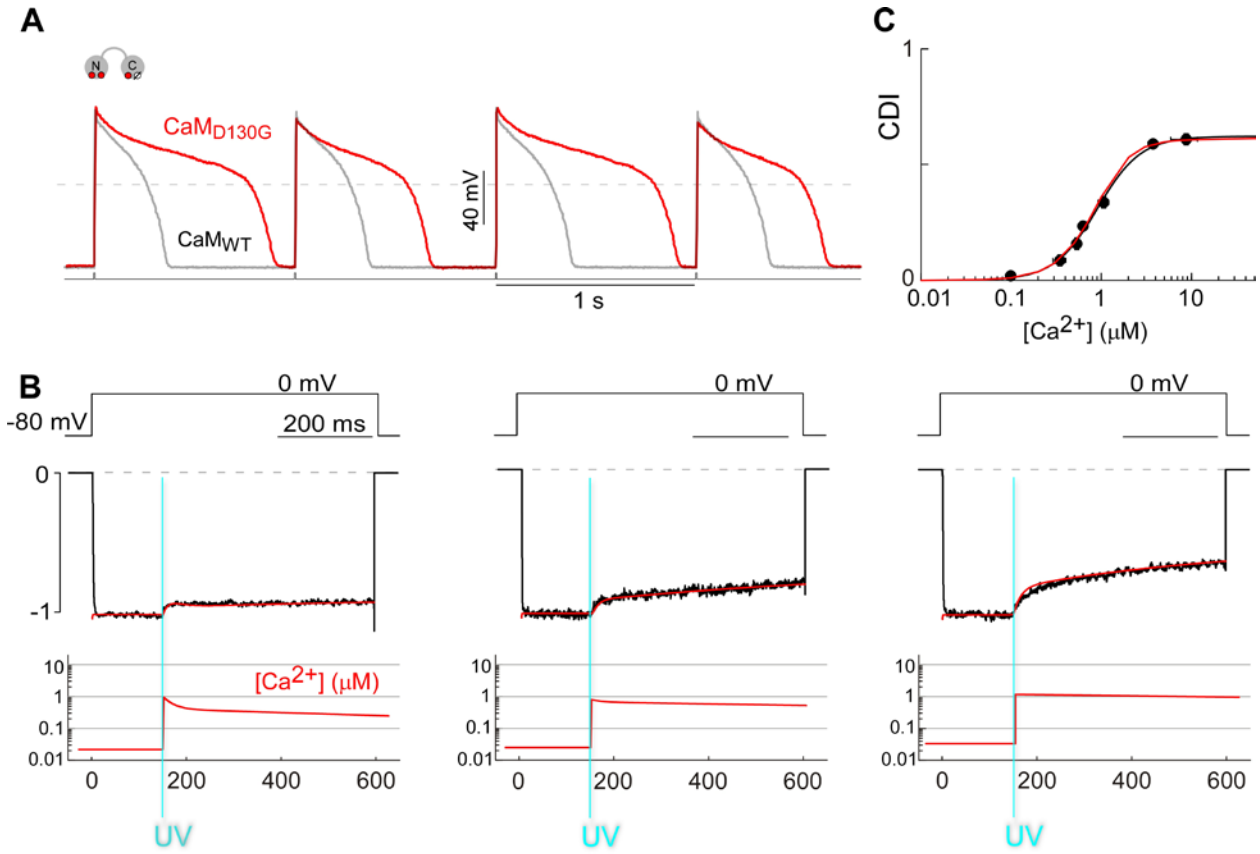

Figure 4.6 Steady-state and kinetic behavior of LQTS-associated CaM_{D130G}. (**A**) Disruption of action potentials in guinea-pig ventricular myocytes by CaM_{D130G}. When CaM_{D130G} was overexpressed, cardiac action potentials become markedly lengthened and irregular (red) compared to CaM_{WT} (shown in gray). Figure adapted from (Limpitikul et al., 2014) with permission. (**B**) Bi-lobal model of CDI can precisely recapitulate the kinetic behavior of pathologic CaM_{D130G} at various Ca^{2+} levels. Idealized $[Ca^{2+}](t)$ bottom row. (**C**) Experimental data showing steady-state CDI as function of $[Ca^{2+}]$ of CaM_{D130G} (black) with Hill coefficient of 1.8 and K_d of 0.9 μM, similarly to the N-lobe-mediated CDI. Steady-state CDI predicted by 16-state bi-lobal CDI model (red) precisely matches the experimental data (black).

4.6 Appendix

4.6.1 Derivation of apparent and true CDI (Equation (4.2))

Let b = absolute current size at 600 ms after voltage activation at baseline Ca^{2+} level and r = absolute current size 450 ms after UV flash (600 ms after voltage activation) at step Ca^{2+}.

Fraction of current after pore block (u),

$$u = 1 - f_{block}$$

Therefore, absolute current left at 450 ms post-flash (r) is

$$r = b * u * (1 - f_{CDI,true})$$

Thus, apparent CDI can be described as

$$f_{CDI,app} = 1 - \frac{r}{b}$$

$$f_{CDI,app} = \frac{b - b * u * (1 - f_{CDI,true})}{b}$$

$$f_{CDI,app} = 1 - (1 - f_{block}) * (1 - f_{CDI,true})$$

4.6.2 Differential Equations for N-lobe and C-lobe CDI (Figures 4.3A and 4.4A)

Let $M_x(t)$ be the probability of being in state x at time t. Therefore,

$$M_4(t) = 1 - M_1(t) - M_2(t) - M_3(t)$$

$$\frac{dM_1(t)}{dt} = -a_y * M_1(t) + b_y * M_2(t)$$

$$\frac{dM_2(t)}{dt} = a_y * M_1(t) - \left(b_y + k_{on,y} * [Ca]^{nHill,y}(t)\right) * M_2(t) + k_{off,y} * M_3(t)$$

$$\frac{dM_3(t)}{dt} = k_{on,y} * [Ca]^{nHill,y}(t) * M_2(t) - \left(k_{off,y} + e_y\right) * M_3(t) + d_y * (1 - M_1(t) - M_2(t) - M_3(t))$$

and

$$\frac{I_f(t)}{I_{nf}(t)} = CDI(t) = M_1(t) + f_y * (M_2(t) + M_3(t) + M_4(t))$$

where y represents value from either N- or C-lobe (Table 4.1), $[Ca]^{nHill,y}(t)$ represent Ca^{2+} concentration in mM as a function of time, and I_{nf} and I_f are experimental currents at baseline and step Ca^{2+}, respectively.

For all simulations, we set initial values $[M_1(t_0), M_2(t_0), M_3(t_0), M_4(t_0)]$ to [1,0,0,0].

4.6.3 Differential Equations for bi-local CDI (Figure 4.5A)

Let $M_x(t)$ be the probability of being in state x at time t. Therefore,

$$M_{16}(t) = 1 - M_1(t) - M_2(t) - M_3(t) - M_4(t) - M_5(t) - M_6(t) - M_7(t) - M_8(t) - M_9(t) - M_{10}(t) - M_{11}(t) - M_{12}(t) - M_{13}(t) - M_{14}(t) - M_{15}(t)$$

$$\frac{dM_1(t)}{\mathrm{dt}} = b_N * M_2(t) + b_C * M_5(t) - (a_N + a_C) * M_1(t)$$

$$\frac{dM_2(t)}{\mathrm{dt}} = a_N * M_1(t) + b_C * M_6(t) + k_{off,N} * M_3(t) - \left(b_N + m * a_C + k_{on,N} * [Ca]^{nHill,N}(t)\right) * M_2(t)$$

$$\frac{dM_3(t)}{\mathrm{dt}} = k_{on,N} * [Ca]^{nHill,N}(t) * M_2(t) + d_N * M_4(t) + b_C * M_7(t) - \left(k_{off,N} + e_N + m * a_C\right) * M_3(t)$$

$$\frac{dM_4(t)}{\mathrm{dt}} = e_N * M_3(t) + b_C * M_8(t) - (d_N + p * a_C) * M_4(t)$$

$$\frac{dM_5(t)}{\mathrm{dt}} = a_C * M_1(t) + b_N * M_6(t) + k_{off,C} * M_9(t) - \left(b_C + g * a_N + k_{on,C} * [Ca]^{nHill,C}(t)\right) * M_5(t)$$

$$\frac{dM_6(t)}{\mathrm{dt}} = m * a_C * M_2(t) + g * a_N * M_5(t) + k_{off,N} * M_7(t) + k_{off,C} * M_{10}(t) - \left(b_N + b_C + k_{on,N} * [Ca]^{nHill,N}(t) + k_{on,C} * [Ca]^{nHill,C}(t)\right) * M_6(t)$$

$$\frac{dM_7(t)}{\mathrm{dt}} = k_{on,N} * [Ca]^{nHill,N}(t) * M_6(t) + m * a_C * M_3(t) + d_N * M_8(t) + k_{off,C} * M_{11}(t) - \left(k_{off,N} + b_C + h * e_N + k_{on,C} * [Ca]^{nHill,C}(t)\right) * M_7(t)$$

$$\frac{dM_8(t)}{\mathrm{dt}} = h * e_N * M_7(t) + p * a_C * M_4(t) + k_{off,C} * M_{12}(t) - \left(d_N + b_C + k_{on,C} * [Ca]^{nHill,C}(t)\right) * M_8(t)$$

$$\frac{dM_9(t)}{\mathrm{dt}} = k_{on,C} * [Ca]^{nHill,C}(t) * M_5(t) + b_N * M_{10}(t) + d_C * M_{13}(t) - \left(k_{off,C} + g * a_N + e_C\right) * M_9(t)$$

$$\frac{dM_{10}(t)}{\mathrm{dt}} = \mathrm{g} * a_N * M_9(t) + k_{on,C} * [Ca]^{nHill,C}(t) * M_6(t) + k_{off,N} * M_{11}(t) + d_C * M_{14}(t) - \left(b_N + k_{off,C} + k_{on,N} * [Ca]^{nHill,N}(t) + n * e_C\right) * M_{10}(t)$$

$$\frac{dM_{11}(t)}{\mathrm{dt}} = k_{on,N} * [Ca]^{nHill,N}(t) * M_{10}(t) + k_{on,C} * [Ca]^{nHill,C}(t) * M_7(t) + d_N * M_{12}(t) + d_C * M_{15}(t) - \left(k_{off,N} + k_{off,C} + h * e_N + n * e_C\right) * M_{11}(t)$$

$$\frac{dM_{12}(t)}{\mathrm{dt}} = h * e_N * M_{11}(t) + k_{on,C} * [Ca]^{nHill,C}(t) * M_8(t) + d_C * (1 - M_1(t) - M_2(t) - M_3(t) - M_4(t) - M_5(t) - M_6(t) - M_7(t) - M_8(t) - M_9(t) - M_{10}(t) - M_{11}(t) - M_{12}(t) - M_{13}(t) - M_{14}(t) - M_{15}(t)) - \left(d_N + k_{off,C} + q * e_C\right) * M_{12}(t)$$

$$\frac{dM_{13}(t)}{\mathrm{dt}} = e_C * M_9(t) + b_N * M_{14}(t) - (d_C + k * a_N) * M_{13}(t)$$

$$\frac{dM_{14}(t)}{\mathrm{dt}} = k * a_N * M_{13}(t) + n * e_C * M_{10}(t) + k_{off,N} * M_{15}(t) - \left(b_N + d_C + k_{on,N} * [Ca]^{nHill,N}(t)\right) * M_{14}(t)$$

$$\frac{dM_{15}(t)}{\mathrm{dt}} = k_{on,N} * [Ca]^{nHill,N}(t) * M_{14}(t) + n * e_C * M_{11}(t) + d_N * (1 - M_1(t) - M_2(t) - M_3(t) - M_4(t) - M_5(t) - M_6(t) - M_7(t) - M_8(t) - M_9(t) - M_{10}(t) - M_{11}(t) - M_{12}(t) - M_{13}(t) - M_{14}(t) - M_{15}(t)) - \left(k_{off,N} + d_C + l * e_N\right) * M_{15}(t)$$

and

$$CDI(t) = M_1(t) + f_N * \left(M_2(t) + M_3(t) + M_4(t)\right) + f_C * (M_5(t) + M_9(t) + M_{13}(t)) + f_{WT} * (M_6(t) + M_7(t) + M_8(t) + M_{10}(t) + M_{11}(t) + M_{12}(t) + M_{14}(t) + M_{15}(t) + M_{16}(t))$$

where $[Ca]^{nHill,y}(t)$ represent Ca^{2+} concentration in mM as a function of time and y is a parameter from either N- or C-lobe CDI (parameters from Table 4.1).

With microscopic reversibility,

$$m = g$$

$$p = g * h$$

$$k = g * n$$

$$l = \frac{q * h}{n}$$

For all simulations, we set initial values $[M_x(t_0)]$ to $\begin{cases} 1, & x = 1 \\ 0, & x = 2 - 16 \end{cases}$.

4.6.4 Derivation of cooperativity between CaM lobes

Let P_y' be the absolute open probabilities of channels in mode y and P_y be the relative open probabilities of mode y compared to Ca^{2+}-free mode 1 (P_1), where

$$y = \begin{cases} N, & N - lobe\ CDI \\ C, & C - lobe\ CDI \\ WT, & bi - lobal\ CDI \end{cases}$$

CDI of $Ca_V1.2$ with Ca^{2+} ions as charge carrier during any voltage step is defined as

$$CDI = \frac{I_{peak} - I_{end}}{I_{peak}} = 1 - \frac{I_{end}}{I_{peak}}$$

where I_{peak} and I_{end} represent current magnitude at the beginning and the end of voltage step.

Here, since I_{peak} and I_{end} are recorded from the same cell, they have the same number of channels, channel conductance, and electrochemical driving force. Therefore, CDI can be re-written as

$$CDI = 1 - \frac{P_{O,end}}{P_{O,peak}}$$

where $P_{O,peak}$ and $P_{O,end}$ represent open probability of a channel at the beginning and the end of voltage step.

At any given amount of Ca^{2+},

$$P_O = P_1 * \frac{1}{1 + K_C * Ca^{nHill,C} + K_N * Ca^{nHill,N} + K_C * K_N * \lambda * Ca^{nHill,WT}}$$

where K_y, $nHill, y$, and λ are dissociation constant of y-lobe of CaM, Hill coefficient of y-lobe of CaM, and cooperativity factor between two CaM lobes, respectively.

Instantaneously right after the beginning of the voltage step, no significant amount of Ca^{2+} has entered the cells so $Ca \sim 0$. Therefore,

$$P_{O,peak} = P_1$$

That is, all channels effectively reside in mode 1.

At the end of the voltage step,

$$P_{O,end} = P_1 * \frac{1}{1 + K_C * Ca^{nHill,C} + K_N * Ca^{nHill,N} + K_C * K_N * \lambda * Ca^{nHill,WT}}$$

Thus,

$$P_{O,CDI} = P_1 * \frac{1}{z} + P_C^{'} * \frac{K_C * Ca^{nHill,C}}{z} + P_N^{'} * \frac{K_N * Ca^{nHill,N}}{z} + P_{WT}^{'} * \frac{K_C * K_N * \lambda * Ca^{nHill,WT}}{z}$$

where

$$z = 1 + K_C * Ca^{nHill,C} + K_N * Ca^{nHill,N} + K_C * K_N * \lambda * Ca^{nHill,WT}$$

Thus, CDI can be written as

$$CDI = 1 - \frac{P_1 * \frac{1}{z} + P_C^{'} * \frac{K_C * Ca^{nHill,C}}{z} + P_N^{'} * \frac{K_N * Ca^{nHill,N}}{z} + P_{WT}^{'} * \frac{K_C * K_N * \lambda * Ca^{nHill,WT}}{z}}{P_1}$$

which is equivalent to

$$CDI = \frac{K_C * Ca^{nHill,C} * (1 - P_C) + K_N * Ca^{nHill,N} * (1 - P_N) + K_C * K_N * \lambda * Ca^{nHill,WT} * (1 - P_{WT})}{1 + K_C * Ca^{nHill,C} + K_N * Ca^{nHill,N} + K_C * K_N * \lambda * Ca^{nHill,WT}}$$

CHAPTER 5

An autism-associated mutation in $Ca_V1.3$ channels has opposing effects on voltage- and calcium-dependent regulation

5.1 Introduction

The $Ca_V1.3$ channel represents a distinctive subtype of LTCCs, important in neurological (Berger and Bartsch, 2014; Striessnig et al., 2014; Zamponi et al., 2015; Pinggera and Striessnig, 2016), cardiac (Striessnig et al., 2014; Mesirca et al., 2015; Zamponi et al., 2015), and endocrine (Marcantoni et al., 2007; Zamponi et al., 2015; Barrett et al., 2016) function. The biophysical properties of these channels are thus precisely tuned to this function, as they are activated at relatively hyperpolarized potentials compared to other LTCCs (Koschak et al., 2001; Scholze et al., 2001; Xu and Lipscombe, 2001; Lipscombe et al., 2013; Lieb et al., 2014; Striessnig et al., 2014) and undergo distinct forms of negative feedback regulation (Tadross et al., 2010; Satin et al., 2011; Striessnig et al., 2014).

$Ca_V1.3$ channels employ two major forms of feedback regulation, VDI and CDI (Tadross et al., 2010). These two regulatory processes are controlled within each cell type, utilizing splice variation (Liu et al., 2010; Tan et al., 2011; Adams et al., 2014; Striessnig et al., 2014), RNA editing (Huang et al., 2012; Bazzazi et al., 2013), and auxiliary subunit pairing (Dolphin, 2009; Roberts-Crowley and Rittenhouse, 2009) to tune the inactivation properties of the channel to specific cellular functions. In particular, both splice variation and RNA editing are able to modulate both CDI (Shen et al., 2006; Singh et al., 2008; Bock et al., 2011; Tan et al., 2011; Huang et al., 2012; Bazzazi et al., 2013; Lipscombe et al., 2013; Striessnig et al., 2014) and channel open probability (Adams et al., 2014) by tailoring the components contained within the

channel carboxy tail. In addition, channel beta subunits are known to both traffic channels to the membrane (Dolphin, 2012; Buraei and Yang, 2013) and alter their voltage inactivation properties (Colecraft et al., 2002; Dolphin, 2003, 2009; Buraei and Yang, 2013).

The precise control of these regulatory processes are a vital component of normal physiology and disruption of this regulation has been linked to multiple human disorders including autism (O'Roak et al., 2012; Striessnig et al., 2014; Breitenkamp et al., 2015; Pinggera et al., 2015), auditory deficits (Platzer et al., 2000; Baig et al., 2011), and hyperaldosteronism (Azizan et al., 2013; Scholl et al., 2013). In mice, knockout of $Ca_V1.3$ results in profound deafness and severe bradycardia (Platzer et al., 2000; Dou et al., 2004), while in humans a similar phenotype is observed in patients harboring a 3-base pair insertion in exon 8b (Baig et al., 2011). This insertion abolishes channel conduction, resulting in sinoatrial node dysfunction and deafness (SANDD) syndrome, a phenotype similar to that described in $Ca_V1.3$-knockout mice. Moreover, multiple gain-of-function mutations have been linked to patients with hyperaldosteronism (Azizan et al., 2013; Scholl et al., 2013). Finally, two gain-of-function mutations in $Ca_V1.3$ (G407R and A749G) have been linked to autism spectrum disorders (ASD) (Iossifov et al., 2012; O'Roak et al., 2012; Pinggera et al., 2015). Prior studies of these two mutations demonstrated alterations in channel gating including a hyperpolarizing shift in channel activation and inactivation curves (Pinggera et al., 2015), but the differential effects on CDI versus VDI have yet to be determined. Discerning these precise effects may be highly relevant to understanding the mechanism of pathogenesis, as disruption of each of these components in the related $Ca_V1.2$ L-type channel has been shown to underlie Timothy syndrome (a severe multisystem disorder including autism and cardiac deficits) (Splawski et al., 2004; Splawski et al., 2005; Dick I. E., 2016), as well as long-QT syndrome associated with mutations in

calmodulin (Limpitikul et al., 2014). It is interesting to note that, unlike the $Ca_V1.2$ channelopathies, $Ca_V1.3$ mutations have often been associated with single-system phenotypes (Iossifov et al., 2012; O'Roak et al., 2012), despite the multi-system distribution of $Ca_V1.3$ channels. This isolation of symptoms is curious and requires further mechanistic investigation.

Here, we examine the underlying channel regulatory deficits of the autism-associated A760G mutation in rat $Ca_V1.3$ (equivalent to the A749G (Pinggera et al., 2015) or A769G (O'Roak et al., 2012) mutation in the human, depending on the channel backbone), focusing on the specific biophysical alterations produced by the mutation. We find that the mutation causes a significant reduction of CDI and a delay in channel deactivation in two major channel splice variants. In addition, we utilize an allosteric model of channel gating to gain insight into the underlying mechanism of this CDI deficit. Further examination of the biophysical defects of this mutation also revealed a beta subunit-dependent increase in VDI, an effect which would oppose the Ca^{2+} overload due to the decrease in CDI and a delay in channel deactivation. Thus the severe effects of this 'gain-of-function' mutation could be mitigated by a 'loss-of-function' effect on VDI.

5.2 Materials and methods

5.2.1 Molecular Biology

The point mutation (A760G) was introduced into rat $Ca_V1.3$ short and long splice variants (gifts from Dr. Tuck Wah Soong (Huang et al., 2013)) in the homologous position to that found in humans using QuikChange™ site-directed mutagenesis (Agilent). The equivalent human mutation was found in patients at A769G in chromosome 3, position 53764493 (O'Roak

et al., 2012) and corresponds to the A749G mutation previously described in an alternate human splice variant (Pinggera et al., 2015).

5.2.2 Transfection of HEK293 cells

HEK293 cells were cultured on glass coverslips in 10-cm dishes and WT or mutant $Ca_V1.3$ channels, along with their auxiliary subunits, were transiently transfected using a standard calcium phosphate method (Peterson et al., 1999). 8 µg of rat $Ca_V1.3$ was co-expressed with 8 µg of rat brain β_{2a} (M80545) or β_{1b} (NM_017346), 8 µg of rat brain $\alpha_2\delta$ (NM012919.2) subunits, and 2 µg of simian virus 40 T antigen cDNA. Expression of all constructs was driven by a cytomegalovirus promoter and β subunits were contained within an EGFP-IRES bicistronic vector to allow visualization of transfected cells.

5.2.3 Whole Cell Electrophysiology

Whole-cell voltage-clamp recordings of HEK293 cells were done 1-2 days after transfection at room temperature. Recordings were obtained using an Axopatch 200B amplifier (Axon Instruments). Whole-cell voltage-clamp records were low pass filtered at 2 kHz, and then digitally sampled at 10 kHz. P/8 leak subtraction was used, with series resistances of 1-2 MΩ. For voltage-clamp experiments, internal solutions contained (in mM): $CsMeSO_3$, 114; CsCl, 5; $MgCl_2$, 1; MgATP, 4; HEPES (pH 7.3), 10; and either BAPTA, 10 or EGTA, 0.5; at 295 mOsm adjusted with $CsMeSO_3$. External solutions contained (in mM): TEA-$MeSO_3$, 140; HEPES (pH 7.4), 10; and $CaCl_2$ or $BaCl_2$, 40; at 300 mOsm, adjusted with TEA-$MeSO_3$.

For simultaneous ratiometric Ca^{2+} measurements and current recordings, a fixed ratio of two Ca^{2+}-sensitive dyes (Fluo-2 high affinity, TEFLabs; Fluo-2 low affinity, TEFLabs) and Alexa568 (Invitrogen) were added into a 0.5-mM EGTA internal solution. Two Ca^{2+} indicators

at different binding affinity were chosen to accurately measure both baseline and peak Ca^{2+} concentrations. The dye mixture was calibrated to obtain absolute Ca^{2+} concentrations (Joiner and Lee, 2015). The external solution (Tyrode's solution) contained (in mM): NaCl, 135; KCl, 5.4; $CaCl_2$, 1.8; $MgCl_2$, 0.33; NaH_2PO_4, 0.33; HEPES, 5; glucose, 5 (pH 7.4). During current recordings, Ca^{2+} concentration was measured by exciting dyes using a 514-nm Argon laser, via a 545DCLP dichroic mirror and either a 545/40BP (Fluo) or 580LP (Alexa568) filter. Cells were held at -80 mV and a 1-Hz train of neuronal action potential recordings from cortical neurons of E18 mouse embryos were used as voltage stimulus.

5.2.4 Generation of a $Ca_V1.3$ Homology Model

We used MODELLER v9.14 (Sali and Blundell, 1993) to build a homology model of $Ca_V1.3$ pore regions (Figure 1A) based on the crystal structure of the bacterial Na channel Na_VAb (PDB accession code: 4EKW) (Payandeh et al., 2012) as previously described (Tadross et al., 2010). Briefly, we generated 10 decoy models from which a model with lower objective function was chosen. The four domains of $Ca_V1.3$ were constrained to adopt a clockwise orientation when viewed from the extracellular surface by analogy to the orientation of the related voltage-gated sodium channels (Li et al., 2001). The alignment used for the various pore subsegments are as follows:

S5 Segment

Na_VAb	SVAALLTVVFYIAAVMATNLYGATFP
$Ca_V1.3$ Domain I	HIALLVLFVIIIYAIIGLELFIGKMH
$Ca_V1.3$ Domain II	SLLLLLFLFIIIFSLLGMQLFGGKFN

$Ca_V1.3$ Domain III NIMIVTTLLQFMFACIGVQLFKGKFY

$Ca_V1.3$ Domain IV YVALLIAMLFFIYAVIGMQMFGKVAM

P Loop

Na_VAb EWFGDLSKSLYTLFQVMTLESWSMGIVRPVMNV

$Ca_V1.3$ Domain I TNFDNFAFAMLTVFQCITMEGWTDVLYWVNDAI

$Ca_V1.3$ Domain II STFDNFPQALLTVFQILTGEDWNAVMYDGIMAY

$Ca_V1.3$ Domain III FNFDNVLSAMMVLFTVSTFEGWPALLYKAIDSN

$Ca_V1.3$ Domain IV NNFQTFPQAVLLLFRCATGEAWQEIMLACLPGK

S6 Segment

Na_VAb HPNAWVFFIPFIMLTTFTVLNLFIGII

$Ca_V1.3$ Domain I WEWPWVYFVSLIILGSFFVLNLVLGVL

$Ca_V1.3$ Domain II GMIVCIYFIILFICGNYILLNVFLAIA

$Ca_V1.3$ Domain III RVEISIFFIIYIIIVAFFMMNIFVGFV

$Ca_V1.3$ Domain IV SNFAIVYFISFYMLCAFLIINLFVAVI

5.2.5 Data Analysis and Statistics

The fraction of current remaining after 300 ms of channel activation (r_{300}) was calculated as:

$$r_{300} = \frac{I(300)}{I(t_{peak})} \tag{5.1}$$

and CDI measurements were corrected for VDI effects by calculating a metric for pure CDI (f_{300}) as follows:

$$f_{300} = \frac{r_{300}^{Ba} - r_{300}^{Ca}}{r_{300}^{Ba}} \tag{5.2}$$

r_{300} and f_{300} values were reported at 10 mV for the $Ca_V1.3_{short}$ channel and at 0 mV for $Ca_V1.3_{long}$. The relative open probability ($P_{O,rel}$) was determined by a tail activation protocol (Tadross et al., 2008) where channels are fully activated at 100 mV prior to stepping to variable test potentials. The ratio of peak and steady state currents then represent the relative $P_{O,rel}$ of each voltage. The voltage activation curve was fit by the Boltzmann equation:

$$P_{O,rel} = scale * (1 + e^{-\frac{V - V_{1/2}}{k}})^{-1} \tag{5.3}$$

where $V_{1/2}$ and k represent the half activation voltage and slope factor, respectively.

Time constants for channel deactivation (τ_{fast} and τ_{slow} in Figures 5.1F, 5.1K, 5.3E, and 5.3J) were calculated by fitting the deactivating Ba^{2+} tail currents resulting from a transition from 80 mV (channels maximally open based on the activation curve, Figures 1D, 1I, 3C, 3H) to multiple voltages near the base of the activation curve (channels closed) with the equation:

$$I_{fit} = A * (f * e^{-\left(\frac{t - t_0}{\tau_{fast}}\right)} + (1 - f) * e^{-\left(\frac{t - t_0}{\tau_{slow}}\right)}) \tag{5.4}$$

where f is the fraction of the faster portion of the current decay, and time constants τ_{fast} and τ_{slow} represent the fast and slow components of the current decay.

All data are presented as mean ± SEM. Statistical significance for variability was determined by a two-tailed student's t-test.

5.3 Results

5.3.1 A760G significantly decreases CDI and alters $Ca_V1.3$ channel gating

Voltage-gated Ca^{2+} channel α1-subunits are composed of four domains, each containing six transmembrane α -helices (Figure 5.1A). The four S6 helices line the channel pore through which Ca^{2+} enters the cell. The intracellular portion of these S6 helices form the activation gate of the channel, and mutations within this region are known to alter channel activation (Kraus et al., 2000; Hoda et al., 2005; Hohaus et al., 2005; Raybaud et al., 2006; Raybaud et al., 2007; Pinggera et al., 2015). Moreover, the S6 helices are known to contribute to VDI and CDI in many Ca_V channels, including $Ca_V1.3$ (Kraus et al., 2000; Stotz et al., 2000; Stotz and Zamponi, 2001; Splawski et al., 2004; Stotz et al., 2004; Hoda et al., 2005; Hohaus et al., 2005; Raybaud et al., 2006; Raybaud et al., 2007; Barrett and Tsien, 2008; Tadross et al., 2010). Thus, the effect of the A760G mutation on channel activation and inactivation (Pinggera et al., 2015) may be explained by its location in the S6 helix of domain II (IIS6).

In order to study the effects of the A760G mutation on Ca^{2+} regulation of channels, we undertook whole-cell voltage clamp recordings of $Ca_V1.3$ channels heterologously expressed in HEK293 cells. To minimize the possible confounding effects on CDI measurements, the channels were co-expressed with the β_{2a} subunit which is known to minimize VDI (Stea et al., 1994; Colecraft et al., 2002; Dafi et al., 2004; Dolphin, 2009; Buraei and Yang, 2013). In addition, an internal solution containing 10 mM BAPTA was utilized to restrict Ca^{2+} elevation to only the nanodomain of the channel, thus diminishing cell-to-cell variability (Dick et al., 2008;

Tadross et al., 2008). Figure 5.1B shows exemplar current traces for wild-type (WT) $Ca_V1.3$. The sharp decay of Ca^{2+} current (red) evoked by a 10-mV depolarizing step depicts CDI, while the Ba^{2+} current trace (black) exhibits only VDI, which is mostly absent here due to the choice of β subunit. This robust CDI can be observed in the population data, where the fraction of current remaining after 300-ms depolarization (r_{300}) is displayed as a function of voltage (Figure 5.1C), and the U-shaped dependence on voltage recapitulates a classic hallmark of CDI (Brehm and Eckert, 1978; Brehm et al., 1980). Here, the difference between the r_{300} values for Ca^{2+} and Ba^{2+}, normalized by the Ba^{2+} $r_{300,}$ gauges the magnitude of CDI (f_{300}). However, when the A760G mutation is introduced into these channels, a drastic reduction in the speed and magnitude of CDI is observed (Figure 5.1G, Supplementary Figure 5.1). This effect is further evident in the population data across multiple voltages (Figure 5.1H) illustrating a clear CDI deficit due to the autism-associated A760G mutation.

Beyond CDI, S6 mutations are likely to affect channel activation (Kraus et al., 2000; Hoda et al., 2005; Hohaus et al., 2005; Raybaud et al., 2006; Raybaud et al., 2007; Pinggera et al., 2015). We therefore probed the effect of the A760G on the voltage dependence of $Ca_V1.3$ channel activation. Here, we measured the relative open probability ($P_{o,rel}$) of the channels across voltages via a tail activation protocol optimized for $Ca_V1.3$ channels (Tadross et al., 2008) (Figure 5.1D). Introduction of the A760G mutation produced a significant hyperpolarizing shift (13 mV; $p < 0.01$) in channel activation (Figure 5.1I), consistent with previous studies of this channel (Pinggera et al., 2015). Moreover, analysis of the deactivation kinetics during the tail activation protocol revealed a marked effect of A760G on channel deactivation. Evaluation of the deactivation kinetics during transitions from 80 mV to multiple voltages near the foot of the activation curve provided an estimation of the kinetics of channels transitioning from fully open

to closed (Figures 5.1E, F). A double exponential function was used to quantify a fast and slow component of channel deactivation (τ_{fast}, τ_{slow} respectively). The A760G mutation significantly increased both time constants across voltages, indicating a considerable slowing of channel closing (Figures 5.1J, K).

L-type channel S6 mutations have previously been shown to affect CDI via modulation of modal channel gating (Imredy and Yue, 1994; Tadross et al., 2010; Dick I. E., 2016). We therefore consider the underlying mechanism linking channel activation and CDI. An allosteric model of channel gating (Figure 5.2A) is known to describe CDI of $Ca_V1.3$ channels well (Tadross et al., 2010). Within this model, channels initially open within the mode 1 regime, which is characterized by a relatively large open probability ($P_{O/mode1}$). Upon channel opening, Ca^{2+} influx drives channels into the mode Ca regime where channels maintain the ability to open, but with a significantly reduced P_O ($P_{O/modeCa}$). It is this reduction in P_O that results in the CDI seen in whole-cell currents, such that

$$CDI = F_{CDI} * \frac{(P_{O/mode\ 1} - P_{O/modeCa})}{P_{O/mode\ 1}} \tag{5.5}$$

where F_{CDI} is the fraction of channels within mode Ca. Therefore at a saturating level of Ca^{2+}, F_{CDI} will approach unity as virtually all channels will reside within mode Ca. Under this condition, a maximal level of CDI (CDI_{max}) is achieved:

$$CDI_{max} = \frac{(P_{O/mode\ 1} - P_{O/modeCa})}{P_{O/mode\ 1}} \tag{5.6}$$

We now consider the effects of the S6 mutation A760G within our model. As we and others (Pinggera et al., 2015) have shown that this mutation causes a hyperpolarizing shift in channel activation, the variable a was introduced to account for the altered free energy ($\Delta\Delta G_a$)

required to open the mutant channels (Tadross et al., 2010). For a hyperpolarizing mutation such as A760G, $\Delta\Delta G_a$ will be negative, indicating decreased energy required to open the mutant channel. This decrease in free energy will result in increased channel opening in both mode 1 and mode Ca, thus decreasing CDI_{max} (Eq 5.6, Figure 5.2B, green). This reduction of CDI_{max} could account for the overall decrease in CDI (Figure 5.2B, black) observed in whole-cell experiments (Figure 5.1), despite the increased F_{CDI} (Figure 5.2B, blue) due to increased Ca^{2+} influx.

To test the hypothesis that the CDI deficit due to A760G is primarily a result of a decrease in CDI_{max}, we undertook whole-cell patch clamp recordings in which conditions enabled a sustained saturating level of Ca^{2+} at the mouth of the channel. By significantly reducing the intracellular Ca^{2+} buffer (0.5 mM EGTA), the accumulation of Ca^{2+} within the cell should overpower the nanodomain Ca^{2+} signal, thus raising Ca^{2+} to saturating levels as whole cell current increases (Yang et al., 2006) and providing an estimation of CDI_{max} (Tadross et al., 2008). For WT $Ca_V1.3$ channels, exemplar Ca^{2+} traces illustrate a saturating amount of CDI as a function of current density (Figures 5.2C, D). The lack of additional CDI accumulation beyond a current density of 50 pA/pF indicates that we reached CDI_{max} at a value of ~ 0.9 for WT channels (Figure 5.2D, red dashed line). A760G channels, however, demonstrate a significant reduction in CDI_{max} to ~ 0.7 (Figures 5.2E, F), which can be observed at multiple test potentials (Supplementary Figure 5.2), confirming the underlying mechanism of CDI loss (Figure 5.2B).

5.3.2 The A760G mutation differentially affects $Ca_V1.3$ splice variants

Ca_V channels are a critical conduit for Ca^{2+} entry into multiple cell types and must therefore be precisely tuned for specific cellular functions. Nature employs multiple mechanisms

with which to accomplish such fine tuning, including modulation of channel splice patterns (Shen et al., 2006; Bock et al., 2011; Tan et al., 2011; Huang et al., 2013; Striessnig et al., 2014). An example of such splicing in $Ca_V1.3$ channels results from inclusion of exon 42 or 42a, yielding a channel with a long versus short C-terminus (Huang et al., 2013). The long channel variant activates at a somewhat more positive potential (Singh et al., 2008; Striessnig et al., 2014), has a lower open probability (Adams et al., 2014), and exhibits dramatically reduced CDI as compared to the short splice variant (Liu et al., 2010; Striessnig et al., 2014). Due to these distinct properties, we examined the effect of the A760G mutation in both relevant splice variants. Having already demonstrated a significant reduction in CDI within the short channel variant, the isoform with more robust CDI (Huang et al., 2013; Striessnig et al., 2014) (Figure 5.1), we next undertook a similar approach within the long $Ca_V1.3$ splice variant ($Ca_V1.3_{long}$).

Examination of CDI within the WT $Ca_V1.3_{long}$ channel under high buffering conditions (10 mM BAPTA) demonstrated significantly smaller, yet appreciable CDI (Figures 5.3A, B), as compared to the short channel variant (Figures 5.1B, C). Introduction of the A760G mutation blunted this CDI (Figures 5.3F, G), though to a lesser extent as compared to the short variant. We next examined the activation of WT and A760G $Ca_V1.3_{long}$ channels. The resulting $P_{o,rel}$ versus voltage relationships (Figures 5.3C, H) demonstrated an 11 mV hyperpolarizing shift due to the introduction of A760G ($p < 0.01$), similar to that observed in the short variant (Figures 5.1D, I). Likewise, analysis of the deactivation kinetics also revealed a significant slowing of channel closing across multiple voltages (Figures 5.3D, E, I, and J). Thus, the biophysical deficits produced by the A760G mutation are qualitatively similar within each relevant channel backbone, although the magnitude of the CDI effect is somewhat decreased in the long splice variant.

5.3.3 Opposing VDI changes may mitigate the detrimental effects of A760G

In addition to the critical Ca^{2+}-dependent feedback, VDI also plays a major role in controlling Ca^{2+} entry through Ca_V1 channels. The underlying structural components for VDI have been shown to involve the linker region between domains I and II (I-II linker), which acts as a hinged-lid to close the pore following depolarization (Stotz et al., 2000; Tadross et al., 2010). This process is known to be variably modulated by the binding of different isoforms of channel β subunits to the I-II linker (Tadross et al., 2010; Buraei and Yang, 2013). For example, when coexpressed with β_{2a}, Ca_V1 channels display little VDI due to restricted movement caused by palmitoylation, and thus membrane anchoring, of the β_{2a} (Figure 5.4A, blue) (Stea et al., 1994; Colecraft et al., 2002; Dafi et al., 2004). On the other hand, if the channels are coexpressed with the β_{1b} subunit, most Ca_V1 isoforms will display strong VDI due to the lack of the palmitoylation site (Colecraft et al., 2002; Shen et al., 2006). $Ca_V1.3$ channels, however, are unique in that their S6 helices have been shown to act as a shield (Figures 5.4A, D, red) to prevent closing of the I-II linker lid, thus, endowing the channels with minimal VDI regardless of β subunit isoform co-expressed.

A close inspection of the Ba^{2+} current through the A760G $Ca_V1.3$ channels reveals a slight, but significant re-emergence of VDI despite the presence of the β_{2a} subunit (Figures 5.4B, C). Importantly, this mutation-induced VDI can be discerned in either of the two channel variants (Figures 5.1G versus B, Figures 5.3F versus A). This re-emergence of VDI is accentuated when A760G $Ca_V1.3$ is coexpressed with β subunits lacking a palmitoylation site. Figures 5.4E, F demonstrate a significant increase in VDI in channels harboring the A760G mutation in the presence of the β_{1b} subunit. Note that the WT $Ca_V1.3$ channels (black) have minimal VDI even in the presence of the β_{1b} subunit due to the existence of the 'shield'. Thus the

re-emergence of VDI in these channels indicates that the A760G mutation may disrupt the VDI shield (Figures 5.4A, D, bottom). This increase in VDI may act in opposition to the loss of CDI within these mutant channels, thus mitigating the detrimental effects of increased Ca^{2+} flux into cells.

5.3.4 The A760G mutation can cause an increase in intracellular Ca^{2+}

We now know that the A760G mutation has a significant effect on CDI, VDI, and deactivation. Given the known link between excess cytosolic Ca^{2+} and severe disease states (Splawski et al., 2005; Schulz, 2007; Zhang et al., 2011), we wondered if Ca^{2+} overload due to an increased Ca^{2+} influx may play a role in the phenotype of A760G patients. However, the effects of the A760G mutation on Ca^{2+} entry are multi-fold, such that a decrease in CDI and slowing of channel deactivation are opposed by an increase in VDI. We therefore sought to confirm the cumulative effect of the A760G mutation on overall Ca^{2+} entry and intracellular Ca^{2+} concentration ($[Ca^{2+}]_i$).

To this end, we stimulated HEK293 cells expressing $Ca_V1.3$ channels with a 1-Hz train of neuronal action potentials (Figure 5.5A, top) and recorded both the Ca^{2+} current passing through the channels as well as the intracellular Ca^{2+} level. This stimulation protocol was chosen as it matches well with the spontaneous neuronal firing frequencies in some populations of hippocampal neurons, thus mimicking a basal activity level (Hirase et al., 2001; Mizuseki and Buzsaki, 2013). When this protocol was applied to WT $Ca_V1.3$ channels, a small decrease in peak current amplitude was observed over time as CDI accumulated (Figure 5.5A, middle panel). This amplitude decay matches well with the relatively small increase in $[Ca^{2+}]_{i,}$ (Figure 5.5A, bottom panel). When the A760G mutation was introduced into the channel, however, a

significant increase in both the rate and extent of intracellular Ca^{2+} accumulation was observed (Figures 5.5B-D, blue) due to an increased duration of Ca^{2+} entry during each action potential (Figure 5.5B, left). This increased Ca^{2+} entry is likely a net result of decreased channel inactivation, and a slowing of channel deactivation. This excess $[Ca^{2+}]_i$ increased the extent of CDI observed in the current recordings over time although this decrease in current entry was not sufficient to counteract the Ca^{2+} overload within the cytosol. Overall, the cumulative effect was a steady state Ca^{2+} level approaching 0.8 uM (Figure 5.5C), substantially larger than the normal resting $[Ca^{2+}]_i$ of a neuron (Verkhratsky et al., 1994). This excess cytosolic Ca^{2+} due to A760G could be a significant contributing factor to the disease pathogenesis.

5.4 Discussion

We have demonstrated a significant effect of the autism-associated mutation A760G on the gating of $Ca_V1.3$ such that channel activation is significantly left-shifted, CDI is decreased, and deactivation is slowed, resulting in excess Ca^{2+} entry through channels. However, these effects are mitigated by an increase in VDI. Importantly, the balance between these opposing mechanisms may be dependent on the specific properties of the particular channel complex harboring the mutation. In particular, we have demonstrated that two major $Ca_V1.3$ splice variants respond to the introduction of the A760G mutation with distinct levels of CDI disruption (Figures 5.1, 5.3). As each of these splice variants has a significantly different affinity for commonly used L-type channel blockers (Huang et al., 2013), such a variation in CDI effects may have important implications on the response of patients to treatment. Moreover, these two splice variants represent only a subset of a panoply of channel isoforms found across different tissues, each with uniquely tuned channel gating and feedback regulation (Tan et al., 2011; Huang et al., 2012; Bazzazi et al., 2013; Huang et al., 2013; Lieb et al., 2014; Striessnig et al.,

2014). Like the short versus long splice isoforms, it is possible that the A760G mutation may differentially alter the biophysical properties of these variants. Thus the extent of channel alteration may depend on the expression pattern within each specific cell type resulting in variable phenotypes across different tissues.

The original case report for A760G describes a patient exhibiting primarily neurological deficits classified as ASD (O'Roak et al., 2012). Upon further examination of the Simons Simplex Collection database, the classification of ASD in this proband appeared to be of a relatively milder nature on the autism spectrum (pervasive developmental disorder not otherwise specified or PDD NOS) without additional non-neurological symptoms. Such a narrow symptom profile without any cardiac or hearing deficits stands in contrast to the broad tissue distribution of $Ca_V1.3$. Moreover, this lack of severe multisystem characteristics is unusual for autism-related Ca^{2+} channelopathies (Splawski et al., 2004; Hemara-Wahanui et al., 2005; Splawski et al., 2005; Breitenkamp et al., 2015). The multitude of $Ca_V1.3$ channel variants across different tissues (Shen et al., 2006; Bock et al., 2011; Tan et al., 2011) may account for some of this lack of a multi-system phenotype. The relatively moderate symptoms of this proband may be due, in part, to differential effects of the A760G mutation on specific channel variants expressed in each system. In addition, the VDI effects of the A760G mutation could also contribute to the milder phenotype displayed by the proband. In particular, the increased Ca^{2+} entry due to altered CDI and channel activation/deactivation may be partially offset by increased VDI. As this VDI enhancement is accentuated in the presence of select beta subunits (Figure 5.4), expression patterns of different beta subunits (Ludwig et al., 1997) may further increase the variability of A760G effects across systems.

The A760G mutation is capable of substantially raising cytosolic Ca^{2+} concentration when overexpressed in HEK293 cells (Figure 5.5). Of note, this effect was achieved even at a relatively slow 1-Hz pacing rate, comparable to the spontaneous firing rate of some hippocampal neurons (Hirase et al., 2001; Mizuseki and Buzsaki, 2013). The experimental conditions utilized here were optimized for maximal resolution of the A760G effect. However, under physiological heterozygous expression levels, the effect of the A760G channels will likely be considerably less. Nonetheless, the idea of excessive Ca^{2+} entry underlying ASD is not unprecedented as the ASD phenotype has been linked to Ca^{2+} overload through a myriad of Ca^{2+} handling molecules (Chen et al., 2003; Barnby et al., 2005; Zhou et al., 2006), including multiple voltage-gated Ca^{2+} channels (Splawski et al., 2004; Hemara-Wahanui et al., 2005; Splawski et al., 2005; Krey and Dolmetsch, 2007). Overall, it seems plausible that the gating defects of the $Ca_V1.3$ channels harboring the A760G mutation may result in excess Ca^{2+} entry, which in turn may be over-activating the downstream Ca^{2+} signaling pathways involved in neural development and plasticity (Chen et al., 2003; Barnby et al., 2005; Zhou et al., 2006; Krey and Dolmetsch, 2007). While the mechanisms underlying ASD remain elusive, the identification of mutations such as A760G, hint at important contributing factors.

5.5 Tables and figures

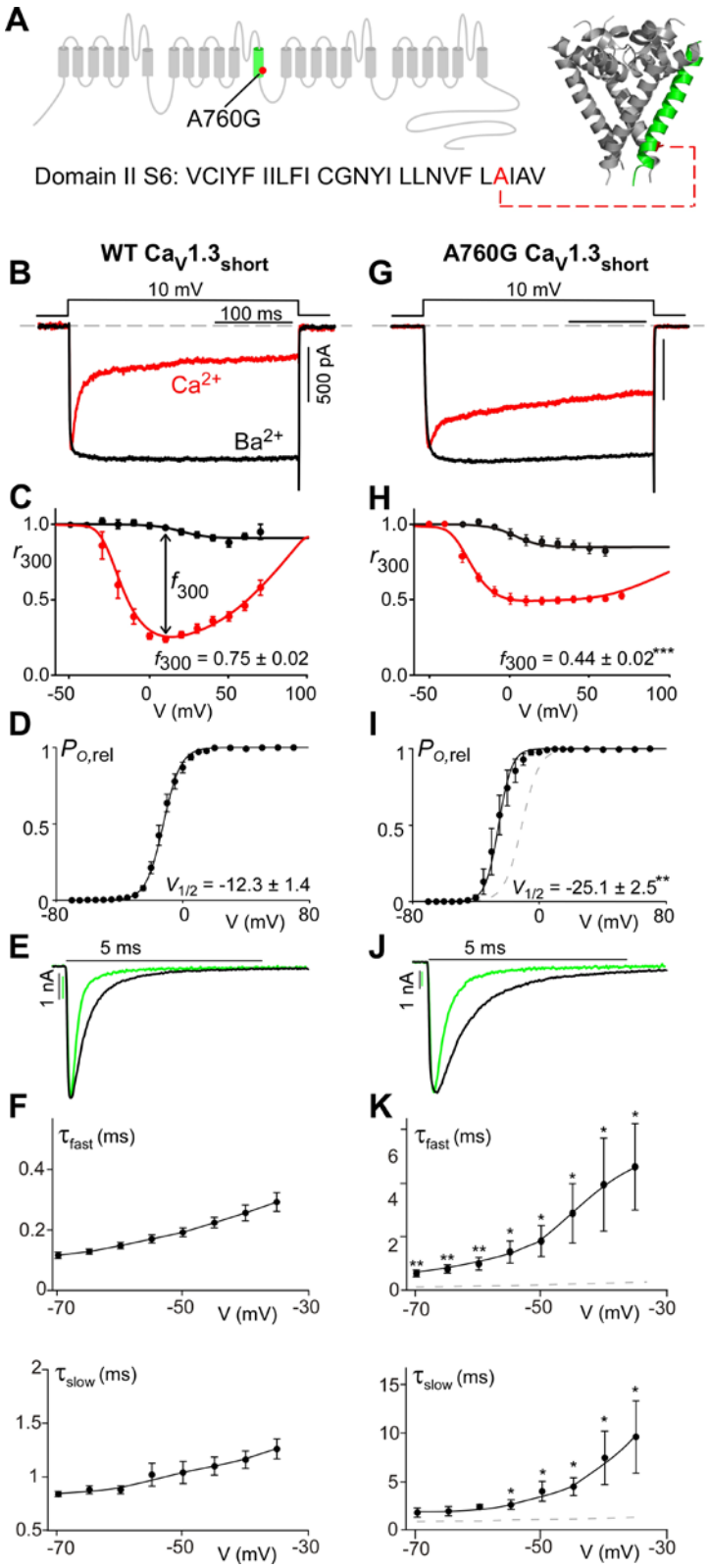

Figure 5.1 A760G decreases CDI and promotes channel activation. (**A**) Cartoon representing $Ca_V1.3$ and the location of the autism-associated mutation A760G. Left, the A760G missense mutation resides in the S6 helix of domain II. Right, structural homology model of $Ca_V1.3$ S5/S6 segments, based on Na_VAb with the A760G highlighted in red. (**B**) Exemplar Ca^{2+} (red) and Ba^{2+} (black) current traces through WT $Ca_V1.3_{short}$ evoked by a 10-mV depolarizing step. Currents are normalized for comparison. Scale bar corresponds to the Ca^{2+} trace. (**C**) Population data of fraction of current remaining after 300 ms (r_{300}) for Ca^{2+} (red) and Ba^{2+} (black). f_{300} determined at 10 mV (n=12). Data are plotted as mean ± SEM here and throughout. (**D**) The activation curve for WT $Ca_V1.3_{short}$ obtained via a tail activation protocol with Ba^{2+} as the charge carrier (n = 6). (**E**) Exemplar Ba^{2+} tail currents obtained from a transition from 80 mV to -40 mV (black) and -60 mV (green). Traces are normalized to one another. Scale bars correspond to the traces of the same color. (**F**) Population data of the fast (top) and slow (bottom) deactivation time constants (τ) plotted as a function of voltage (n = 5). (**G**) Exemplar Ca^{2+} (red) and Ba^{2+} (black) current traces through A760G $Ca_V1.3_{short}$ evoked by a 10-mV depolarizing step. Compared to that of WT (B), Ca^{2+} current through A760G channels displays significantly less CDI. (**H**) Population data of r_{300} for Ca^{2+} (red) and Ba^{2+} (black) currents through A760G channels. CDI is significantly smaller (*** $p < 0.001$, n = 6) than that of the WT channels. (**I**) The activation curve of A760G $Ca_V1.3_{short}$ channels (black) shows a 13-mV hyperpolarizing shift (** $p < 0.01$, n = 4) compared to WT (reproduced in gray). (**J**) Exemplar Ba^{2+} tail currents for the A760G channel, obtained from a transition from 80 mV to -40 mV (black) and -60 mV (green). (**K**) Population data of the fast (top) and slow (bottom) deactivation time constants (τ) plotted as a function of voltage for the A760G channel. Deactivation is significantly slowed as compared to WT reproduced as the gray dashed line (* $p < 0.05$, ** $p < 0.01$, n = 4).

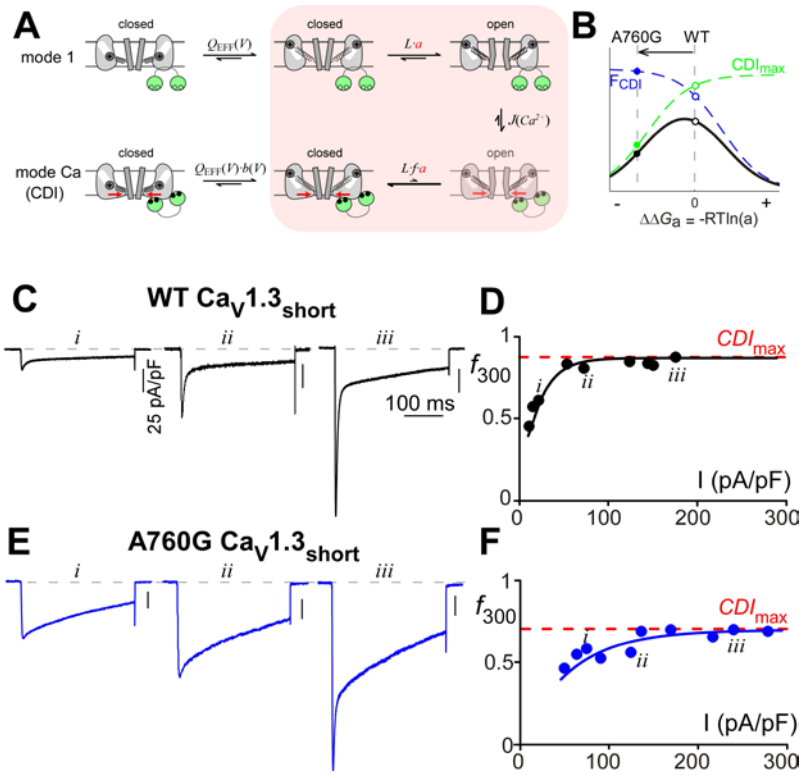

Figure 5.2 An allosteric mechanism underlying the CDI reduction. (**A**) Diagram representing an allosteric model of CDI. Channels transition from mode 1 with high P_O, to mode Ca^{2+} with lower P_O, in response to Ca^{2+} entry. Equilibrium constants Q_{EFF} (concerted movement of S1-S4 segments), L (S6 movement), and a (mutation effect) govern transitions between open and closed channel configurations (Tadross et al., 2010; Dick I. E., 2016), while the effective equilibrium constant $J(Ca^{2+})$ governs entry into mode Ca^{2+}. The parameter f ($0 < f < 1$) scales the P_O in mode Ca^{2+} resulting in CDI. State transitions expected to be effected by the A760G are shaded pink. (**B**) Total CDI (black), the product of F_{CDI} (blue) and CDI_{max} (green), is plotted as a function of $\Delta\Delta G_a$ for the model shown in panel A. The A760G mutation left-shifts voltage activation ($\Delta\Delta G_a < 0$, $a > 1$), predicting a decrease in CDI due to a decrease in CDI_{max}. (**C**) Exemplar Ca^{2+} current traces through WT $Ca_V1.3_{short}$ channels. Larger current amplitudes (*ii, iii*) allow a greater influx of Ca^{2+}, enhancing entry into mode Ca and thus increasing CDI as compared to diminutive Ca^{2+} currents (*i*). (**D**) f_{300} values for individual cells expressing WT $Ca_V1.3_{short}$ are plotted as a function of current density. The curve saturates at $CDI_{max} \sim 0.9$ (red dashed line). Traces in C correspond to *i-iii*. (**E**) Exemplar Ca^{2+} current traces through A760G $Ca_V1.3_{short}$ channels. Similar to that of WT (C), larger current amplitude increases f_{300} values. (**F**) Population data representing CDI of A760G $Ca_V1.3_{short}$ channels. f_{300} values saturate at $CDI_{max} \sim 0.7$ (red dashed line), significantly lower than WT.

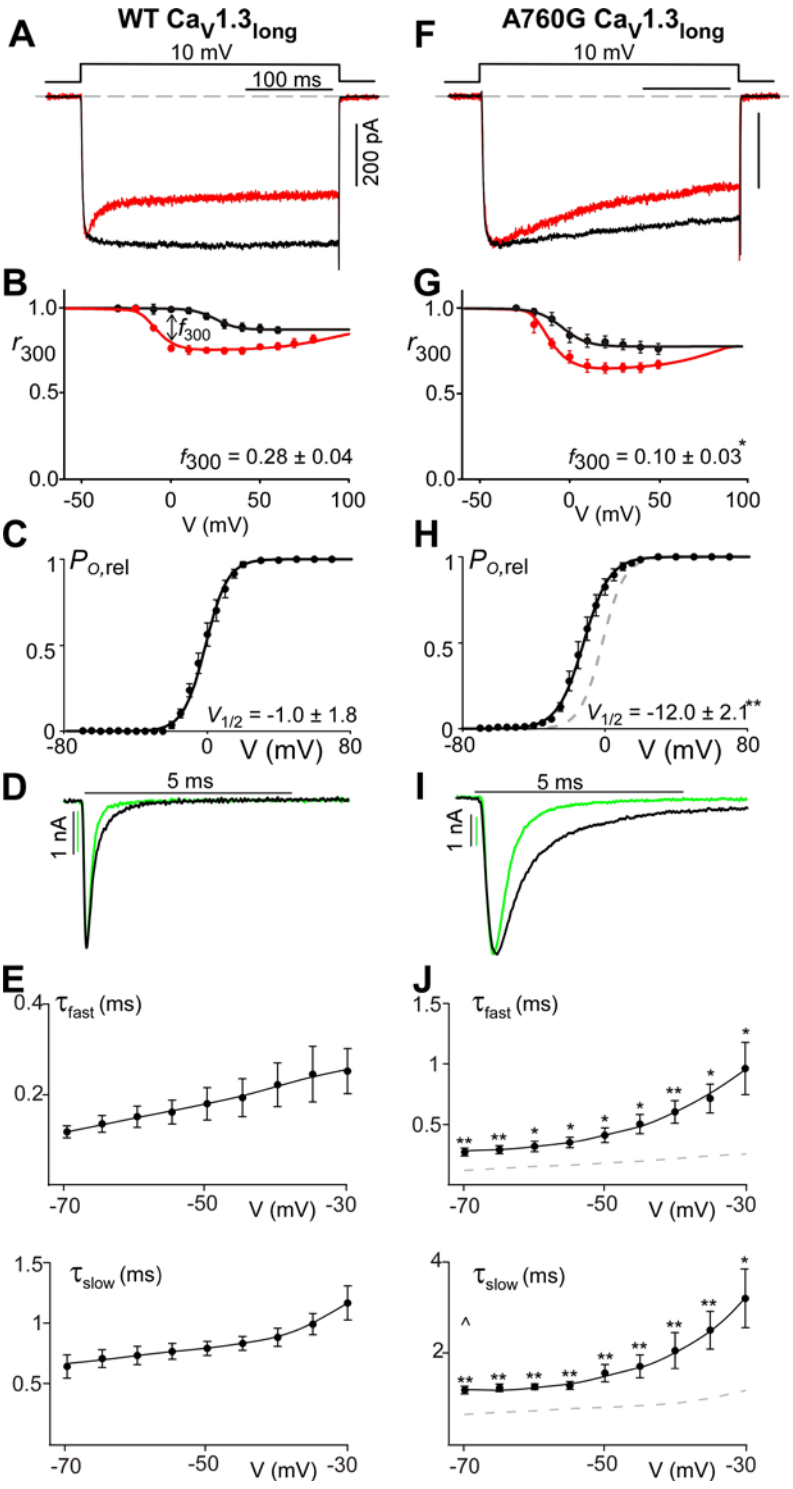
A
WT $Ca_V1.3_{long}$
10 mV
100 ms
200 pA
F
A760G $Ca_V1.3_{long}$
10 mV
B
r_{300}
f_{300}
f_{300} = 0.28 ± 0.04
V (mV)
G
f_{300} = 0.10 ± 0.03*
C
$P_{O,rel}$
$V_{1/2}$ = -1.0 ± 1.8
V (mV)
H
$V_{1/2}$ = -12.0 ± 2.1**
D
5 ms
1 nA
I
E
τ_{fast} (ms)
τ_{slow} (ms)
J

Figure 5.3 CDI reduction due to A760G mutation under $Ca_V1.3$ long variant. (**A**) Exemplar Ca^{2+} (red) and Ba^{2+} (black) current traces through the alternate splice variant $Ca_V1.3_{long}$ illustrating decreased CDI as compared to the short splice variant (Figure 5.1B). (**B**) Despite the reduction in magnitude, significant CDI is demonstrated by the difference in r_{300} for Ca^{2+} (red) and Ba^{2+} (black), plotted across multiple voltages. (f_{300} = 0.28 ± 0.04, n=3). (**C**) Voltage activation curve for Ba^{2+} current through WT $Ca_V1.3_{long}$ channels ($V_{1/2}$ = -1.0 ± 1.8 mV, n = 5). (**D**) Exemplar Ba^{2+} tail currents obtained from a transition from 80 mV to -40 mV (black) and -60 mV (green). Traces are normalized to one another such that the scale bars correspond to the traces of the same color. (**E**) Population data of the fast (top) and slow (bottom) deactivation time constants (τ) plotted as a function of voltage. Error bars indicate ± SEM, n=5. (**F**) Exemplar current traces through A760G $Ca_V1.3_{long}$ channels depicting diminished CDI as compared to WT channels. (**G**) Population data for r_{300} (red = Ca^{2+}, black = Ba^{2+}) plotted across multiple voltages (f_{300} = 0.10 ± 0.03; n=4, * $p < 0.05$). (**H**) The activation curve of A760G $Ca_V1.3_{long}$ channels (black, $V_{1/2}$ = -12.0 ± 2.1 mV, n = 4) shows an 11-mV hyperpolarizing shift (** $p < 0.01$) compared to WT (reproduced in gray for reference). (**I**) Exemplar Ba^{2+} tail currents for the A760G $Ca_V1.3_{long}$ channel, obtained from a transition from 80 mV to -40 mV (black) and -60 mV (green). Traces are normalized to one another such that the scale bars correspond to the traces of the same color. (**J**) Population data of the fast (top) and slow (bottom) deactivation time constants (τ) plotted as a function of voltage for the A760G $Ca_V1.3_{long}$ channel. Deactivation is significantly slowed as compared to WT reproduced as the gray dashed line (* $p < 0.05$, ** $p < 0.01$). Error bars indicate ± SEM, n=4.

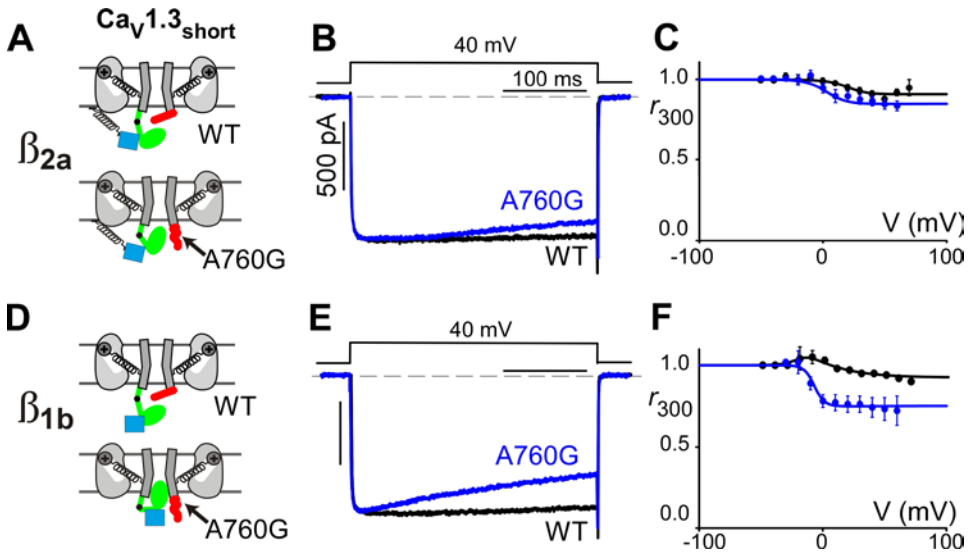

Figure 5.4 A760G increases VDI. (**A**) Cartoon depicting a β_{2a} subunit (blue) interacting with the VDI hinged lid (green) of a $Ca_V1.3_{short}$ channel. With palmitoylation, the β_{2a} subunit is anchored to the plasma membrane (black coil) restricting the movement of the channel hinged lid. $Ca_V1.3_{short}$ channels also possess a 'VDI shield' (red). The A760G mutation disrupts this shield (bottom). (**B**) Exemplar Ba^{2+} current through WT (black) and A760G (blue) $Ca_V1.3_{short}$ channels shows re-emergence of VDI even in the presence of β_{2a}. (**C**) Population data displaying Ba^{2+} r_{300} values as a function of voltage for WT (black) and A760G (blue). At 10 mV, WT: r_{300} =0.98 ±0.01; n=10; A760G: r_{300} = 0.89 ±0.03, n=6. VDI is significantly increased in A760G channels ($p < 0.01$). (**D**) Cartoon depicting a β_{1b} subunit (blue) interacting with the hinged lid (green) of a $Ca_V1.3$ channel. Note the absence of palmitoylation of this β subunit which allows the VDI hinged lid to move freely. (**E**) Exemplar Ba^{2+} current trace through WT (black) and A760G (blue) $Ca_V1.3_{short}$ channels in the presence of β_{1b}. Note the absence of VDI in WT channels despite the lack of β subunit palmitoylation due to the presence of a VDI shield. A760G causes a pronounced re-emergence of VDI under these conditions. (**F**) The increase in VDI is confirmed in population data where Ba^{2+} r_{300} values for WT (black) and A760G (blue) are plotted as a function of voltage. At 10 mV, WT: r_{300} = 0.98 ±0.01, n=3; A760G: r_{300} = 0.77 ±0.05, n=4. VDI is significantly increased for A760G channels ($p < 0.01$).

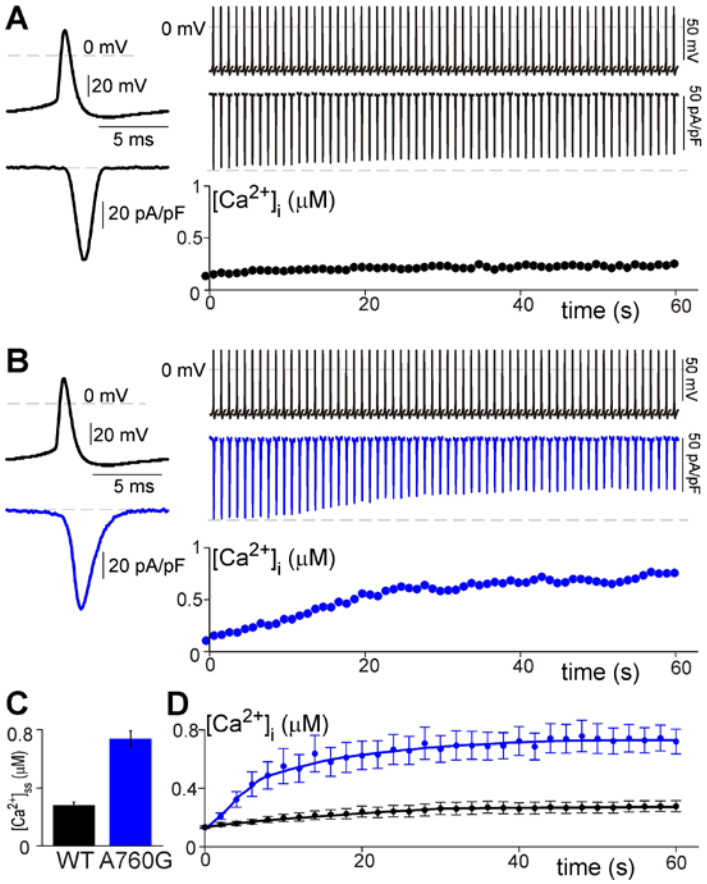

Figure 5.5 Effects of A760G on cytosolic Ca^{2+}. (**A**) Exemplar Ca^{2+} currents in response to a 1-Hz train of neuronal action potentials delivered to HEK293 cells expressing WT $Ca_V1.3_{short}$ channels. On the left, a single action potential and corresponding Ca^{2+} current is displayed on an expanded time course for resolution. Each action potential (top) and corresponding current response (middle) is magnified for display purposes and represents a 23 ms interval. The peak of each action potential is aligned with the time course displayed on the bottom panel. Note the gradual decrease in peak current as the level of cytosolic Ca^{2+} (bottom right panel) rises. (**B**) Exemplar Ca^{2+} currents in response to a 1-Hz train of neuronal action potentials delivered to HEK293 cells expressing A760G $Ca_V1.3_{short}$ channels. On the left, a magnified view demonstrates an increased duration of Ca^{2+} entry (blue) during a single action potential as compared to WT (A). At a comparable current density, A760G causes considerably more cytosolic Ca^{2+} accumulation (bottom right panel) as compared to WT channels. This increased cytosolic Ca^{2+} persists despite causing an enhancement of CDI (middle right panel). (**C**) Steady state level of intracellular Ca^{2+} in response to a 1-Hz train of action potentials. $[Ca^{2+}]_{ss}$ is measured after 60 s of stimulation. A760G $Ca_V1.3$ channels display significantly higher levels of $[Ca^{2+}]_{ss}$ than WT channels (WT: 0.28 ± 0.05, n=7; A760G: 0.73 ± 0.13, n=8; $p < 0.01$). (**D**) Average $[Ca^{2+}]_i$ as a function of time as HEK293 cells expressing WT or A760G $Ca_V1.3_{short}$ channels are stimulated by a train of 1-Hz action potential. Error bars indicate ± SEM, n=7, 8 for WT and A760G respectively.

5.6 Supplementary materials

5.6.1 The residual inactivation of A760G $Ca_V1.3$ remains Ca^{2+}/CaM dependent

CDI of Ca_V channels is known to be orchestrated by the Ca^{2+} sensor molecule calmodulin (CaM) (Halling et al., 2006; Christel and Lee, 2012; Ben-Johny and Yue, 2014). To ensure that the residual inactivation of Ca^{2+} current observed in $Ca_V1.3$ channels harboring the A760G mutation remains entirely dependent on Ca^{2+}/CaM, we co-expressed the mutant channel with a dominant negative mutant CaM (CaM_{1234}) (Xia et al., 1998), incapable of binding Ca^{2+}. The A760G $Ca_V1.3_{short}$ channels displayed no CDI (Supplementary Figure 5.1), confirming that the A760G mutation did not alter the mechanism underlying CDI of these channels. Gratifyingly, this Ca^{2+}/CaM dependence is identical to that seen in WT $Ca_V1.3$ channels co-expressing with CaM_{1234} (Yang et al., 2006).

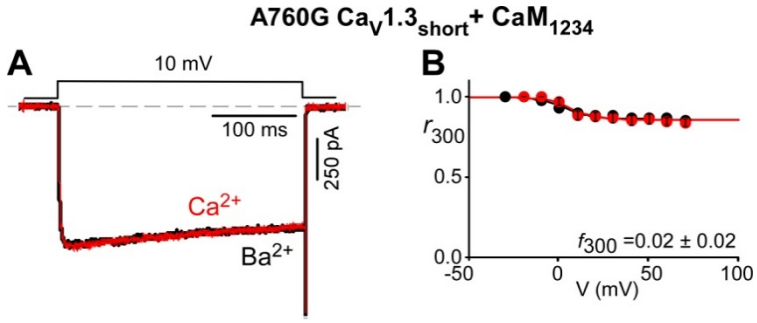

Supplementary Figure 5.1 Elimination of CDI of A760G $Ca_V1.3$ upon co-expression of CaM_{1234}. (**A**) Exemplar Ca^{2+} (red) and Ba^{2+} (black) currents from $Ca_V1.3_{short}$ channels harboring the A760G mutation with CaM_{1234} overexpressed. Scale bar corresponds to Ca^{2+} trace. Ba^{2+} trace is normalized to Ca^{2+} for comparison. (**B**) Population data of Ca^{2+} (red) and Ba^{2+} (black) current remaining after 300 ms (r_{300}). Error bars indicate ± SEM.

5.6.2 A760G decreases CDI_{max} of $Ca_V1.3$ at multiple voltages

In the main text, we illustrate a reduction in CDI_{max} at a 10-mV test potential (main text Figure 5.2). To account for the shift in channel activation produced by the A760G mutation, we also quantified CDI_{max} of both WT and A760G $Ca_V1.3_{short}$ at 0-mV and 20-mV test potentials (Supplementary Figure 5.2). CDI_{max} of the WT channels is significantly higher than that of the A760G channels at each voltage tested, confirming a reduction of CDI_{max} in A760G channels across voltages.

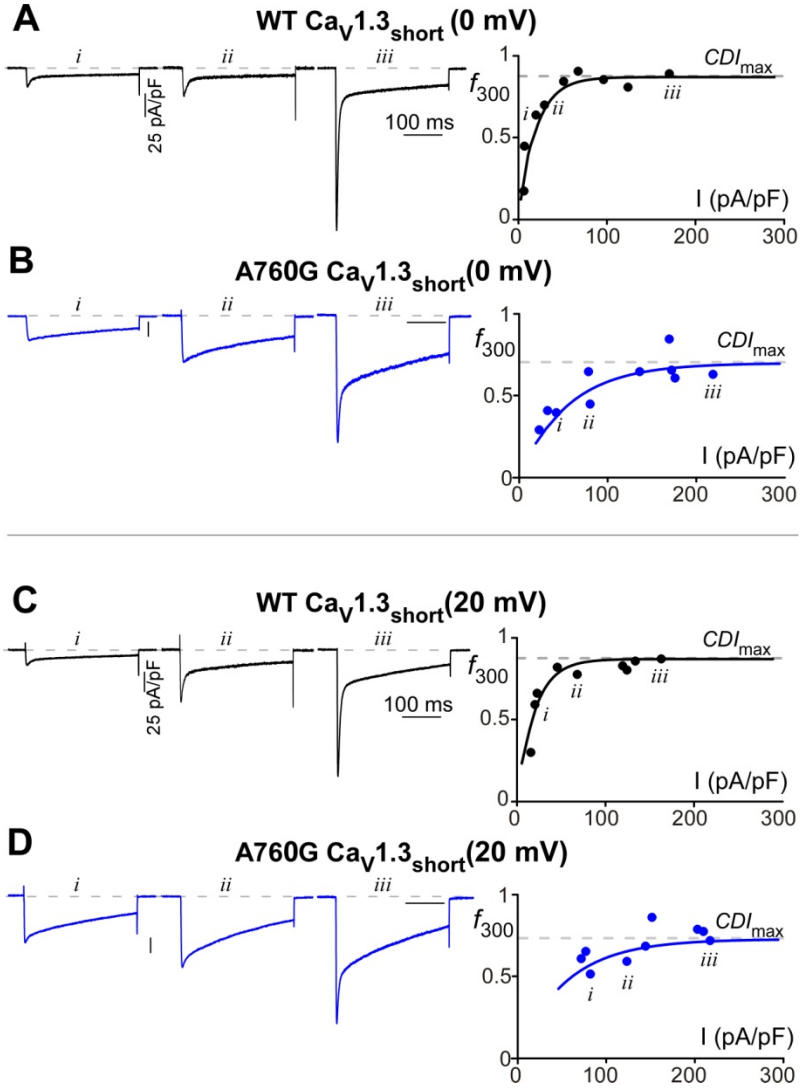

Supplementary Figure 5.2 Reduction of CDI_{max} at various voltages. (**A**) Ca^{2+} currents of WT $Ca_V1.3_{short}$ obtained under low Ca^{2+} buffering (0.5 mM EGTA) evoked by a 0-mV test potential. The extent of CDI increases as a function of current density and reaches a maximal value of ~ 0.9. (**B**) Ca^{2+} traces from A760G $Ca_V1.3_{short}$ obtained in a similar manner as 2A. The extent of CDI increases as the current density increases and reaches a CDI_{max} of ~ 0.7, significantly lower than that of the WT channel. (**C-D**) Ca^{2+} currents through WT and A760G $Ca_V1.3_{short}$ channels evoked by a 20-mV test potential under 0.5-mM EGTA buffering. At this test potential, CDI_{max} of the WT channels (~ 0.9) remains consistently higher than that of the A760G channels (~ 0.75).

CHAPTER 6

Conservation of cardiac L-type calcium channels and their regulation in *Drosophila*

6.1 Introduction

Cardiac action potentials, which drive rhythmic contractions of the heart, are the result of well-choreographed opening and closing of multiple ion channels. Among these is the LTCCs which not only permit Ca^{2+} entry to initiate myocyte shortening, but also set the length of the plateau phase of the cardiac action potential and, thereby, determine its duration (Nerbonne and Kass, 2005). Disruption of this critical channel or its precise regulations underlies numerous pathologies. For example, mutations in $Ca_V1.2$, a major type of LTCC in cardiac muscle, lead to Timothy syndrome, a multi-system disorder featuring autism, polydactyly, and long-QT syndrome, associated with cardiac arrhythmia (Splawski et al., 2004; Splawski et al., 2005; Barrett and Tsien, 2008; Dick et al., 2016), while mutations in $Ca_V1.3$, an LTCC in nodal cells, lead to bradycardia and congenital deafness (Platzer et al., 2000; Baig et al., 2011). Additionally, changes in channel density and function are associated with atrial fibrillation (Yue et al., 1997; Van Wagoner et al., 1999) and heart failure (Balke and Shorofsky, 1998; Hasenfuss, 1998; Mukherjee and Spinale, 1998; Richard et al., 1998; Schroder et al., 1998; He et al., 2001).

Mechanistic dissection of alterations in LTCC regulation is typically conducted using recombinant channels expressed in a heterologous system. Unfortunately, these systems often lack key auxiliary elements that are readily available in the context of cardiac myocytes. Studying Ca^{2+}channel regulation in native mammalian myocytes is, however, challenging due to cellular complexity, including redundancy among genes, and the difficulty of endogenously

manipulating the channels, raising the need for an intermediate system that is both genetically pliable and is reflective of a cardiac muscle cell.

Cardiomyocytes from *Drosophila melanogaster*, the fruit fly, offer an attractive, though as-yet-incompletely explored alternative. *Drosophila* benefit from a completely sequenced genome, conservation of disease orthologs (Chorna and Hasan; Rubin et al., 2000; Reiter et al., 2001; Bier, 2005; Chintapalli et al., 2007; Pandey and Nichols, 2011), and a host of readily available genetic tools (Wolf and Rockman; Adams and Sekelsky, 2002; St Johnston, 2002; Chintapalli et al., 2007; Pfeiffer et al., 2010; Pandey and Nichols, 2011). For example, the bipartite Gal4-UAS expression system (Brand and Perrimon, 1993; Elliott and Brand, 2008) permits straightforward control of gene expression across space (Lo and Frasch, 2001; Lai and Lee, 2006; Luan et al., 2006; Monnier et al., 2012) (by means of tissue-specific promoters) and time (via drug- or temperature-inducible expression (Roman et al., 2001; Kim and Wolf, 2009)). This system readily supports investigation of gain- or loss-of-function genes of interest, owing to large resources and libraries that include thousands of independent GAL4 and UAS *Drosophila* lines that permit selective transgene overexpression or RNAi (interfering RNA)-mediated gene silencing (Dietzl et al., 2007; Haley et al., 2008; Neely et al., 2010). Importantly, mutant genes can easily be studied in the same genetic environment as their wild-type counterparts, thus minimizing confounding effects, such as those that may result from insertion of transgenes in different locations throughout the genome (Rong and Golic, 2000)' (Rong and Golic, 2001). Many *Drosophila* proteins are encoded by a single gene that generates multiple distinct isoforms through alternative splicing of the primary transcript, simplifying knockout (Wolf and Rockman) and/or gene suppression experiments. Flies can also tolerate severe manipulation of heart components because oxygen transport occurs through trachea that invaginate from the cuticle

into the interior of the flies (Demerec, 1994). The effects of potentially lethal cardiac mutations can therefore be studied *in vivo* without necessarily initiating death. Furthermore, recent development of techniques to image (Wolf et al., 2006; Wu and Sato, 2008; Cooper et al., 2009; Vogler and Ocorr, 2009; Cammarato et al., 2015; Men et al., 2016) and record electrical field potentials (Papaefthmiou and Theophilidis, 2001; Cooper et al., 2009) of both larval (Wu and Sato, 2008; Cooper et al., 2009; Vogler and Ocorr, 2009; Men et al., 2016) and adult (Papaefthmiou and Theophilidis, 2001; Wolf et al., 2006; Vogler and Ocorr, 2009; Cammarato et al., 2015; Men et al., 2016) hearts readily allows functional assessment of different developmental stages of *Drosophila* myocardium after manipulation of genes of interest. Finally, flies are economical and easy to breed, generate numerous offspring, and feature a short lifecycle, making large-scale genetic and small-compound screens, in wild-type and disease models, eminently feasible.

Drosophila have an open circulatory system with a dorsal vessel or "cardiac tube" (Figure 6.1A), which in many ways functionally and developmentally resembles the embryonic vertebrate heart (Wolf and Rockman; Bodmer, 1995; Tao and Schulz, 2007; Wu and Sato, 2008). The tube is composed of a single layer of two opposing rows of cardiac myocytes (Miller, 1950; Wu and Sato, 2008) whose action potential, as found in higher organisms, is myogenic in origin, i.e. action potentials originate from muscle itself as opposed to in response to neuronal impulses (neurogenic origin) (Dowse et al., 1995; Gu and Singh, 1995; Johnson et al., 2000). The activity of these myocytes is modulated by a neurohormonal system that features the adrenaline analog octopamine (Johnson et al., 2002). Action potentials of *Drosophila* heart tubes have been coarsely measured (Papaefthmiou and Theophilidis, 2001; Ocorr et al., 2007a; Cooper et al., 2009; Ocorr et al., 2017), and the voltage waveforms appear comparable in duration and

amplitude to those recorded in vertebrate ventricular myocytes. As LTCCs play a major role in shaping vertebrate cardiac action potentials, it is plausible that a *Drosophila* analog is playing a similar role in the heart tube. Like vertebrates, flies express hetero-oligomeric voltage gated Ca^{2+} channels (Ca_V) composed of α_1, β, $\alpha_2\delta$, and, in some tissues, Υ subunits (Chorna and Hasan; Hofmann et al., 1994; Isom et al., 1994). Three distinct genes, *Ca-α1D* (*CG4894*), *cacophony* (*CG43368*), and *Ca-α1T* (*CG15899*) encode the α_1 subunits A1D, cac, and T-type, which specify three oligomeric voltage gated Ca^{2+} channels that correspond to Ca_V1, Ca_V2, and Ca_V3, the main Ca^{2+} channel families in vertebrates (Supplementary Table 6.1). *Drosophila* A1D is similar to the dihydropyridine-sensitive (L-type) channels of vertebrates; cac to N-, P/Q-, R-type channels; and T-type to Ca_V3 channels (Chorna and Hasan). RNA microarray data demonstrate enrichment of *A1D* in the hearts of adult fruit flies compared to the whole body, hinting at the potential presence of A1D in *Drosophila* cardiac tubes (Chintapalli et al., 2007; Robinson et al., 2013). Still, the complete molecular biosignature of heart-tube Ca^{2+} channels in *Drosophila* is unknown.

Here, we have elucidated the identity of the Ca^{2+} channels in the *Drosophila* heart. Direct visualization and quantitation of mRNA revealed an abundance of *Ca-α1D* and *Ca-α1T* and a paucity of *cacophony* Ca^{2+} channel messages in the heart tubes. Suppression of *Ca-α1D* effectively eliminated contraction and Ca^{2+} cycling activity, while knocking down other channels yielded minimal disruption of contraction and Ca^{2+} activity. Although these two lines of evidence suggested the presence of A1D and T-type channels, definitive validation required direct measurement of Ca^{2+} current across the sarcolemma of *Drosophila* cardiomyocytes. To this end, we devised a method for isolating viable single cardiomyocytes from adult *Drosophila* heart tubes. These myocytes enabled whole-cell patch clamp recordings of Ca^{2+} currents. Utilizing pharmacological agents and existing *Drosophila* lines with hypomorphic channels, we

verified the presence of both A1D and T-type Ca^{2+} currents in fly cardiomyocytes with A1D being the major contributor of the Ca^{2+} influx for contraction. Similar to mammalian LTCCs, *Drosophila* A1D also possesses CDI, a critical feedback regulation of the channel, and Ca^{2+} current augmentation through adrenergic stimulation. Overall, we established the identity of Ca^{2+} channels in the adult *Drosophila* heart and devised a novel technique for isolating single cardiomyocytes, which highlights the fly as a feasible alternative for studying diseases involving misregulation of cardiac LTCCs.

6.2 Materials and methods

6.2.1 Drosophila strains and maintenance

TinCΔ4-Gal4 (Lo and Frasch, 2001), *TinCΔ4-Gal4;UAS-GCaMP3* (a generous gift from Dr. Rolf Bodmer), and $Hand^{4.2}$*-GS-Gal4* (Monnier et al., 2012) *Drosophila* were employed to drive *UAS-transgene* expression in a cardiac-restricted fashion. *UAS-RNAi* stocks, obtained from the Vienna Drosophila Resource Center (VDRC), included $UAS\text{-}Ca\text{-}\alpha1D^{RNAi}$: 51491 (*RNAi Ca-α1D #1*), 52644 (*RNAi Ca-α1D* #2), $UAS\text{-}cacophony^{RNAi}$: 104168, and $UAS\text{-}Ca\text{-}\alpha1T^{RNAi}$: 108827. Background (control) RNAi strains included w^{1118} wild-type and KK injection lines. *GFP-Zasp52* (BDSC Stock no. 6838, which expresses a fluorescently labeled scaffold protein that binds α-actinin and localizes to muscle Z-discs), hypomorphic cacophony Cac^{S} (a generous gift from Dr. Chun-Fang Wu (Smith et al., 1996)), and T-type channel knock out (a generous gift from Dr. Carsten Duch (Ryglewski et al., 2012)) flies were used for electrophysiological studies. All *Drosophila* were maintained at room temperature (25 ˚C) on a standard cornmeal-yeast-sucrose-agar medium.

6.2.2 Fluorescence RNA in situ hybridization (FISH)

TinCΔ4-Gal4 virgin females were crossed with w^{1118} males. Five days post eclosion, the heart tubes of the progeny were surgically exposed under artificial hemolymph (Vogler and Ocorr, 2009) and the semi-intact preparations fixed as described above. Cardiac *in situ* hybridization was performed as reported previously (Viswanathan et al., 2016) using the QuantiGene® ViewRNA Cell Assay kit from Panomics (Affymetrix Inc.), following the manufacturer's recommendations. Fluorophore-tagged probes were custom designed to target *Drosophila* mRNA coding for *Ca-α1D* (VF1-18656, VF4-18190), *cacophony* (VF4-18657), and *Ca-α1T* (VF4-18658), and a house keeping gene glyceraldehyde 3-phosphate dehydrogenase (*GAPDH*, VF6-18191). The sequences chosen for probe design are present in all splice variants of each channel subunit to ensure complete coverage of mRNA molecules encoding each Ca^{2+} channel. A pre-designed probe targeting *human alpha feto-protein* (*h-AFP*, VA1-10125) was used as a negative control (Supplementary Figure 6.1).

Following RNA hybridization, heart tubes were mounted on coverslips in Prolong Gold Antifade mounting media with DAPI (Thermo Fisher Scientific, Catalog No. P36941) and imaged using a Leica TCS SPE confocal microscope (Leica Microsystems) at 40X magnification. Micrographs of heart tubes were analyzed with ImageJ software (National Institute of Health). To quantitate transcripts from the confocal micrographs, individual channels were separated following binary conversion of the images using the same intensity threshold for each channel across all samples. Regions of interest, which included only the cardiomyocytes, were outlined using the freehand selection tool. An automated ImageJ particle counting plugin was used to determine the number of mRNA particles. Particle numbers were normalized to total area and to GAPDH. mRNA quantitation was performed on 10-11 hearts and at least 20

cardiomyocytes from each animal. One-way ANOVA and one-way Student's t-test adjusted for non-uniform distribution were used to assess the statistical significance of mRNA abundance.

6.2.3 Cardiac functional analysis and Ca^{2+} transient imaging

Homozygous *TinCΔ4-Gal4;UAS-GCaMP3* or *Hand$^{4.2}$-GS-Gal4* virgin females were crossed with males carrying a *UAS-RNAi* cassette that targeted a specific Ca^{2+} channel. Two weeks post eclosion, the female progenies' hearts were surgically exposed and beating semi-intact heart tubes were recorded using a Hamamatsu Orca Flash 2.8 CMOS camera at ~120 frames per second on a Leica DM5000B TL microscope with a 10× (NA, 0.30) immersion lens. Cardiac performance was assessed from the videos using the Semi-automated Optical Heartbeat Analysis (SOHA) motion analysis program (Fink et al., 2009; Cammarato et al., 2015). M-modes, which provide an edge trace documenting heart wall movement over time, were generated via the program. Cardiac function metrics used in this study are similar to those described in Fink et al (2009). Heart rate variability, akin to the previously reported arrhythmicity index (Fink et al., 2009), is calculated as heart rate standard deviation divided by median heart rate. Significant differences in physiological variables were determined using one-way ANOVAs with Bonferroni post-hoc tests.

After filming, heart tubes were incubated with 5 μM CellTracker Orange CMTR dye (Thermo Fisher Scientific, Catalog No. C2927), a live cell labeling fluorescence dye, at room temperature for 30 minutes and rinsed with hemolymph thrice at room temperature for 10-15 minutes. Flies were then imaged using a dual-camera Andor Revolution X1 spinning disc confocal on an inverted microscope (Olympus, Inc) in both green (GCaMP3; ex/em. 488/525 nm) and red (CellTracker Orange CMTR dye; ex/em 561/617 nm) channels simultaneously.

Ca^{2+} transient analysis was performed using in-house Matlab (MathWorks, Inc.)-based algorithms. The green signal was normalized to the red signal and the fractional change of this ratio was used to gauge cardiomyocyte Ca^{2+} handling activity. A single exponential fit was performed on the decay phase of the Ca^{2+} transient to estimate the decay kinetics. One-way ANOVAs and unpaired Student's t-tests adjusted for non-uniform distribution were used to assess significant differences in Ca^{2+} dynamics between groups.

6.2.4 Isolation of live cardiomyocytes from Drosophila heart tubes

Heart tubes from 30-40 two-week old adult flies were surgically removed and placed into modified Ca^{2+}-free hemolymph. The heart-tube suspension was supplemented with collagenase type I to achieve a final concentration of 0.2% (weight/volume) and incubated at room temperature on a shaker for 20 minutes. Trypsin was added to the suspension to achieve a final concentration of 0.1% (weight/volume) and the suspension was further incubated for 10 minutes with gentle shaking at room temperature. The digesting tissue was gently triturated every 3 minutes after addition of trypsin. The reaction was quenched by adding fetal bovine serum at 2:1 ratio. The solution was centrifuged at 550 x g for 5 minutes. The supernatant was aspirated and the cell pellet resuspended in Ca^{2+}-free hemolymph. Cell suspensions were plated on glass coverslips 1 hour prior to electrophysiological studies to allow cardiomyocytes to attach to the coverslips.

6.2.5 Assessing Drosophila cardiomyocyte and sarcomeric dimensions

Heart tubes of *GFP-Zasp52 Drosophila* were surgically exposed and maintained in artificial hemolymph under low Ca^{2+} as previously described (Vogler and Ocorr, 2009). We evaluated the sarcomeric length in three configurations: (1) semi-intact hearts where heart tubes

were left attached to the cuticle; (2) detached whole hearts where heart tubes were extracted from the cuticle and suspended in hemolymph; and (3) single cardiomyocytes where heart tubes undergo enzymatic dissociation. For each configuration, tissues or cells were subjected to 3 conditions which include (1) low Ca^{2+} hemolymph; (2) 0.1 mM blebbistatin in DMSO; or (3) 0.1% volume/volume DMSO. Blebbistatin was used to prevent active myosin crossbridge cycling. Tissues or cells from these 9 conditions were then fixed in 4% formaldehyde in 1X PBS, washed, and mounted on coverslips in Prolong Gold Antifade mounting media with DAPI (Thermo Fisher Scientific, Catalog No. P36941). These specimens were imaged using a Leica TCS SPE confocal microscope (Leica Microsystems) at 63X magnification and sarcomere lengths were measure using ImageJ. We also measured cellular dimensions (length, width, area) in isolated cardiomyocytes under low-Ca^{2+} condition using ImageJ.

6.2.6 Electrophysiology

Whole-cell recordings of individual cardiomyocytes were performed at room temperature using an Axopatch 200B amplifier (Axon Instruments). Internal solutions contained (in mM): $CsMeSO_3$, 114; CsCl, 5; $MgCl_2$, 1; MgATP, 4; HEPES (pH 7.3), 10; and BAPTA, 10; at 295 mOsm adjusted with $CsMeSO_3$. Seals were formed in hemolymph solution and following patch rupture, the bath solution was switched to Ca^{2+}- or Ba^{2+}- external solution containing (in mM): TEA-$MeSO_3$, 140; HEPES (pH 7.4), 10; and $CaCl_2$ or $BaCl_2$, 5; at 300 mOsm, adjusted with TEA-$MeSO_3$. Traces were lowpass filtered at 2 kHz, and digitally sampled at 10 kHz. A P/8 leak subtraction protocol, where a leak pulse is 1/8 of the test pulse, was used with series resistances of 1-2 MΩ. 10 μM nifedipine (Sigma-Aldrich, N7634) or 10 μM forskolin (Sigma-Aldrich, F6886) was applied to the bath solution in some experiments to assess the pharmacological specificity of the observed Ca^{2+} currents. Statistical significance of current density among three

Drosophila lines at each test potential was assessed by one-way ANOVA and one-way Student's t-test adjusted for non-uniform distribution.

6.2.7 Ca^{2+} channel sequence alignment

Amino acid sequences of CACNA1C from *Oryctolagus* (Gene ID: 100101555; mRNA ID: NM_001136522) and A1D from *Drosophila* (Gene ID: 34950 or *CG4894*; mRNA ID: NM_165147) were aligned using Clustal Omega(McWilliam et al., 2013) to assess sequence homology.

6.3 Results

6.3.1 Drosophila cardiomyocytes express genes that encode specific voltage-gated Ca^{2+} channels

The fly genome encodes three α_1-subunits (*Ca-α1D*, *cacophony*, and *Ca-α1T*) of Ca_V. These subunits define three distinct *Drosophila* hetero-oligomeric channels: A1D, cac, and T-type (Chorna and Hasan; Cooper et al., 2009; Iniguez et al., 2013; Breitenkamp et al., 2015) that are homologous to the major mammalian classes Ca_V1, Ca_V2, and Ca_V3, respectively. Fluorescence *in situ* RNA hybridization (FISH), which allows direct visualization and relative quantitation of individual mRNA molecules, was utilized to decipher the cardiomyocyte Ca_V biosignature in control *TinCΔ4-Gal4* x w^{1118} *Drosophila*. Semi-intact fly hearts, which remained suspended within the dissected abdominal segment, were fixed, permeabilized, and incubated with fluorescent probes that possessed base sequence complementarity to specific α_1-subunit mRNAs. On average, when normalized to *GAPDH* particles, *Drosophila* cardiomyocytes showed an abundance of *Ca-α1D* (0.51±0.03) and *Ca-α1T* (0.45±0.03) mRNA molecules relative to a limited number of *cacophony* (0.06±0.01) messages (Figures 6.1B-C). Thus, the fly

heart expresses significantly higher amounts of *A1D* and *T-type* vs. *cacophony* Ca^{2+} channel mRNA.

6.3.2 RNA interference reveals the predominant types of functioning Ca_V in Drosophila hearts

The prevalence of *Ca-α1D* and *Ca-α1T* Ca_V mRNA implies that A1D and T-type are the major channels that orchestrate cardiac contraction in *Drosophila*. To verify a direct role of A1D, T-type, and potentially of cacophony in cardiomyocyte Ca^{2+} signaling, functional consequences of heart-specific RNAi-mediated silencing of each gene were evaluated. Previous studies have shown that transmembrane Ca^{2+} and not Na^{+} current substantially contributes to *Drosophila* cardiac action potentials (Gielow et al., 1995; Johnson et al., 1998). Therefore, alteration in heart tube contraction after Ca_V α_1-subunit knockdown could hint at the predominant type(s) of Ca^{2+} channels operating in *Drosophila* cardiomyocytes. A cardiac-specific driver line, *TinCΔ4-Gal4; UAS-GCaMP3*, was crossed with multiple *UAS-RNAi* lines, yielding progenies with selective reduction of one of the three Ca^{2+} channels (Figure 6.2A). A highly significant reduction of *Ca-α1D*, *cacophony*, and *Ca-α1T* transcripts was verified using fluorescence *in situ* RNA hybridization (Supplemental Figure 6.3). Spontaneous, myogenic contractions and Ca^{2+} cycling properties in semi-intact heart tubes were assessed in two-week-old adult offspring.

TinCΔ4-Gal4; UAS-GCaMP3 > RNAi Ca-α1D #1 Drosophila exhibited minimal heart tube motion compared to the rhythmic contractions in *TinCΔ4-Gal4; UAS-GCaMP3 x* w^{1118} controls as demonstrated by M-mode recordings (Figure 6.2B). To account for potential confounding positional effects that may result from insertion of the RNAi cassette in discrete locations throughout the *Drosophila* genome, two different RNAi lines with the same genetic background as the controls were evaluated, and the effects of gene silencing on several cardiac

parameters were quantified. Compared to control, both *TinCΔ4-Gal4; UAS-GCaMP3 > RNAi Ca-α1D #1* and *> RNAi Ca-α1D #2* showed significantly decreased heart rates (0.35±0.16 and 0.36±0.10 vs. 1.24±0.10 beats/s in controls) and increased heart rate variabilities (0.45±0.12 and 0.22±0.06 vs. 0.10±0.02 in controls) (Figure 6.2C). Moreover, the extent of contraction was significantly diminished in the RNAi-expressing heart tubes as demonstrated by ~4 fold reduction in fractional shortening (0.08±0.01 and 0.05±0.01 vs. 0.42±0.01 in controls) and ~4.5 fold reduction in shortening velocities (52.9±17.7 and 69.3±18.7 vs. 872.7±21.3 μm/s in controls).

We next ascertained if Ca^{2+} signaling was altered following *Ca-α1D* knock down. GCaMP3-based green fluorescence, emitted from actively beating heart cells, was recorded simultaneously with orange fluorescence that originated from CellTracker, a fluorescent dye that was passively loaded into the cardiomyocytes to monitor cell movement. The relative change in ratio between the two signals was used to determine the Ca^{2+} cycling properties. The ratiometric approach helped correct for heart contraction motion artifacts and for different amounts of GCaMP3 expression or CellTracker loading within and among the samples. Following *Ca-α1D* knockdown, fluorescent signal analysis suggested a completely abolished Ca^{2+} transient (Figure 6.2D). Moreover, population data of cyclical fluorescent fluctuations confirm significant reductions of Ca^{2+} transient rates (*RNAi Ca-α1D* #1, #2 vs. control: 0.04±0.02, 0.03±0.02 vs. 1.32±0.08 Hz) and peak Ca^{2+} transient magnitudes (0.005±0.003, 0.001±0.001 vs. 0.182±0.017) upon suppression of *Ca-α1D* expression (Figure 6.2E) compared to control. This observation is consistent with the nearly complete cessation of contraction upon *Ca-α1D* knockdown described above.

These experimental results demonstrate the effects of constitutive *Ca-α1D* suppression, i.e. both during and after heart tube development. To assess functional changes in hearts with *Ca-α1D* knockdown post cardiogenesis, the same *UAS-RNAi* lines were crossed with the inducible, cardiac-specific driver *Hand*$^{4.2}$*-GS-Gal4* line. Expression of *Ca-α1D* RNAi in the offspring was activated from two days after eclosion by supplementing the food with RU486 and the heart tubes of two-week-old *Drosophila* were imaged. Reduced fractional shortening and shortening velocity were observed when *Ca-α1D* was knocked down post-developmentally, although to a lesser extent compared to flies with cardiac-restricted *Ca-α1D* knockdown throughout development (Supplementary Figure 6.2). Overall, these results suggest a key role of A1D Ca_V in cardiac function in flies, both during and post-development.

In addition to A1D, potential contributions from cac and, given its high expression levels, T-type Ca^{2+} channels in defining *Drosophila* cardiac contraction and Ca^{2+}-handling properties, were also explored. Individually suppressing expression of these channels in *TinCΔ4-Gal4; UAS-GCaMP3* > *RNAi cacophony* and > *RNAi Ca-α1T* did not significantly alter heart rates (*RNAi cacophony*, *RNAi Ca-α1T* vs. controls: 2.50±0.17, 1.70±0.14 vs. 1.95±0.19 beats/s), heart rate variabilities (0.16±0.02, 0.15±0.03 vs. 0.12±0.03), or shortening velocities (1056±79.3, 960±58.4 vs. 982.4±67.1 μm/s) (Figures 6.2B-C) compared to *TinCΔ4-Gal4; UAS-GCaMP3 x KK* controls. Although there was a statistically significant reduction of fractional shortening subsequent to *cacophony* or *Ca-α1T* channel knockdown (0.40±0.01 or 0.40±0.01 vs. 0.44±0.01 in controls), the extent of reduction is minimal compared to that following *Ca-α1D* knockdown. Similarly, *cacophony* or *Ca-α1T* channel knockdown did not yield statistically significant changes in Ca^{2+} transient rate (*RNAi cacophony*, *RNAi Ca-α1T* vs. control: 2.04±0.15, 1.32±0.11 vs. 1.66±0.10 Hz), Ca^{2+} transient magnitude (0.16±0.02, 0.15±0.02 vs. 0.17±0.02), time to peak

(165.0±10.8, 214.0±8.5 vs. 184.6±8.5 ms), or decay time constant (261.2±16.9, 332.6±18.6 vs. 303.3±16.6 ms) compared to controls (Figures 6.2E). Collectively, these data indicate that A1D plays a major role in defining the *Drosophila* cardiac Ca^{2+} transient with potentially minor contributions from cac and T-type Ca^{2+} channels.

6.3.3 Isolation and morphological characterization of Drosophila cardiomyocytes

So far, we have examined the sources of plasmalemmal Ca^{2+} flux in *Drosophila* cardiomyocytes using multiple indirect approaches. However, voltage clamping individual cells and directly measuring Ca^{2+} current across the membrane could ultimately confirm the major types of active Ca^{2+} channels functioning in *Drosophila* myocardium. Although isolated cardiomyocytes have been a mainstay for cellular electrophysiology in mammalian systems for decades, no published reports of analogous protocols for flies exist. Therefore, we devised a method for isolating viable single cells from *Drosophila* heart tubes, which consist of a single layer of bilateral rows of opposing cardiomyocytes (Supplementary Figure 6.4A). Following enzymatic dissociation of *GFP-Zasp52* hearts, individual cells, which maintain their curved shape (Figure 6.3A, Supplementary Figure 6.4B), were successfully obtained. Consistent with a gradual tapering of the heart's diameter along its length, the cardiomyocytes exhibited modest variability in dimensions, which on average were 51.3±2.7 μm in length, 32.2±1.0 μm in width, and 1561±115 μm^2 in maximally projected area. Sarcomere lengths were determined by measuring the distance between peak fluorescent signals emanating from the Z-disc-associated, GFP-tagged Zasp52. Interestingly, the average sarcomere length along myofibrils of myocytes isolated and maintained under low Ca^{2+} was significantly lower than that determined for semi-intact or detached whole hearts maintained under a similar condition (1.38±0.04 vs. 2.50±0.0.3 and 2.54±0.02 μm under low Ca^{2+} condition, respectively, $p < 0.001$, Table 6.1, Figure 6.3B). To

determine if the shortened sarcomeres resulted from excessive actomyosin associations activated upon myocyte dissociation, we compared the distance between the middle of consecutive Z-discs along myofibrils of semi-intact hearts, detached whole hearts, and single cells maintained in DMSO or in the presence of blebbistatin, a small-molecule inhibitor of several striated muscle myosins. The sarcomere lengths in the presence of blebbistatin for these three configurations (2.53±0.02, 2.53±0.02, and 1.46±0.04 μm, respectively, $p > 0.05$, Table 6.1, Figures 6.3B-C) were not significantly different from those determined under conditions of low Ca^{2+}, which suggests the shortened sarcomeres result from passive processes that accompany cellular separation. Despite reduced sarcomere lengths, the individual myocytes nonetheless remained viable, as demonstrated by rhythmic contractions and the presence of Ca^{2+} transients (Supplementary Figure 6.4C) for up to 2-3 hours in Ca^{2+}-containing artificial hemolymph at 25°C.

6.3.4 Voltage clamp experiments confirm A1D as a predominant mediator of Ca^{2+} current in Drosophila cardiomyocytes

Isolated *Drosophila* cardiomyocytes were voltage clamped at -80 mV (resting potential) and the Ca^{2+} current, induced by various depolarizing voltage steps, was measured. For example, the Ca^{2+} current evoked by a 0-mV step potential in control (*GFP-Zasp52*) cells was characterized by a rapid influx of Ca^{2+} ions, which slowly decayed over time (Figure 6.4A, black) and resembled the characteristic inactivating mammalian Ca_V1 Ca^{2+} current. Peak Ca^{2+} current density at various test potentials is shown in Figure 6.4B (black). To explore potential contributions of Ca^{2+} current from cac and T-type channels, peak Ca^{2+} current density was measured in cardiomyocytes isolated from hypomorphic cac and null T-type *Drosophila* lines. No significant differences in the peak current density between cardiomyocytes from the control

(Figure 6.4B, black) and hypomorphic cac hearts (Figure 6.4B, blue) across all test voltages were observed. For example, the current densities of cac hypomorphic vs. control cardiomyocytes at -30 mV and 0 mV were -9.3±1.7 vs. -11.0±2.6 pA/pF and -13.9±0.9 vs. -12.2±1.4 pA/pF, respectively. These results imply a negligible contribution of cac channels in establishing *Drosophila* myocardial Ca^{2+} currents. However, peak Ca^{2+} current density measured from T-type null cardiomyocytes was significantly reduced relative to control at the lower voltage range (defined here as $V < 0$ mV with the employed external and internal solutions), e.g. -3.2±0.5 pA/pF at -30 mV, while there was no significant difference in peak current density between T-type null and control cells at the higher voltage range (defined as $V > 0$ mV), e.g. -13.0±2.3 pA/pF at 0 mV. As both mammalian Ca_V3 and *Drosophila* T-type Ca^{2+} channels are activated mainly at low voltages (Hagiwara et al., 1988; Perez-Reyes et al., 1998; Perez-Reyes, 2003; Rossier, 2016), the current density profile from null T-type cells compared to the control suggests the presence of functional T-type Ca^{2+} channels in *Drosophila* heart tubes.

Finally, to unequivocally validate the necessity of A1D Ca_V in Ca^{2+} signaling in *Drosophila* cardiomyocytes, a dihydropyridine, nifedipine, a specific mammalian Ca_V1 and *Drosophila* A1D channel blocker, was added to the bathing solution of control cells. Application of 10 μM nifedipine significantly decreased the magnitude of Ca^{2+} current (Figure 6.4A, blue) as confirmed by population data of current reduction after application of nifedipine across multiple test potentials (Figure 6.4C). In sum, these results corroborate the fluorescence RNA *in situ* hybridization data (Figure 6.1), and suggest that both A1D and T-type Ca^{2+} channels are abundantly present and functionally active in *Drosophila* cardiomyocytes.

6.3.5 Properties of cardiac A1D channels in Drosophila

Multiple lines of evidence suggest A1D is a major contributor to transmembrane Ca^{2+} currents in fly cardiomyocytes. Because A1D is homologous to mammalian Ca_V1, it may possess similar properties to its mammalian counterpart including Ca^{2+}-dependent inactivation (CDI). CDI is a negative feedback mechanism and key feature of Ca_V1 channels ($Ca_V1.2$, $Ca_V1.3$, and $Ca_V1.4$) that helps regulate the level of intracellular Ca^{2+}. After entering through Ca_V channels, Ca^{2+} ions bind to calmodulin (CaM), a resident Ca^{2+} sensor molecule that is pre-bound to the C-terminus of the channel (Imredy and Yue, 1994; Zuhlke et al., 1999; Adams et al., 2014). This Ca^{2+}/CaM induces a conformational change, which decreases open probability of individual channels leading to a reduction of current amplitude at the whole cell level (Yue et al., 1990; Dick et al., 2008). In addition to CaM, other key components for orchestrating CDI include N-terminal spatial Ca^{2+} transforming element (NSCaTE) (Ben Johny et al., 2013; Taiakina et al., 2013; Rossier, 2016) (on the N-terminus of the channel), two EF hands (Hagiwara et al., 1988; Johnson et al., 2000; Perez-Reyes, 2003; Lalevee et al., 2006; Sanyal et al., 2006), an IQ domain (Dowse et al., 1995; Lalevee et al., 2006; Sanyal et al., 2006), and Ca^{2+}-free CaM (apoCaM) binding sites (on the C-terminus of the channels) (Imredy and Yue, 1994; Zuhlke et al., 1999) (Figure 6.5A). Since *Drosophila* A1D possesses domains homologous to all the aforementioned key CDI components, it also likely exhibits CDI. Ca^{2+} current recordings (Figure 6.5B, red) showed Ca^{2+} influx due to channel opening followed by a gradual decrease in the current size or channel inactivation (Figure 6.5B, red). CDI can be distinguished from voltage-dependent inactivation (VDI), another form of channel feedback regulation, by comparing Ca^{2+} vs. Ba^{2+} current (Figure 6.5B, black) passing through the same channel. Because Ba^{2+} is unable to

efficiently bind to CaM, Ba^{2+} current inactivation solely represents the degree of VDI. Thus, the true extent of CDI (Figure 6.5B, shaded pink) can be calculated as $f_{300} = (r_{300/Ba} - r_{300/Ca})/r_{300/Ba}$, where $r_{300/x}$ is the fraction of Ca^{2+} and Ba^{2+} currents remaining after 300 ms of channel opening. For example, at a 0 mV test potential the f_{300} = 0.35±0.14, which confirms that the *Drosophila* Ca^{2+} current demonstrates robust CDI.

Another key property of the mammalian cardiac Ca_V ($Ca_V1.2$) channel is current augmentation in response to adrenergic stimulation. During the fight-or-flight response, epinephrine binds to the β_1-adrenergic receptor, a type of G-protein-coupled receptor, and initiates a signaling cascade that results in protein kinase A (PKA)-mediated $Ca_V1.2$ phosphorylation. The phosphorylated channels demonstrate higher open probability, which leads to an increased whole cell Ca^{2+} current size. The larger Ca^{2+} influx augments the force of cardiac contraction that is necessary during the flight response. The adrenaline-like octopamine receptors (OctαRs, and OctβRs) (Evans and Maqueira, 2005), adenyl cyclase (*rutabaga*) (Pavot et al., 2015), phosphodiesterase (*dunce*) (Pavot et al., 2015), and both regulatory (Taylor et al., 1990) and catalytic (Kato et al., 1996) subunits of PKA are also expressed in *Drosophila*, suggesting that A1D may also exhibit PKA-mediated current augmentation. Application of 10 μM forskolin, an upstream activator of PKA (Figure 6.6A), increased the amplitude of Ca^{2+} currents through the A1D channels (Figure 6.6B). For example, at 0-mV test potential, peak Ca^{2+} currents were greatly amplified by 1.58±0.13-fold after forskolin application. Similar current augmentation by forskolin was observed across multiple voltages, confirming the presence of PKA-mediated current augmentation in A1D channels in *Drosophila* cardiomyocytes.

6.4 Discussion

Drosophila represents a potentially ideal platform for studying regulation of, and diseases involving, cardiac Ca^{2+} channel function and dysfunction. In addition to their genetic pliability, flies also possess a Ca^{2+} channel ensemble akin to that of mammalian cardiac cells. *Drosophila* cardiomyocytes, as shown here, harbor A1D and T-type Ca^{2+} channels (orthologs of mammalian Ca_V1 and Ca_V3 channels, respectively (Chorna and Hasan)), which is analogous to the Ca^{2+} channel composition of mammalian cardiomyocytes (Bean, 1985; Nilius et al., 1985; Bodi et al., 2005). Moreover, *Drosophila* A1D also possesses striking conservation of two key properties of Ca_V1 channels, which are CDI and PKA-dependent current augmentation.

In the current study, we show for the first time, that *Drosophila* cardiomyocytes express significantly higher amounts of *Ca-α1D* and *Ca-α1T* relative to *cacophony* mRNA. Functional analyses revealed significantly impaired heart tube contraction and decreased Ca^{2+} transient amplitude when *Ca-α1D* expression was suppressed by RNAi as opposed to a minimal change in contractile properties resulting from *Ca-α1T* or *cacophony* silencing. These results imply that not only is A1D highly enriched in *Drosophila* cardiomyocytes, but that A1D channels are the major contributor to Ca^{2+} flux responsible for contraction. However, despite an abundance of *Ca-α1T* mRNA, T-type channels were shown to contribute minimally to heart tube contraction. These results suggest that there is a potential discordance between *Ca-α1T* mRNA versus protein load, a high transcriptional reserve to ensure an adequate T-type channel stoichiometry, and/or poorly effective RNA interference and gene suppression. Direct assessment of plasmalemmal Ca^{2+} currents in cardiomyocytes that are genetically devoid of T-type channels could reveal insight into this discrepancy.

Although multiple reports previously described changes in contraction rates or chamber dimension of intact heart tubes during larval (Gu and Singh, 1995; Zornik et al., 1999; Cooper et al., 2009) and pupal (Johnson et al., 1998; Johnson et al., 2002) stages, at baseline or in response to pharmacological manipulation, the effort to directly probe plasmalemmal currents in adult *Drosophila* cardiomyocytes is still in its infancy. Field potentials across the surface of the heart tubes were recorded (Papaefthmiou and Theophilidis, 2001; Cooper et al., 2009) while a rudimentary current clamp recording performed by inserting electrodes into intact hearts successfully measured transmembrane voltages (Dulcis and Levine, 2005; Ocorr et al., 2007a; Ocorr et al., 2007b). However, the gold standard to directly probe plasmalemmal current is the voltage clamp technique, which yields high resolution data when performed on single cells as opposed to cellular networks. Voltage clamp experiments have been carried out on neurons of *Drosophila* embryos (Peng and Wu, 2007), pupae (Gu et al., 2009), and adult (Gu et al., 2009) brains, motoneurons of adult indirect flight muscle (Ryglewski et al., 2012), motoneurons of larval body-wall muscle (Worrell and Levine, 2008), larval retinal cells (Sullivan et al., 2000), and larval body wall muscles (Gielow et al., 1995; Ren et al., 1998; Bhattacharya et al., 1999). However, to date, no report describes voltage clamp recordings of adult *Drosophila* cardiomyocytes despite multiple well-established methods for isolation of mammalian cardiomyocytes in various species. Therefore, based on these approaches, we developed a method to enzymatically dissociate viable single cardiomyocytes from *Drosophila* heart tubes.

Following brief enzymatic digestion of adult *Drosophila* cardiac tubes, we obtained viable individual cardiomyocytes that appeared well suited for electrophysiological studies. As reported for vertebrate cardiomyocytes, which show a significant 17% reduction in sarcomere length upon isolation from the intact heart (Bub et al., 2010), fly sarcomeres likewise displayed

reduced lengths following cardiomyocyte dissociation. Comparing the sarcomere lengths from cells of semi-intact relative to those of detached heart tubes revealed that changes in sarcomere length did not transpire in response to heart removal from the abdominal segment. Moreover, incubating the hearts in artificial hemolymph blebbistatin, a myosin ATPas inhibitor, did not prevent sarcomere shortening upon cell-to-cell detachment. These findings suggest that the change in sarcomere length was not due excessive or unregulated Ca^{2+}-mediated tension or active actomyosin-based contraction in general. The heightened sarcomeric shortening event that occurs upon fly vs. rat cardiomyocyte isolation (i.e. ~40% vs. 17% reduction in sarcomere length) may be related to several factors. Firstly, the extreme geometric constraints that are imposed upon fly cardiomyocytes, due to two opposing cells establishing the tubular nature of the organ, are partially released following proteolytic digestion. Consequently, relatively large changes in *Drosophila* myofibril and sarcomere deformation are therefore expected to occur in conjunction with changes in cellular stress/strain upon isolation. Secondly, the Z-discs of *Drosophila* cardiomyocytes are discontinuous or "perforated", which allow muscles to contract to greater than 50% of their resting lengths (Vigoreaux, 1994), a significantly larger degree of sarcomere length changes relative to those of vertebrate cardiomyocytes.

Despite the exaggerated changes in sarcomere length that transpire upon dissociation, we show that *Drosophila* cardiomyocytes are exceptionally amenable to voltage clamp experiments. We confirmed the presence of Ca^{2+} currents through both A1D and T-type Ca^{2+} channels, which are remarkably similar to the those observed in mammalian cardiomyocytes (Bean, 1985; Nilius et al., 1985). In mammals, T-type or Ca_V3 are activated at lower potentials and open with a small conductance (Bean, 1985; Nilius et al., 1985), hence the namesake 'T' for tiny current. Cardiac LTCCs or $Ca_V1.2$, however, are activated at relatively higher potentials compared to Ca_V3 with

higher pore conductance (Bean, 1985; Nilius et al., 1985) ('L' for large current) and, thus, are better-suited to drive the shape and duration of the cardiac action potential (Nerbonne and Kass, 2005). As heart tube contraction is the end-point of a multi-step process, from pacemaker cells firing, action potential transmission to myocytes, and Ca^{2+}-centric conversion of electrical to mechanical activities, alteration in contractile properties could stem from modulations of any of these critical steps. T-type Ca^{2+} current was proposed to play a modulatory role in pacemaking, which is predominantly driven by a Na^{+}/Ca^{2+} exchanger-dependent Ca^{2+} clock (Maltsev et al., 2004; Maltsev and Lakatta, 2007). Therefore, consistent with our finding, suppression of *Ca-α1T* expression by RNAi minimally affects the contractile properties of the heart tubes. LTCCs, on the other hand, are responsible for transsarcolemmal Ca^{2+} flux that triggers the Ca^{2+}-induced Ca^{2+} release from the sarcoplasmic reticulum leading to cardiomyocyte contraction. Hence, it is not surprising that *Ca-α1D* knock down nearly abolishes the heart tube contraction (Figure 6.2). Most interestingly, *Drosophila* A1D also shares key modulatory elements with those of mammalian $Ca_V1.2$, which include CDI and PKA-mediated current augmentation. This conservation of channel modulations might hint at the evolutionary importance of this channel and thus their tightly controlled functions.

In summary, *Drosophila* proves to be an efficient platform to study regulation of and diseases involving cardiac Ca^{2+} channels. Due to its genetic versatility, readily available tools, and multiple modalities for functional assessment, screens to dissect physiological or pathological mechanisms can be readily conducted using this animal model.

6.5 Tables and figures

Table 6.1 Sarcomere lengths (µm) in all configurations and conditions.

mean±SE (n)	Low Ca^{2+}	Blebbistatin	DMSO
Semi-intact hearts	2.50±0.03 (30)	2.53±0.02 (30)	2.52±0.02 (30)
Detached hearts	2.54±0.02 (30)	2.53±0.02 (30)	2.55±0.02 (30)
Isolated cardiomyocytes	1.38±0.04 (31)	1.46±0.04 (22)	1.36±0.04 (25)

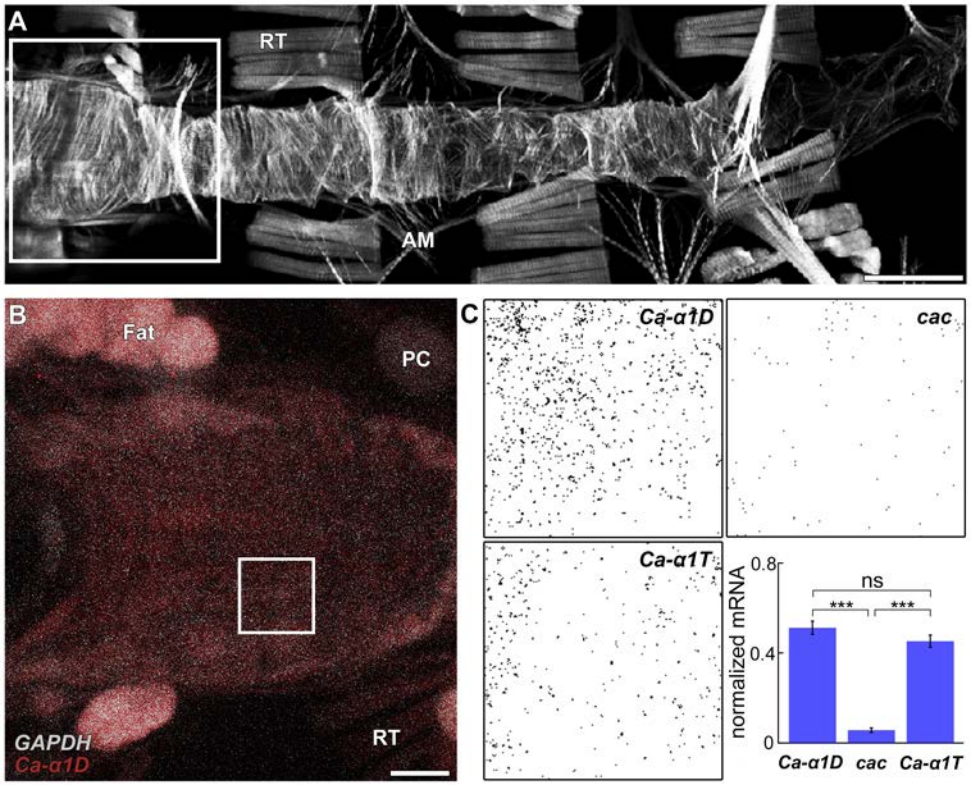

Figure 6.1 *Ca-α1D* and *Ca-α1T* transcripts are abundant in *Drosophila* heart tubes. (**A**) Confocal micrograph of a wild-type w^{1118} *Drosophila* heart tube extending along the dorsal side of the abdomen. The anterior conical chamber is outlined and displayed in **B**. Note the non-cardiac alary muscles (AM) attaching to the heart tube. RT, retractors of tergite muscles. Scale bar = 100 µm. (**B**) Micrograph of the conical chamber after *Ca-α1D* (red) and *GAPDH* (white) mRNA molecules were labeled by FISH. A representative small region of a single cardiomyocyte used for mRNA quantitation is outlined in grey. VM, ventral muscle; PC, pericardial cell. Scale bar = 25 µm. (**C**) Examples of Ca^{2+} channel mRNA particle densities in an area of interest (e.g. grey box in Figure 1B) and the quantitative determination of the number of Ca^{2+} channel messages normalized to the number of *GAPDH* messages within the same region of interest. There are significantly more *Ca-α1D* and *Ca-α1T* Ca^{2+} channel transcripts compared to *cacophony* transcripts. *** $p < 0.001$. (n = 11, 10, 11 for *Ca-α1D*, *cacophony*, and *Ca-α1T*).

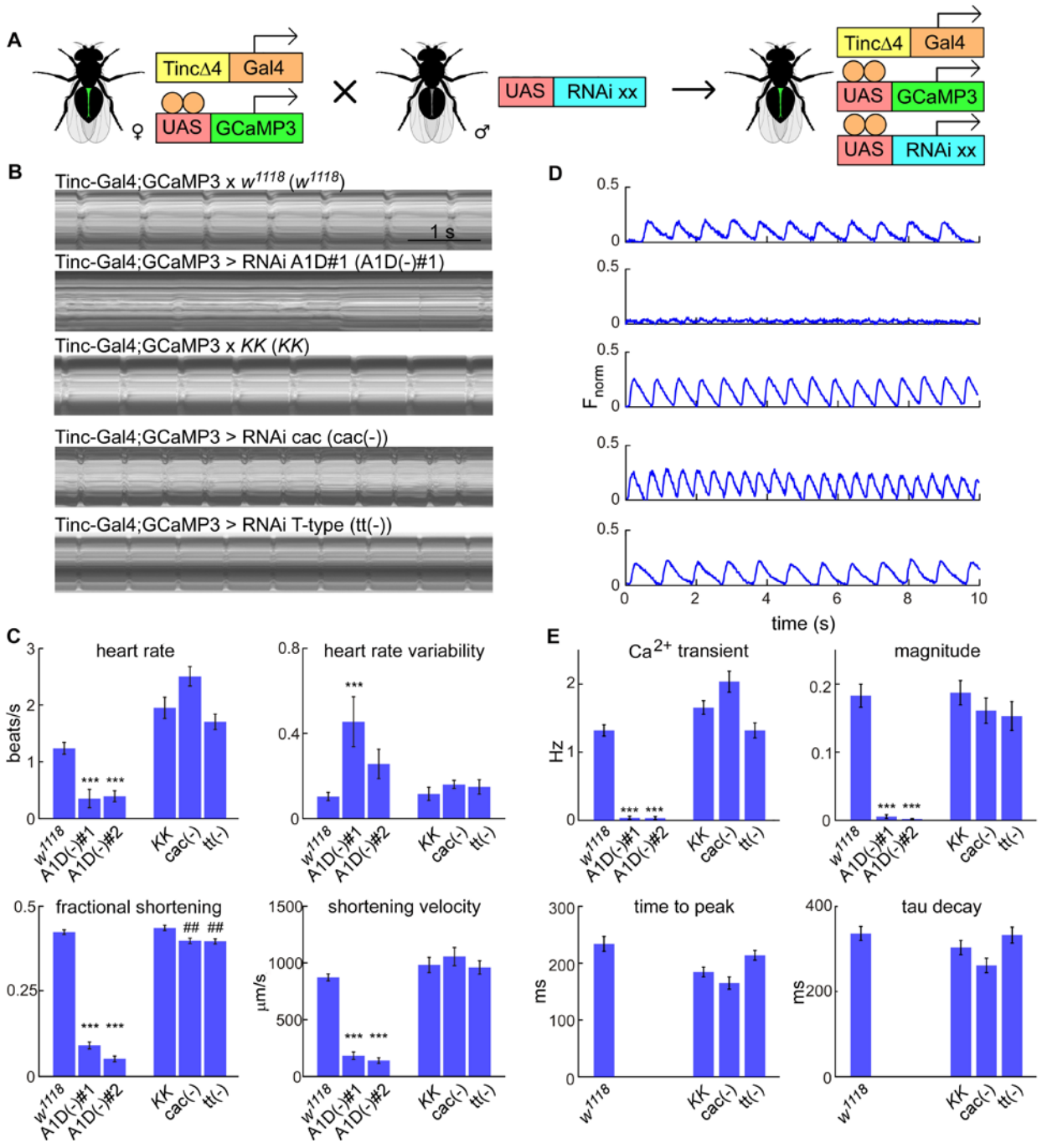

Figure 6.2 Cardiac contraction and Ca^{2+} transients are suppressed by *A1D* knockdown. (**A**) The *Drosophila* UAS-GAL4 bipartite expression system. Cardiac-specific TinCΔ4-Gal4 drives expression of *UAS-transgenes* including the simultaneous expression of a Ca^{2+} biosensor (*UAS-GCaMP3*) and *UAS-RNAi*. (**B**) Exemplar M-mode tracings of heart tubes with A1D, cacophony (cac), or T-type (tt) Ca^{2+} channels knocked down. w^{1118} and injection lines (*KK*) crossed with the driver line serve as controls. *A1D* knockdown completely suppresses contraction. (**C**) Quantitative measurements of cardiac physiological parameters. Population data confirm substantially altered contraction following *A1D* suppression. *** $p < 0.0001$ compared to w^{1118};

$p < 0.01$ compared to *KK*. There are no significant differences in cardiac variables between the controls. (n=31, 25, 30, 25, and 28, respectively) (**D**) Representative Ca^{2+} transient recordings from the same population of heart tubes examined in B-C. *Ca-α1D* knockdown completely suppressed Ca^{2+} transients in the heart tubes. (**E**) Measurements of Ca^{2+} transients confirm a significant reduction in Ca^{2+} transient frequency and magnitude of the peak Ca^{2+} transient upon *Ca-α1D* RNAi expression. The time required to reach the peak Ca^{2+} transient magnitude (time to peak) and the time constant for the Ca^{2+} transient decay (tau decay) are not shown for A1D(-)#1 and A1D(-)#2 because of inaccurate measurements due to minimal Ca^{2+} activity in these heart tubes. Suppression of *cacophony* or *Ca-α1T* produces no significant change in Ca^{2+} transient frequency, Ca^{2+} transient magnitude, time to peak, or tau decay. *** $p < 0.001$ compared to w^{1118}. (n=21-30).

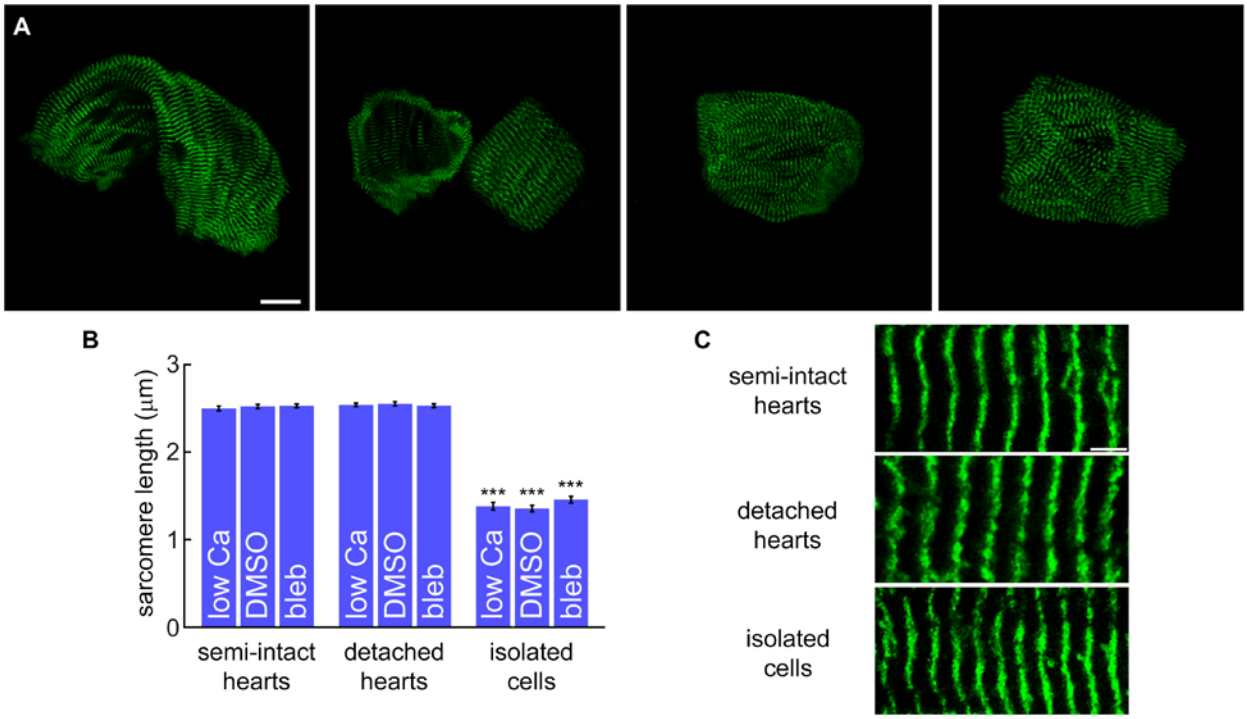

Figure 6.3 Isolated *Drosophila* cardiomyocytes and their sarcomere length. (**A**) Isolated cardiomyocytes from *GFP-Zasp52* heart tubes where z-lines are highlighted by GFP fluorescence proteins. Displayed in multiple orientations, all cells maintained the curved shape. Cells were suspended in low-Ca^{2+} hemolymph. Scale bar 20 µm. (**B**) Sarcomere length for the three configurations (semi-intact hearts, detached hearts, and isolated cells) under three conditions (low Ca^{2+}, DMSO, and 0.1 mM blebbistatin). Sarcomere length was significantly shorter in isolated cells compared to the semi-intact and detached hearts for all three conditions. (**C**) Magnified images of sarcomeres treated with 0.1 mM blebbistatin. Sarcomeres of the isolated cardiomyocytes are significantly shorter than those in semi-intact and detached heart tubes. Scale bar 2.5 µm

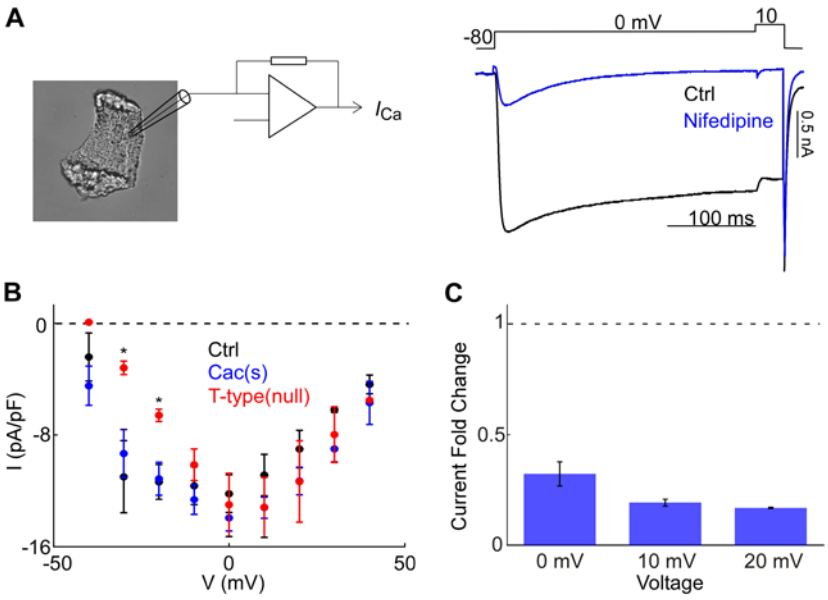

Figure 6.4 Ca^{2+} current recordings confirm A1D channels conduct the predominant transsarcolemmal Ca^{2+} current in *Drosophila* cardiomyocytes. (**A**) Ca^{2+} current recording of dissociated fly myocytes. The current in wildtype cardiomyocytes is suppressed by a dihydropyridine, nifedipine, a hallmark of Ca_V1 channels. (**B**) Mean peak current density in control, hypomorphic cacophony (*cac*(*s*)), and T-type null cardiomyocytes across test potentials. At high voltages, comparable to the plateau phase of mammalian cardiac action potentials, peak currents of cac(s) hypomorphic and T-type (null) cardiomyocytes are similar to that observed in control, indicating that A1D is the major high-voltage-activated Ca^{2+} channel isoform in the *Drosophila* heart. At low voltages, T-type (null) cardiomyocytes show reduced current densities, suggesting a contribution of T-type channels at low activation voltages. * $p < 0.5$ compared to control. (n=4, 6, and 4 for control, Cac (s), and T-type (null)). (**C**) Population data of the Ca^{2+} current response to 10 μM nifedipine as compared to untreated control myocytes. (n=5).

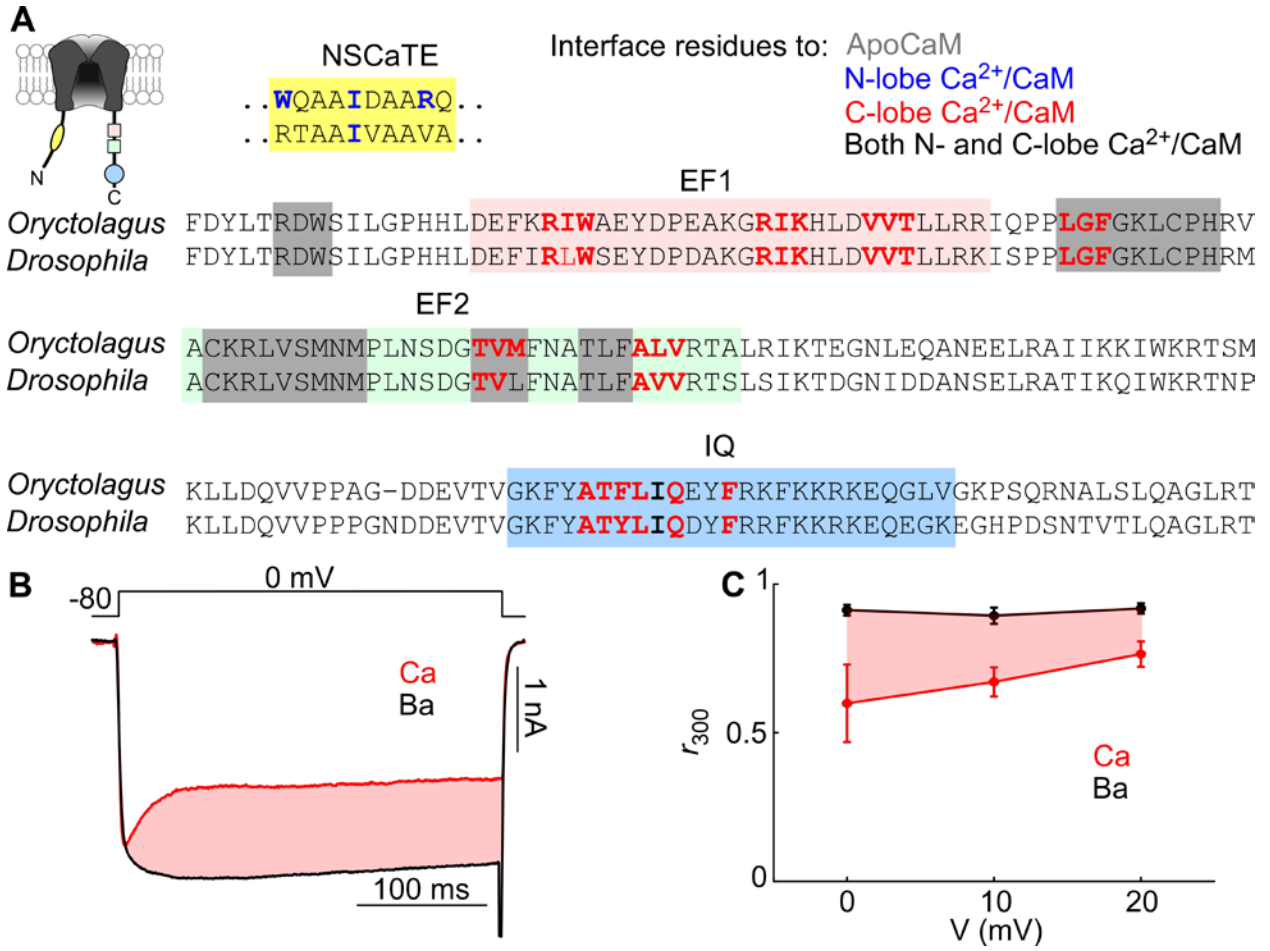

Figure 6.5 Ca^{2+}-independent inactivation is a conserved feature of *Drosophila* A1D. (**A**) Illustration of the alpha subunit of the vertebrate LTCC with CDI interface regions NSCaTE, two EF hands, and the IQ domain shown in yellow, rose, green, and blue respectively. Sequence comparison of *Oryctolagus*'s CACNA1C and *Drosophila*'s A1D with CDI interface regions highlighted in the same color as in the diagram on the left. The binding sites of Ca^{2+}-free CaM (apoCaM) are highlighted in grey with key amino acid residues interacting with N-, C-, and both lobes of apoCaM bolded in blue, red, and black. (**B**) Ca^{2+} currents in fly cardiomyocytes decay more rapidly than Ba^{2+} currents in the same cell, demonstrating CDI (shaded rose) as Ba^{2+} cannot effectively bind calmodulin. (**C**) Population data showing the fraction of current remaining after 300 ms of activation (r_{300}). The different degree of decay between Ca^{2+} and Ba^{2+} currents represents the extent of CDI (shaded rose). (n=7).

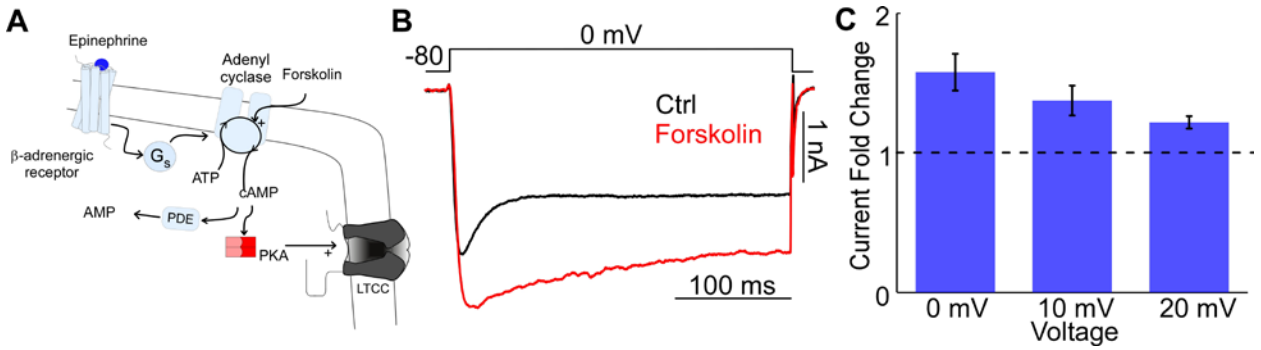

Figure 6.6 Ca^{2+} current augmentation by protein kinase A is conserved in *Drosophila* cardiomyocytes. (**A**) Depiction of the β-adrenergic pathway. Epinephrine binds to a G-protein coupled receptor and activates the enzyme adenyl cyclase receptor, which converts ATP to cyclic AMP (cAMP). This small signaling molecule activates protein kinase A (PKA), which phosphorylates LTCCs, augmenting their current size. Phosphodiesterase (PDE) deactivates cAMP. Forskolin bypasses this signaling cascade by directly activating adenyl cyclase. *Drosophila* homologs of β-adrenergic pathway elements are in parentheses. Oct, octopamine. (**B**) Ca^{2+} current in *Drosophila* cardiomyocytes increases in amplitude after application of 10 μM forskolin. (**C**) Population data confirm augmentation of *Drosophila* A1D current by PKA. (n=4).

6.6 Supplementary materials

6.6.1 Homo sapiens and Drosophila melanogaster Ca^{2+} channel classes

There are three major classes of voltage-gated Ca^{2+} channels in mammals, including *Homo sapiens*. Each class contains multiple channel subtypes with different biophysical properties, tuned to best serve their biological functions. While class III channels are found in various types of tissues, class I channels are commonly found in cardiovascular, muscular, and nervous systems and class II channels are mostly responsible for neuronal activities(Hofmann et al., 1994). Intriguingly, *Drosophila* also possess three major classes of voltage-gated Ca^{2+} channels although each contains only one subtype(Chorna and Hasan), reflecting the relative genetic simplicity of this animal model. Supplementary Table 6.1 summarizes *Drosophila* orthologs for each class of human voltage-gated Ca^{2+} channels.

	Homo sapiens	*Drosophila melanogaster*
Class I	$Ca_V1.1$, α_{1S} (CACNA1S)	A1D, α_{1D} (DmCa1D/CG4894)
	$Ca_V1.2$, α_{1C} (CACNA1C)	
	$Ca_V1.3$, α_{1D} (CACNA1D)	
	$Ca_V1.4$, α_{1F} (CACNA1F)	
Class II	$Ca_V2.1$, α_{1A} (CACNA1A)	cacophony (DmCa1A/CG43368)
	$Ca_V2.2$, α_{1B} (CACNA1B)	
	$Ca_V2.3$, α_{1E} (CACNA1E)	
Class III	$Ca_V3.1$, α_{1G} (CACNA1G)	Dmα1G, Dmα1T, T-type (DmαG/CG15899)
	$Ca_V3.2$, α_{1H} (CACNA1H)	
	$Ca_V3.3$, α_{1I} (CACNA1I)	

Supplementary Table 6.1 Major classes of voltage-gated Ca^{2+} channels in *Homo sapiens* and *Drosophila melanogaster*.

6.6.2 Negative controls for fluorescence RNA in situ hybridization in Drosophila cardiomyocytes

In order to ensure that the fluorescence signal from the complex between voltage-gated Ca^{2+} channel subunit mRNA molecules and custom designed probes was not the result of nonspecific artifacts, heart tubes were also incubated with a probe designed to target human alpha-fetoprotein (h-AFP), which is not found in *Drosophila*. This negative control probe was simultaneously mixed with probes targeting *Drosophila* Ca^{2+} channel subunits and the house-keeping gene GAPDH. Supplementary Figure 6.1 shows a lack of signal from the h-AFP probe and the presence of a GAPDH signal, which confirms the specificity of this fluorescence RNA *in situ* hybridization assay.

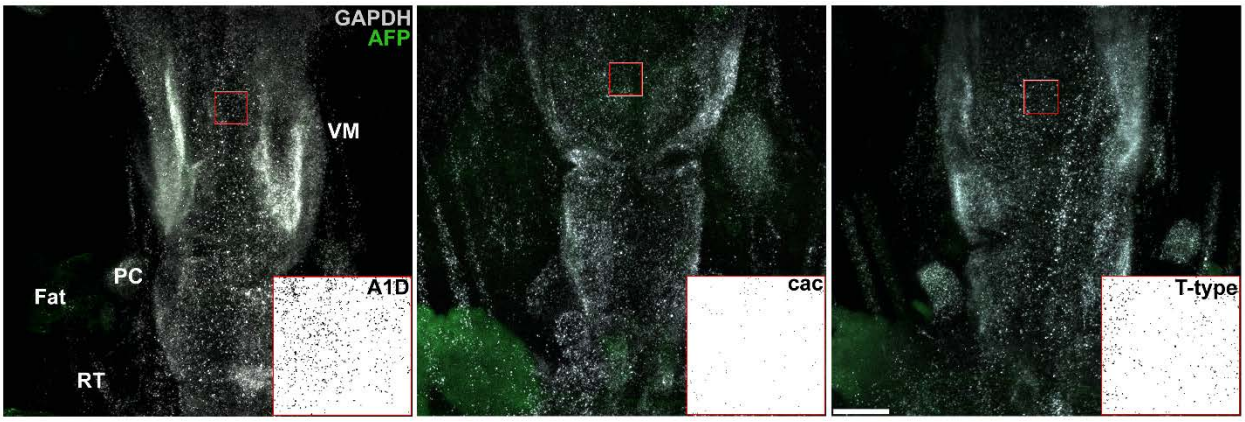

Supplementary Figure 6.1 Treatment of *Drosophila* heart tubes with probes targeting human AFP mRNA yields limited fluorescence signals. The same heart tube regions shown in Figures 6.1B-C are displayed above. Here, however, only the fluorescence channels for probes against h-AFP (green) and GAPDH (white) are presented. The insets reveal the presence of specific voltage-gated Ca^{2+} channel subunit mRNA molecules (from Figure 6.1C). VM, ventral longitudinal muscle layer; PC, pericardial cells; RT, retractors of tergite muscles. Scale bar = 25 µm.

6.6.3 Post-developmental suppression of A1D expression hampers Drosophila heart tube contraction

Ca-α1D silencing during and after heart tube development leads to cessation of myocardial contraction and the generation of Ca^{2+} transients (Figure 6.2) in adult flies. However, it is plausible that A1D only plays a role during development and is not the key driver of contraction in mature hearts and, therefore, phenotypes of cardiac tubes with suppression of *Ca-α1D* expression post developmentally must be explored. To this end, expression of A1D channels was suppressed by RNAi driven by a chemically inducible cardiac-specific promoter. Upon supplementing fly food with RU486 two days post-eclosion, and activation of RNAi expression, the heart tubes displayed significantly lower fractional shortening and shortening velocities (Supplementary Figure 6.2). The effect, however, was not as severe as that observed when the *A1D* expression was silenced throughout cardiogenesis and adulthood (Figure 6.2). Therefore, it is likely that A1D channels play a role in the developing heart tube and are also required for proper function of mature hearts.

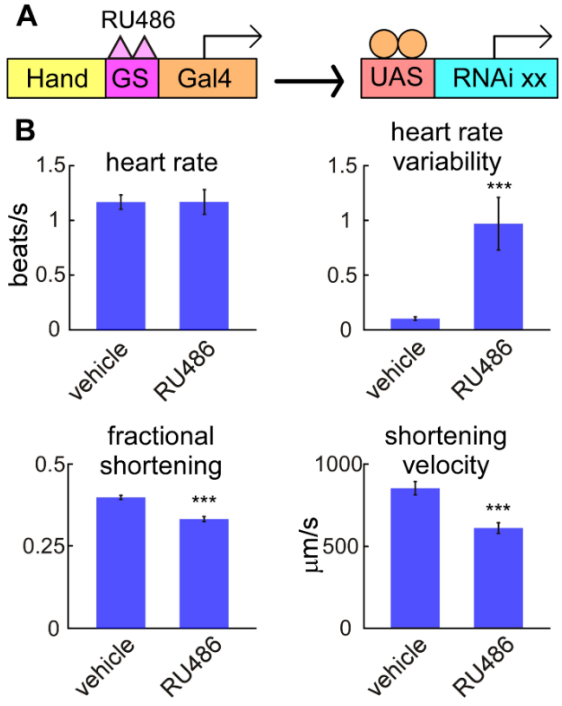

Supplementary Figure 6.2. Adult-specific, cardiac-restricted suppression of *A1D* expression. (**A**) The *Drosophila* Hand-GS-GAL4 inducible expression system. Cardiac-specific Hand-Gal4 drives expression of *UAS-RNAi* upon induction by RU486. (**B**) Inducible cardiac-specific knockdown of *A1D* post-developmentally engenders functional consequences similar those observed when *A1D* is silenced during and after heart development. *** $p <$ 0.001 compared to vehicle treatment. (n= 29 and 28, respectively).

6.6.4 Quantitation of Ca^{2+} channel transcripts in various experimental conditions

To ensure sufficient Ca^{2+} channel suppression by RNAi prior to functional assessment (Figure 6.2), the amount of channel transcripts in the female progenies' hearts was quantitated using the fluorescence RNA *in situ* hybridization (FISH) technique. More than half of the Ca^{2+} channel transcripts were knocked down by RNAi (Supplementary Figures 6.3A, B, D).

Moreover, the amount of *cacophony* and *Ca-α1T* transcripts in the hypomorph and null lines, respectively, was measured prior to the Ca^{2+} current measurement (Figure 6.4). In cac^{S} line, a missense mutation (Phe to Ile mutation) is introduced into the S6 segment of domain III which results in reduction of current density (Smith et al., 1996; Smith et al., 1998). This mutation renders decreased transcription of the *cacophony* gene (Supplementary Figures 6.3C). In *Ca-α1T null* line, the proximal 50 kbp of the *Ca-α1T* gene was deleted (Ryglewski et al., 2012). All of our designed FISH *Ca-α1T* mRNA probes lie in this 50-kbp deleted region.

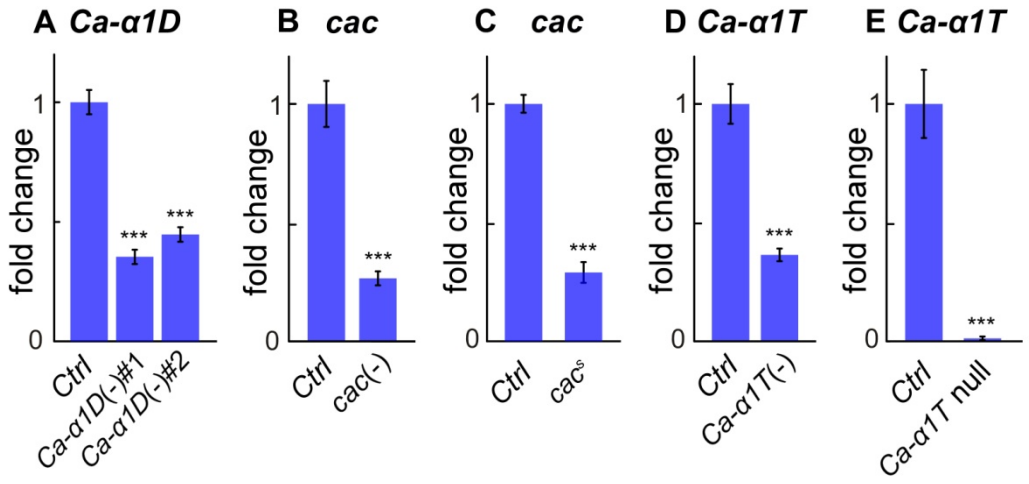

Supplementary Figure 6.3. Ca^{2+} channel transcripts in heart tubes in various experimental conditions. (**A**) Expression level of *Ca-α1D* transcripts in control and *Ca-α1D* RNAi-knockdown lines. *** $p < 0.001$, n = 9, 8, and 10 hearts for Ctrl, *Ca-α1D*(-)#1, and #2, respectively. (**B-C**) The amount of *cacophony* transcripts after RNAi knockdown (n = 9, 10) (B) and in the cac^{S}, a *cacophony* hypomorph line (n = 7, 7) (C). (**D-E**) The amount of *Ca-α1T* transcripts after RNAi knockdown (n = 10, 11) (D) and in the *Ca-α1T* null, a line with a complete knockout of the T-type Ca^{2+} channel (n = 6, 11) (E). Ctrl used for each condition is described in Supplementary Method.

6.6.5 Viable single cardiomyocytes after enzymatic dissociation from adult Drosophila heart tubes

As single cardiomyocytes are the mainstay of cellular electrophysiology, we devised a method to dissociate single cardiomyocytes from adult *Drosophila* hearts. Here, enzymatic digestion was utilized and the protocol was optimized to obtain the greatest number of single fly myocytes while maintaining their viability. The isolated cardiac cells continued to spontaneously contract regularly at room temperature as evident by the presence of fluorescently monitored Ca^{2+} transients (Supplementary Figure 6.4).

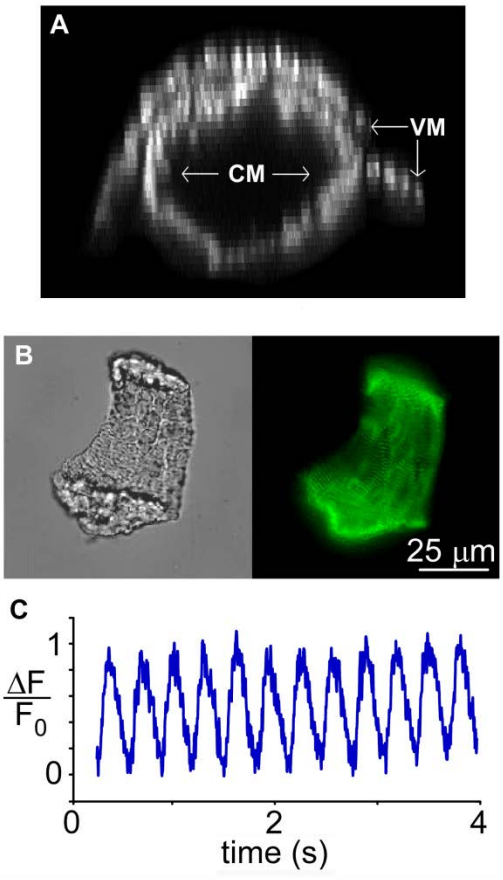

Supplementary Figure 6.4 Single cardiomyocytes from *Drosophila* heart tube dissociation are viable. (**A**) An intact GFP-ZASP52 *Drosophila* heart tube in cross section demonstrating two opposing C-shaped cardiomyocytes (CM) forming a hollow tube covered by the ventral longitudinal muscle layer (VM). (**B**) Isolated GFP-ZASP52 cardiomyocytes after dissociation maintain their curved morphology. (**C**) Isolated myocytes from *TinCΔ4-Gal4 > UAS-GCaMP5* flies remain viable after enzymatic digestion as evident by the presence of fluorescently monitored Ca^{2+} transients. Cells were imaged under a Nikon TE300 Eclipse fluorescence microscope and signal intensity was measured by a custom fluorometer (University of Pennsylvania Biomedical Instrumentation Group) (Erickson et al., 2003).

6.6.6 Supplementary Methods

Post-developmental suppression of A1D channel expression in adult Drosophila heart tubes

Female virgins harboring the inducible *Hand-GS-Gal4*(Nicholson et al., 2008) cardiac-specific driver (a kind gift from Dr. Rolf Bodmer) were crossed with males obtained from the Vienna *Drosophila* RNAi Stock Center carrying a cassette of UAS-RNAi targeting the A1D subunit of Ca^{2+} channels (Catalog No. 51491). Two-days post-eclosion, adult progeny were placed on food supplemented with 100 µg/ml of RU486 (dissolved in 100% ethanol) or vehicle (100% vehicle). Flies were transferred onto new food every day to ensure constant exposure to the drug or vehicle. At two weeks, flies were dissected(Vogler and Ocorr, 2009) to expose the heart tubes and contractions were imaged and quantified as described in the main text.

Quantitation of Ca^{2+} channel transcripts in various experimental conditions

Prior to functional assessment, the amount of Ca^{2+} channel transcripts was assessed using the fluorescence RNA *in situ* hybridization (FISH) technique. The experimental procedure, measurement, and statistics are described in the main text. For the *Ca-α1D* RNAi knockdown experiment, *TinCΔ4-Gal4* was crossed with either w^{1118} (Ctrl) or *UAS-Ca-α1D*^{RNAi}: 51491 or 52644 (*Ca-α1D*(-)#1, or #2, respectively). Five days post eclosion, the heart tubes of the progenies were surgically exposed and underwent an *in situ* hybridization using a fluorophore-tagged probe custom designed to target *Drosophila* mRNA coding for *Ca-α1D* (VF4-18190). For the *cacophony* and *Ca-α1T* RNAi knockdown experiments, *TinCΔ4-Gal4* was crossed with either KK injection line (Ctrl), *UAS-cacophony*^{RNAi}: 104168, or *UAS-Ca-α1T*^{RNAi}: 108827. Custom designed probes targeting *cacophony* (VF4-18657) and *Ca-α1T* (VF4-18658) were utilized, respectively. For the cac hypomorph and T-type null lines, we used Canton-S as a

control to match the background genetic of these two lines (Smith et al., 1996; Smith et al., 1998; Ryglewski et al., 2012).

Heart tube morphology

Confocal microscopy was performed as detailed by Alayari *et al.* (2009)(Alayari et al., 2009). Briefly, w^{1118} *Drosophila* hearts were surgically exposed according to the method of Vogler and Ocorr (2009)(Vogler and Ocorr, 2009) and arrested using 10mM EGTA in artificial hemolymph. The relaxed, semi-intact hearts were fixed (4% formaldehyde in 1X PBS) and washed three times with 1X PBST (PBS with 0.1% Triton X-100). Fixed hearts were then stained with Alexa594 TRITC-phalloidin (1:1000 in PBST), rinsed three times in 1X PBST, mounted and imaged with a Leica TCS SPE RGBV confocal microscope (Supplementary Figure 6.4A).

REFERENCES

Adams, M.D., and J.J. Sekelsky. 2002. From sequence to phenotype: reverse genetics in Drosophila melanogaster. *Nature reviews. Genetics*. 3:189-198.

Adams, P.J., M. Ben-Johny, I.E. Dick, T. Inoue, and D.T. Yue. 2014. Apocalmodulin itself promotes ion channel opening and Ca(2+) regulation. *Cell*. 159:608-622.

Alayari, N.N., G. Vogler, O. Taghli-Lamallem, K. Ocorr, R. Bodmer, and A. Cammarato. 2009. Fluorescent labeling of Drosophila heart structures. *J Vis Exp*.

Alseikhan, B.A., C.D. DeMaria, H.M. Colecraft, and D.T. Yue. 2002. Engineered calmodulins reveal the unexpected eminence of Ca2+ channel inactivation in controlling heart excitation. *Proceedings of the National Academy of Sciences of the United States of America*. 99:17185-17190.

Arevalo, H., B. Rodriguez, and N. Trayanova. 2007. Arrhythmogenesis in the heart: Multiscale modeling of the effects of defibrillation shocks and the role of electrophysiological heterogeneity. *Chaos*. 17:015103.

Azizan, E.A., H. Poulsen, P. Tuluc, J. Zhou, M.V. Clausen, A. Lieb, C. Maniero, S. Garg, E.G. Bochukova, W. Zhao, L.H. Shaikh, C.A. Brighton, A.E. Teo, A.P. Davenport, T. Dekkers, B. Tops, B. Kusters, J. Ceral, G.S. Yeo, S.G. Neogi, I. McFarlane, N. Rosenfeld, F. Marass, J. Hadfield, W. Margas, K. Chaggar, M. Solar, J. Deinum, A.C. Dolphin, I.S. Farooqi, J. Striessnig, P. Nissen, and M.J. Brown. 2013. Somatic mutations in ATP1A1 and CACNA1D underlie a common subtype of adrenal hypertension. *Nature genetics*. 45:1055-1060.

Baig, S.M., A. Koschak, A. Lieb, M. Gebhart, C. Dafinger, G. Nurnberg, A. Ali, I. Ahmad, M.J. Sinnegger-Brauns, N. Brandt, J. Engel, M.E. Mangoni, M. Farooq, H.U. Khan, P. Nurnberg, J. Striessnig, and H.J. Bolz. 2011. Loss of Ca(v)1.3 (CACNA1D) function in a human channelopathy with bradycardia and congenital deafness. *Nature neuroscience*. 14:77-84.

Balke, C.W., and S.R. Shorofsky. 1998. Alterations in calcium handling in cardiac hypertrophy and heart failure. *Cardiovascular research*. 37:290-299.

Barnby, G., A. Abbott, N. Sykes, A. Morris, D.E. Weeks, R. Mott, J. Lamb, A.J. Bailey, A.P. Monaco, and C. International Molecular Genetics Study of Autism. 2005. Candidate-gene screening and association analysis at the autism-susceptibility locus on chromosome 16p: evidence of association at GRIN2A and ABAT. *American journal of human genetics*. 76:950-966.

Barrett, C.F., and R.W. Tsien. 2008. The Timothy syndrome mutation differentially affects voltage- and calcium-dependent inactivation of CaV1.2 L-type calcium channels. *Proceedings of the National Academy of Sciences of the United States of America*. 105:2157-2162.

Barrett, P.Q., N.A. Guagliardo, P.M. Klein, C. Hu, D.T. Breault, and M.P. Beenhakker. 2016. Role of voltage-gated calcium channels in the regulation of aldosterone production from zona glomerulosa cells of the adrenal cortex. *The Journal of physiology*.

Barry, P.H. 1994. JPCalc, a software package for calculating liquid junction potential corrections in patch-clamp, intracellular, epithelial and bilayer measurements and for correcting junction potential measurements. *Journal of neuroscience methods*. 51:107-116.

Bassani, J.W., R.A. Bassani, and D.M. Bers. 1995. Calibration of indo-1 and resting intracellular [Ca]i in intact rabbit cardiac myocytes. *Biophysical journal*. 68:1453-1460.

Bayley, P., P. Ahlstrom, S.R. Martin, and S. Forsen. 1984. The kinetics of calcium binding to calmodulin: Quin 2 and ANS stopped-flow fluorescence studies. *Biochemical and biophysical research communications*. 120:185-191.

Bazzazi, H., M. Ben Johny, P.J. Adams, T.W. Soong, and D.T. Yue. 2013. Continuously tunable Ca(2+) regulation of RNA-edited CaV1.3 channels. *Cell reports*. 5:367-377.

Bean, B.P. 1985. Two kinds of calcium channels in canine atrial cells. Differences in kinetics, selectivity, and pharmacology. *The Journal of general physiology*. 86:1-30.

Ben-Johny, M., and D.T. Yue. 2014. Calmodulin regulation (calmodulation) of voltage-gated calcium channels. *The Journal of general physiology*. 143:679-692.

Ben Johny, M., P.S. Yang, H. Bazzazi, and D.T. Yue. 2013. Dynamic switching of calmodulin interactions underlies Ca2+ regulation of CaV1.3 channels. *Nature communications*. 4:1717.

Berger, S.M., and D. Bartsch. 2014. The role of L-type voltage-gated calcium channels Cav1.2 and Cav1.3 in normal and pathological brain function. *Cell and tissue research*. 357:463-476.

Bhattacharya, A., G.G. Gu, and S. Singh. 1999. Modulation of dihydropyridine-sensitive calcium channels in Drosophila by a cAMP-mediated pathway. *Journal of neurobiology*. 39:491-500.

Bier, E. 2005. Drosophila, the golden bug, emerges as a tool for human genetics. *Nature reviews. Genetics*. 6:9-23.

Black, D.J., D.B. Halling, D.V. Mandich, S.E. Pedersen, R.A. Altschuld, and S.L. Hamilton. 2005. Calmodulin interactions with IQ peptides from voltage-dependent calcium channels. *American journal of physiology. Cell physiology*. 288:C669-676.

Bock, G., M. Gebhart, A. Scharinger, W. Jangsangthong, P. Busquet, C. Poggiani, S. Sartori, M.E. Mangoni, M.J. Sinnegger-Brauns, S. Herzig, J. Striessnig, and A. Koschak. 2011. Functional properties of a newly identified C-terminal splice variant of Cav1.3 L-type Ca2+ channels. *The Journal of biological chemistry*. 286:42736-42748.

Boczek, N.J., N. Gomez-Hurtado, D. Ye, M.L. Calvert, D.J. Tester, D. Kryshtal, H.S. Hwang, C.N. Johnson, W.J. Chazin, C.G. Loporcaro, M. Shah, A.L. Papez, Y.R. Lau, R. Kanter, B.C. Knollmann, and M.J. Ackerman. 2016. Spectrum and Prevalence of CALM1-, CALM2-, and CALM3-Encoded Calmodulin (CaM) Variants in Long QT Syndrome (LQTS) and Functional Characterization of a Novel LQTS-Associated CaM Missense Variant, E141G. *Circulation. Cardiovascular genetics*.

Boczek, N.J., M.L. Will, C.G. Loporcaro, D.J. Tester, and M.J. Ackerman. 2013. Abstract 14699: Spectrum and Prevalence of CALM1, CALM2, and CALM3 Mutations in Long QT Syndrome, Catecholaminergic Polymorphic Ventricular Tachycardia, Idiopathic Ventricular Fibrillation, and Sudden Unexplained Death in the Young. *Circulation*. 128:A14699.

Bodi, I., G. Mikala, S.E. Koch, S.A. Akhter, and A. Schwartz. 2005. The L-type calcium channel in the heart: the beat goes on. *The Journal of clinical investigation*. 115:3306-3317.

Bodmer, R. 1995. Heart development in Drosophila and its relationship to vertebrates. *Trends in cardiovascular medicine*. 5:21-28.

Brand, A.H., and N. Perrimon. 1993. Targeted gene expression as a means of altering cell fates and generating dominant phenotypes. *Development*. 118:401-415.

Brehm, P., and R. Eckert. 1978. Calcium entry leads to inactivation of calcium channel in Paramecium. *Science*. 202:1203-1206.

Brehm, P., R. Eckert, and D. Tillotson. 1980. Calcium-mediated inactivation of calcium current in Paramecium. *The Journal of physiology*. 306:193-203.

Breitenkamp, A.F., J. Matthes, and S. Herzig. 2015. Voltage-gated Calcium Channels and Autism Spectrum Disorders. *Current molecular pharmacology*. 8:123-132.

Bub, G., P. Camelliti, C. Bollensdorff, D.J. Stuckey, G. Picton, R.A. Burton, K. Clarke, and P. Kohl. 2010. Measurement and analysis of sarcomere length in rat cardiomyocytes in situ and in vitro. *American journal of physiology. Heart and circulatory physiology*. 298:H1616-1625.

Buraei, Z., and J. Yang. 2013. Structure and function of the beta subunit of voltage-gated Ca(2)(+) channels. *Biochimica et biophysica acta*. 1828:1530-1540.

Busch, A.E., H. Suessbrich, S. Waldegger, E. Sailer, R. Greger, H. Lang, F. Lang, K.J. Gibson, and J.G. Maylie. 1996. Inhibition of IKs in guinea pig cardiac myocytes and guinea pig IsK channels by the chromanol 293B. *Pflugers Arch*. 432:1094-1096.

Cammarato, A., S. Ocorr, and K. Ocorr. 2015. Enhanced assessment of contractile dynamics in Drosophila hearts. *BioTechniques*. 58:77-80.

Chambers, J.S., D. Thomas, L. Saland, R.L. Neve, and N.I. Perrone-Bizzozero. 2005. Growth-associated protein 43 (GAP-43) and synaptophysin alterations in the dentate gyrus of

patients with schizophrenia. *Progress in neuro-psychopharmacology & biological psychiatry*. 29:283-290.

Chan, C.S., J.N. Guzman, E. Ilijic, J.N. Mercer, C. Rick, T. Tkatch, G.E. Meredith, and D.J. Surmeier. 2007. 'Rejuvenation' protects neurons in mouse models of Parkinson's disease. *Nature*. 447:1081-1086.

Chaudhuri, D., B.A. Alseikhan, S.Y. Chang, T.W. Soong, and D.T. Yue. 2005. Developmental activation of calmodulin-dependent facilitation of cerebellar P-type Ca2+ current. *The Journal of neuroscience : the official journal of the Society for Neuroscience*. 25:8282-8294.

Chen, T.W., T.J. Wardill, Y. Sun, S.R. Pulver, S.L. Renninger, A. Baohan, E.R. Schreiter, R.A. Kerr, M.B. Orger, V. Jayaraman, L.L. Looger, K. Svoboda, and D.S. Kim. 2013. Ultrasensitive fluorescent proteins for imaging neuronal activity. *Nature*. 499:295-300.

Chen, W.G., Q. Chang, Y. Lin, A. Meissner, A.E. West, E.C. Griffith, R. Jaenisch, and M.E. Greenberg. 2003. Derepression of BDNF transcription involves calcium-dependent phosphorylation of MeCP2. *Science*. 302:885-889.

Chintapalli, V.R., J. Wang, and J.A. Dow. 2007. Using FlyAtlas to identify better Drosophila melanogaster models of human disease. *Nature genetics*. 39:715-720.

Chorna, T., and G. Hasan. The genetics of calcium signaling in Drosophila melanogaster. *Biochimica et biophysica acta*. 1820:1269-1282.

Christel, C., and A. Lee. 2012. Ca2+-dependent modulation of voltage-gated Ca2+ channels. *Biochimica et biophysica acta*. 1820:1243-1252.

Colecraft, H.M., B. Alseikhan, S.X. Takahashi, D. Chaudhuri, S. Mittman, V. Yegnasubramanian, R.S. Alvania, D.C. Johns, E. Marban, and D.T. Yue. 2002. Novel functional properties of Ca(2+) channel beta subunits revealed by their expression in adult rat heart cells. *The Journal of physiology*. 541:435-452.

Cooper, A.S., K.E. Rymond, M.A. Ward, E.L. Bocook, and R.L. Cooper. 2009. Monitoring heart function in larval Drosophila melanogaster for physiological studies. *J Vis Exp*.

Crotti, L., C.N. Johnson, E. Graf, G.M. De Ferrari, B.F. Cuneo, M. Ovadia, J. Papagiannis, M.D. Feldkamp, S.G. Rathi, J.D. Kunic, M. Pedrazzini, T. Wieland, P. Lichtner, B.M. Beckmann, T. Clark, C. Shaffer, D.W. Benson, S. Kaab, T. Meitinger, T.M. Strom, W.J. Chazin, P.J. Schwartz, and A.L. George, Jr. 2013. Calmodulin mutations associated with recurrent cardiac arrest in infants. *Circulation*. 127:1009-1017.

Dafi, O., L. Berrou, Y. Dodier, A. Raybaud, R. Sauve, and L. Parent. 2004. Negatively charged residues in the N-terminal of the AID helix confer slow voltage dependent inactivation gating to CaV1.2. *Biophysical journal*. 87:3181-3192.

Decker, K.F., J. Heijman, J.R. Silva, T.J. Hund, and Y. Rudy. 2009. Properties and ionic mechanisms of action potential adaptation, restitution, and accommodation in canine epicardium. *American journal of physiology. Heart and circulatory physiology*. 296:H1017-1026.

Demerec, M. 1994. Biology of drosophila. CSHL Press.

Dick I. E., J.-M.R., Yang W, Yue D. T. . 2016. Arrhythmogenesis in Timothy Syndrome is associated with defects in Ca2+ dependent inactivation. *Nature communications*. 7:10370.

Dick, I.E., R. Joshi-Mukherjee, W. Yang, and D.T. Yue. 2016. Arrhythmogenesis in Timothy Syndrome is associated with defects in Ca(2+)-dependent inactivation. *Nature communications*. 7:10370.

Dick, I.E., R. Joshi-Mukherjee, and D.T. Yue. 2012. Nonlinear behavior in the induction of arrhythmias by channels bearing Timothy Syndrome mutations. *In* Biophysical Society. Biophysical Journal, San Diego. 542a.

Dick, I.E., M.R. Tadross, H. Liang, L.H. Tay, W. Yang, and D.T. Yue. 2008. A modular switch for spatial Ca2+ selectivity in the calmodulin regulation of CaV channels. *Nature*. 451:830-834.

Dietzl, G., D. Chen, F. Schnorrer, K.C. Su, Y. Barinova, M. Fellner, B. Gasser, K. Kinsey, S. Oppel, S. Scheiblauer, A. Couto, V. Marra, K. Keleman, and B.J. Dickson. 2007. A genome-wide transgenic RNAi library for conditional gene inactivation in Drosophila. *Nature*. 448:151-156.

Dolphin, A.C. 2003. Beta subunits of voltage-gated calcium channels. *Journal of bioenergetics and biomembranes*. 35:599-620.

Dolphin, A.C. 2009. Calcium channel diversity: multiple roles of calcium channel subunits. *Current opinion in neurobiology*. 19:237-244.

Dolphin, A.C. 2012. Calcium channel auxiliary alpha2delta and beta subunits: trafficking and one step beyond. *Nature reviews. Neuroscience*. 13:542-555.

Dou, H., A.E. Vazquez, Y. Namkung, H. Chu, E.L. Cardell, L. Nie, S. Parson, H.S. Shin, and E.N. Yamoah. 2004. Null mutation of alpha1D Ca2+ channel gene results in deafness but no vestibular defect in mice. *Journal of the Association for Research in Otolaryngology : JARO*. 5:215-226.

Dowse, H., J. Ringo, J. Power, E. Johnson, K. Kinney, and L. White. 1995. A congenital heart defect in Drosophila caused by an action-potential mutation. *Journal of neurogenetics*. 10:153-168.

Du, D.T., N. Hellen, C. Kane, and C.M. Terracciano. 2015. Action potential morphology of human induced pluripotent stem cell-derived cardiomyocytes does not predict cardiac chamber specificity and is dependent on cell density. *Biophysical journal*. 108:1-4.

Dulcis, D., and R.B. Levine. 2005. Glutamatergic innervation of the heart initiates retrograde contractions in adult Drosophila melanogaster. *The Journal of neuroscience : the official journal of the Society for Neuroscience*. 25:271-280.

Eder, P., and J.D. Molkentin. 2011. TRPC channels as effectors of cardiac hypertrophy. *Circulation research*. 108:265-272.

Ellinor, P.T., J. Yang, W.A. Sather, J.F. Zhang, and R.W. Tsien. 1995. Ca2+ channel selectivity at a single locus for high-affinity Ca2+ interactions. *Neuron*. 15:1121-1132.

Elliott, D.A., and A.H. Brand. 2008. The GAL4 system : a versatile system for the expression of genes. *Methods in molecular biology*. 420:79-95.

Erickson, M.G., B.A. Alseikhan, B.Z. Peterson, and D.T. Yue. 2001. Preassociation of calmodulin with voltage-gated Ca(2+) channels revealed by FRET in single living cells. *Neuron*. 31:973-985.

Erickson, M.G., H. Liang, M.X. Mori, and D.T. Yue. 2003. FRET two-hybrid mapping reveals function and location of L-type Ca2+ channel CaM preassociation. *Neuron*. 39:97-107.

Evans, P.D., and B. Maqueira. 2005. Insect octopamine receptors: a new classification scheme based on studies of cloned Drosophila G-protein coupled receptors. *Invertebrate neuroscience : IN*. 5:111-118.

Faber, G.M., J. Silva, L. Livshitz, and Y. Rudy. 2007. Kinetic properties of the cardiac L-type Ca2+ channel and its role in myocyte electrophysiology: a theoretical investigation. *Biophysical journal*. 92:1522-1543.

Findlay, I., S. Suzuki, S. Murakami, and Y. Kurachi. 2008. Physiological modulation of voltage-dependent inactivation in the cardiac muscle L-type calcium channel: a modelling study. *Progress in biophysics and molecular biology*. 96:482-498.

Fink, M., C. Callol-Massot, A. Chu, P. Ruiz-Lozano, J.C. Izpisua Belmonte, W. Giles, R. Bodmer, and K. Ocorr. 2009. A new method for detection and quantification of heartbeat parameters in Drosophila, zebrafish, and embryonic mouse hearts. *BioTechniques*. 46:101-113.

Ghosh, S., D.A. Nunziato, and G.S. Pitt. 2006. KCNQ1 assembly and function is blocked by long-QT syndrome mutations that disrupt interaction with calmodulin. *Circulation research*. 98:1048-1054.

Gielow, M.L., G.G. Gu, and S. Singh. 1995. Resolution and pharmacological analysis of the voltage-dependent calcium channels of Drosophila larval muscles. *The Journal of neuroscience : the official journal of the Society for Neuroscience*. 15:6085-6093.

Gilbert, L.A., M.H. Larson, L. Morsut, Z. Liu, G.A. Brar, S.E. Torres, N. Stern-Ginossar, O. Brandman, E.H. Whitehead, J.A. Doudna, W.A. Lim, J.S. Weissman, and L.S. Qi. 2013. CRISPR-mediated modular RNA-guided regulation of transcription in eukaryotes. *Cell*. 154:442-451.

Grandi, E., S. Morotti, K.S. Ginsburg, S. Severi, and D.M. Bers. 2010. Interplay of voltage and Ca-dependent inactivation of L-type Ca current. *Progress in biophysics and molecular biology*. 103:44-50.

Greenstein, J.L., and R.L. Winslow. 2002. An integrative model of the cardiac ventricular myocyte incorporating local control of Ca2+ release. *Biophysical journal*. 83:2918-2945.

Gu, G.G., and S. Singh. 1995. Pharmacological analysis of heartbeat in Drosophila. *Journal of neurobiology*. 28:269-280.

Gu, H., S.A. Jiang, J.M. Campusano, J. Iniguez, H. Su, A.A. Hoang, M. Lavian, X. Sun, and D.K. O'Dowd. 2009. Cav2-type calcium channels encoded by cac regulate AP-independent neurotransmitter release at cholinergic synapses in adult Drosophila brain. *Journal of neurophysiology*. 101:42-53.

Hagiwara, N., H. Irisawa, and M. Kameyama. 1988. Contribution of two types of calcium currents to the pacemaker potentials of rabbit sino-atrial node cells. *The Journal of physiology*. 395:233-253.

Haley, B., D. Hendrix, V. Trang, and M. Levine. 2008. A simplified miRNA-based gene silencing method for Drosophila melanogaster. *Developmental biology*. 321:482-490.

Halling, D.B., P. Aracena-Parks, and S.L. Hamilton. 2006. Regulation of voltage-gated Ca2+ channels by calmodulin. *Science's STKE : signal transduction knowledge environment*. 2006:er1.

Hasenfuss, G. 1998. Alterations of calcium-regulatory proteins in heart failure. *Cardiovascular research*. 37:279-289.

He, J., M.W. Conklin, J.D. Foell, M.R. Wolff, R.A. Haworth, R. Coronado, and T.J. Kamp. 2001. Reduction in density of transverse tubules and L-type Ca(2+) channels in canine tachycardia-induced heart failure. *Cardiovascular research*. 49:298-307.

Heigwer, F., G. Kerr, and M. Boutros. 2014. E-CRISP: fast CRISPR target site identification. *Nature methods*. 11:122-123.

Hemara-Wahanui, A., S. Berjukow, C.I. Hope, P.K. Dearden, S.B. Wu, J. Wilson-Wheeler, D.M. Sharp, P. Lundon-Treweek, G.M. Clover, J.C. Hoda, J. Striessnig, R. Marksteiner, S. Hering, and M.A. Maw. 2005. A CACNA1F mutation identified in an X-linked retinal disorder shifts the voltage dependence of Cav1.4 channel activation. *Proceedings of the National Academy of Sciences of the United States of America*. 102:7553-7558.

Hirano, Y., and M. Hiraoka. 2003. Ca2+ entry-dependent inactivation of L-type Ca current: a novel formulation for cardiac action potential models. *Biophysical journal*. 84:696-708.

Hirase, H., X. Leinekugel, A. Czurko, J. Csicsvari, and G. Buzsaki. 2001. Firing rates of hippocampal neurons are preserved during subsequent sleep episodes and modified by novel awake experience. *Proceedings of the National Academy of Sciences of the United States of America*. 98:9386-9390.

Hoda, J.C., F. Zaghetto, A. Koschak, and J. Striessnig. 2005. Congenital stationary night blindness type 2 mutations S229P, G369D, L1068P, and W1440X alter channel gating or functional expression of Ca(v)1.4 L-type Ca2+ channels. *The Journal of neuroscience : the official journal of the Society for Neuroscience*. 25:252-259.

Hodgkin, A.L., and A.F. Huxley. 1952. A quantitative description of membrane current and its application to conduction and excitation in nerve. *The Journal of physiology*. 117:500-544.

Hoeflich, K.P., and M. Ikura. 2002. Calmodulin in action: diversity in target recognition and activation mechanisms. *Cell*. 108:739-742.

Hofmann, F., M. Biel, and V. Flockerzi. 1994. Molecular basis for Ca2+ channel diversity. *Annual review of neuroscience*. 17:399-418.

Hohaus, A., S. Beyl, M. Kudrnac, S. Berjukow, E.N. Timin, R. Marksteiner, M.A. Maw, and S. Hering. 2005. Structural determinants of L-type channel activation in segment IIS6 revealed by a retinal disorder. *The Journal of biological chemistry*. 280:38471-38477.

Huang, H., B.Z. Tan, Y. Shen, J. Tao, F. Jiang, Y.Y. Sung, C.K. Ng, M. Raida, G. Kohr, M. Higuchi, H. Fatemi-Shariatpanahi, B. Harden, D.T. Yue, and T.W. Soong. 2012. RNA editing of the IQ domain in Ca(v)1.3 channels modulates their Ca(2)(+)-dependent inactivation. *Neuron*. 73:304-316.

Huang, H., D. Yu, and T.W. Soong. 2013. C-terminal alternative splicing of CaV1.3 channels distinctively modulates their dihydropyridine sensitivity. *Molecular pharmacology*. 84:643-653.

Hullin, R., D. Singer-Lahat, M. Freichel, M. Biel, N. Dascal, F. Hofmann, and V. Flockerzi. 1992. Calcium channel beta subunit heterogeneity: functional expression of cloned cDNA from heart, aorta and brain. *The EMBO journal*. 11:885-890.

Hund, T.J., and Y. Rudy. 2004. Rate dependence and regulation of action potential and calcium transient in a canine cardiac ventricular cell model. *Circulation*. 110:3168-3174.

Hwang, H.S., D.O. Kryshtal, T.K. Feaster, V. Sanchez-Freire, J. Zhang, T.J. Kamp, C.C. Hong, J.C. Wu, and B.C. Knollmann. 2015. Comparable calcium handling of human iPSC-derived cardiomyocytes generated by multiple laboratories. *Journal of molecular and cellular cardiology*. 85:79-88.

Hwang, H.S., F.R. Nitu, Y. Yang, K. Walweel, L. Pereira, C.N. Johnson, M. Faggioni, W.J. Chazin, D. Laver, A.L. George, Jr., R.L. Cornea, D.M. Bers, and B.C. Knollmann. 2014. Divergent regulation of ryanodine receptor 2 calcium release channels by arrhythmogenic human calmodulin missense mutants. *Circulation research*. 114:1114-1124.

Ikeda, S., A. He, S.W. Kong, J. Lu, R. Bejar, N. Bodyak, K.H. Lee, Q. Ma, P.M. Kang, T.R. Golub, and W.T. Pu. 2009. MicroRNA-1 negatively regulates expression of the hypertrophy-associated calmodulin and Mef2a genes. *Molecular and cellular biology*. 29:2193-2204.

Imredy, J.P., and D.T. Yue. 1994. Mechanism of Ca(2+)-sensitive inactivation of L-type Ca2+ channels. *Neuron*. 12:1301-1318.

Iniguez, J., S.S. Schutte, and D.K. O'Dowd. 2013. Cav3-type alpha1T calcium channels mediate transient calcium currents that regulate repetitive firing in Drosophila antennal lobe PNs. *Journal of neurophysiology*. 110:1490-1496.

Iossifov, I., M. Ronemus, D. Levy, Z. Wang, I. Hakker, J. Rosenbaum, B. Yamrom, Y.H. Lee, G. Narzisi, A. Leotta, J. Kendall, E. Grabowska, B. Ma, S. Marks, L. Rodgers, A. Stepansky, J. Troge, P. Andrews, M. Bekritsky, K. Pradhan, E. Ghiban, M. Kramer, J. Parla, R. Demeter, L.L. Fulton, R.S. Fulton, V.J. Magrini, K. Ye, J.C. Darnell, R.B. Darnell, E.R. Mardis, R.K. Wilson, M.C. Schatz, W.R. McCombie, and M. Wigler. 2012. De novo gene disruptions in children on the autistic spectrum. *Neuron*. 74:285-299.

Isom, L.L., K.S. De Jongh, and W.A. Catterall. 1994. Auxiliary subunits of voltage-gated ion channels. *Neuron*. 12:1183-1194.

Jafri, M.S., J.J. Rice, and R.L. Winslow. 1998. Cardiac Ca2+ dynamics: the roles of ryanodine receptor adaptation and sarcoplasmic reticulum load. *Biophysical journal*. 74:1149-1168.

Jaren, O.R., J.K. Kranz, B.R. Sorensen, A.J. Wand, and M.A. Shea. 2002. Calcium-induced conformational switching of Paramecium calmodulin provides evidence for domain coupling. *Biochemistry*. 41:14158-14166.

Johnson, E., J. Ringo, N. Bray, and H. Dowse. 1998. Genetic and pharmacological identification of ion channels central to the Drosophila cardiac pacemaker. *Journal of neurogenetics*. 12:1-24.

Johnson, E., J. Ringo, and H. Dowse. 2000. Native and heterologous neuropeptides are cardioactive in Drosophila melanogaster. *Journal of insect physiology*. 46:1229-1236.

Johnson, E., T. Sherry, J. Ringo, and H. Dowse. 2002. Modulation of the cardiac pacemaker of Drosophila: cellular mechanisms. *Journal of comparative physiology*. 172:227-236.

Joiner, M.L., and A. Lee. 2015. Voltage-Gated Cav1 Channels in Disorders of Vision and Hearing. *Current molecular pharmacology*. 8:143-148.

Joshi-Mukherjee, R., I.E. Dick, T. Liu, B. O'Rourke, D.T. Yue, and L. Tung. 2013. Structural and functional plasticity in long-term cultures of adult ventricular myocytes. *Journal of molecular and cellular cardiology*. 65C:76-87.

Kane, C., L. Couch, and C.M. Terracciano. 2015. Excitation-contraction coupling of human induced pluripotent stem cell-derived cardiomyocytes. *Frontiers in cell and developmental biology*. 3:59.

Kapoor, A., R.B. Sekar, N.F. Hansen, K. Fox-Talbot, M. Morley, V. Pihur, S. Chatterjee, J. Brandimarto, C.S. Moravec, S.L. Pulit, Q.T.I.-I.G. Consortium, A. Pfeufer, J. Mullikin, M. Ross, E.D. Green, D. Bentley, C. Newton-Cheh, E. Boerwinkle, G.F. Tomaselli, T.P. Cappola, D.E. Arking, M.K. Halushka, and A. Chakravarti. 2014. An enhancer polymorphism at the cardiomyocyte intercalated disc protein NOS1AP locus is a major regulator of the QT interval. *American journal of human genetics*. 94:854-869.

Kato, Y., H. Masumiya, N. Agata, H. Tanaka, and K. Shigenobu. 1996. Developmental changes in action potential and membrane currents in fetal, neonatal and adult guinea-pig ventricular myocytes. *Journal of molecular and cellular cardiology*. 28:1515-1522.

Keen, J.E., R. Khawaled, D.L. Farrens, T. Neelands, A. Rivard, C.T. Bond, A. Janowsky, B. Fakler, J.P. Adelman, and J. Maylie. 1999. Domains responsible for constitutive and Ca(2+)-dependent interactions between calmodulin and small conductance Ca(2+)-activated potassium channels. *The Journal of neuroscience : the official journal of the Society for Neuroscience*. 19:8830-8838.

Kim, I.M., and M.J. Wolf. 2009. Serial examination of an inducible and reversible dilated cardiomyopathy in individual adult Drosophila. *PloS one*. 4:e7132.

Koschak, A., D. Reimer, I. Huber, M. Grabner, H. Glossmann, J. Engel, and J. Striessnig. 2001. alpha 1D (Cav1.3) subunits can form l-type Ca2+ channels activating at negative voltages. *The Journal of biological chemistry*. 276:22100-22106.

Kraus, R.L., M.J. Sinnegger, A. Koschak, H. Glossmann, S. Stenirri, P. Carrera, and J. Striessnig. 2000. Three new familial hemiplegic migraine mutants affect P/Q-type Ca(2+) channel kinetics. *The Journal of biological chemistry*. 275:9239-9243.

Krey, J.F., and R.E. Dolmetsch. 2007. Molecular mechanisms of autism: a possible role for Ca2+ signaling. *Current opinion in neurobiology*. 17:112-119.

Lai, S.L., and T. Lee. 2006. Genetic mosaic with dual binary transcriptional systems in Drosophila. *Nature neuroscience*. 9:703-709.

Lalevee, N., B. Monier, S. Senatore, L. Perrin, and M. Semeriva. 2006. Control of cardiac rhythm by ORK1, a Drosophila two-pore domain potassium channel. *Current biology : CB*. 16:1502-1508.

Lambert, R.C., Y. Maulet, J.L. Dupont, S. Mykita, P. Craig, S. Volsen, and A. Feltz. 1996. Polyethylenimine-mediated DNA transfection of peripheral and central neurons in

primary culture: probing Ca2+ channel structure and function with antisense oligonucleotides. *Molecular and cellular neurosciences*. 7:239-246.

Lee, D., S.Y. Lee, E.N. Lee, C.S. Chang, and S.R. Paik. 2002. alpha-Synuclein exhibits competitive interaction between calmodulin and synthetic membranes. *Journal of neurochemistry*. 82:1007-1017.

Lee, P., M. Klos, C. Bollensdorff, L. Hou, P. Ewart, T.J. Kamp, J. Zhang, A. Bizy, G. Guerrero-Serna, P. Kohl, J. Jalife, and T.J. Herron. 2012. Simultaneous voltage and calcium mapping of genetically purified human induced pluripotent stem cell-derived cardiac myocyte monolayers. *Circulation research*. 110:1556-1563.

Lee, S.R., P.J. Adams, and D.T. Yue. 2015. Large Ca(2)(+)-dependent facilitation of Ca(V)2.1 channels revealed by Ca(2)(+) photo-uncaging. *The Journal of physiology*. 593:2753-2778.

Li, R.A., I.L. Ennis, R.J. French, S.C. Dudley, Jr., G.F. Tomaselli, and E. Marban. 2001. Clockwise domain arrangement of the sodium channel revealed by (mu)-conotoxin (GIIIA) docking orientation. *The Journal of biological chemistry*. 276:11072-11077.

Lieb, A., N. Ortner, and J. Striessnig. 2014. C-terminal modulatory domain controls coupling of voltage-sensing to pore opening in Cav1.3 L-type Ca(2+) channels. *Biophysical journal*. 106:1467-1475.

Limphong, P., H. Zhang, E. Christians, Q. Liu, M. Riedel, K. Ivey, P. Cheng, K. Mitzelfelt, G. Taylor, D. Winge, D. Srivastava, and I. Benjamin. 2013. Modeling human protein aggregation cardiomyopathy using murine induced pluripotent stem cells. *Stem cells translational medicine*. 2:161-166.

Limpitikul, W.B., I.E. Dick, R. Joshi-Mukherjee, M.T. Overgaard, A.L. George, Jr., and D.T. Yue. 2014. Calmodulin mutations associated with long QT syndrome prevent inactivation of cardiac L-type Ca(2+) currents and promote proarrhythmic behavior in ventricular myocytes. *Journal of molecular and cellular cardiology*. 74:115-124.

Limpitikul, W.B., I.E. Dick, D.J. Tester, N.J. Boczek, P. Limphong, W. Yang, M.H. Choi, J. Babich, D. DiSilvestre, R.J. Kanter, G.F. Tomaselli, M.J. Ackerman, and D.T. Yue. 2017. A Precision Medicine Approach to the Rescue of Function on Malignant Calmodulinopathic Long-QT Syndrome. *Circulation research*. 120:39-48.

Limpitikul, W.B., and D.T. Yue. 2014. Ca2+ Sensitivity of LType Calcium Channel Inactivation Probed by Ca2+ Photouncaging--- Window onto Calmodulinopathies. *In* Biophysical Society. Biophysical Journal, San Franscisco. 553a.

Linse, S., A. Helmersson, and S. Forsen. 1991. Calcium binding to calmodulin and its globular domains. *The Journal of biological chemistry*. 266:8050-8054.

Lipp, P., C. Luscher, and E. Niggli. 1996. Photolysis of caged compounds characterized by ratiometric confocal microscopy: a new approach to homogeneously control and measure the calcium concentration in cardiac myocytes. *Cell calcium*. 19:255-266.

Lipscombe, D., A. Andrade, and S.E. Allen. 2013. Alternative splicing: functional diversity among voltage-gated calcium channels and behavioral consequences. *Biochimica et biophysica acta*. 1828:1522-1529.

Liu, X., P.S. Yang, W. Yang, and D.T. Yue. 2010. Enzyme-inhibitor-like tuning of Ca(2+) channel connectivity with calmodulin. *Nature*. 463:968-972.

Livshitz, L.M., and Y. Rudy. 2007. Regulation of Ca2+ and electrical alternans in cardiac myocytes: role of CAMKII and repolarizing currents. *American journal of physiology. Heart and circulatory physiology*. 292:H2854-2866.

Lo, P.C., and M. Frasch. 2001. A role for the COUP-TF-related gene seven-up in the diversification of cardioblast identities in the dorsal vessel of Drosophila. *Mechanisms of development*. 104:49-60.

Lopez-Izquierdo, A., M. Warren, M. Riedel, S. Cho, S. Lai, R.L. Lux, K.W. Spitzer, I.J. Benjamin, M. Tristani-Firouzi, and C.J. Jou. 2014. A near-infrared fluorescent voltage-sensitive dye allows for moderate-throughput electrophysiological analyses of human induced pluripotent stem cell-derived cardiomyocytes. *American journal of physiology. Heart and circulatory physiology*. 307:H1370-1377.

Luan, H., N.C. Peabody, C.R. Vinson, and B.H. White. 2006. Refined spatial manipulation of neuronal function by combinatorial restriction of transgene expression. *Neuron*. 52:425-436.

Ludwig, A., V. Flockerzi, and F. Hofmann. 1997. Regional expression and cellular localization of the alpha1 and beta subunit of high voltage-activated calcium channels in rat brain. *The Journal of neuroscience : the official journal of the Society for Neuroscience*. 17:1339-1349.

Luo, C.H., and Y. Rudy. 1994a. A dynamic model of the cardiac ventricular action potential. I. Simulations of ionic currents and concentration changes. *Circulation research*. 74:1071-1096.

Luo, C.H., and Y. Rudy. 1994b. A dynamic model of the cardiac ventricular action potential. II. Afterdepolarizations, triggered activity, and potentiation. *Circulation research*. 74:1097-1113.

Ma, J., L. Guo, S.J. Fiene, B.D. Anson, J.A. Thomson, T.J. Kamp, K.L. Kolaja, B.J. Swanson, and C.T. January. 2011. High purity human-induced pluripotent stem cell-derived cardiomyocytes: electrophysiological properties of action potentials and ionic currents. *American journal of physiology. Heart and circulatory physiology*. 301:H2006-2017.

Mahajan, A., D. Sato, Y. Shiferaw, A. Baher, L.H. Xie, R. Peralta, R. Olcese, A. Garfinkel, Z. Qu, and J.N. Weiss. 2008a. Modifying L-type calcium current kinetics: consequences for cardiac excitation and arrhythmia dynamics. *Biophysical journal*. 94:411-423.

Mahajan, A., Y. Shiferaw, D. Sato, A. Baher, R. Olcese, L.H. Xie, M.J. Yang, P.S. Chen, J.G. Restrepo, A. Karma, A. Garfinkel, Z. Qu, and J.N. Weiss. 2008b. A rabbit ventricular action potential model replicating cardiac dynamics at rapid heart rates. *Biophysical journal*. 94:392-410.

Makita, N., N. Yagihara, L. Crotti, C.N. Johnson, B.-M. Beckermann, D. Shigemizu, H. Watanabe, T. Ishikawa, T. Aiba, E. Mastantuono, T. Tsunoda, H. Nakagawa, Y. Tsuji, T. Tsuchiya, H. Yamamoto, Y. Miyamoto, N. Endo, A. Kimura, K. Ozaki, H. Motomura, K. Suda, T. Tanaka, P.J. Schwartz, T. Meitinger, S. Kaab, W. Shimizu, W. Chazin, and A.L. George. 2013. Abstract 13371: CALM2 Mutations Associated With Atypical Juvenile Long QT Syndrome. *Circulation*. 128:A13371.

Makita, N., N. Yagihara, L. Crotti, C.N. Johnson, B.M. Beckmann, M.S. Roh, D. Shigemizu, P. Lichtner, T. Ishikawa, T. Aiba, T. Homfray, E.R. Behr, D. Klug, I. Denjoy, E. Mastantuono, D. Theisen, T. Tsunoda, W. Satake, T. Toda, H. Nakagawa, Y. Tsuji, T. Tsuchiya, H. Yamamoto, Y. Miyamoto, N. Endo, A. Kimura, K. Ozaki, H. Motomura, K. Suda, T. Tanaka, P.J. Schwartz, T. Meitinger, S. Kaab, P. Guicheney, W. Shimizu, Z.A. Bhuiyan, H. Watanabe, W.J. Chazin, and A.L. George, Jr. 2014. Novel calmodulin mutations associated with congenital arrhythmia susceptibility. *Circulation. Cardiovascular genetics*. 7:466-474.

Maltsev, V.A., and E.G. Lakatta. 2007. Normal heart rhythm is initiated and regulated by an intracellular calcium clock within pacemaker cells. *Heart, lung & circulation*. 16:335-348.

Maltsev, V.A., T.M. Vinogradova, K.Y. Bogdanov, E.G. Lakatta, and M.D. Stern. 2004. Diastolic calcium release controls the beating rate of rabbit sinoatrial node cells: numerical modeling of the coupling process. *Biophysical journal*. 86:2596-2605.

Mandegar, M.A., N. Huebsch, E.B. Frolov, E. Shin, A. Truong, M.P. Olvera, A.H. Chan, Y. Miyaoka, K. Holmes, C.I. Spencer, L.M. Judge, D.E. Gordon, T.V. Eskildsen, J.E. Villalta, M.A. Horlbeck, L.A. Gilbert, N.J. Krogan, S.P. Sheikh, J.S. Weissman, L.S. Qi, P.L. So, and B.R. Conklin. 2016. CRISPR Interference Efficiently Induces Specific and Reversible Gene Silencing in Human iPSCs. *Cell stem cell*.

Marban, E. 2002. Cardiac channelopathies. *Nature*. 415:213-218.

Marcantoni, A., P. Baldelli, J.M. Hernandez-Guijo, V. Comunanza, V. Carabelli, and E. Carbone. 2007. L-type calcium channels in adrenal chromaffin cells: role in pace-making and secretion. *Cell calcium*. 42:397-408.

Marsman, R.F., J. Barc, L. Beekman, M. Alders, D. Dooijes, A. van den Wijngaard, I. Ratbi, A. Sefiani, Z.A. Bhuiyan, A.A. Wilde, and C.R. Bezzina. 2013. A mutation in CALM1

encoding calmodulin in familial idiopathic ventricular fibrillation in childhood and adolescence. *Journal of the American College of Cardiology*.

Martin, S.R., A. Andersson Teleman, P.M. Bayley, T. Drakenberg, and S. Forsen. 1985. Kinetics of calcium dissociation from calmodulin and its tryptic fragments. A stopped-flow fluorescence study using Quin 2 reveals a two-domain structure. *European journal of biochemistry*. 151:543-550.

McKemy, D.D., W. Welch, J.A. Airey, and J.L. Sutko. 2000. Concentrations of caffeine greater than 20 mM increase the indo-1 fluorescence ratio in a Ca(2+)-independent manner. *Cell calcium*. 27:117-124.

McWilliam, H., W. Li, M. Uludag, S. Squizzato, Y.M. Park, N. Buso, A.P. Cowley, and R. Lopez. 2013. Analysis Tool Web Services from the EMBL-EBI. *Nucleic acids research*. 41:W597-600.

Men, J., J. Jerwick, P. Wu, M. Chen, A. Alex, Y. Ma, R.E. Tanzi, A. Li, and C. Zhou. 2016. Drosophila Preparation and Longitudinal Imaging of Heart Function In Vivo Using Optical Coherence Microscopy (OCM). *J Vis Exp*.

Mesirca, P., A.G. Torrente, and M.E. Mangoni. 2015. Functional role of voltage gated Ca(2+) channels in heart automaticity. *Frontiers in physiology*. 6:19.

Miller, A. 1950. The internal anatomy and histology of the image ofDrosophila melanogaster. Harrier, New York.

Mitcheson, J.S., J.C. Hancox, and A.J. Levi. 1996. Action potentials, ion channel currents and transverse tubule density in adult rabbit ventricular myocytes maintained for 6 days in cell culture. *Pflugers Arch*. 431:814-827.

Mizuseki, K., and G. Buzsaki. 2013. Preconfigured, skewed distribution of firing rates in the hippocampus and entorhinal cortex. *Cell reports*. 4:1010-1021.

Monnier, V., M. Iche-Torres, M. Rera, V. Contremoulins, C. Guichard, N. Lalevee, H. Tricoire, and L. Perrin. 2012. dJun and Vri/dNFIL3 are major regulators of cardiac aging in Drosophila. *PLoS genetics*. 8:e1003081.

Moretti, A., M. Bellin, A. Welling, C.B. Jung, J.T. Lam, L. Bott-Flugel, T. Dorn, A. Goedel, C. Hohnke, F. Hofmann, M. Seyfarth, D. Sinnecker, A. Schomig, and K.L. Laugwitz. 2010. Patient-specific induced pluripotent stem-cell models for long-QT syndrome. *The New England journal of medicine*. 363:1397-1409.

Mori, M.X., M.G. Erickson, and D.T. Yue. 2004. Functional stoichiometry and local enrichment of calmodulin interacting with Ca2+ channels. *Science*. 304:432-435.

Morotti, S., E. Grandi, A. Summa, K.S. Ginsburg, and D.M. Bers. 2012. Theoretical study of L-type Ca(2+) current inactivation kinetics during action potential repolarization and early afterdepolarizations. *The Journal of physiology*. 590:4465-4481.

Mukherjee, R., and F.G. Spinale. 1998. L-type calcium channel abundance and function with cardiac hypertrophy and failure: a review. *Journal of molecular and cellular cardiology*. 30:1899-1916.

Murphy, L.L., C.M. Campbell, L. Crotti, C.N. Johnson, J.D. Kunic, P.J. Schwartz, W.J. Chazin, and A.L. George. 2013. Abstract 14999: Calmodulin Mutation Associated With Neonatal Long-QT Syndrome Evokes Increased Persistent Sodium Current From a Fetal Nav1.5 Splice Variant. *Circulation*. 128:A14999.

Nakahama, H., and E. Di Pasquale. 2016. Generation of Cardiomyocytes from Pluripotent Stem Cells. *Methods in molecular biology*. 1353:181-190.

Neely, G.G., K. Kuba, A. Cammarato, K. Isobe, S. Amann, L. Zhang, M. Murata, L. Elmen, V. Gupta, S. Arora, R. Sarangi, D. Dan, S. Fujisawa, T. Usami, C.P. Xia, A.C. Keene, N.N. Alayari, H. Yamakawa, U. Elling, C. Berger, M. Novatchkova, R. Koglgruber, K. Fukuda, H. Nishina, M. Isobe, J.A. Pospisilik, Y. Imai, A. Pfeufer, A.A. Hicks, P.P. Pramstaller, S. Subramaniam, A. Kimura, K. Ocorr, R. Bodmer, and J.M. Penninger. 2010. A global in vivo Drosophila RNAi screen identifies NOT3 as a conserved regulator of heart function. *Cell*. 141:142-153.

Neher, E. 1998. Vesicle pools and Ca2+ microdomains: new tools for understanding their roles in neurotransmitter release. *Neuron*. 20:389-399.

Nerbonne, J.M., and R.S. Kass. 2005. Molecular physiology of cardiac repolarization. *Physiological reviews*. 85:1205-1253.

Nicholson, L., G.K. Singh, T. Osterwalder, G.W. Roman, R.L. Davis, and H. Keshishian. 2008. Spatial and temporal control of gene expression in Drosophila using the inducible GeneSwitch GAL4 system. I. Screen for larval nervous system drivers. *Genetics*. 178:215-234.

Nilius, B., P. Hess, J.B. Lansman, and R.W. Tsien. 1985. A novel type of cardiac calcium channel in ventricular cells. *Nature*. 316:443-446.

Nyegaard, M., M.T. Overgaard, M.T. Sondergaard, M. Vranas, E.R. Behr, L.L. Hildebrandt, J. Lund, P.L. Hedley, A.J. Camm, G. Wettrell, I. Fosdal, M. Christiansen, and A.D. Borglum. 2012. Mutations in calmodulin cause ventricular tachycardia and sudden cardiac death. *American journal of human genetics*. 91:703-712.

O'Hara, T., L. Virag, A. Varro, and Y. Rudy. 2011. Simulation of the undiseased human cardiac ventricular action potential: model formulation and experimental validation. *PLoS computational biology*. 7:e1002061.

O'Roak, B.J., L. Vives, S. Girirajan, E. Karakoc, N. Krumm, B.P. Coe, R. Levy, A. Ko, C. Lee, J.D. Smith, E.H. Turner, I.B. Stanaway, B. Vernot, M. Malig, C. Baker, B. Reilly, J.M. Akey, E. Borenstein, M.J. Rieder, D.A. Nickerson, R. Bernier, J. Shendure, and E.E. Eichler. 2012. Sporadic autism exomes reveal a highly interconnected protein network of de novo mutations. *Nature*. 485:246-250.

O'Rourke, B., D.A. Kass, G.F. Tomaselli, S. Kaab, R. Tunin, and E. Marban. 1999. Mechanisms of altered excitation-contraction coupling in canine tachycardia-induced heart failure, I: experimental studies. *Circulation research*. 84:562-570.

Ocorr, K., N.L. Reeves, R.J. Wessells, M. Fink, H.S. Chen, T. Akasaka, S. Yasuda, J.M. Metzger, W. Giles, J.W. Posakony, and R. Bodmer. 2007a. KCNQ potassium channel mutations cause cardiac arrhythmias in Drosophila that mimic the effects of aging. *Proceedings of the National Academy of Sciences of the United States of America*. 104:3943-3948.

Ocorr, K., A. Zambon, Y. Nudell, S. Pineda, S. Diop, M. Tang, T. Akasaka, and E. Taylor. 2017. Age-dependent electrical and morphological remodeling of the Drosophila heart caused by hERG/seizure mutations. *PLoS genetics*. 13:e1006786.

Ocorr, K.A., T. Crawley, G. Gibson, and R. Bodmer. 2007b. Genetic variation for cardiac dysfunction in Drosophila. *PloS one*. 2:e601.

Olcese, R., N. Qin, T. Schneider, A. Neely, X. Wei, E. Stefani, and L. Birnbaumer. 1994. The amino terminus of a calcium channel beta subunit sets rates of channel inactivation independently of the subunit's effect on activation. *Neuron*. 13:1433-1438.

Pandey, U.B., and C.D. Nichols. 2011. Human disease models in Drosophila melanogaster and the role of the fly in therapeutic drug discovery. *Pharmacological reviews*. 63:411-436.

Papaefthmiou, C., and G. Theophilidis. 2001. An in vitro method for recording the electrical activity of the isolated heart of the adult Drosophila melanogaster. *In vitro cellular & developmental biology. Animal*. 37:445-449.

Parker, R.A., and N.G. Berman. 2003. Sample Size. *The American Statistician*. 57:166-170.

Pavot, P., E. Carbognin, and J.R. Martin. 2015. PKA and cAMP/CNG Channels Independently Regulate the Cholinergic Ca(2+)-Response of Drosophila Mushroom Body Neurons(1,2,3). *eNeuro*. 2.

Payandeh, J., T.M. Gamal El-Din, T. Scheuer, N. Zheng, and W.A. Catterall. 2012. Crystal structure of a voltage-gated sodium channel in two potentially inactivated states. *Nature*. 486:135-139.

Peng, I.F., and C.F. Wu. 2007. Drosophila cacophony channels: a major mediator of neuronal Ca2+ currents and a trigger for K+ channel homeostatic regulation. *The Journal of neuroscience : the official journal of the Society for Neuroscience*. 27:1072-1081.

Perez-Reyes, E. 2003. Molecular physiology of low-voltage-activated t-type calcium channels. *Physiological reviews*. 83:117-161.

Perez-Reyes, E., L.L. Cribbs, A. Daud, A.E. Lacerda, J. Barclay, M.P. Williamson, M. Fox, M. Rees, and J.H. Lee. 1998. Molecular characterization of a neuronal low-voltage-activated T-type calcium channel. *Nature*. 391:896-900.

Peterson, B.Z., C.D. DeMaria, J.P. Adelman, and D.T. Yue. 1999. Calmodulin is the Ca2+ sensor for Ca2+ -dependent inactivation of L-type calcium channels. *Neuron*. 22:549-558.

Petryszak, R., T. Burdett, B. Fiorelli, N.A. Fonseca, M. Gonzalez-Porta, E. Hastings, W. Huber, S. Jupp, M. Keays, N. Kryvych, J. McMurry, J.C. Marioni, J. Malone, K. Megy, G. Rustici, A.Y. Tang, J. Taubert, E. Williams, O. Mannion, H.E. Parkinson, and A. Brazma. 2014. Expression Atlas update--a database of gene and transcript expression from microarray- and sequencing-based functional genomics experiments. *Nucleic acids research*. 42:D926-932.

Pfeiffer, B.D., T.T. Ngo, K.L. Hibbard, C. Murphy, A. Jenett, J.W. Truman, and G.M. Rubin. 2010. Refinement of tools for targeted gene expression in Drosophila. *Genetics*. 186:735-755.

Pinggera, A., A. Lieb, B. Benedetti, M. Lampert, S. Monteleone, K.R. Liedl, P. Tuluc, and J. Striessnig. 2015. CACNA1D de novo mutations in autism spectrum disorders activate Cav1.3 L-type calcium channels. *Biological psychiatry*. 77:816-822.

Pinggera, A., and J. Striessnig. 2016. Ca 1.3 (CACNA1D) L-type Ca channel dysfunction in CNS disorders. *The Journal of physiology*.

Pitt, G.S. 2007. Calmodulin and CaMKII as molecular switches for cardiac ion channels. *Cardiovascular research*. 73:641-647.

Pitt, G.S., R.D. Zuhlke, A. Hudmon, H. Schulman, H. Reuter, and R.W. Tsien. 2001. Molecular basis of calmodulin tethering and Ca2+-dependent inactivation of L-type Ca2+ channels. *The Journal of biological chemistry*. 276:30794-30802.

Platzer, J., J. Engel, A. Schrott-Fischer, K. Stephan, S. Bova, H. Chen, H. Zheng, and J. Striessnig. 2000. Congenital deafness and sinoatrial node dysfunction in mice lacking class D L-type Ca2+ channels. *Cell*. 102:89-97.

Qi, L.S., M.H. Larson, L.A. Gilbert, J.A. Doudna, J.S. Weissman, A.P. Arkin, and W.A. Lim. 2013. Repurposing CRISPR as an RNA-guided platform for sequence-specific control of gene expression. *Cell*. 152:1173-1183.

Ran, F.A., L. Cong, W.X. Yan, D.A. Scott, J.S. Gootenberg, A.J. Kriz, B. Zetsche, O. Shalem, X. Wu, K.S. Makarova, E.V. Koonin, P.A. Sharp, and F. Zhang. 2015. In vivo genome editing using Staphylococcus aureus Cas9. *Nature*. 520:186-191.

Raybaud, A., E.E. Baspinar, F. Dionne, Y. Dodier, R. Sauve, and L. Parent. 2007. The role of distal S6 hydrophobic residues in the voltage-dependent gating of CaV2.3 channels. *The Journal of biological chemistry*. 282:27944-27952.

Raybaud, A., Y. Dodier, P. Bissonnette, M. Simoes, D.G. Bichet, R. Sauve, and L. Parent. 2006. The role of the GX9GX3G motif in the gating of high voltage-activated Ca2+ channels. *The Journal of biological chemistry*. 281:39424-39436.

Reed, G.J., N.J. Boczek, S. Etheridge, and M.J. Ackerman. 2014. CALM3 Mutation Associated with Long QT Syndrome. *Heart rhythm : the official journal of the Heart Rhythm Society*.

Reiter, L.T., L. Potocki, S. Chien, M. Gribskov, and E. Bier. 2001. A systematic analysis of human disease-associated gene sequences in Drosophila melanogaster. *Genome research*. 11:1114-1125.

Ren, D., H. Xu, D.F. Eberl, M. Chopra, and L.M. Hall. 1998. A mutation affecting dihydropyridine-sensitive current levels and activation kinetics in Drosophila muscle and mammalian heart calcium channels. *The Journal of neuroscience : the official journal of the Society for Neuroscience*. 18:2335-2341.

Richard, S., F. Leclercq, S. Lemaire, C. Piot, and J. Nargeot. 1998. Ca2+ currents in compensated hypertrophy and heart failure. *Cardiovascular research*. 37:300-311.

Roberts-Crowley, M.L., and A.R. Rittenhouse. 2009. Arachidonic acid inhibition of L-type calcium (CaV1.3b) channels varies with accessory CaVbeta subunits. *The Journal of general physiology*. 133:387-403.

Robinson, S.W., P. Herzyk, J.A. Dow, and D.P. Leader. 2013. FlyAtlas: database of gene expression in the tissues of Drosophila melanogaster. *Nucleic acids research*. 41:D744-750.

Rocchetti, M., L. Sala, L. Dreizehnter, M. Mura, C. Altomare, J. Bernardi, C. Ronchi, S. Severi, A.L. George, P.J. Schwartz, D. Sinnecker, M. Gnecchi, L. Crotti, A. Moretti, and A. Zaza. Human Induced Pluripotent Stem Cells-Derived Cardiomyocytes Carrying CALM1-F142l Mutation Recapitulate LQTS Phenotype in Vitro. *Biophysical journal*. 110:263a.

Roden, D.M. 2006. A new role for calmodulin in ion channel biology. *Circulation research*. 98:979-981.

Rokita, A.G., and M.E. Anderson. 2012. New therapeutic targets in cardiology: arrhythmias and Ca2+/calmodulin-dependent kinase II (CaMKII). *Circulation*. 126:2125-2139.

Roman, G., K. Endo, L. Zong, and R.L. Davis. 2001. P[Switch], a system for spatial and temporal control of gene expression in Drosophila melanogaster. *Proceedings of the National Academy of Sciences of the United States of America*. 98:12602-12607.

Rong, Y.S., and K.G. Golic. 2000. Gene targeting by homologous recombination in Drosophila. *Science*. 288:2013-2018.

Rong, Y.S., and K.G. Golic. 2001. A targeted gene knockout in Drosophila. *Genetics*. 157:1307-1312.

Rossier, M.F. 2016. T-Type Calcium Channel: A Privileged Gate for Calcium Entry and Control of Adrenal Steroidogenesis. *Frontiers in endocrinology*. 7:43.

Rubin, G.M., M.D. Yandell, J.R. Wortman, G.L. Gabor Miklos, C.R. Nelson, I.K. Hariharan, M.E. Fortini, P.W. Li, R. Apweiler, W. Fleischmann, J.M. Cherry, S. Henikoff, M.P. Skupski, S. Misra, M. Ashburner, E. Birney, M.S. Boguski, T. Brody, P. Brokstein, S.E. Celniker, S.A. Chervitz, D. Coates, A. Cravchik, A. Gabrielian, R.F. Galle, W.M. Gelbart, R.A. George, L.S. Goldstein, F. Gong, P. Guan, N.L. Harris, B.A. Hay, R.A. Hoskins, J. Li, Z. Li, R.O. Hynes, S.J. Jones, P.M. Kuehl, B. Lemaitre, J.T. Littleton, D.K. Morrison, C. Mungall, P.H. O'Farrell, O.K. Pickeral, C. Shue, L.B. Vosshall, J. Zhang, Q. Zhao, X.H. Zheng, and S. Lewis. 2000. Comparative genomics of the eukaryotes. *Science*. 287:2204-2215.

Ryglewski, S., K. Lance, R.B. Levine, and C. Duch. 2012. Ca(v)2 channels mediate low and high voltage-activated calcium currents in Drosophila motoneurons. *The Journal of physiology*. 590:809-825.

Sali, A., and T.L. Blundell. 1993. Comparative protein modelling by satisfaction of spatial restraints. *Journal of molecular biology*. 234:779-815.

Sanyal, S., T. Jennings, H. Dowse, and M. Ramaswami. 2006. Conditional mutations in SERCA, the Sarco-endoplasmic reticulum Ca2+-ATPase, alter heart rate and rhythmicity in Drosophila. *Journal of comparative physiology*. 176:253-263.

Sathaye, A., N. Bursac, S. Sheehy, and L. Tung. 2006. Electrical pacing counteracts intrinsic shortening of action potential duration of neonatal rat ventricular cells in culture. *Journal of molecular and cellular cardiology*. 41:633-641.

Satin, J., E.A. Schroder, and S.M. Crump. 2011. L-type calcium channel auto-regulation of transcription. *Cell calcium*. 49:306-313.

Saucerman, J.J., and D.M. Bers. 2008. Calmodulin mediates differential sensitivity of CaMKII and calcineurin to local Ca2+ in cardiac myocytes. *Biophysical journal*. 95:4597-4612.

Saucerman, J.J., and D.M. Bers. 2012. Calmodulin binding proteins provide domains of local Ca2+ signaling in cardiac myocytes. *Journal of molecular and cellular cardiology*. 52:312-316.

Scheel, O., S. Frech, B. Amuzescu, J. Eisfeld, K.H. Lin, and T. Knott. 2014. Action potential characterization of human induced pluripotent stem cell-derived cardiomyocytes using automated patch-clamp technology. *Assay and drug development technologies*. 12:457-469.

Scholl, U.I., G. Goh, G. Stolting, R.C. de Oliveira, M. Choi, J.D. Overton, A.L. Fonseca, R. Korah, L.F. Starker, J.W. Kunstman, M.L. Prasad, E.A. Hartung, N. Mauras, M.R. Benson, T. Brady, J.R. Shapiro, E. Loring, C. Nelson-Williams, S.K. Libutti, S. Mane, P. Hellman, G. Westin, G. Akerstrom, P. Bjorklund, T. Carling, C. Fahlke, P. Hidalgo, and R.P. Lifton. 2013. Somatic and germline CACNA1D calcium channel mutations in aldosterone-producing adenomas and primary aldosteronism. *Nature genetics*. 45:1050-1054.

Scholze, A., T.D. Plant, A.C. Dolphin, and B. Nurnberg. 2001. Functional expression and characterization of a voltage-gated CaV1.3 (alpha1D) calcium channel subunit from an insulin-secreting cell line. *Molecular endocrinology*. 15:1211-1221.

Schroder, F., R. Handrock, D.J. Beuckelmann, S. Hirt, R. Hullin, L. Priebe, R.H. Schwinger, J. Weil, and S. Herzig. 1998. Increased availability and open probability of single L-type calcium channels from failing compared with nonfailing human ventricle. *Circulation*. 98:969-976.

Schulz, J.B. 2007. Mechanisms of neurodegeneration in idiopathic Parkinson's disease. *Parkinsonism & related disorders*. 13 Suppl 3:S306-308.

Shamgar, L., L. Ma, N. Schmitt, Y. Haitin, A. Peretz, R. Wiener, J. Hirsch, O. Pongs, and B. Attali. 2006. Calmodulin is essential for cardiac IKS channel gating and assembly: impaired function in long-QT mutations. *Circulation research*. 98:1055-1063.

Sharma, A., J.C. Wu, and S.M. Wu. 2013. Induced pluripotent stem cell-derived cardiomyocytes for cardiovascular disease modeling and drug screening. *Stem cell research & therapy*. 4:150.

Shen, Y., D. Yu, H. Hiel, P. Liao, D.T. Yue, P.A. Fuchs, and T.W. Soong. 2006. Alternative splicing of the Ca(v)1.3 channel IQ domain, a molecular switch for Ca2+-dependent inactivation within auditory hair cells. *The Journal of neuroscience : the official journal of the Society for Neuroscience*. 26:10690-10699.

Singh, A., M. Gebhart, R. Fritsch, M.J. Sinnegger-Brauns, C. Poggiani, J.C. Hoda, J. Engel, C. Romanin, J. Striessnig, and A. Koschak. 2008. Modulation of voltage- and Ca2+-dependent gating of CaV1.3 L-type calcium channels by alternative splicing of a C-terminal regulatory domain. *The Journal of biological chemistry*. 283:20733-20744.

Sinnecker, D., A. Goedel, T. Dorn, R.J. Dirschinger, A. Moretti, and K.L. Laugwitz. 2013. Modeling long-QT syndromes with iPS cells. *Journal of cardiovascular translational research*. 6:31-36.

Smith, L.A., A.A. Peixoto, E.M. Kramer, A. Villella, and J.C. Hall. 1998. Courtship and visual defects of cacophony mutants reveal functional complexity of a calcium-channel alpha1 subunit in Drosophila. *Genetics*. 149:1407-1426.

Smith, L.A., X.J. Wang, A.A. Peixoto, E.K. Neumann, L.M. Hall, and J.C. Hall. 1996. A Drosophila calcium channel alpha 1 subunit gene maps to a genetic locus associated with behavioral and visual defects. *Journal of Neuroscience*. 16:7868-7879.

Spencer, C.I., S. Baba, K. Nakamura, E.A. Hua, M.A. Sears, C.C. Fu, J. Zhang, S. Balijepalli, K. Tomoda, Y. Hayashi, P. Lizarraga, J. Wojciak, M.M. Scheinman, K. Aalto-Setala, J.C. Makielski, C.T. January, K.E. Healy, T.J. Kamp, S. Yamanaka, and B.R. Conklin. 2014. Calcium transients closely reflect prolonged action potentials in iPSC models of inherited cardiac arrhythmia. *Stem cell reports*. 3:269-281.

Splawski, I., K.W. Timothy, N. Decher, P. Kumar, F.B. Sachse, A.H. Beggs, M.C. Sanguinetti, and M.T. Keating. 2005. Severe arrhythmia disorder caused by cardiac L-type calcium channel mutations. *Proceedings of the National Academy of Sciences of the United States of America*. 102:8089-8096; discussion 8086-8088.

Splawski, I., K.W. Timothy, L.M. Sharpe, N. Decher, P. Kumar, R. Bloise, C. Napolitano, P.J. Schwartz, R.M. Joseph, K. Condouris, H. Tager-Flusberg, S.G. Priori, M.C. Sanguinetti, and M.T. Keating. 2004. Ca(V)1.2 calcium channel dysfunction causes a multisystem disorder including arrhythmia and autism. *Cell*. 119:19-31.

St-Pierre, F., J.D. Marshall, Y. Yang, Y. Gong, M.J. Schnitzer, and M.Z. Lin. 2014. High-fidelity optical reporting of neuronal electrical activity with an ultrafast fluorescent voltage sensor. *Nature neuroscience*. 17:884-889.

St Johnston, D. 2002. The art and design of genetic screens: Drosophila melanogaster. *Nature reviews. Genetics*. 3:176-188.

Stea, A., W.J. Tomlinson, T.W. Soong, E. Bourinet, S.J. Dubel, S.R. Vincent, and T.P. Snutch. 1994. Localization and functional properties of a rat brain alpha 1A calcium channel reflect similarities to neuronal Q- and P-type channels. *Proceedings of the National Academy of Sciences of the United States of America*. 91:10576-10580.

Stemmer, P.M., and C.B. Klee. 1994. Dual calcium ion regulation of calcineurin by calmodulin and calcineurin B. *Biochemistry*. 33:6859-6866.

Stotz, S.C., J. Hamid, R.L. Spaetgens, S.E. Jarvis, and G.W. Zamponi. 2000. Fast inactivation of voltage-dependent calcium channels. A hinged-lid mechanism? *The Journal of biological chemistry*. 275:24575-24582.

Stotz, S.C., S.E. Jarvis, and G.W. Zamponi. 2004. Functional roles of cytoplasmic loops and pore lining transmembrane helices in the voltage-dependent inactivation of HVA calcium channels. *The Journal of physiology*. 554:263-273.

Stotz, S.C., and G.W. Zamponi. 2001. Identification of inactivation determinants in the domain IIS6 region of high voltage-activated calcium channels. *The Journal of biological chemistry*. 276:33001-33010.

Striessnig, J., A. Pinggera, G. Kaur, G. Bock, and P. Tuluc. 2014. L-type Ca channels in heart and brain. *Wiley interdisciplinary reviews. Membrane transport and signaling*. 3:15-38.

Sullivan, K.M., K. Scott, C.S. Zuker, and G.M. Rubin. 2000. The ryanodine receptor is essential for larval development in Drosophila melanogaster. *Proceedings of the National Academy of Sciences of the United States of America*. 97:5942-5947.

Sun, H., N. Leblanc, and S. Nattel. 1997. Mechanisms of inactivation of L-type calcium channels in human atrial myocytes. *The American journal of physiology*. 272:H1625-1635.

Tadross, M.R., M. Ben Johny, and D.T. Yue. 2010. Molecular endpoints of Ca2+/calmodulin-and voltage-dependent inactivation of Ca(v)1.3 channels. *The Journal of general physiology*. 135:197-215.

Tadross, M.R., I.E. Dick, and D.T. Yue. 2008. Mechanism of local and global Ca2+ sensing by calmodulin in complex with a Ca2+ channel. *Cell*. 133:1228-1240.

Tadross, M.R., R.W. Tsien, and D.T. Yue. 2013. Ca2+ channel nanodomains boost local Ca2+ amplitude. *Proceedings of the National Academy of Sciences of the United States of America*. 110:15794-15799.

Taiakina, V., A.N. Boone, J. Fux, A. Senatore, D. Weber-Adrian, J.G. Guillemette, and J.D. Spafford. 2013. The calmodulin-binding, short linear motif, NSCaTE is conserved in L-type channel ancestors of vertebrate Cav1.2 and Cav1.3 channels. *PloS one*. 8:e61765.

Tan, B.Z., F. Jiang, M.Y. Tan, D. Yu, H. Huang, Y. Shen, and T.W. Soong. 2011. Functional characterization of alternative splicing in the C terminus of L-type CaV1.3 channels. *The Journal of biological chemistry*. 286:42725-42735.

Tang, Z.Z., M.C. Liang, S. Lu, D. Yu, C.Y. Yu, D.T. Yue, and T.W. Soong. 2004. Transcript scanning reveals novel and extensive splice variations in human l-type voltage-gated calcium channel, Cav1.2 alpha1 subunit. *The Journal of biological chemistry*. 279:44335-44343.

Tanskanen, A.J., J.L. Greenstein, B. O'Rourke, and R.L. Winslow. 2005. The role of stochastic and modal gating of cardiac L-type Ca2+ channels on early after-depolarizations. *Biophysical journal*. 88:85-95.

Tao, Y., and R.A. Schulz. 2007. Heart development in Drosophila. *Seminars in cell & developmental biology*. 18:3-15.

Taylor, S.S., J.A. Buechler, and W. Yonemoto. 1990. cAMP-dependent protein kinase: framework for a diverse family of regulatory enzymes. *Annual review of biochemistry*. 59:971-1005.

Teleman, A., T. Drakenberg, and S. Forsen. 1986. Kinetics of Ca2+ binding to calmodulin and its tryptic fragments studied by 43Ca-NMR. *Biochimica et biophysica acta*. 873:204-213.

ten Tusscher, K.H., D. Noble, P.J. Noble, and A.V. Panfilov. 2004. A model for human ventricular tissue. *American journal of physiology. Heart and circulatory physiology*. 286:H1573-1589.

ten Tusscher, K.H., and A.V. Panfilov. 2006. Alternans and spiral breakup in a human ventricular tissue model. *American journal of physiology. Heart and circulatory physiology*. 291:H1088-1100.

Van Petegem, F., P.A. Lobo, and C.A. Ahern. 2012. Seeing the forest through the trees: towards a unified view on physiological calcium regulation of voltage-gated sodium channels. *Biophysical journal*. 103:2243-2251.

Van Wagoner, D.R., A.L. Pond, M. Lamorgese, S.S. Rossie, P.M. McCarthy, and J.M. Nerbonne. 1999. Atrial L-type Ca2+ currents and human atrial fibrillation. *Circulation research*. 85:428-436.

Verkhratsky, A., A. Shmigol, S. Kirischuk, N. Pronchuk, and P. Kostyuk. 1994. Age-dependent changes in calcium currents and calcium homeostasis in mammalian neurons. *Annals of the New York Academy of Sciences*. 747:365-381.

Vigoreaux, J.O. 1994. The muscle Z band: lessons in stress management. *Journal of muscle research and cell motility*. 15:237-255.

Viswanathan, M.C., A.C. Blice-Baum, T.K. Sang, and A. Cammarato. 2016. Cardiac-Restricted Expression of VCP/TER94 RNAi or Disease Alleles Perturbs Drosophila Heart Structure and Impairs Function. *Journal of cardiovascular development and disease*. 3.

Vogler, G., and K. Ocorr. 2009. Visualizing the beating heart in Drosophila. *J Vis Exp*.

Wang, B., K.M. Sullivan, and K. Beckingham. 2003. Drosophila calmodulin mutants with specific defects in the musculature or in the nervous system. *Genetics*. 165:1255-1268.

Wolf, M.J., H. Amrein, J.A. Izatt, M.A. Choma, M.C. Reedy, and H.A. Rockman. 2006. Drosophila as a model for the identification of genes causing adult human heart disease. *Proceedings of the National Academy of Sciences of the United States of America*. 103:1394-1399.

Wolf, M.J., and H.A. Rockman. Drosophila, genetic screens, and cardiac function. *Circulation research*. 109:794-806.

Worrell, J.W., and R.B. Levine. 2008. Characterization of voltage-dependent Ca2+ currents in identified Drosophila motoneurons in situ. *Journal of neurophysiology*. 100:868-878.

Wu, M., and T.N. Sato. 2008. On the mechanics of cardiac function of Drosophila embryo. *PloS one*. 3:e4045.

Xia, X.M., B. Fakler, A. Rivard, G. Wayman, T. Johnson-Pais, J.E. Keen, T. Ishii, B. Hirschberg, C.T. Bond, S. Lutsenko, J. Maylie, and J.P. Adelman. 1998. Mechanism of calcium gating in small-conductance calcium-activated potassium channels. *Nature*. 395:503-507.

Xie, L.H., and J.N. Weiss. 2009. Arrhythmogenic consequences of intracellular calcium waves. *American journal of physiology. Heart and circulatory physiology*. 297:H997-H1002.

Xu, W., and D. Lipscombe. 2001. Neuronal Ca(V)1.3alpha(1) L-type channels activate at relatively hyperpolarized membrane potentials and are incompletely inhibited by

dihydropyridines. *The Journal of neuroscience : the official journal of the Society for Neuroscience*. 21:5944-5951.

Yang, P.S., B.A. Alseikhan, H. Hiel, L. Grant, M.X. Mori, W. Yang, P.A. Fuchs, and D.T. Yue. 2006. Switching of Ca2+-dependent inactivation of Ca(v)1.3 channels by calcium binding proteins of auditory hair cells. *The Journal of neuroscience : the official journal of the Society for Neuroscience*. 26:10677-10689.

Yazawa, M., B. Hsueh, X. Jia, A.M. Pasca, J.A. Bernstein, J. Hallmayer, and R.E. Dolmetsch. 2011. Using induced pluripotent stem cells to investigate cardiac phenotypes in Timothy syndrome. *Nature*. 471:230-234.

Yazawa, M., M. Ikura, K. Hikichi, L. Ying, and K. Yagi. 1987. Communication between two globular domains of calmodulin in the presence of mastoparan or caldesmon fragment. Ca2+ binding and 1H NMR. *The Journal of biological chemistry*. 262:10951-10954.

Ye, Z., C.F. Liu, L. Lanikova, S.N. Dowey, C. He, X. Huang, R.A. Brodsky, J.L. Spivak, J.T. Prchal, and L. Cheng. 2014. Differential sensitivity to JAK inhibitory drugs by isogenic human erythroblasts and hematopoietic progenitors generated from patient-specific induced pluripotent stem cells. *Stem cells*. 32:269-278.

Yin, G., F. Hassan, A.R. Haroun, L.L. Murphy, L. Crotti, P.J. Schwartz, A.L. George, and J. Satin. 2014. Arrhythmogenic calmodulin mutations disrupt intracellular cardiomyocyte Ca2+ regulation by distinct mechanisms. *Journal of the American Heart Association*. 3:e000996.

Yue, D.T., P.H. Backx, and J.P. Imredy. 1990. Calcium-sensitive inactivation in the gating of single calcium channels. *Science*. 250:1735-1738.

Yue, L., J. Feng, R. Gaspo, G.R. Li, Z. Wang, and S. Nattel. 1997. Ionic remodeling underlying action potential changes in a canine model of atrial fibrillation. *Circulation research*. 81:512-525.

Zamponi, G.W., J. Striessnig, A. Koschak, and A.C. Dolphin. 2015. The Physiology, Pathology, and Pharmacology of Voltage-Gated Calcium Channels and Their Future Therapeutic Potential. *Pharmacological reviews*. 67:821-870.

Zhang, L., H. Yang, H. Zhao, and C. Zhao. 2011. Calcium-related signaling pathways contributed to dopamine-induced cortical neuron apoptosis. *Neurochemistry international*. 58:281-294.

Zhou, Z., E.J. Hong, S. Cohen, W.N. Zhao, H.Y. Ho, L. Schmidt, W.G. Chen, Y. Lin, E. Savner, E.C. Griffith, L. Hu, J.A. Steen, C.J. Weitz, and M.E. Greenberg. 2006. Brain-specific phosphorylation of MeCP2 regulates activity-dependent Bdnf transcription, dendritic growth, and spine maturation. *Neuron*. 52:255-269.

Zornik, E., K. Paisley, and R. Nichols. 1999. Neural transmitters and a peptide modulate Drosophila heart rate. *Peptides*. 20:45-51.

Zuhlke, R.D., G.S. Pitt, K. Deisseroth, R.W. Tsien, and H. Reuter. 1999. Calmodulin supports both inactivation and facilitation of L-type calcium channels. *Nature*. 399:159-162.

CURRICULUM VITAE

Worawan (Boombim) Limpitikul

2723 N. Charles Street, Apt. 3A, Baltimore, MD 21218; Tel: (443)854-4864; Email: wlimpit1@jhmi.edu

Personal Details

Born May 12, 1986 in Songkhla, Thailand. Moved to the USA at age 18.

Education

Johns Hopkins University School of Medicine (JHSOM), Baltimore, MD — 2009 – Present

MD-PhD Program
M.D., Anticipated May 2018
Ph.D., Biomedical Engineering, Anticipated May 2018

Johns Hopkins University (JHU), Baltimore, MD — 2005 – 2009

B.S., Biomedical Engineering (Primary Major), **graduated top 10% of class**
B.A., Public Health Studies (Secondary Major)

Honors and Awards

Siebel Scholarship, Siebel Scholars Foundation — Sep 2017

For distinguished students of business, computer science, and bioengineering

David Yue Young Investigator Award, 2017 Young Investigators' Day, JHSOM — May 2017

For exemplary research in biomedical science

Young Investigator Award, Heart Rhythm Society (HRS), 37th Annual Meeting — May 2016

Received the first place prize for a research presentation

Courts K. Cleveland Young Investigator Award, Sudden Arrhythmic Death Syndrome (SADS) Foundation, 9th Annual Meeting — May 2016

For outstanding basic science research into cardiac channelopathies

Student Research Achievement Award, **Biophysical Society**, 60th Annual Meeting — Feb 2016

Best Poster Award for Emerging Scientists, International Symposium on Calcium Binding Proteins and Calcium Function in Health and Disease — June 2015

First Place in Poster Presentation Competition, 6th Annual Johns Hopkins Cardiology Retreat, JHSOM — May 2015

Travel Award, Graduate Student Association, JHSOM — May 2015

Emerging Women's Leadership Program (EWLP), JHSOM — Sep 2014 – May 2015

One of three students selected to participate in a professional development program designed for faculty members to promote leadership skills in early-career female scientists

Excellence in Medical Student Research Award, JHSOM — Jan 2011

Given for the top presentations during the Johns Hopkins Medical Student Research Day

Richard J. Johns Award, JHU

For outstanding academic achievement (top 10% of the class) in Biomedical Engineering — May 2009

Tau Beta Pi, the National Engineering Honor Society — Sep 2007

Alpha Epsilon Delta, the National Premedical Honor Society — Mar 2007

Gold Medal, 15th International Biology Olympiad (IBO2004), Brisbane, Australia — Jul 2004

International scientific competition for high school students

Fellowships and Scholarships

American Heart Association One-Year Predoctoral Fellowship — Jul 2015 – Jun 2016

Tuition and stipend awarded to study the mechanism of and devise therapies for the new form of long-QT syndrome

American Heart Association Two-Year Predoctoral Fellowship — Jul 2013 – Jun 2015

Tuition and stipend awarded to develop *Drosophila* as a new animal model to study the regulation of cardiac calcium channels

Albert Schweitzer Fellowship — Aug 2011 – Jul 2012

Year-long interdisciplinary fellowship promoting health-related community service and leadership development

Dean's Summer Research Fund, JHSOM — May 2010 – Aug 2010

Stipend supporting medical students in summer research projects

Provost Undergraduate Research Award, JHU — May 2007 – Aug 2007

Stipend given to selected excellent research projects conducted by undergraduates

King's Scholarship, Thailand — 2004

Highly selective full scholarship with five recipients selected from across the country to study abroad through Bachelor's and Medical degrees

Research Experience

PhD Thesis Work, Calcium Signals Laboratory, under supervision of Dr. David T. Yue — Nov 2011 – Present

- Utilized cutting-edge human induced pluripotent stem cell and genome editing techniques to elucidate the mechanism behind a new form of long-QT syndrome associated with calmodulin mutations
- Devised a novel personalized therapeutic strategy for the treatment of calmodulinopathic long-QT (patent submission pending)
- Constructed a computational model to explain calcium/calmodulin-dependent inactivation (CDI) of cardiac calcium channels
- Developed *Drosophila* as an alternative model for studying calcium channel regulation *in situ*

- Mentored undergraduate students, junior graduate students, and research specialists in conducting research

Medical Student Researcher, **Prospective Observational Study of Implantable Cardioverter Defibrillator (PROSE-ICD),** under supervision of Dr. Gordon F. Tomaselli

Mar 2010 – Mar 2012

- Established serum biomarkers and ECG metrics to predict sudden cardiac death in over 800 patients with ICD implantation
- Developed software tools to analyze over 3,000 ECG recordings and serum biomarker measurements

Undergraduate Researcher, **Cardiac Bioelectric Systems Laboratory**, under supervision of Dr. Leslie Tung

Jan 2006 – May 2009

- Carried out an independent project as an undergraduate student which led to a first-author publication
- Investigated the effect of electrical stimulation on the electrophysiological maturation of mouse embryonic stem cell-derived cardiomyocytes

Work Experience

Student Preceptorship Program, JHSOM

Sep 2017 – Present

- Provide 3 first-year medical students with an early exposure to clinical medicine
- Design teaching plan and hands-on activities in the hospital setting based on the students' needs and interest

Medical Education Scholar, Department of Medicine, JHSOM

May 2017 – Present

- Develop the clerkship curriculum for medical students in internal medicine, in collaboration with the clerkship director
- Lecture 25 medical students during each quarter
- Analyze the fidelity of objective structured clinical examination (OSCE)

Editor, American Medical Student Research Journal (AMSRJ), Louisiana State University, Health Shreveport School of Medicine, Shreveport, LA

May 2014 – Present

- Selected member of the editorial board
- Review manuscripts and make decisions on publication
- Coordinate faculty and student reviews of manuscripts

Teaching Assistant, System Bioengineering I, Biomedical Engineering, JHU

Sep 2013 – Dec 2013

- Taught weekly recitation sessions and administered office hours for over 50 students
- Developed grading rubrics and graded midterm and final examinations for over 100 students

Organizer, Health Disparity Course, JHSOM

Apr 2010 – Aug 2010

- Chosen to organize an intersession course for first-year medical students
- Assessed the needs of local communities and arranged hands-on opportunities for medical students to volunteer

- Designed and led discussion groups for students to raise awareness for health disparity issues in local communities

Teaching Assistant, Freshman Modeling and Design, Biomedical Engineering, JHU — Sep 2007 – Dec 2007

- Taught and supervised students on experiments with emphasis on engineering and problem solving skills

Translator and Coder, Development of Cross-Cultural Measures of Parental Regulation Project for the World Health Organization, Johns Hopkins School of Public Health — Sep 2006 – Dec 2006

- Translated responses to questionnaires distributed to adolescents in Thailand in a manner designed to preserve and convey both linguistic and cultural aspects
- Categorized responses to questionnaires and created a code which was used as a tool to convert qualitative data to quantitative data

Leadership and Community Outreach Experience

President, MD-PhD Advising Program, JHSOM — Mar 2015 – Present

- Recruit over 40 MD-PhD faculty and clinical fellows to serve as advisors
- Pair up over 100 MD-PhD students and advisors and organize advising sessions

Supervisor, Thread, JHSOM — Aug 2009 – Dec 2014

- Led a group of 20 mentors and 4 leaders to tutor and mentor high school students with psychosocial challenges and at risk of high school dropout
- Supervised volunteers in day-to-day activities and cultivated their leadership skills

Executive Committee, Association of Woman Student MD-PhDs (AWSM), JHSOM — Mar 2014 – Feb 2015

- Organized events to promote mentorship among female faculty advisors and students at Johns Hopkins University and University of Maryland Schools of Medicine
- Promoted the admission of qualified female candidates into the Medical Scientist Training Program

Leader of the Healthy Lifestyle Program, Bienestar Baltimore — Aug 2010 – July 2012

- Developed a curriculum for cardiovascular health education based on the assessed health needs of local Latino communities
- Led a group of over 20 volunteers to give weekly *charlas*, a series of cardiovascular health-related discussions in Spanish, healthy cooking classes, and weekly walking groups for over 40 clients

President, Peer Advising Program, College Advisory Program, JHSOM — Mar 2010 – Feb 2011

- Elected by 30 peer mentors to organize events promoting relationship building among 30 medical student advisors and 120 advisees

Executive Board Member, Internal Medicine Interest Group, JHSOM — Mar 2010 – Feb 2011

- Planned events to promote an understanding of the internal medicine career path for over 40 students

Supervisor, JHU Toturial Project, JHU — Sep 2005 – May 2009

- Supervised 6 tutors to provide mathematics and English tutoring sessions to elementary school students from Baltimore area
- Evaluated elementary school students on their academic standing and created tutoring plans based on their needs
- Designed and organized enrichment activities such as hands-on scientific experiments for elementary school students

Professional Memberships

American Medical Association	2016 – Present
Heart Rhythm Society	2015 – Present
American Heart Association	2013 – 2016
Biophysical Society	2012 – 2016

Publications

Limpitikul WB, Dick IE, Greenstein JL, Winslow RL, Yue DT. "Bi-lobal calmodulation of L-type Ca^{2+} channels." Journal of General Physiology. *Manuscript in Preparation*

Limpitikul WB, Viswanathan MC, O'Rourke B, Yue DT, Cammarato A. "Conservation of cardiac L-type Ca^{2+} channels and their regulation in *Drosophila*: a novel genetically pliable channelopathic model." Journal of Molecular and Cellular Cardiology. *In Revision*

Blice-Baum AC, Vogler G, Viswanathan MC, Trinh B, **Limpitikul WB**, Cammarato A. "Gettin' FISHy with *FOXO*: Quantifying tissue-specific overexpression of *FOXO* in *Drosophila* via mRNA fluorescence *in situ* hybridization using branched DNA probe technology." *Methods in Molecular Biology.* Ed. John Walker. Springer, *In Press*

Limpitikul WB, Ong CS, Tomaselli GF. **"**Neuromuscular disease: cardiac manifestations and sudden death risk." Cardiac *Electrophysiology Clinics: Contemporary Challenges in Sudden Cardiac Death*. Ed. Mohammad Shenasa, Ed. N.A. Mark Estes III, Ed. Gordon F. Tomaselli. Philadelphia: Elsevier, 2017. 731-747. Print.

Limpitikul WB, Dick IE, Tester DJ, Boczek NJ, Limphong P, Yang W, Choi M, Babich J, DiSilvestre D, Kanter RJ, Tomaselli GF, Ackerman MJ, and Yue DT. "A precision medicine approach to the rescue of function in malignant calmodulinopathic long QT syndrome." Circulation Research 120(1): 39-48 (2017).

Limpitikul WB*, Dick IE, Ben-Johny M, Yue DT. "An autism-associated mutation in $Ca_V1.3$ channels has opposing effects on voltage- and Ca^{2+}-dependent regulation." Scientific Reports 6:27235 (2016). ***Corresponding Author.**

Demazumder D, **Limpitikul WB**, Dorante M, Dey S, Mukhopadhyay B, Zhang Y, Moorman JR, Cheng A, Berger RD, Guallar E, Jones SR, Tomaselli GF. "Entropy of cardiac repolarization predicts ventricular arrhythmias and mortality in patients receiving an implantable cardioverter-defibrillator for primary prevention of sudden death." Europace 18(12):1818-1828 (2016).

Dick IE, **Limpitikul WB**, Niu J, Banerjee R, Issa JB, Ben-Johny M, Adams PJ, Kang PW, Lee SR, Sang L, Yang W, Babich J, Zhang M, Bazazzi H, Yue NC, Tomaselli GF. "A rendezvous with the queen of ion channels: Three decades of ion channel research by David T. Yue and his Calcium Signals Laboratory." Channels 10(1): 1-13 (2015).

Ben-Johny M, Dick IE, Sang L, **Limpitikul WB**, Kang PW, Niu J, Banerjee R, Yang W, Babich JS, Issa JB, Lee SR, Namkung H, Li J, Zhang M, Yang PS, Bazzazi H, Adams PJ, Joshi-Mukherjee R, Yue DN, Yue DT. "Towards a unified theory of calmodulin regulation (calmodulation) of voltage-gated calcium and sodium channels." Current Molecular Pharmacology 8(2): 188-205 (2015).

Limpitikul WB, Dick IE, Joshi-Mukherjee R, Overgaard MT, George AL Jr, Yue DT. "Calmodulin mutations associated with long QT syndrome prevent inactivation of cardiac L-type Ca^{2+} currents and promote proarrhythmic behavior in ventricular myocytes." Journal of Molecular and Cellular Cardiology 74: 115-124 (2014).

Limpitikul W, Christoforou N, Thompson S, Gearhart J, Tung L, Lipke E. "Influence of electromechanical activity on cardiac differentiation of mouse embryonic stem cells." Cardiovascular Engineering and Technology 1(3): 179-193, (2010).

Platform Presentations

Limpitikul WB, Limphong P, Dick IE, Choi M, Yang W, Babich J, DiSilvestre D, Tester DJ, Ackerman MJ, Tomaselli GF, and Yue DT. "A Foray into personalized medicine: rescue of function in calmodulinopathy iPSC-derived cardiomyocytes." Heart Rhythm Society 37th Annual Scientific Sessions, San Francisco, CA, May 2016. **(Young Investigator Award)**

Limpitikul W, Joshi-Mukherjee R, Dick IE, George AL Jr, Yue DT. "Calmodulin mutants associated with long QT syndrome suppress inactivation of cardiac L-type Ca^{2+} currents and prolong action potentials in guinea-pig ventricular myocytes." American Heart Association's Scientific Sessions 2013, Dallas, TX, November 2013.

DeMazumder D, **Limpitikul W**, Lake DE, Moorman JR, Tomaselli GF. "A novel strategy for prediction of sudden cardiac death in patients with heart failure receiving cardiac resynchronization therapy." Heart Rhythm Society 33rd Annual Scientific Sessions, Boston, MA, May 2012.

Lipke EA, Christoforou N, **Limpitikul W**, Gearhart JD, Tung L. "Electrophysiological characterization of embryonic stem cell derived cardiomyocytes for use in cardiac tissue engineering." American Institute of Chemical Engineers Annual Meeting, Salt Lake City, UT, November 2007.

Poster Presentations

Limpitikul WB, Limphong P, Dick IE, Choi M, Yang W, Babich J, Tester DJ, Ackerman MJ, Tomaselli GF, Yue DT. "Functional rescue of calmodulinopathy iPSC-derived cardiomyocytes -- a foray into personalized medicine." Biophysical Society 60th Annual Meeting, San Diego, CA, February 2016. **(Student Research**

Achievement Award)

Limpitikul WB, Viswanathan MC, Cammarato A, Yue DT."Conservation of cardiac L-type Ca^{2+} channels and their modulation in *Drosophila*: a novel genetically pliable channelopathic model." American Heart Association's Basic Cardiovascular Sciences Scientific Sessions, New Orleans, LA, July 2015.**(Travel Award)**

Limpitikul WB, Dick IE, Issa JB, Boczek NJ, Tester DJ, Ackerman MJ, Yue DT. "IPSC-derived cardiomyocytes from calmodulinopathy patients demonstrate deficits in L-type channel regulations." International Symposium on Calcium Binding Proteins and Calcium Function in Health and Disease, Nashville, TN, May 2015.**(Best Poster Award for Emerging Scientists)**

Limpitikul WB, Viswanathan MC, Blice-Baum AC, Cammarato A, Yue DT."Conservation of cardiac Ca^{2+} channels and their modulations across *Drosophila* and mammals: a novel technique to probe Ca^{2+} channel electrophysiology." 6th Annual Johns Hopkins Cardiology Retreat. Johns Hopkins University School of Medicine, Baltimore, MD, May 2015.**(First Place in Poster Presentation Competition)**

Limpitikul WB, Yue DT. "Ca^{2+} sensitivity of L-type calcium channel inactivation probed by Ca^{2+} photouncaging --- Window onto Calmodulinopathies." Biophysical Society 58th Annual Meeting, San Francisco, CA, February 2014.

Limpitikul W, Johny MB, Yue DT. "Autism-Associated point mutation in $Ca_V1.3$ calcium channels alters their regulation by Ca^{2+}." Biophysical Society 57th Annual Meeting, Philadelphia, PA, February 2013.

DeMazumder D, **Limpitikul W**, Dorante D, Mukhopadhyay B, Dey S, Berger RD, Guallar E, Lake DE, Jones S, Moorman JR, Tomaselli GF. "A novel strategy based on dynamic analysis of cardiac repolarization predicts mortality in patients with implantable cardioverter-defibrillators." American Heart Association's Scientific Sessions 2012, Los Angeles, CA, November 2012.

Limpitikul W, Dalal D, Tjong F, Butcher B, Tomaselli GF. "High Levels of Serum Biomarkers for Inflammation (C-reactive protein, Interleukin-6) and Myocardial Injury (Cardiac Troponin T, Myoglobin) Are Strong Predictors for Sudden Cardiac Death." Medical Student Research Day, Johns Hopkins University School of Medicine, Baltimore, MD, January 2011.**(Excellence in Medical Student Research Award)**

Limpitikul W, Lipke EA, Edmonds S, Tung L. "Does suppression of spontaneous beating of mouse embryonic stem cells during differentiation into cardiomyocytes affect their electrophysiological function?" Biomedical Engineering Society 2008 Annual Meeting, St. Louis, MO, October 2008.**(Travel Award)**

Lipke EA, Christoforou N, **Limpitikul W**, Gearhart JD, Tung L. "Derivation and functional characterization of cardiomyocytes from embryonic stem cells." Biomedical Engineering Society 2007 Annual Meeting, Los Angeles, CA, September 2007.